Origin, evolution and significance of anhydrite-bearing vein arrays and breccias, Lienetz orebody, Lihir gold deposit, Papua New Guinea

Stephanie Sykora
BSc

Submitted in fulfillment of the requirements for the degree of
Doctor of Philosophy (PhD)

December, 2016

University of Tasmania

CODES | TMVC

Declaration of Originality

This thesis contains no material which has been accepted for a degree or diploma by the University or any other institution, except by way of background information and duly acknowledged in the thesis, and to the best of my knowledge and belief no material previously published or written by another person except where due acknowledgment is made in the text of the thesis.

Date: ***December 23rd 2016***

Signature:

Authority of Access

This thesis is not made available for distribution, copying or loan for 1.5 years after the date this statement was signed; following that time, this thesis may be made available for loan and limited copy and communication in accordance with the Copyright Act of 1968.

Date: ***December 23rd 2016***

Signature:

Abstract

The Lihir gold deposit (also known as Ladolam), has a 56 Moz resource and is the world's largest alkalic gold deposit in terms of contained gold. It is located on Lihir Island, part of the Tabar-Lihir-Tanga-Feni island chain, New Ireland Province, Papua New Guinea.

The Tabar-Lihir-Tanga-Feni island chain formed in a complex tectonic environment over the past four million years. Docking of the colossal Ontong Java Plateau at the Melanesian trench during the Miocene caused near-complete cessation of magmatism and a reversal of subduction polarity, forming the markedly northward-convex New Britain Trench. Pliocene to Recent subduction along the New Britain Trench was coeval with sinistral transposition of New Ireland relative to New Britain, and the formation of the Tabar-Lihir-Tanga-Feni island chain. Lavas of Lihir and other islands in the chain are shoshonitic, alkali- and volatile-rich, silica-undersaturated, and highly oxidized with elevated large-ion lithophile element contents. Their hybrid geochemical characteristics are consistent with partial melting of an already metasomatized, oxidized and hydrous mantle wedge originally formed by the Miocene Melanesian subduction zone.

Lihir Island is composed of five volcanic centers, presently inactive. The Luise volcano consists of a 4 × 3.5 km wide amphitheater, elongated and breached to the northeast. This is inferred to be a remnant of the original ~ 1.1 km high volcanic cone that underwent sector collapse(s). The Lihir gold deposit is situated in the foot wall of the sector collapse detachment surface and consists of several adjacent and partly overlapping orebodies (Lienetz, Minifie, Kapit, Kapit NE, etc.).

The sector collapse event(s) marked an important stage in the deposit's evolution by superimposing late-stage, gold-rich, alkalic low-sulfidation epithermal mineralization upon early-stage, porphyry-style alteration. A broad, three-fold vertical alteration zonation at Lihir is interpreted to represent this evolution. With increasing depth, the alteration zones consist of: (1) a ~ 0.2 Ma to 0.0 Ma, surficial, generally barren, steam-heated clay alteration zone that is a product of modern high-temperature geothermal activity; (2) a ~ 0.6 to 0.2 Ma, high-grade (> 3 g/t Au), refractory sulfide and adularia alteration zone that represents the ancient epithermal environment; and (3) a ~ 0.9 to 0.3 Ma, comparatively low-grade (< 1 g/t Au) zone rich in anhydrite ± carbonate, coupled with biotite alteration, that represents the ancient porphyry-style environment. Recent volcanism has occurred during the modern geothermal-stage, with the emplacement of several diatreme breccia bodies.

Early porphyry-style hydrothermal activity in the Lienetz orebody resulted in a magmatic-hydrothermal breccia complex and associated hydrothermal veins and breccia veins, most of which contain abundant anhydrite. An eight-stage vein paragenesis, linked with a five-stage breccia paragenesis, records the transition from porphyry-style to epithermal conditions.

A spectacular anhydrite ± carbonate vein array is exposed in the deeper levels of the Lienetz open pit. They reveal a dynamic structural evolution, where veins were reactivated, but with grossly similar geometries and kinematic histories. Overall, discrete sets of veins record a history of early compression and protracted, or multistage, northwest-directed extension, with predominant east-northeast and northeast strikes for both veins and faults.

Early northwest and/or southeast-directed compression and west-northwest-directed extension is evident from low-angle thrust faults and tensile vein arrays with both sub-vertical and sub-horizontal dips. Early vein formation occurred in the porphyry-style environment, under low differential stress, an oscillating sub-horizontal to sub-vertical σ_1, and temporarily elevated fluid-pressures that resulted from mineral sealing.

Protracted, or multistage, northwest-directed extension with a mostly sub-vertical σ_1 predominated for the rest of the porphyry-stage and into the epithermal-stage vein paragenesis at Lienetz. This is best documented by the principal vein array at Lienetz, which consists of large hybrid and shear veins with low-angle dips (~ 30°) to the north. Linking these large, low-angle veins are sets of tensile to hybrid veins and breccia veins with high-angle dips (~ 65°) to the northwest. Kinematic indicators record dominantly extensional displacement, with north- to northwest-directed, top-block down sense of shear.

Significant modification of the early formed veins and breccias occurred during the transition from porphyry-style to epithermal conditions, leading to recrystallization, dissolution seams, stylolites, volume loss and solution collapse breccias. Modification was most likely facilitated by anhydrite dissolution and recrystallization, probably due to changing temperatures ± pressures ± salinities. The modified veins localized shearing, and their sub-horizontal to low-angle northward-dipping geometry may have had some control on the geometry of, and lubrication for, the sector collapse event(s). However, the modified veins appear not to be kinematically linked to the northeast-directed collapse event(s) due to their top-block down to the northwest or north-northwest sense of shear.

High-grade, epithermal-style, gold mineralization followed vein modification and sector collapse(s). Mineralization was partly facilitated by preconditioning provided by porphyry-stage events, as auriferous hydrothermal fluids utilized permeable and porous open spaces and cavities that were created by the dissolution of early formed anhydrite. Mineralization was also localized at depth by northeast-striking faults. Continued extension with top-block down to the northwest preferentially reactivated the principal vein array with low-angle dips to the north. Porphyry-stage veins were modified during epithermal mineralization due to reactivation under extensional conditions. Reactivation produced northeast-striking tensile to hybrid veins and breccia veins with high-angle dips and rhombic dilational jogs that localized high-grade gold.

The northeast to east-northeast-striking structural grain, evident at both the regional island scale and the deposit scale, was inherited from the basement. These structures were weaknesses that were reactivated throughout the evolution of Lienetz. Similarly oriented deep-seated faults are considered to have contributed to the northeast-elongation of the volcanic amphitheater, and were fundamental for the structural control of vein formation and gold localization.

The $\delta^{34}S$ values of anhydrite and pyrite from Lihir are consistent with deposition from oxidized magmatic-hydrothermal fluids ($\delta^{34}S_{sulfate}$ from 7.2 to 13.6 ‰, and $\delta^{34}S_{sulfide}$ from −13.0 to 3.6 ‰). $^{87}Sr/^{86}Sr$ values indicate a primitive (mantle) source. The $\delta^{34}S_{sulfate}$ values increased (+1.3 ‰) from porphyry-style to epithermal conditions with time. The $\delta^{34}S_{sulfide}$ values of pyrite grains are heterogeneous or bimodal, and vary significantly at the microscopic scale, and in time and space.

Late-stage epithermal mineralization superimposed on early porphyry-style alteration created complications with regards to ore processing, specifically with regards to the difficulties in mineral processing of the refractory gold-rich pyritic ore. Early generations of coarse-grained pyrites are interpreted to have formed under porphyry-style conditions. Later generations of pyrites display oscillatory zones and are interpreted to have formed under epithermal conditions. The porphyry-stage pyrite grains are relatively trace element poor, except for Co, Ni and Se, whereas the epithermal pyrite grains are enriched in As, Mo, Ag, Sb, Au and Tl. Most of the pyrite grains in the anhydrite-rich zone at Lienetz are composite grains, and display some textural and geochemical evidence of modification. The composite pyrite grains have porphyry-stage trace element-depleted cores, and epithermal-stage delicate banded rims enriched in gold, arsenic and other trace elements. Because gold is concentrated only along their rims, these pyrite grains can be subjected to a shorter period of oxidation and leaching in order to liberate most of their gold. In contrast, for areas dominated by high-grade epithermal-stage mineralization, pyrite grains are arsenic- and gold-rich throughout, and thus require longer oxidation and processing time. Understanding gold deportment in telescoped deposits is therefore essential for optimizing mineral processing and can impact significantly on the economics of mining these complex, hybrid ore deposits.

The unique characteristics of the Lihir gold deposit, in particular the preserved relationships of hybrid ore and volcanic architecture, provides insights into transitional processes between porphyry and epithermal end-members. Reactivated structures and anhydrite dissolution were significant factors in gold mineralization at Lihir. As such, they should be regarded in the exploration and understanding of other magmatic-hydrothermal ore deposits.

Acknowledgments

Thank you first and foremost to my supervisors, David Cooke and David Selley. I have learned so much, and have had so many great opportunities, thanks to the 'Daves'. I apologize to them for all the hassle I must have caused as a stubborn PhD student. The time and effort they put into my PhD candidature, considering how busy they both are, was a most phenomenal feat and I am forever grateful for their support.

I would humbly like to acknowledge and thank Newcrest Mining Ltd. for their financial and logistic support of this research, particularly Anthony Harris and Karyn Gardner. I would also like to thank all the personnel at Newcrest and at the Lihir gold mine who have been a huge help to me. Tenkyu tru: Fiona Karaut, Paul Napier, Pamella Pinia, Chris Allickson, Dorothy Penny, Jon Rutter, Kellis Manating, Martin Kanaka, Hugo Baibai, Julius Pakule, Maxine Kumbamong, Mark Reynolds, Brigette Hendersonhall, Dinah Maibani, Dinella Bran, David Cesar, Lynell Stevens, Stephen Perkins, Rob Taube, Will Clarke, Soel Snowball, Nick Fitzpatrick, as well as many others. Thanks especially to all the folks at Lihir who helped with spotting while I mapped in the open pit, and at the core shed with moving and cutting rocks.

I am lucky to have been able to interact with (i.e., pester) all the brilliant and lovely people here at CODES, Earth Sciences and the CSL. For their conversions, inputs and help, my sincerest thanks goes to Sebastien Meffre, Sarah Gilbert, Anthony Crawford, José Piquer, Michael Roach, Trevor Falloon, Al Cuison, Sasha Stepanov, Rob Scott, Paul Olin, Bruce Gemmell, Ron Berry, Karsten Goemann, Sandrin Feig, Nic Jansen, Ross Large, Jeffery Steadman, Jocelyn McPhie, Christian Dietz, Anya Reading, Izzy Von Lichtan, Catherine McGoldrick, Garry Davidson, Keith Dobson, Jane Higgins, Helen Scott and more!

I am grateful as well to the people who have contributed to my thesis via email conversations, sample locations, reviews of written documents, troubleshooting and help with software, among many other things. Thank you: John Thompson, Julie Rowland, Stuart Simmons, Andrew Cantwell, Scott Halley, Daniel Müller, Martin Gysel and Mark Hannington. Also, I would kindly like to thank the reviewers of this thesis.

Thank you to the various organizations that allowed me to present research at conferences, and thank you to the Society of Economic Geologists and Anglo American for the graduate student fellowship.

A huge thanks to my friends and colleagues here in Tasmania: Erin (for both your friendship and help regarding Lihir), Evan, Angela, Nathan, Emily, Lennart, Anika, Josh, Nic, Indrani, Jacob, Marc, Billy, Ayesha, Shawn, Jing, Wei, Martin, Doreen, Stu and the family, Mike, Esi, Dan, Selina, José, Niall, Jen, Subira, Sam, Claire, Rachel and everyone else who was kind and helpful to me during my time here.

And most importantly, thank you to my family, especially my mom and dad. I know it was not ideal having your daughter so far south of north, but your constant love and support is beyond words. Lastly, I would like to dedicate my PhD to Oko, who always believed I would do this and I'm sure would be proud...

Table of contents

*Appendices are available on-line in a cloud storage as part of the TMVC hub, University of Tasmania, Australia. Please email Stephanie Sykora (sykorastephanie@gmail.com) for access to data.

**Leapfrog™ model is only available with permission from Newcrest Mining Ltd., even after thesis confidentiality expires.

List of figures

Chapter 1: Introduction

Chapter 2: Regional tectonic setting, Lihir Island

Chapter 3: Geological framework of Lihir

Chapter 4: Veins and hydrothermal breccias

Chapter 5: Structural geology

Chapter 6: Pyrite trace element compositions

Chapter 7: Sulfur and strontium isotopes

Chapter 8: Conclusions

List of tables

CHAPTER 1: INTRODUCTION

1.1: Introduction

Gold on Earth is rare, valued and extra-terrestrial, having originated from prodigious star explosions and possibly brought to Earth by catastrophic asteroid bombardments around four billion years ago (e.g., Willbold et al., 2011; Berger et al., 2013). With time, gold has been concentrated in the Earth's crust by a variety of geological, physical, chemical and biological processes, locally forming ore deposits. While gold occurs in a wide range of ore deposit types (e.g., Walshe and Cleverley, 2009), some of the major sources of gold, and including those most highly sought after by producers, are hydrothermal ore deposits that formed around magmatic centers. These include porphyry Au ± Cu and associated epithermal Au ± Ag deposits (e.g., Sillitoe, 2000; Taylor, 2007). Ore minerals that comprise these deposits precipitated from aqueous high-temperature fluids (i.e., liquid, vapour or supercritical fluid), that are typically magmatic-hydrothermal in origin, i.e., fluids that were dissolved in magma and exsolved on its decompression and/or crystallization (e.g., Burnham, 1979; Hedenquist and Lowenstern, 1994). Magmatic-hydrothermal fluids can carry large quantities of metals and produce vein, breccia and disseminated styles of mineralization (e.g., Hedenquist and Lowenstern, 1994). Although the economically important part of these ore deposits are the large accumulations of gold, copper and other metals, magmatic-hydrothermal ore deposits are essentially giant accumulations of sulfur. Sulfur is therefore fundamental to the formation of these ore deposits (e.g., Simon and Ripley, 2011). Sulfur is commonly in the form of sulfide minerals such as pyrite, chalcopyrite or bornite, however, a substantial component also occurs as sulfate minerals, such as anhydrite or alunite.

This thesis is a case study of a gold deposit on Lihir Island in Papua New Guinea (Figure 1.1). The deposit is named Lihir, but is also known as Ladolam. It is one of the most well-endowed (56 Moz), and youngest (< 1 Ma) gold deposits in the world (Davies and Ballantyne, 1987; Moyle et al., 1990; Carman, 1994, 2003; Newcrest Mining Ltd., 2016). It contains an active high-temperature geothermal system that continues to alter rocks, cause brecciation and carry gold (e.g., Pichler et al., 1999; Simmons and Brown, 2006). Remarkably, the volcanic edifice within which the deposit resides is reasonably well-preserved: a breached strato-volcanic cone, cored by hypabyssal intrusive rocks and diatreme breccia facies (Carman, 1994; Blackwell, 2010; Lawlis et al., 2015). A complex history of alteration has affected the core of the amphitheater, extending to > 400 m below its base.

Porphyry and epithermal ore deposits have characteristic mineral alteration assemblages and spatial patterns (Figure 1.2). In general, porphyry Cu ± Au ± Mo deposits are associated with porphyritic dikes and magmatic-hydrothermal breccias, and have distal chlorite-rich alteration and proximal biotite- and K-feldspar-rich alteration (Figure 1.2A). This is zoned vertically upward to more acidic alteration assemblages containing micas and clays (Figure 1.2A; e.g., Meyer and Hemley, 1967; Lowell and Guilbert, 1970; Gig-

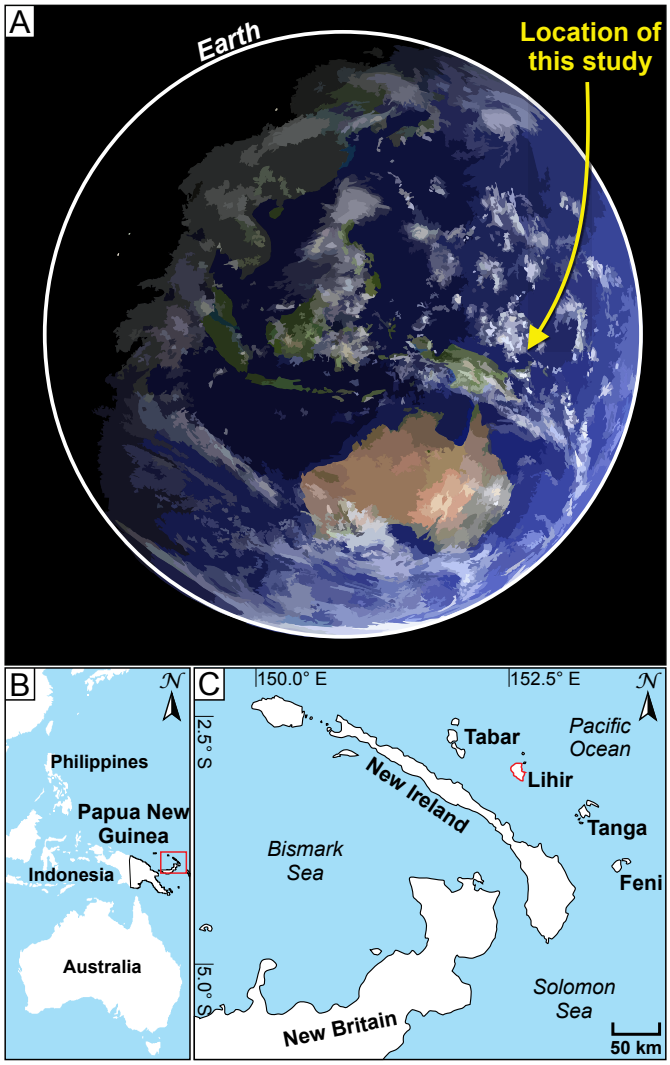

Figure 1.1: Location of study area. A) Illustration of Earth (courtesy NASA), with location of study area. **B)** Map (Mercator projection) of the southwest Pacific with Papua New Guinea outlined. **C)** Location of Lihir Island, as well as eastern Papua New Guinea islands, including New Britain, New Ireland and the Tabar-Lihir-Tanga-Feni island chain.

genbach, 1997; Sinclair, 2007; Sillitoe, 2010). Typical low-sulfidation epithermal Au ± Ag deposits will have narrower structurally controlled zones of veins and breccias with adularia- and illite-rich alteration, and are zoned vertically upward to clay-rich alteration and silica (opal) sinter (Figure 1.2B; e.g., Buchanan, 1981; Simmons et al., 2005; Taylor, 2007).

Lihir is the exemplar of a telescoped magmatic-hydrothermal system, whereby volcanic sector collapse led to superposition of shallow level auriferous epithermal mineralization upon pre-existing, but genetically related, porphyry-style alteration (Carman, 1994; Sillitoe, 1994). High-grade refractory sulfide gold ores at Lihir largely reside in a near-surface zone of adularia ± illite alteration. This near neutral pH potassic alteration assemblage, along with an association of alkaline host rocks, provides the basis for the deposit's alkalic epithermal gold classification, similar to the Cripple Creek and Porgera gold deposits (e.g., Richards, 1995; Jensen and Barton, 2000; Simmons et al., 2005). Beneath the adularia alteration zone at Lihir is a broad zone of biotite ± K-feldspar-altered rocks that contain thick (0.1 to > 30 m) anhydrite ± carbonate veins and breccias. The mineralogy of this zone, coupled with dominantly magmatic signatures obtained from sulfur and strontium isotope studies (Carman, 1994; Müller et al., 2002b), and again, the association with alkaline igneous rocks, are compatible with alkalic porphyry Cu ± Au deposits (e.g., Galore Creek – Lang et al., 1995; Bissig and Cooke, 2014). In contrast to the shallow-level epithermal domain, high-grade gold within the deeper-level anhydrite-rich zone at Lihir are erratic and the controls on their distribution are poorly understood. The focus of this PhD thesis is Lihir's anhydrite – biotite alteration zone, with emphasis on its genesis, structural evolution and relationships to gold mineralization.

1.2: Anhydrite in magmatic-hydrothermal ore deposits

Anhydrite can precipitate when sulfate is the predominant sulfur species in solution (i.e., oxidized conditions; Cooke and Simmons, 2000). Such conditions are typical in porphyry Cu deposits where the

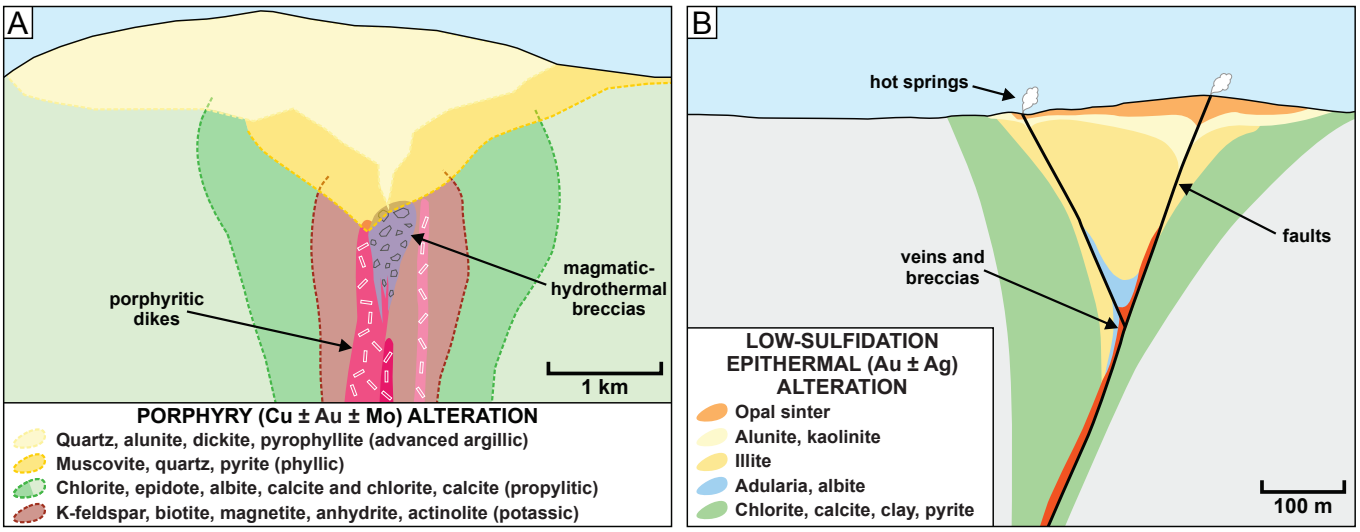

Figure 1.2: Characteristic alteration assemblages and patterns in porphyry and low-sulfidation epithermal ore deposits. **A)** Simplified porphyry Cu ± Au ± Mo alteration (modified after Sillitoe, 2010). **B)** Simplified low-sulfidation epithermal Au ± Ag alteration (modified after Buchanan, 1981). Note the different scales.

ore-forming fluids were relatively oxidized (e.g., Rohrlach and Loucks, 2005). Therefore, anhydrite should be very abundant early and deep within magmatic-hydrothermal ore deposits. Indeed, studies of arc volcanic systems (e.g., Pinatubo – Bernard et al. 1991; Scaillet and Evans 1999) and magmatic-hydrothermal ore deposits (e.g., Yerington – Streck and Dilles 1998; Yanachona – Chambefort et al., 2008) have documented magmatic anhydrite from what would have been hydrous, oxidized and sulfate-saturated melts. Therefore, it is not surprising that anhydrite is a common mineral found in many magmatic-hydrothermal ore deposits (e.g., Table 1.1). Anhydrite, however, is generally overlooked and in some cases absent from

Table 1.1: Anhydrite in magmatic-hydrothermal ore deposits

Ore deposit type and name	Anhydrite occurrence	Interpreted origin of anhydrite	References
Alkalic-type epithermal Au deposits			
Cripple Creek, USA	Anh veins, breccias and large (up to 50 m thick) masses, with bio + mag + or alt. in deep and shallow levels	Early > late, magmatic	Thompson et al. (1985); Jensen (2003)
Emperor, Fiji	Anh with ksp + bio + musc + mag + hem + py alt.; lesser anh with ser + ill + qtz + cal + py alt.	Early, magmatic	Anderson and Eaton (1990); Begg (1996)
Lihir, Papua New Guinea	Anh veins, breccia, and large (up to 30 m thick) masses, with bio + ksp alt.; bladed anh + qtz + py with adu alt.	Early > late, magmatic	Davies and Ballantyne (1987); Carman (1994); Müller et al. (2002b); this study
Porgera, Papua New Guinea	Anh ± qtz ± cal veins within fault zones	Late, evolved seawater	Richards (1992); Richards and Kerrich (1993); Ronacher et al. (2004)
Low ± intermediate sulfidation epithermal Au ± Ag deposits			
Acupan, Philippines	Anh with bio + mag ± ksp ± cpy; anh with qtz ± cal ± py veins	Late > early, mixed meteoric and magmatic	Cooke and Bloom (1990); Cooke and McPhail (2001); Cooke et al. (2011)
Thames District, New Zealand	Anh with qtz + sph + gn + py + cpy + gold ± cal vein; anh with ill + cal alt. within and around intrusions	Late, mixed meteoric and magmatic	Brathwaite et al. (2001)

Ore deposit type and name	Anhydrite occurrence	Interpreted origin of anhydrite	References
High sulfidation epithermal Au-Cu deposits			
Yanachoca, Peru	Anh inclusions in amph and pyx phenocrysts within volcanic units	Early, magmatic	Chambefort et al. (2008); Longo et al. (2010)
Radka, Bulgaria	Anh massive veins with ± gyp ± py	Late, magmatic	Strashimirov and Kovachev (1992); Kouzmanov et al. (2004);
Porphyry Cu ± Au ± Mo deposits			
Candelaria, Chile	Anh ± chl + cal + qtz + clay veins and breccias in deep parts of several orebodies	Early, coeval with Cu	Ullrich and Clark (1999); Marschik and Fontboté (2001)
Caspiche, Chile	Anh with bio + ksp + alb + mag + cpy + bn alt. in deep 'sulfate zone'; anh as cross-cutting veinlets	Early > late, magmatic-hydrothermal	Sillitoe et al. (2013)
Chuquicamata, Chile	Anh with bio + ksp + mag alt. in deep 'sulfate zone'; anh with hem + py alt.	Early > late	Ossandón et al. (2001); Rivera et al. (2012)
El Salvador, Chile	Anh + qtz + or + cpy + bn veins with ksp alt. in deep 'sulfate zone'; cross-cutting vuggy anh + qtz; anh + py ± cpy + bn + en + tennt + sph + gn veins	Early to late	Gustafson and Hunt (1975)
El Teniente, Chile	Anh breccias and veins in deep parts of orebody	Early, magmatic	Skewes et al. (2002); Cannell et al. (2005); Vry et al. (2010)
Galore Creek, Canada	Anh with ksp + phl + mag + hem ± bn ± cpy and gnt + pyx alt.; lesser anh with ser + cal ± py alt.	Early > late, magmatic	Micko (2010); Byrne and Tosdal (2014)
Grasberg, Indonesia	Anh + qtz veins with cpy + bn	Early, magmatic	Pollard et al. (2005)
Rio Blanco – Los Bronces, Chile	Anh breccias and qtz + anh veins with bio alt. in deep levels; gradation to anh + spec + py + cpy + mo at shallow levels	Early, magmatic-hydrothermal	Warnaars et al. (1985); Candela and Piccoli (2005); Frikken et al. (2005)
Sub-aerial geothermal ± Au deposits			
Palinpinon, Philippines	Anh with bio + mag; bladed anh with ill ± cal ± amorphous silica	Mixing with acid-sulfate waters	Rae et al. (2011)
Rotokawa, New Zealand	Anh with ± wai ± cal ± mont ± kao ± ill	Late, sulfate-rich lake waters mixed with deep fluids	Krupp and Seward (1987, 1990)
White Island, New Zealand	Sparse anh inclusions (and inferred anh + cal accumulation at volcano-seawater contact from heated seawater)	Early, magmatic	Giggenbach (1987); Giggenbach et al. (1989); Hedenquist et al. (1993)
Sub-aqueous geothermal ± Cu ± Zn systems			
Grimsey fields, Iceland	Anh chimneys (and inferred anh accumulation beneath hydrothermal field)	Mixed seawater and hydrothermal fluids	Hannington et al. (2001); Kuhn et al. (2003)
TAG, Mid-Atlantic Ridge (26°N)	Anh masses beneath active submarine hydrothermal system	Mixed seawater and hydrothermal fluids	Humphris et al. (1995); Chiba et al. (1998); Mills et al. (1998); Mills and Tivey (1999)

Abbreviations: alb = albite, alt. = alteration, amph = amphibole, anh = anhydrite, bio = biotite, bn = bornite, cal = calcite, chl = chlorite, cpy = chalcopyrite, en = enargite, gn = galena, gnt = garnet, gyp = gypsum, hem = hematite, ill = illite, kao = kaolinite, ksp = K-feldspar, mag = magnetite, mo = molybdenite, mont = montmorillonite, mrc = marcasite, musc = muscovite, or = orthoclase, phl = phlogopite, py = pyrite, pyx = pyroxene, qtz = quartz, ros = roscoelite, ser = sericite, spec = specularite, sph = sphalerite, tell = tellurides, tennt = tennantite, wai = wairakite.

porphyry and epithermal deposits. It is more common in the deeper and early-formed mineral assemblages of magmatic-hydrothermal ore deposits, typically within potassic alteration zones in porphyry Cu ± Au ± Mo deposits, where if occurs with K-feldspar ± biotite ± quartz ± amphibole ± magnetite (Table 1.1; Lowell and Guilbert, 1970; Sinclair, 2007; Sillitoe, 2010). In shallower levels and later formed mineral assemblages, anhydrite is typically rare, but does occur in some deposits (Table 1.1).

Anhydrite has retrograde solubility, and can be dissolved by cold groundwater during weathering (Blount and Dickson, 1969; Holland and Malinin, 1979). The amount of anhydrite preserved in ancient porphyry deposits is therefore most likely to be lower, because it may have been dissolved away after formation (e.g., the Ordovician Cadia porphyry Cu-Au deposit – Williford et al., 2011). Anhydrite is absent from upper levels of many large porphyry Cu deposits, particularly in arid Chile, where supergene weathering results in anhydrite preservation only below a particular level, known as the sulfate front, and anhydrite above this has been dissolved away due to the inward and downward movement of cool groundwater in the mineralized zone (Table 1.1; e.g., Caspiche – Sillitoe et al., 2013; Chuquicamatra – Ossandon et al., 2001; Faunes et al., 2005; Rivers, 2012; El Salvador – Gustafson and Hunt, 1975; El Teniente – Cannell et al., 2005; Los Bronces-Rio Blanco – Warnaars et al., 1985; Frikken et al., 2005).

1.3: Location and access

The Lihir gold deposit is located in UTM zone 56, at 459500 E, 9654000 N, on the east coast of Lihir Island (formally known as Aniolam Island), New Ireland Province, Papua New Guinea (Figures 1.1C, 1.3A). It has a dirt airstrip on the north side of the island near the town of Londolovit, served by charter flights from Cairns, Australia, and other localities. The common language spoken on the island is Tok Pisin (i.e., Pidgin English) and English, as well as native languages of the locals on Lihir Island. Lihir is located in the tropics, and as such has a year-round hot and humid climate, with a temperature range from 19° to 35°C, and annual rainfall accumulation > 3500 mm (Newcrest Mining Ltd., 2015). Most of the island is covered in a thick tropical rainforest (Figure 1.3D–E).

The gold deposit and mining operation are hosted within the Luise amphitheater (Figure 1.3A–C). While volcanism is inactive today, the Luise amphitheater does contain an active high-temperature geothermal system (Figure 1.3F). As such, geothermal energy has been used for the mine's power requirements since 2003 (Villaguerte et al., 2007; Newcrest Mining Ltd., 2015). Refractory gold ore is processed on site using pressure oxidation and conventional leaching techniques. Due to the lack of a suitable area for a tailings storage facility, combined with the high seismicity of the region, a deep sea tailings placement method is used at Lihir (Newcrest Mining Ltd., 2015). Tailings are diluted and stabilized before discharged from a sub-sea pipeline onto the deep seabed, below the biologically active upper layers of the ocean (Newcrest Mining Ltd., 2015).

Figure 1.3: Photographs of Lihir Island and Lihir gold deposit. A) Oblique GoogleEarth™ view of Lihir Island with a 3× elevation exaggeration. **B)** Photographs of the Lihir gold mine, looking approximately south, and **C)** north. **D)** Photographs of the flora and **E)** fauna of the tropic rainforest covering Lihir Island. **F)** Photograph of a boiling mud pool in the Lienetz open pit, designated as a potential geothermal outburst area. **G)** Photograph of sunset from the air, near Lihir Island.

1.4: Discovery and previous work

The Lihir gold deposit was discovered in 1982 by a joint Kennecott and Niugini Mining exploration program. The discovery outcrop is a gold-rich, alunite-altered, coastal bluff known Alaia rock (Figure 1.3B–C; Hope, 2011). The first diamond drillhole was in 1983, and since then over 2,000 drillholes have been completed at the Lihir gold mine. Mining has commenced since 1997, and the gold mine has been 100% operated by Newcrest Mining Limited since August 2010 (Newcrest Mining Ltd., 2015). Alaia rock remains unmined to this day, as it is a sacred site to native Lihirians (Figure 1.3B–C).

The first study of the Lihir gold deposit was by Davies and Ballantyne (1987), who documented the geology from the Minifie and Lienetz orebodies based on drill-core logging. This research was expanded on by Moyle et al. (1990). Carman (1994) conducted the first detailed PhD study of Lihir, based on drill-core data and samples from Minifie and Lienetz. Two papers were published from this thesis (Carman, 2002, 2003), which emphasized the transition from an early porphyry-style to a late epithermal system, based on results from a variety of analytical techniques. At the same time, Sillitoe (1994) proposed that the Lihir gold deposit formed due to sector collapse, which superimposed the epithermal environment on earlier-formed porphyry-style alteration. Papers in the early 2000s by Müller et al. (2002a, 2002b) further enhanced the understanding of Lihir with analytical data (e.g., stable and radiogenic isotopes, multi-element geochemistry, etc.). A MSc thesis by Cater (2002) documented alteration and mineralization in deep geothermal wells. This work was followed by similar studies of different geothermal boreholes by Rae et al. (2010) and Micko (unpublished report, 2012). Simmons and Brown (2006) quantified metal concentrations in deep geothermal waters at Lihir, estimating with the recorded 24 kg/yr Au flux that the entire Lihir gold deposit could have formed in ~ 55,000 years. Blackwell's (2010) PhD thesis characterized breccias in the Minifie, Lienetz and parts of the Luise amphitheater, based on drill-core logging and, for the first time, open-pit mapping. A paper on the Minifie orebody was a product of this research (Blackwell et al., 2014). The geology of the Kapit orebody was the topic of Kidd and Robinson (2004)'s extended abstract and Ageneau (2012)'s PhD thesis. Ageneau (2012) also conducted a geochemical comparison of Kapit with Minifie and Lienetz. Today, an on-going PhD study by Lawlis (in prep.) is documenting the Kapit NE orebody, as well as diatreme breccias throughout the entire deposit (Lawlis et al., 2015). Various unpublished consultant reports throughout the 1990s and 2000s also contributed to the present-day knowledge of Lihir.

1.5: Aims of thesis

The unique characteristics of Lihir, in particular the well-preserved relationships between porphyry-style and epithermal features and the volcanic edifice, provide a rare opportunity to understand processes that led to the transition from porphyry-style to epithermal conditions. This thesis is focused on understanding the processes operating throughout the porphyry-epithermal transition by examining the evolution of

anhydrite ± carbonate-rich veins and breccias within the deeper parts of the Lienetz orebody, which have recently been exposed by open-pit mining.

The thesis aims are to document the compositional, geometric and kinematic features of the various anhydrite ± carbonate-rich veins in order to provide constraints on the relative roles of tectonic, magmatic, hydrothermal and gravitational forces that led to broad-scale permeability and porosity development. The deposit-scale structural template is in turn used to examine the distribution of gold within the deeper parts of the Lienetz orebody, and place constraints on gold introduction, remobilization, and precipitation throughout the evolution from porphyry-style to epithermal conditions. Some of the questions that are addressed include: How do anhydrite, pyrite and gold relate to the porphyry- and epithermal-events that led to the formation of Lihir? What is the relationship to, location of, and controls on gold within the anhydrite-rich deeper parts of the Lienetz orebody? What is the relationship of anhydrite veins to the volcanic sector collapse? Why is there so much anhydrite and what is the origin of the sulfur that formed sulfate and sulfide minerals? Resolving these questions provides new insights into how Lihir formed, and also how to better process and explore for gold mineralization in similar settings elsewhere.

1.6: Thesis organization

This thesis contains eight chapters: introductory chapter (**Chapter 1**: Introduction); literature review and summary chapters (**Chapter 2**: Regional tectonic setting, Lihir Island, and **Chapter 3**: Geological framework of Lihir); data chapters (**Chapters 4**: Veins and hydrothermal breccias, **Chapter 5**: Structural geology, **Chapter 6**: Pyrite trace element compositions, and **Chapter 7**: Sulfur and strontium isotopes); and conclusions and genetic model chapter (**Chapter 8**: Conclusions).

Each of the data chapters have their own method sections, as well as their own individual conclusions. Chapters 5 (with parts of Chapter 4), and Chapter 6 have been compiled and written into two manuscripts and were submitted to the journal Economic Geology in 2016 for publication in 2017 or 2018. One manuscript has been reviewed and is currently being revised (i.e., Sykora et al., submitted May 2016). The other is in review (i.e., Sykora et al., submitted December 2016). Working titles of the manuscripts are "The structure and significance of anhydrite-bearing vein arrays, Lihir gold deposit, Papua New Guinea", and "Evolution of pyrite trace elements compositions from porphyry-style and epithermal conditions at the Lihir gold deposit: Implications for ore genesis and mineral processing". The primary author on both manuscripts is Stephanie Sykora. Contributions from the co-authors were primarily of a supervisory/advisory nature – all field and analytical work and the interpretations were made by the primary author.

Chapter 2: Regional tectonic setting, Lihir Island

2.1: Introduction

This chapter provides a review of the tectonic history of Lihir Island and the Tabar-Lihir-Tanga-Feni island chain from the Tertiary to present. A literature review of previous studies of paleo- and modern-day plate tectonics, combined with geochemical studies on volcanic rocks, as well as new analysis of available modern earthquake data, are used to synthesize the complex historic and modern tectonic setting. Following this, a discussion of each tectonic scenario previously proposed leads to the proposition of a new tectonic scenario model that fits several lines of evidence from previous studies.

2.2: Tectonic history of Papua New Guinea islands

Lihir is one of many islands that compose the country of Papua New Guinea in the southwest Pacific (Figure 1.1B–C). Lihir is located northeast of New Ireland, forming part of the young (< 4 Ma) Tabar-Lihir-Tanga-Feni island chain (Figure 1.1C). The tectonic setting is complex, involving a mosaic of rotated and translated microplates, driven principally by protracted oblique westward convergence of the Pacific Plate with the Australian Plate, which initiated around 50 to 42 Ma (Figure 2.1; Gordon et al., 1978; Hall, 2002; Sharp and Clague, 2006). Convergence was in part accommodated by subduction along the Melanesian Trench, until docking of the Ontong Java Plateau occurred around 26 to 23 Ma (Figure 2.1A–B; Curtis, 1973; Falvey and Pritchard, 1982; Weissel et al., 1982; Kroenke and Rodda, 1984; Coffin and Eldholm, 1993; Martinez and Taylor, 1996; Tregoning et al., 1998; Hall, 2002; Knesel et al., 2008). Prior to this event, subduction-related calc-alkaline arc magmatism in the upper plate contributed to crustal growth along a near-continuous arc from New Britain to Fiji (i.e., Melanesian Arc; Figure 2.1A; Blake and Miezitis, 1967; Hohnen, 1978; Falvey and Pritchard, 1982; Lindley, 1988; Hall, 2002).

The Ontong Java Plateau is the largest oceanic igneous province on Earth, with area of ~ 5×10^6 km^2 and a basaltic crustal volume of ~ 5×10^7 km^3 (Coffin and Eldholm, 1993; Neal et al., 1997). Docking of the plateau at the subduction zone caused near complete cessation of magmatism along the Melanesian Arc (Figure 2.1B; Kroenke and Rodda, 1984; Petterson et al., 1997; Hall, 2002; Kroenke et al., 2004; Mann and Taira, 2004), and temporarily inhibited northward motion of the Australian Plate (Knesel et al., 2008). This perturbation in plate motion may have been important for the emplacement of mineralized porphyry deposits in New Britain between 24 and 20 Ma (Holm et al., 2013). A reversal in subduction polarity with the birth of the markedly northward-convex New Britain Trench at ~ 10 Ma led to reactivation of parts of the older Melanesian chain, and the initiation of a new south-facing arc (Figure 2.1C; Weissel et al., 1982; Cooper and Taylor, 1985; Wessel and Kroenke, 2000; Hall, 2002). This phase of arc reversal has been pos-

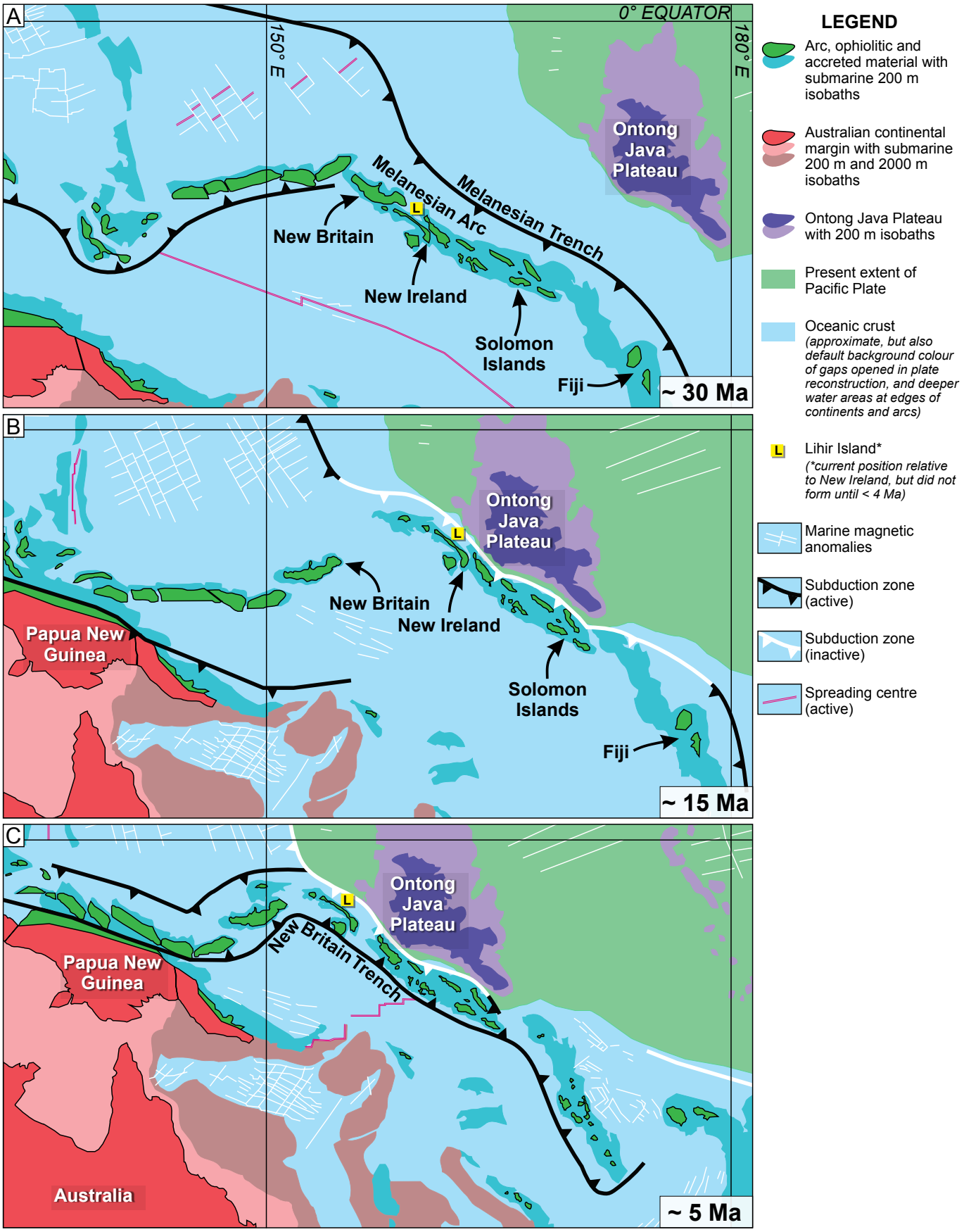

Figure 2.1: Tectonic reconstruction of the southwest Pacific region from the Oligocene to Pliocene, with focus on the Papua New Guinea islands of New Britain and New Ireland. See text for details. Modified after Hall (2002) and references therein. **A)** Mid-Oligocene (~ 30 Ma) tectonic reconstruction. Active subduction along Melanesian Trench, driven by the southwest motion of the Pacific Plate, formed island arc volcanic chains, including the Papua New Guinea island's New Britain and New Ireland. **B)** Mid-Miocene (~ 15 Ma) tectonic reconstruction. The Ontong Java Plateau docked with the Melanesian Trench, causing cessation in subduction. **C)** Early Pliocene (~ 5 Ma) tectonic reconstruction. Subduction was, and continues to be, driven from the south by the Australian Plate, with convergence along the curved New Britain Trench.

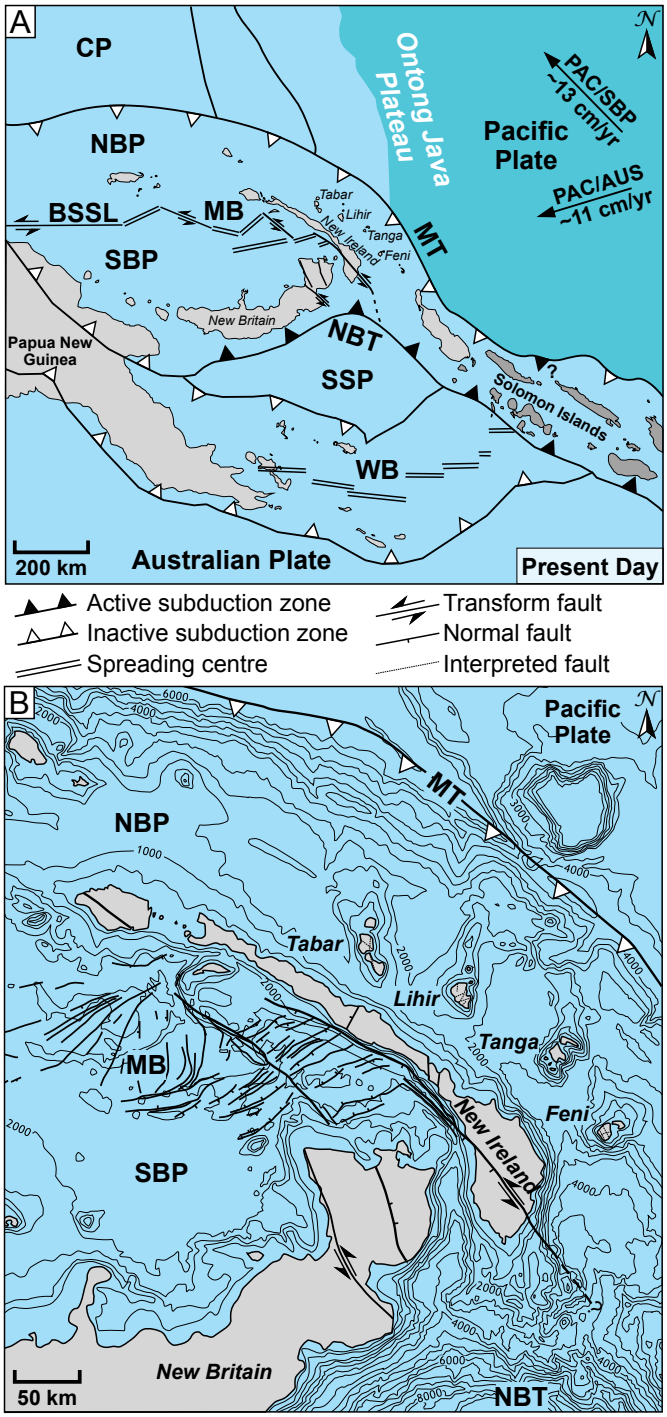

Figure 2.2: Present day tectonic elements of Papua New Guinea. A) Tectonic elements around Papua New Guinea (modified after Taylor et al., 1994; Tregoning et al., 1998; Tregoning, 2002). **B)** Bathymetry (500 m contour spacing) and major geological structures around the Tabar-Lihir-Tanga-Feni island chain, New Britain and Manus Basin (modified after Lindley, 2015, and references therein). BSSL = Bismarck Sea Seismic Lineation; CP = Caroline Plate; MB = Manus basin; MT = Melanesian Trench; NBP = North Bismarck plate; NBT = New Britain trench; SBP = South Bismarck plate; SSP = Solomon Sea plate; WB = Woodlark Basin.

tulated to relate to emplacement of gold and copper porphyry deposits (Solomon, 1990).

The present-day plate configuration for the region is shown in Figure 2.2A. The principal change from ~ 5 Ma (cf. Figure 2.1C) relates to micro-plate segmentation associated with back-arc spreading in the Manus Basin (Figure 2.3), and broadly coeval sinistral transposition of New Ireland relative to New Britain (Figure 2.2A–B). Spreading to the northwest – southeast in the Manus Basin initiated around 4 to 3.5 Ma, with a spreading rate of 13.2 cm/yr since that time (Taylor, 1979; Taylor et al., 1994; Martinez and Taylor, 1996). A linked array of transforms and spreading ridges, defining the Bismarck Sea Seismic Lineation, separates and accommodates oblique motions of the two main microplates in the region, the North and South Bismarck Plate (Figures 2.2A, 2.3; Pascal, 1979; Taylor, 1979). The North Bismarck Plate is currently moving westward at 13 to 14 cm/yr, relative to the South Bismarck Plate, while the South Bismarck Plate is rotating clockwise at ~ 8°/m.y. (Figure 2.4; Tregoning et al., 1999; Tregoning et al., 2000; Tregoning, 2002). The Bismarck Sea Seismic Lineation extends to the southeast across New Ireland as a major northwest-striking sinistral transform fault, which partly links to an ill-defined trench-trench-transform triple junction at the prominent inflection in the New Britain Trench (Figure 2.2A–B; Taylor, 1979; Falvey and Pritchard, 1982; Taylor and Karner, 1983; Lindley, 1988). Tregoning et al. (2000) labeled the triple junction a 'broad deformation zone' based on modern plate velocity data. The section of the North Bismarck Plate where the Tabar-Lihir-Tanga-Feni island chain is located has been noted to be decoupled from, but still moving with, the Pacific Plate (Bruns et al., 1989). The reported ~ 400 km northwestward transposition of New Ireland (Taylor, 1979) was most likely accommodated by the major northwest-striking transform segment of the

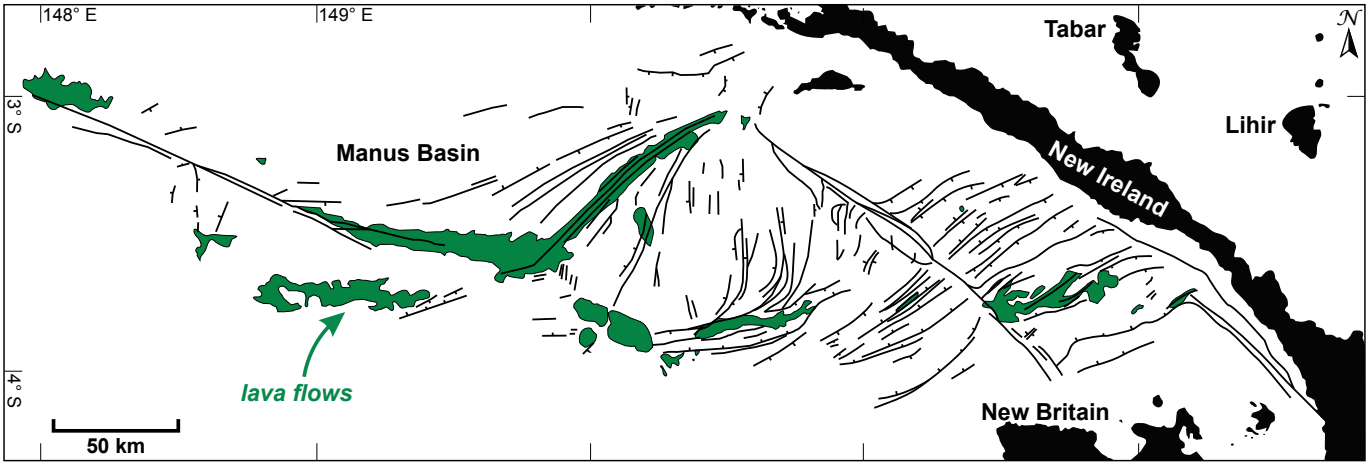

Figure 2.3: Structural features within the Manus Basin. Faults (ticks on down-thrown side), tectonic lineations (lines) and lava flows defining spreading ridges, identified from sidescan and bathymetry data (modified after Martinez and Taylor, 1996).

Bismark Sea Seismic Lineation that transects New Ireland (Figure 2.2B). The Melanesian Trench defines the arcuate boundary of the North Bismarck Plate with the Pacific Plate. Aside from localized evidence of reactivated or continuing southward subduction beneath the Solomon Islands (Cooper and Taylor, 1985; Petterson et al., 1997) and minor modern earthquake activity (Bruns et al., 1989; Bird, 2003; Benz et al., 2011), the Melanesian Trench is considered largely inactive in this region today (Figure 2.2A–B).

2.3: Geodynamic setting of the Tabar-Lihir-Tanga-Feni island chain

The volcanic Tabar-Lihir-Tanga-Feni islands are Pliocene to Holocene in age (Johnson et al., 1976; Wallace et al., 1983). They are evenly distributed (~ 80 km spacing) along a linear northwest-trending chain, which broadly parallels both the eastern margin of New Ireland, and former Melanesian Trench (Figure 2.2B).

Systematic changes in the form and age of the islands occur along the length of the chain. The ocean floor depth decreases northward in step-like fashion, from > 3,000 m on the southern flank of the Feni islands, to ~ 1,200 m on the western flank of the Tabar islands (Figure 2.5A). This mimics the overall decrease in seafloor depth of the North Bismarck Plate toward the northwest, and is in accordance with the gentle uplift and southward tilting that has also been reported on several of the Tabar-Lihir-Tanga-Feni islands (Wallace et al., 1983). Accompanying this northward change in bathymetry is a progressive 25° counter-clockwise shift of the islands' long-axes from east-northeast to north-northwest (Figure 2.5A). A notable linear relationship exists between the angular discordance of island long-axes and their spatial separation (Figure 2.5B), implying a systematic control on their formation. In addition, there is an apparent younging of initial volcanism towards the south, from 3.7 ± 0.2 Ma on Tabar Island to 1.53 ± 0.15 Ma on Feni Island (Table 2.1; Figure 2.5C; Wallace et al., 1983; Rytuba et al., 1993). Volcanism is presently extinct or dormant on the islands, with the most recent volcanic event being the eruption of the Ambitle volcano on Feni Island 2,300 ± 10 years ago (Table 2.1; Licence et al., 1987; Lindley, 2015). Geothermal activity is ubiquitous

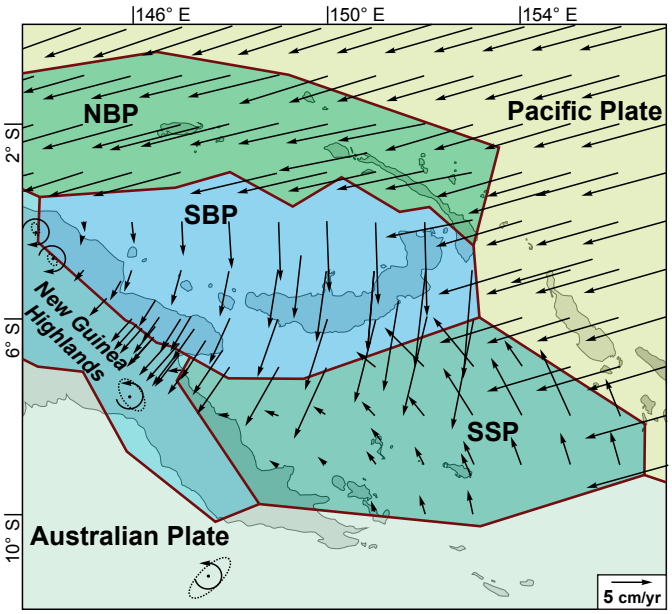

Figure 2.4: Plate velocities and rotations in Papua New Guinea. Rotational part of velocity field is relative to Australia, predicted by Euler vectors from the best fit model. Location of poles of rotation are shown (modified after Wallace et al., 2004, and references therein).

on islands in the Tabar-Lihir-Tanga-Feni chain, and also in the surrounding offshore marine areas (Herzig and Hannington, 1995).

Modern volcanic and earthquake data from the area surrounding the Tabar-Lihir-Tanga-Feni islands show that whereas the chain itself occurs in a region of relative seismic quiescence, the neighboring New Britain Trench system and Bismarck Sea Seismic Lineation are highly active, with over 30 recorded 7.5 + magnitude earthquakes since 1900 (Figure 2.6; Benz et al., 2011). Analysis of recent earthquakes shows that they decrease in abundance and magnitude with increasing distance and depth

Table 2.1: Isotopic ages of volcanic and hydrothermal rocks from the Tabar-Lihir-Tanga-Feni island chain

Island group	K-Ar age (Ma)	Sample type	Material	Method	Reference
Feni Islands	0.0023 ± 0.0001	volcanic tuff	n/a	^{14}C	Licence et al. (1987)
	0.68 ± 0.1, 0.49 ± 0.1	quartz trachyte	biotite	^{40}K–^{40}Ar	Wallace et al. (1983)
	1.53 ± 0.15	mafic lava	hornblende	^{40}K–^{40}Ar	Wallace et al. (1983)
Tanga Islands	1.14 ± 0.08, 1.08 ± 0.08	quartz trachyte	biotite	^{40}K–^{40}Ar	Wallace et al. (1983)
Lihir Islands	0.151 ± 0.015	*alunite-rich rock*	alunite	^{40}K–^{40}Ar	Davies and Ballantyne (1987)
	0.2 ± 0.1	*siliceous breccia zone*	K-feldspar	^{40}K–^{40}Ar	Moyle et al. (1990)
	0.3 ± 0.1	*potassic-altered volcanic*	K-feldspar	^{40}K–^{40}Ar	Moyle et al. (1990)
	0.336 ± 0.027	*biotite – anhydrite vein*	biotite	^{40}K–^{40}Ar	Davies and Ballantyne (1987)
	0.34 ± 0.03	*biotite – magnetite vein*	biotite	^{40}K–^{40}Ar	Rytuba et al. (1993)
	0.342 ± 0.036	*pyroxene monzonite*	biotite	^{40}K–^{40}Ar	Davies and Ballantyne (1987)
	0.36 ± 0.03	*monzonite porphyry*	biotite	^{40}K–^{40}Ar	Rytuba et al. (1993)
	0.5 ± 0.1	*siliceous breccia zone*	K-feldspar	^{40}K–^{40}Ar	Moyle et al. (1990)
	0.52 ± 0.11	*sulfide-rich ore*	adularia	^{40}Ar–^{39}Ar	Carman (1994)
	0.61 ± 0.25	*sulfide-rich ore*	adularia	^{40}Ar–^{39}Ar	Carman (1994)
	0.7 ± 0.2	*clay – silica zone*	illite	^{40}K–^{40}Ar	Moyle et al. (1990)
	0.7 ± 0.2	*propylitized volcanic*	whole rock	^{40}K–^{40}Ar	Moyle et al. (1990)
	0.917 ± 0.100	*biotite-altered volcanic*	biotite	^{40}K–^{40}Ar	Davies and Ballantyne (1987)
Tabar Islands	0.986 ± 0.08	quartz trachyte	plagioclase	^{40}K–^{40}Ar	Wallace et al. (1983)
	1.2 ± 2.0	*vein*	alunite	^{40}K–^{40}Ar	Rytuba et al. (1993)
	1.9 ± 0.1	trachybasalt	whole rock	^{40}K–^{40}Ar	Rytuba et al. (1993)
	2.3 ± 0.4	basalt	whole rock	^{40}K–^{40}Ar	Rytuba et al. (1993)
	2.8 ± 0.6	*vein*	alunite	^{40}K–^{40}Ar	Rytuba et al. (1993)
	2.8 ± 0.2	trachybasalt	whole rock	^{40}K–^{40}Ar	Rytuba et al. (1993)
	3.1 ± 0.3	basalt	whole rock	^{40}K–^{40}Ar	Rytuba et al. (1993)
	3.5 ± 0.2	trachyte	whole rock	^{40}K–^{40}Ar	Rytuba et al. (1993)
	3.7 ± 0.2	trachyte	whole rock	^{40}K–^{40}Ar	Rytuba et al. (1993)

Sample types in *italics* reflect hydrothermal alteration and/or mineralization events, rather than island forming volcanism.

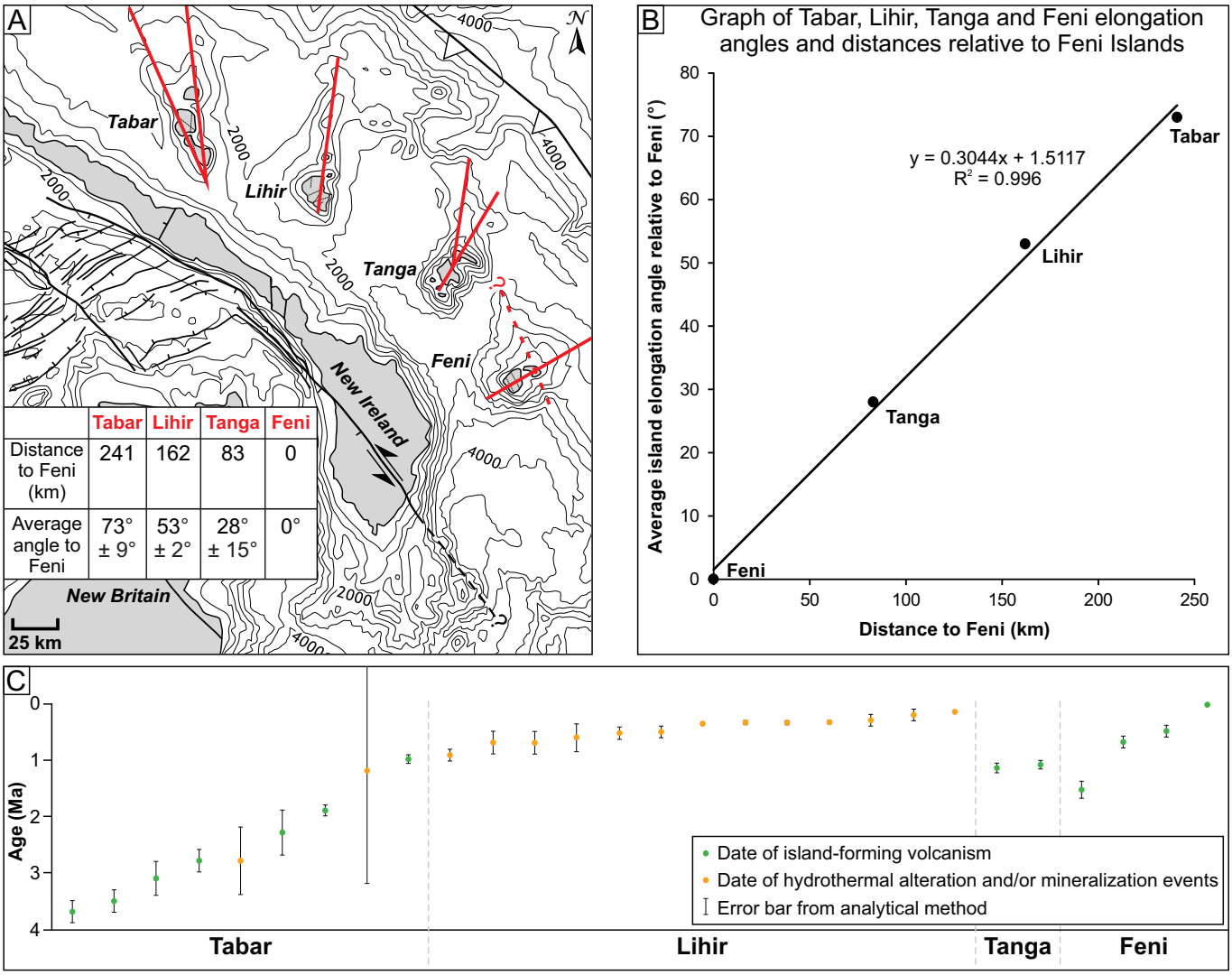

Figure 2.5: Relationship between angles and distances between the Tabar-Lihir-Tanga-Feni islands. A) Elongations angles are inferred via islands' long-axes and offshore submarine mounds. **B)** Graphs of distance versus angle. **C)** Graph of known age dates for island-forming volcanism and hydrothermal alteration and/or mineralization events.

from the New Britain Trench axis (Figure 2.6B). Their reported distribution is consistent with the arched New Britain Trench and the steeply dipping northern edge of the Solomon Sea Plate (Figure 2.6A, C–D). Perturbations in the form of the slab are evident in deep earthquake data. In a zone to the north-northeast of the New Britain Trench inflection, specifically between Lihir and Tanga islands, there appears to be a paucity of deep (300 to 600 km) seismic activity attributable to the down-going Solomon Sea Plate (Figure 2.6D). Southeastward of this zone is a strikingly linear north-trending array of deep seismic activity, with apparent 'splays' that project eastward beneath the trace of the Melanesian Trench (Figure 2.6D). These deep-seated seismic domains have been modeled to represent a tear and overturned segment of the Solomon Sea Plate, respectively (Figure 2.6A, C–D, 2.7; O'Kane, 2008).

In contrast to multi-level seismic activity associated with Solomon Sea Plate subduction, earthquakes along the trace of the Bismarck Sea Seismic Lineation are predominantly shallow (0 to 69 km) and focused on transforms (Figure 2.6A). Minor shallow activity occurs proximal to the Tabar-Lihir-Tanga-Feni islands, with some along traces that extend beyond the island's long-axes and others that parallel the Melanesian Trench (Figure 2.6A).

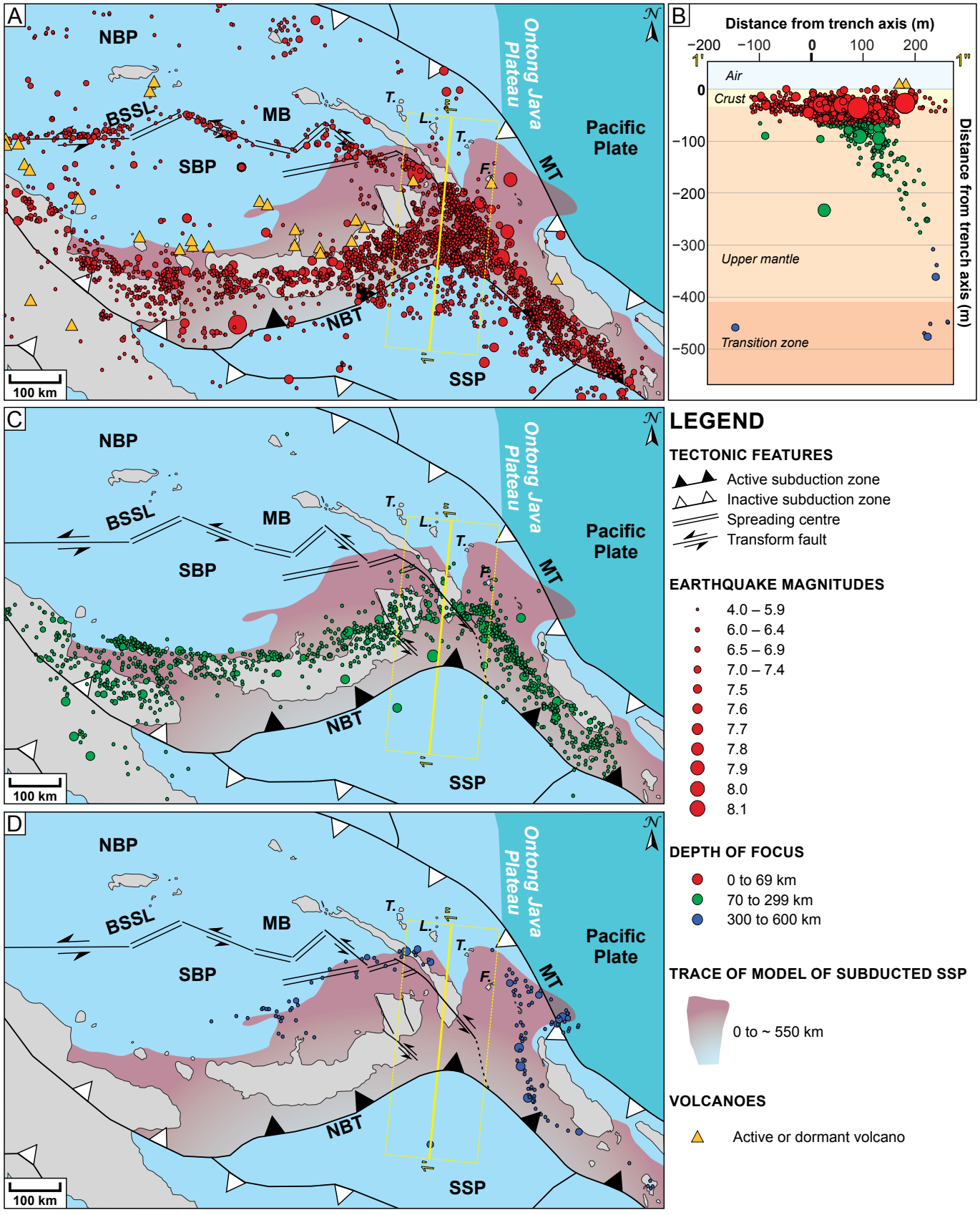

Figure 2.6: Recent earthquakes, volcanoes and depth of subducting slab around eastern Papua New Guinea islands. Maps and thick-section of recorded earthquakes since 1900 to 2011 of magnitude 4+, and surface projected 3-D outline of modeled subducted Solomon Sea Plate at the New Britain Trench (modified after O'Kane, 2008; Benz et al., 2011, and references therein). **A)** Shallow (0 to 69 km) earthquakes and active or dominant volcanoes. **B)** South-to-north thick-section (1' to 1''), across the New Britain Trench towards Lihir Island, of seismicity from the surface to mantle transition zone (~ 500 m below sea level). **C)** Moderate depth (70 to 299 km) earthquakes. **D)** Deep (300 to 600 km) earthquakes. BSSL = Bismarck Sea Seismic Lineation; MB = Manus basin; MT = Melanesian Trench; NBP = North Bismarck plate; NBT = New Britain trench; SBP = South Bismarck plate; SSP = Solomon Sea plate; T. L. T. F. = Tabar-Lihir-Tanga-Feni island chain.

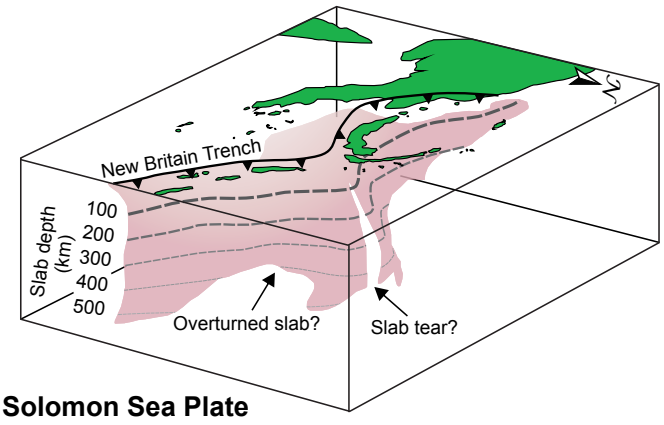

Figure 2.7: Tear in the Solomon Sea Plate. 3-D model and hypothesized tear of the subducted Solomon Sea Plate at the New Britain Trench (modified after O'Kane, 2008).

Focal mechanism data from this region reveal the expected strike-slip and extensional stress states for transform and spreading ridge segments of the Bismarck Sea Seismic Lineation, corresponding to north-south to northwest-southeast directed spreading of the Manus Basin (Figure 2.8; Bird, 2003; International Seismological Centre, 2016). Likewise, shallow- and moderate-level earthquakes parallel to the inflected New Britain Trench are compressional, with fault planes aligned parallel to the trench (Figure 2.8). To the north to northeast of New Ireland, and east of the New Britain Trench, the dominant stress states are less clear. There are a series of shallow earthquakes, dominantly compressional, with resolved fault planes that sub-parallel the former Melanesian Trench (e.g., near Mussau Island, 150° E; Figure 2.8). The deep-seated seismic activity along the linear northward trend of earthquakes (cf. Figure 2.6D) appears to exhibit east-west directed extension, whereas deep-seated earthquakes along the eastward-trending splays exhibit north-south directed extension (i.e., yellow outlined area near 154° E and 4° S; Figure 2.8).

2.4: Composition of the Tabar-Lihir-Tanga-Feni islands

The shoshonitic lavas of the Tabar-Lihir-Tanga-Feni island chain are alkali- and volatile-rich, silica-undersaturated, highly oxidized with elevated large-ion lithophile elements and negative Ce and positive Eu anomalies (Johnson et al., 1976; Johnson et al., 1978a; Kennedy et al., 1990a; Kennedy et al., 1990b; McInnes and Cameron, 1994; McInnes et al., 2001; Kamenov et al., 2008). Mantle xenoliths from submarine volcanoes offshore from Lihir and Tabar islands provide evidence for highly oxidized (fO_2 = FMQ + 4) melts rich in sulfate, carbonate, H_2O and alkali metals, with significant contents of F, Cl, Sr and Ba (McInnes and Cameron, 1994). The melts would have led to crystallization of hydrous minerals (e.g., biotite and amphibole; Green, 1972) and elevated fO_2, enhancing sulfur solubility forming sulfate (e.g., anhydrite; Carroll and Rutherford, 1987).

Rock of the Tabar-Lihir-Tanga-Feni island chain have unique hybrid geochemistry with similarities to both arc volcanism and mid-ocean ridge basalts (Johnson et al., 1976; Johnson et al., 1978b; Heming, 1979; Wallace et al., 1983; Kennedy et al., 1990a; Kennedy et al., 1990b; McInnes and Cameron, 1994; Stracke and Hegner, 1998; Müller et al., 2001; Müller et al., 2003; Kamenov et al., 2008; Blackwell, 2010). Trace element and Sr, Nd and Pb isotopic signatures of the Tabar-Lihir-Tanga-Feni island chain are typical of arc lavas (Kennedy et al., 1990b), but the total Sr concentrations are elevated (average 1504 ppm Sr; Page and Johnson, 1974) and reflect a mantle source signature (Johnson et al., 1976). Studies on the ultramafic

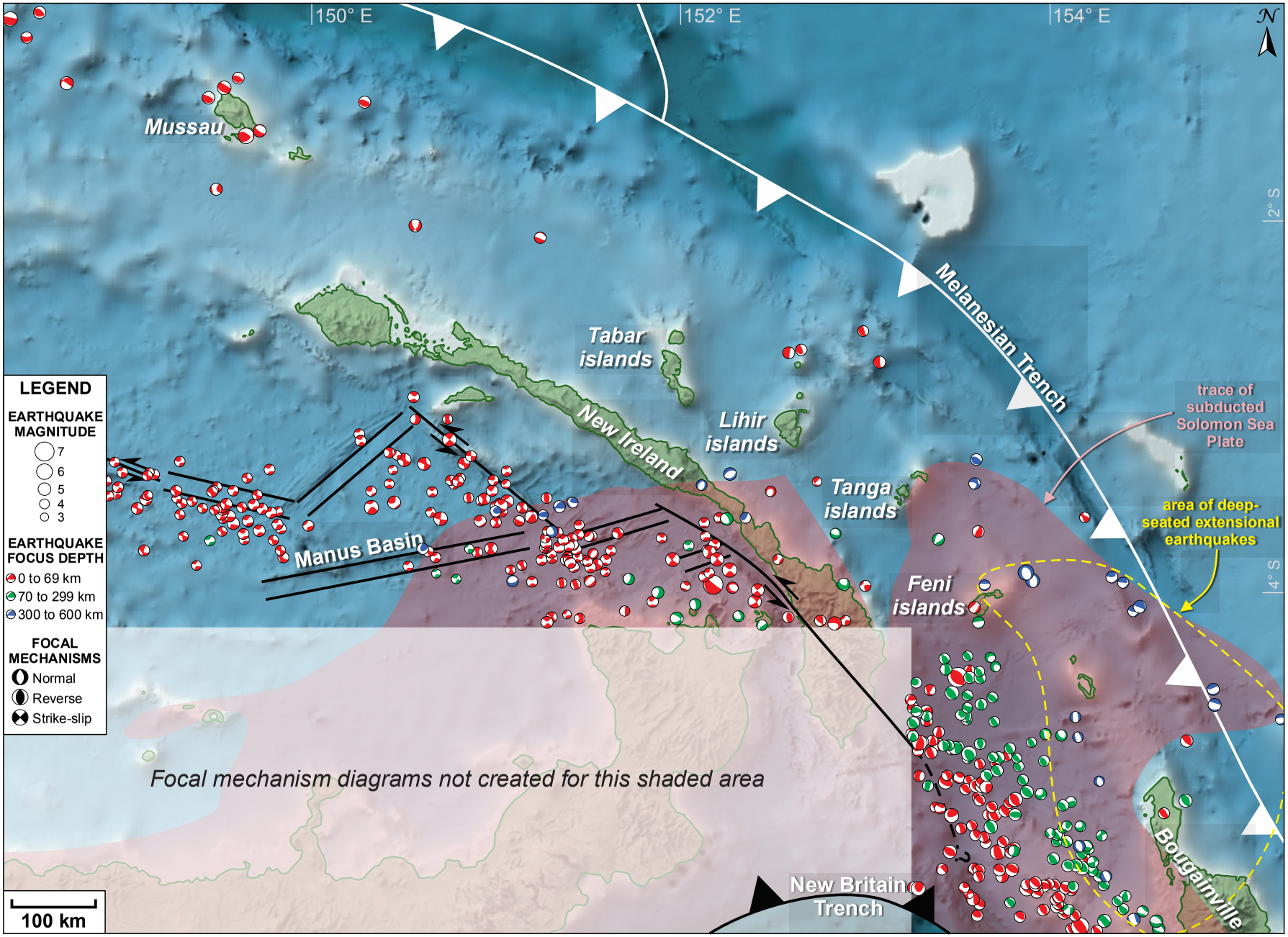

Figure 2.8: Focal mechanism map of 3+ magnitude earthquakes near the Tabar-Lihir-Tanga-Feni island chain, Manus Basin and New Britain Trench, from 1960 to 2016 (International Seismological Centre, 2016). Highlighted is the region are deep-seated earthquakes, and the trace of O'Kane's (2008) 3-D modeled subducted Solomon Sea Plate at the New Britain Trench.

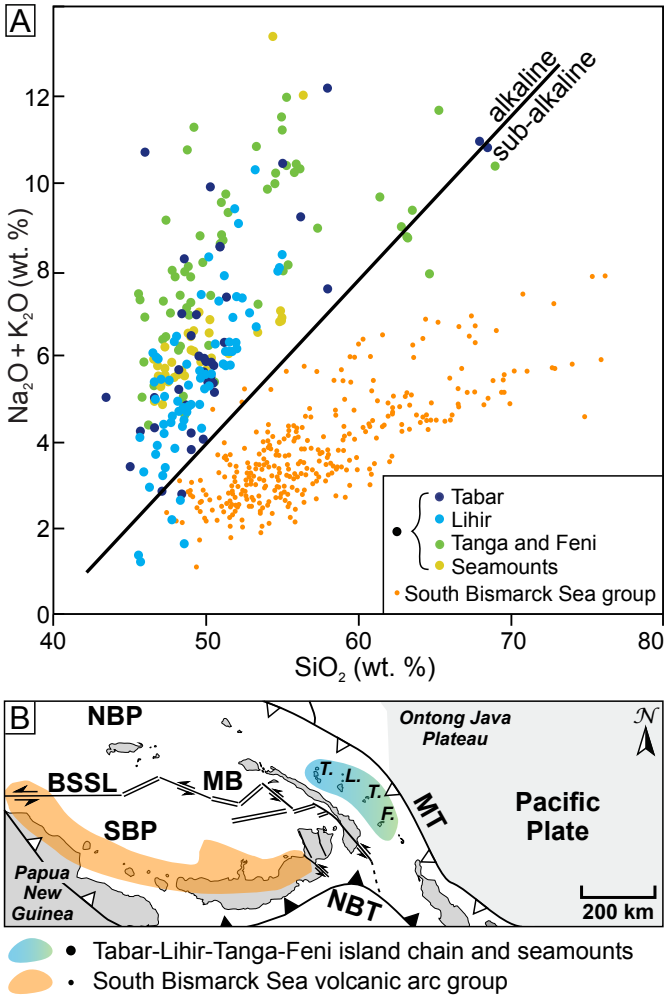

Figure 2.9: Total alkali-silica diagram for volcanic rocks of Papua New Guinea. A) Discrimination line separates Hawaiian alkaline and tholeiitic rocks (i.e., sub-alkaline), as defined by Macdonald (1968) and Irvine and Baragar (1971). **B)** Locations of samples groups (diagram modified from Johnson et al. (1976), with data compiled by Blackwell (2010), from Heming (1979); Wallace et al. (1983); Kennedy et al., 1990a; Kennedy et al., 1990b; McInnes and Cameron, 1994; Stracke and Hegner, 1998; Müller et al., 2001; Müller et al., 2003).

xenoliths show a wide range of Pb isotopic compositions, indicating multiple involvements in the mantle wedge under the Tabar-Lihir-Tanga-Feni islands including Pacific Oceanic mantle, Pacific sediments and Indian Ocean-type mantle or Australian subcontinental lithospheric mantle (Kamenov et al., 2008).

Tabar-Lihir-Tanga-Feni island chain rocks have distinctively high $Na_2O + K_2O$ versus SiO_2 (Figure 2.9A). Comparative studies on volcanic rocks from arcs and mid-ocean ridges have demonstrated broadly linear relationships between increasing depth of magma segregation (i.e., shorter melting columns, thicker crust) with higher Na_2O and lower Ca_2O concentrations (Klein and Langmuir, 1987; Plank and Langmuir, 1988). However, studies of the crust beneath the Tabar-Lihir-Tanga-Feni island chain have inferred it to be relatively thin (~ 30 km; Finlayson and Cull, 1973), and K_2O is significantly higher than what would be expected purely from partial melting (cf. Plank and Langmuir, 1988). Furthermore, the degree of partial melting needed in production of Tabar-Lihir-Tanga-Feni islands remains controversial, as this depends on many factors such as the fertile or depleted or refractory mantle source, amount of added subduction component, amount of volatiles, pressure and temperature, amongst other things. There is no clear consensus on the relative importance of these factors. For example, regarding rocks in Fiji, Leslie et al. (2009) argued for small degrees of partial melting, whereas Rogers and Setterfield (1994) proposed the large degree of melting. It appears that an unusual process must be invoked to explain high $Na_2O \pm K_2O$ of the Tabar-Lihir-Tanga-Feni island chain magmas. This mechanism would require triggering magma generation and extraction from a previously metasomatized mantle, but at abnormal depths (e.g., 60 to 70 km; Kamenov et al., 2008).

2.5: Examples of paleo-subduction enrichment on other Papua New Guinea islands

The Tabar-Lihir-Tanga-Feni shoshonitic lavas have atypical geochemistry with an enhanced subduction signature compared to normal arc lavas, and as such are inferred to have been sourced from subduction

modified mantle lithosphere, which was enriched by processes that occurred along the former Pacific Plate subduction along the Melanesian Trench (e.g., Kamenov et al., 2008). Hints of early enrichment events relating to subduction along the now-inactive Melanesian Trench are seen in arc and back arc volcanic rocks throughout the Melanesian Trench region (Woodhead et al., 1998, and reference therein), as well in volcanic rocks proximal to the Tabar-Lihir-Tanga-Feni island chain. For examples, lavas from the Manus Basin have both mid-ocean ridge basalt and arc-like basalt affinities, with the melts of arc-like character restricted to eastern part of the basin, where their geochemical signatures are interpreted to represents rifted fragments from the inactive Melanesian arc (Woodhead et al., 1998; Sinton et al., 2003). Another example of paleo-subduction enrichment are the quaternary volcanoes on New Britain, which relate to the present-day subduction of the Solomon Sea Plate. Their unusual 'fluid'-related trace element signatures (i.e., elevated large-ion lithophile elements and positive Eu anomalies) of the volcanic front basalts led Woodhead et al. (1998) to attribute inheritance from partial melting of a residual source modified by previous melt extraction episodes along the formerly active Melanesian Trench.

2.6: Discussion: tectonic scenarios for the formation of Lihir Island

The hybrid geochemical characteristics of rocks from the Tabar-Lihir-Tanga-Feni island chain have been interpreted to indicate Pliocene partial melting of an already metasomatized mantle wedge from the Miocene Melanesian subduction zone (Figure 2.10; Johnson et al., 1978a; McInnes and Cameron, 1994). Partial melting was most likely caused by adiabatic decompression due to transtensional or extensional tectonics, or alternatively due to the development of a local, deep-seated heat source. Most previous workers have argued that magma generation was extension-driven, and a variety of structural models have been proposed to account for the localized upper-plate extension interpreted from geochemical data. These include: (1) propagation of deep-seated extensional faults northward of the New Britain Trench inflection (Lindley, 1988; Carman, 1994); (2) propagation of Manus Basin extensional structures eastward of New Ireland (Corbett, unpublished data, 1991; Davies, unpublished data, 1991); (3) development of transtensional pull-apart structures during oblique convergence of the Pacific and Australian plates (McInnes and Cameron, 1994); and most recently, (4) extensional cracks localized in response to plate flexure (Figure 2.11; Lindley, 2016). While it is plausible that transtensional or extensional structures delineated the islands' respective north-northwest to east-northeast long-axes, each of the scenarios outlined above have some limitations. Current shallow-level extensional structures are considered unlikely, as modern earthquake distribution patterns and resolved stress states do not provide any evidence for propagation of the Manus Basin spreading-transform architecture eastward of New Ireland (e.g., Figure 2.8). Lindley (2016) attributed regional fractures throughout the island chain, as well as mantled sedimentary units in the New Ireland Basin, to have formed in response to plate flexure and arc-parallel maximum horizontal compression (Figure 2.11).

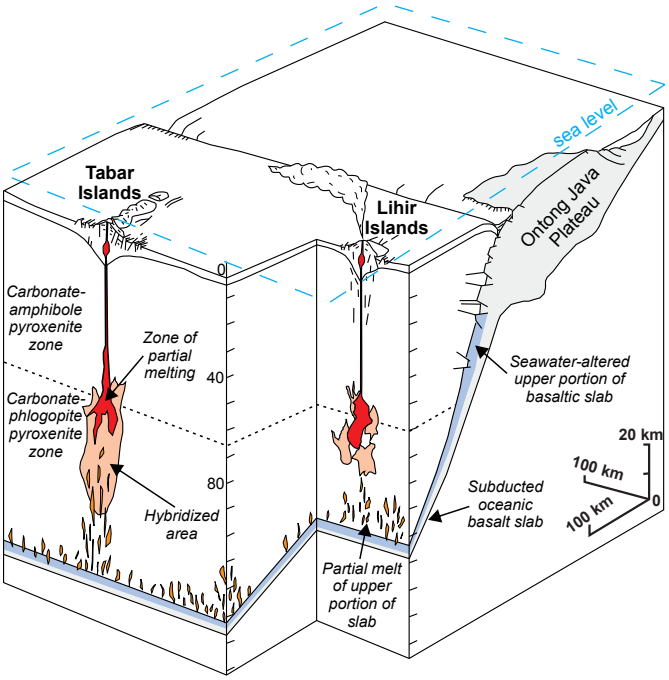

Figure 2.10: Schematic block diagram of superimposed extension and melting to form hybrid geochemical signature of the Tabar-Lihir-Tanga-Feni island chain. Extension would adiabatically decompress the subduction-modified mantle wedge, generating alkaline, silica-undersaturated, high fO_2 magmas (modified after McInnes and Cameron, 1994).

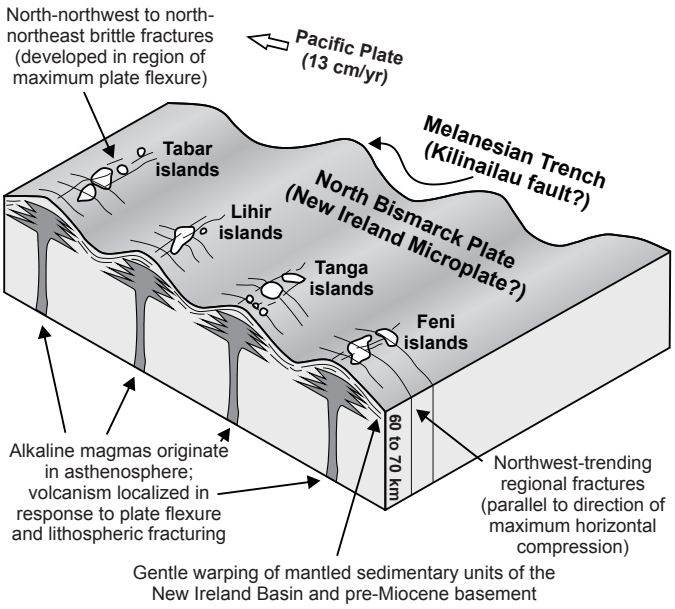

Figure 2.11: Model for the Tabar-Lihir-Tanga-Feni island chain arc volcanism from Lindley (2016). North-northwest, north-northeast and northwest trending regional fractures throughout the Tabar-Lihir-Tanga-Feni islands, as well as mantled sedimentary units in the New Ireland Basin, are attributed to have been formed in response to plate flexure and arc-parallel maximum horizontal compression.

Although a deep-seated structural control on the islands' morphologies is likely, modern earthquake data, albeit sparse, do not provide consistent evidence of extensional faulting parallel to their long-axes (Figure 2.8). Nonetheless, it remains feasible that this type of extensional activity may have occurred in the past to help create the islands.

A new tectonic model, presented in Figure 2.12, integrates aspects of previous models with a broader model of northwestward transposition and rotation of the North Bismarck Plate relative to the South Bismarck Plate, over what has been modeled as perturbations in the subducting Solomon Sea Plate (e.g., O'Kane, 2008; Holm and Richards, 2013). The crust underlying the Tabar-Lihir-Tanga-Feni islands most likely experienced transposition to the northwest in the last ~ 3.5 Ma, similar to neighboring New Ireland (Figure 2.12A–C). This was accommodated in part by sinistral strike-slip shear on the Bismarck Sea Seismic Lineation, which to this day partly dissects New Ireland (Figure 2.12A–C). The progressive counterclockwise shift in island long-axes with time is interpreted to record an additional rotational component of strain (Figure 2.12B). The relatively high length-to-width aspect of New Ireland could be explained by a component of island-parallel extension that occurred during the transposition, and this could have been accompanied by normal faults oriented at high angles to the island's length. This new scenario would mean that the oldest and northernmost islands (including Lihir), formed between 200 and 400 km southeast of their current position (Figure 2.12A). Taking the ~ 240 km and ~ 2 m.y. separation between the oldest islands in the north and the youngest islands in the south, a calculated tectonic plate motion vector would be ~ 12 cm/yr at an azimuth of 309° (Figure 2.12A–C). This tectonic plate speed is consistent with the

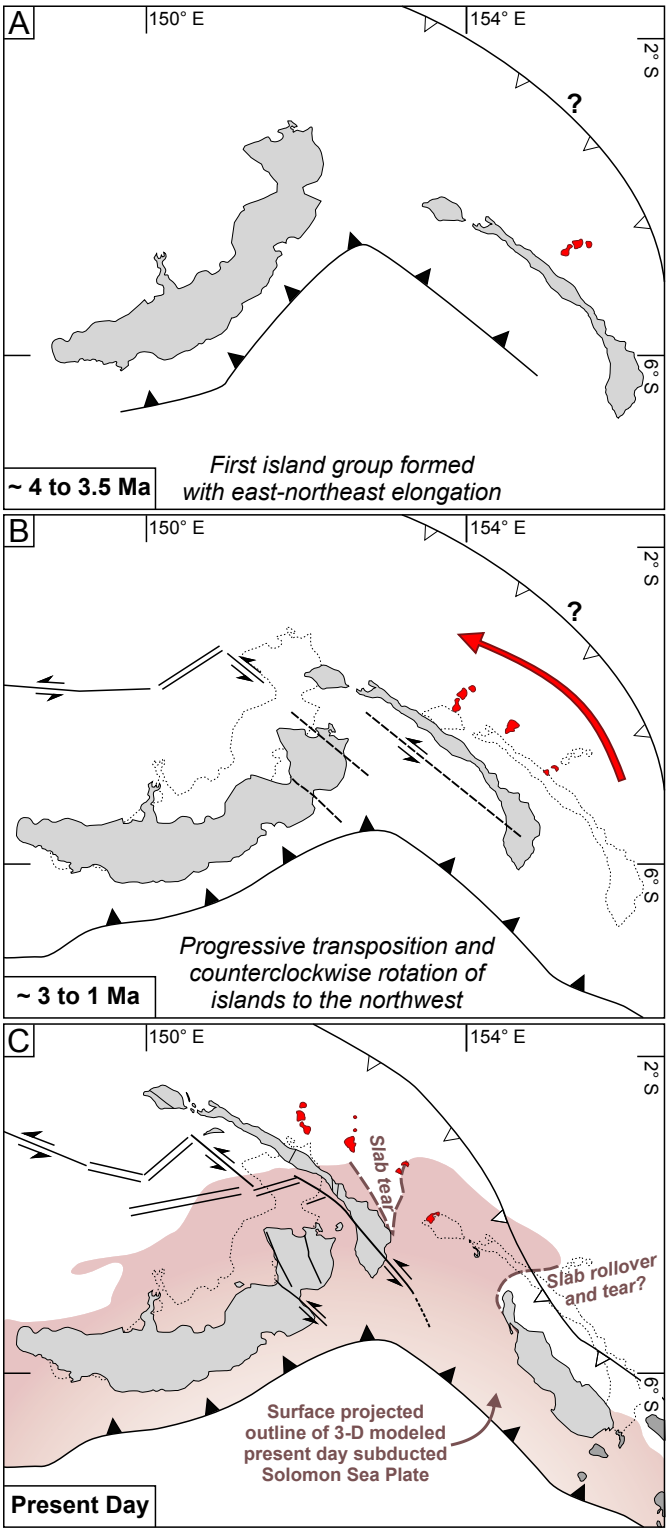

Figure 2.12: Schematic diagram of a new tectonic scenario with dynamic rotation and transposition of the Tabar-Lihir-Tanga-Feni island chain. Surface projected 3-D trace of modeled Present Day subducted Solomon Sea Plate, from O'Kane (2008). **A)** Tectonic reconstruction of New Britain and New Ireland at ~ 3.5 Ma (modified from Holm and Richards, 2013). First island group, Tabar, is shown forming with a distinct eastward-elongation. **B)** Theorized tectonic scenario from ~ 3 to 1 Ma. New Ireland is transposed to the northwest, with counterclockwise rotation. The Tabar-Lihir-Tanga-Feni islands also continue to form in the southeast, and mimic the transposition ± counterclockwise rotation of New Ireland. **C)** Present Day position and tectonic elements of New Britain, New Ireland and the Tabar-Lihir-Tanga-Feni island chain (modified after Taylor et al., 1994; Tregoning et al., 1998; Tregoning, 2002).

current plate tectonic speeds in the area (e.g., Pacific to South Bismarck Plate relative motion vector of 13 cm/yr at an azimuth of 316°; Tregoning et al., 1998; or Pacific to Australia Plate relative motion vector of ~ 11 cm/yr; DeMets et al., 1990; Tregoning et al., 2000; Wallace et al., 2004).

The formation of the island chain is still enigmatic in this new proposed dynamic scenario. The islands may have formed via episodic alkaline magmatism, resulting from the progressive migration of the Tabar-Lihir-Tanga-Feni crust above stationary or mobile perturbations in the subducting Solomon Sea Plate (cf., Hole et al., 1991), possibly aided by a pre-existing island arc structural architecture from the paleo-Melanesian subduction zone. This proposition supports the lines of evidence of linear relationships observed between angular discordance and separation of islands along the chain, and the southward younging of island's ages (e.g., Figure 2.5). It may be that migration of the asthenospheric mantle wedge towards the extended, over-steepened segments of the down-going slab, or asthenospheric upwelling through the inferred slab tear, provided a local heat source that triggered melting of the subduction modified mantle below the island chain. A possible site for one of these perturbations in the down-going slab is located southeast of the Feni islands, where an eastward-trending splay of deep-seated extensional earthquakes is evident (i.e., Figures 2.6D, 2.8, 2.12C). Lastly, it should be noted that progressive counterclockwise rotation of initially extensional or transtensional structures may have led to them being oriented within the compressional field of strain. If steeply-dipping, they would resisted failure. This may account for the limited number

of low magnitude compressional earthquakes along fault traces northwest of the Tabar-Lihir-Tanga-Feni islands (e.g., Figure 2.8). Similarly complex microplate rotations have been recorded in other parts of the southwest Pacific (e.g., Fiji; Kroenke and Rodda, 1984).

2.7: Summary

Lihir Island, and the Tabar-Lihir-Tanga-Feni island chain, are the products of a very complex tectonic history that remains debated to this day. Initial oblique westward convergence of the Pacific Plate with the Australian Plate in the Paleogene resulted in the broad Melanesian Arc. Subduction along this arc was a precursor to later events, and it led to enrichment of the mantle wedge. The docking of the colossal Ontong Java Plateau with the Melanesian Trench during the Oligocene caused a near-complete cessation of magmatism, and eventually aided in a reversal of subduction polarity in the Miocene (Figure 2.1). This new subduction zone was the markedly northward-convex New Britain Trench. Consequences of the initiation of subduction along the New Britain Trench included Pliocene to Recent coeval back-arc spreading in the Manus Basin, arc volcanism along New Britain, sinistral transposition of New Ireland relative to New Britain, and formation of the Tabar-Lihir-Tanga-Feni island chain.

Islands of the Tabar-Lihir-Tanga-Feni chain have notable linear relationships between angular discordance of island long-axes and their spatial separation (Figure 2.5). An apparent younging of volcanism exists, however, the age constraints on the islands remain poor due to a paucity of data. Lavas of the Tabar-Lihir-Tanga-Feni island chain are shoshonitic, alkali- and volatile-rich, silica-undersaturated, highly oxidized with elevated large-ion lithophile elements. They have hybrid geochemical characteristics consistent with melting of a mantle wedge that was potentially metasomatized by the fossil Melanesian subduction zone.

A new tectonic scenario is proposed here, whereby the Tabar-Lihir-Tanga-Feni island chain experienced a progressive northwestward counterclockwise transposition during the last ~ 3.5 Ma (Figure 2.12), as is the case of neighboring New Ireland (Taylor, 1979). Magmatism was transient at different localities during this transposition (e.g., near perturbations in the subducted slab, at structures created from stress in response to transposition, etc.). Further studies are required to confirm the prevalent tectonic environment for the formation of the Tabar-Lihir-Tanga-Feni island chain. This could include refined modeling of the plate configurations over the past ~ 3.5 m.y., with the use of tomographic data, combined with refined models of stresses and strain associated with the subducting Solomon Sea Plate. Detailed investigation of geochemical variations between the islands and better constraints on the magmatic ages for each of the islands would be essential to help resolve these issues. Nevertheless, it is clear that the formation and evolution of the Tabar-Lihir-Tanga-Feni island chain is unique and was certainly an important factor in creating what is now one of the most well-endowed metallogenic regions of the world.

Chapter 3: Geological framework of Lihir

3.1: Introduction

This chapter reviews the geological framework of the Lihir gold deposit. The aims are to document the volcanic and intrusive framework of the Luise amphitheater, and to introduce orebody architecture and associated alteration zones. The alteration zones are of significance because they underpin the geological model employed by Lihir's mining operations. Each zone is mined as a separate 'ore type', with distinct gold grades and distribution, textures, and mineral assemblages. Collectively, they form an extensive three-layer framework (i.e., clay zone, sulfide – adularia zone and anhydrite zone), wherein distinct mineral and alteration assemblages broadly represent the different paleo-physicochemical environments of formation (i.e., porphyry-style versus epithermal and geothermal environments). The 'anhydrite zone' in the Lienetz orebody is the focus of this study.

3.2: Lihir Island geology

Lihir Island has poor exposure, dense tropical rainforest cover, and rugged, often inaccessible terrain. Regional geological mapping is limited. A map produced by Wallace et al. (1983), based largely on geomorphological features and selected hand specimens, is one of the few island-scale interpretations available (Figure 3.1A). These workers identified volcanic trachybasalt and alkali basalt lavas, volcaniclastic deposits, and fringing limestone reef deposits. Five volcanic centers, presently inactive, were identified from geomorphological mapping. Three of the volcanoes are characterized by seaward-breached amphitheaters, each of which are believed to have formed via sector collapse. The most prominent of the amphitheaters, Luise, hosts the Lihir gold deposit (Figure 3.1A–C).

The age of Lihir Island is undetermined, as most age dates have been of hydrothermally altered or mineralized samples. However, Lihir Island is inferred to have begun forming < 4 Ma, based on age constraints of volcanic rocks from the surrounding Tabar-Lihir-Tanga-Feni island chain (e.g., Table 2.1; Figure 2.5C).

The island's fringing limestone reef deposits are absent adjacent to the Luise amphitheater (Figure 3.1A). This has been interpreted to be the result of its removal from volcanic sector collapse (Wallace et al., 1983; Moyle et al., 1990; Blackwell, 2010). Alternatively, high-temperature geothermal activity in the Luise Harbour may have also prevented modern limestone reef deposits from forming due to the increased temperatures and acidity of shallow marine waters (e.g., Pichler et al., 1999).

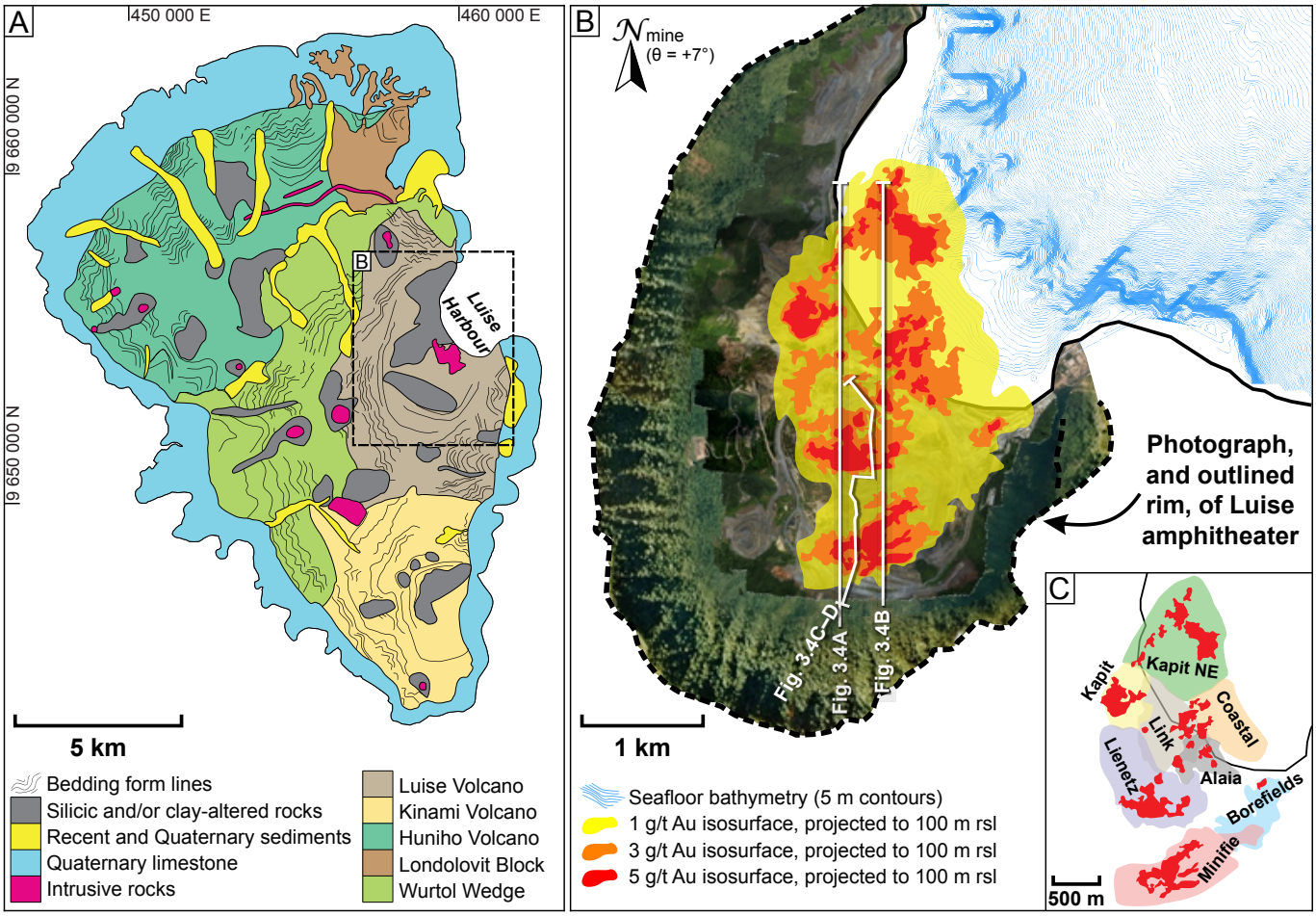

Figure 3.1: Lihir Island geological map and position of the Lihir gold deposit within the Luise volcanic amphitheater. A) Geological map with five Plio-Pleistocene volcanic blocks, interpreted from geomorphological features (modified after Wallace et al., 1983, from Lawlis, in prep.). **B)** Plan view of the Lihir gold deposit, within the Luise amphitheater. Gold grades are from 3-D isosurfaces projected to 100 m rsl. **C)** Insert of the Lihir gold deposit with polygons around, and names of, all orebodies.

3.2.1: Uplift of Lihir Island

Gentle uplift (~ 50 m) with a south- to southwest-directed tilt was interpreted by Wallace et al. (1983) for islands of the Tabar-Lihir-Tanga-Feni chain, based on the distribution of Neogene to Quaternary limestone terraces. Shallow-water reef limestone terraces on Lihir Island have also been used to infer paleo-uplift. Blackwell (2010) constructed a stratigraphic column of uplifted limestone north of the Luise amphitheater, and acquired ^{230}Th–^{234}U ages of 177 ± 28 years, 235,000 ± 3000 years (duplicate value of 274,000 ± 6000 years), and 191,000 ± 2000 years of three limestone samples at 1 m, 15 m and 40 m above sea level (i.e., relative to sea level; rsl). Because open-system U–Th behavior of fossil corals was inferred for the older samples, they were taken to be maximum ages. Based on the age and elevation of the 1 m rsl, 177 year old modern limestone reef sample, Blackwell (2010) proposed a ~ 2 km uplift rate for the past 200,000 years. However, calculated subsidence and uplift rates appear to be more moderate. The oldest age (~ 254,000 years average) of the 15 m rsl sample, and the younger age (~ 190,000 years) of the 40 m rsl sample, imply a subsidence rate of ~ 40 m per 100,000 years from ~ 254,000 to ~ 190,000 years ago, whereas the modern limestone reef's 177 years old age at 1 m rsl, in relation to the 190,000 years age of the sample at 40 m rsl implies a uplift rate of ~ 20 m per 100,000 years from ~ 190,000 years ago to Present Day.

3.3: Luise amphitheater geology: pre-ore constructional volcanism and magmatism

The Luise amphitheater is 4 × 3.5 km wide. It is elongated and breached to the northeast (Figure 3.1B). The pre-mining depth of the amphitheater floor was 80 m rsl and the height of the walls are 640 m rsl (Blackwell, 2010). The original volcanic cone height is estimated to have been ~ 1100 m rsl, determined by extrapolating the dip of the amphitheater walls and assuming a symmetrical cone (Wallace et al., 1983; Blackwell, 2010). Seafloor mapping adjacent to the Luise amphitheater has identified hummocky topography and marginal levees extending ~ 10 km offshore (Figure 3.1B). These features are considered to represent offshore debris avalanche deposits of the sector collapse event(s) that formed the Luise amphitheater (Herzig et al., 1998; Blackwell, 2010; White et al., 2010).

The pre-ore evolution of the Luise amphitheater consisted of multiple phases of constructional volcanism and magmatism, involving basaltic to andesitic volcano-sedimentary strata and emplacement of equigranular to porphyritic intrusions (Figure 3.2). Volcanic and intrusive rock types were first identified by Davies and Ballantyne (1987), Moyle et al. (1990) and Carman (1994), and then examined in detail later by Blackwell (2010), at both the orebody scale and more regionally throughout the amphitheater. The following is a summary of their work, combined with new observations from the current study.

3.3.1: Volcano-sedimentary rocks

The volcano-sedimentary strata consist of clastic rocks (i.e., polymictic matrix-rich breccias and sandstones, mudstone, and mud-rich breccias), interbedded with coherent rocks (i.e., multiple basaltic and andesitic lavas, and shallow intrusions; Figure 3.2). The polymictic matrix-rich breccias and sandstone are massive to weakly bedded, with sandy matrix and stratiform to randomly distributed accretionary lapilli. The mudstones are laminated to massive, and interbedded with, or transitional to, mud-rich breccias. Andesites and basalts are generally tabular, sub-horizontal bodies that variably grade outwards to monomictic breccias. The basalts are volumetrically dominant over the andesites, and are particularly abundant in the upper portions of the strata, where they occur commonly as sub-horizontal lava flows and sills, and less commonly as sub-vertical dikes. Where in contact with mudstone, the margins of some andesite and basalt lavas are peperitic. Clasts of basalt, andesite, as well as rare mudstone, are found within the polymictic breccias.

The volcano-sedimentary package was interpreted by Blackwell (2010) to be typical of a composite volcano. Abundant volcaniclastic debris flows (i.e., polymictic, matrix-rich breccias and sandstones) were deposited throughout the succession, and reflect a continual, abundant source of detritus, driven by gravity transportation. The depositional environment may have been sub-aerial, or at least proximal to sub-aerial, as indicated by the presence of accretionary lapilli (Blackwell, 2010). Sedimentation was interspersed with

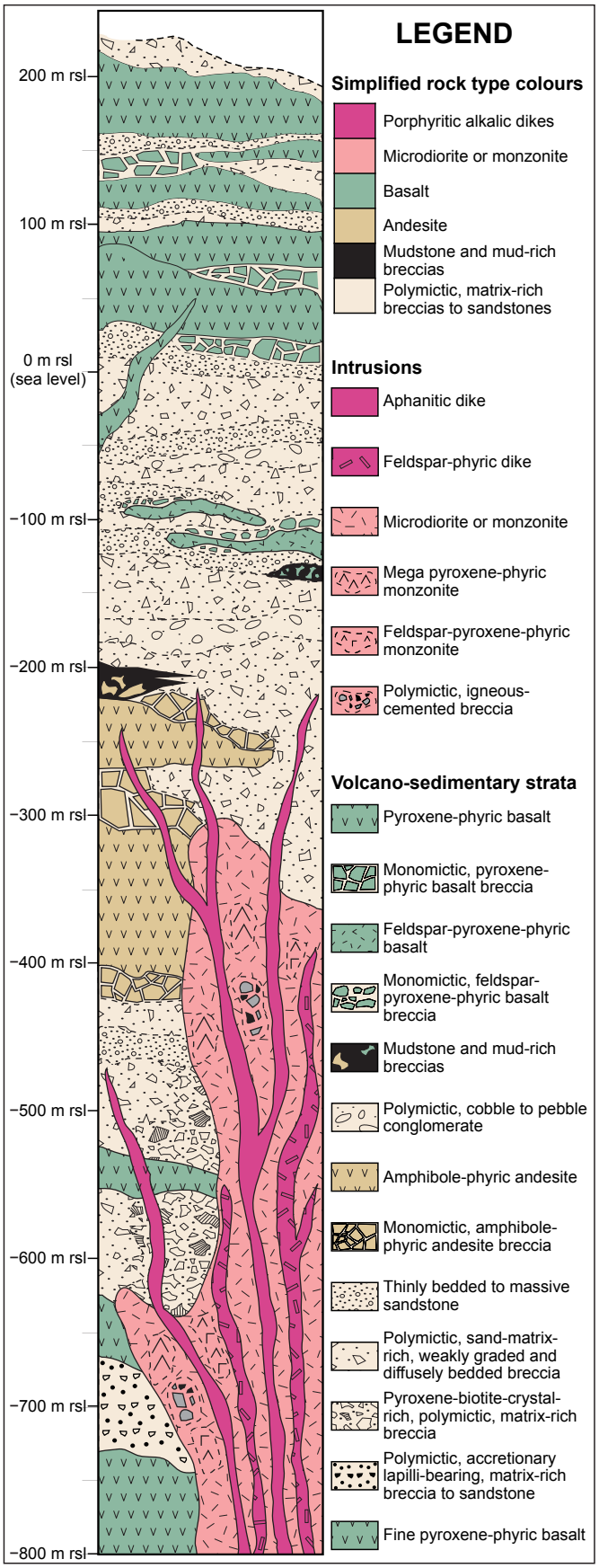

Figure 3.2: Schematic of pre-ore constructional volcanism. Composite graphic log, modified after Blackwell (2010), depicting relationships among major volcano-sedimentary strata and intrusions in the Luise amphitheater.

the emplacement of dikes, sills and autoclastic facies associated with andesitic and basaltic lavas and/or shallow intrusions. Episodes of low energy suspension settling of mud layers raise the possibility of sub-aqueous depositional periods. The highest preserved, lava-dominant part of the strata has a poorly constrained depositional environment. Overall the strata link broadly to the Luise volcano (Blackwell, 2010), however, they may represent an older volcanic phase. The rim of the amphitheater was not included in the stratigraphic studies by Blackwell (2010), and remains unexamined in detail, largely due to deep weathering, dense vegetation cover and poor accessibility.

3.3.2: Intrusive rocks

From −200 m rsl and below is a series of monzonite, microdiorite and porphyritic (i.e., syenite and/or monzonite) intrusions that cross-cut the volcano-sedimentary strata (Figure 3.2; Blackwell, 2010). The largest and oldest intrusions are the monzonite ± microdiorite stocks. They are equigranular- to seriate-textured (Figure 3.3A–B), however, the monzonite has local porphyritic subfacies with pyroxene ± feldspar phenocrysts (Figure 3.2). Feldspar, biotite, magnetite, pyroxene and amphibole are present in both monzonite and microdiorite stocks (Figure 3.3A–B). Cross-cutting the stocks are a series of sub-vertical porphyritic to aphanitic dikes that reach higher levels in the strata (Figure 3.2). Dikes are < 20 m wide with high-angle to sub-vertical dips. Their compositions are close to syenite, with distinct K-feldspar (~ 0.5 cm) and biotite (~ 0.1 cm) phenocrysts set in a K-feldspar-rich aphanitic groundmass (Figure 3.3C), with lesser to trace amounts of plagioclase, titanite, nepheline and apatite.

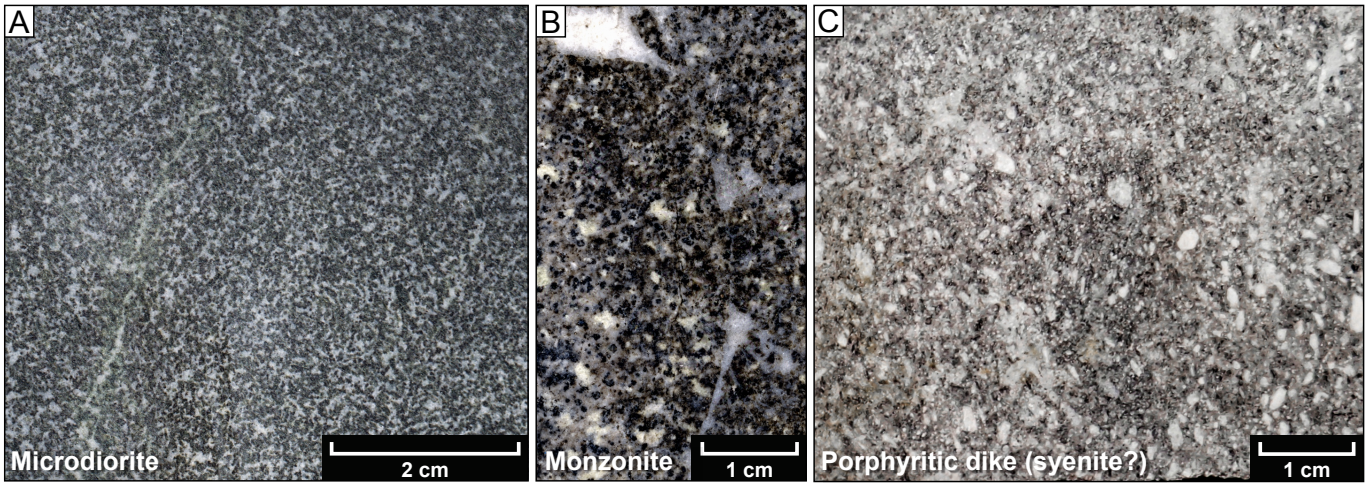

Figure 3.3: Hand sample photographs of intrusive rocks. A) Cut hand-sample specimen of the equigranular microdiorite (sample LH13SS050, located at −258 m rsl, 9653980 N, 459252 E). **B)** Cut drill-core specimen of the seriate-textured monzonite (sample from 300 m in DDHL0791, located at 44 m rsl, 9654196 N, 459133 E). **C)** Cut hand-sample specimen of the porphyritic-textured syenite (?) dikes (sample LH14SS077, located at −230 m rsl, 9654210 N, 459316 E).

The intrusive rocks are interpreted to be either monzonite and microdiorite deep-seated stocks, or alkalic (e.g., syenite, monzonite) porphyritic and aphanitic dike swarms (Blackwell, 2010). The porphyritic texture implies the dikes form by a two-phase crystallization history, and the aphanitic texture also highlights the rapid crystallization of some dikes. This might reflect a change in uplift or exhumation, however, intrusive rocks have not been successfully dated, and therefore exact timing relationships between inferred younger dikes and older stocks is unknown.

3.4: Lihir gold deposit

The Lihir gold deposit is nested within the Luise amphitheater and consists of several adjacent and partly overlapping orebodies (Figure 3.1B–C). Intense alteration from the ancient and modern hydrothermal system has obscured many of the primary rock types. The alteration extends beyond the ore both vertically and laterally (Figure 3.4), but is particularly texturally destructive at upper levels of the deposit. A broad three-fold zonation exists in terms of alteration type and intensity, which corresponds in part to gold tenor and distribution. The mine geological model uses this zonation to classify ore types (Table 3.1; Figure 3.4A–B). With increasing depth, these alteration zones include: (1) a surficial, generally low-grade to barren, steam-heated clay alteration zone, with a flat-lying base that sub-parallels the present-day floor of the Luise amphitheater; (2) a high-grade (> 3 g/t Au) refractory sulfide and adularia alteration zone, again with broadly sub-horizontal form, but in detail, a crenulate base; and (3) a comparatively low-grade to barren zone of anhydrite ± carbonate veins, intergranular cement and breccias, coupled with biotite alteration, that extends both laterally and to depth beyond ore and limits of resource drilling (Figure 3.4A–B; Davies and Ballantyne, 1987; Moyle et al., 1990; Carman, 1994). Rough age constraints of hydrothermal minerals related to the three-fold alteration zones have been determined by Davies and Ballantyne (1987), Moyle et al. (1990), Rytuba et al. (1993) and Carman (1994) using ^{40}K–^{40}Ar and ^{40}Ar–^{39}Ar methods (e.g., Tables 2.1,

Table 3.1: Alteration zones of the Lihir gold mine

Alteration zone	Gold grade	Age (Ma)	Diagnostic mineralogy	Geometry	Alteration interpretation	Interpretation
Clay zone	Low to barren (< 0.3 g/t Au)	0.15 to 0.00[1]	kaolinite, K-alunite, smectite, illite, montmorillonite ± opal	~ 250 m thick, sub-parallel to basal topography of amphitheater	Argillic ± advanced argillic	Steam-heated clay related to the modern geothermal system[2, 4]
Sulfide – adularia zone	High (> 2 g/t Au)	0.6 to 0.2[2, 4]	pyrite, marcasite, adularia, illite, sericite, quartz ± chalcedony ± calcite	Sub-parallel to basal topography of amphitheater with crenulated local downward projecting base	Epithermal-style low-sulfidation	Refractory sulfide ore and vuggy breccias from boiling via sector collapse events[1, 2, 4]
Anhydrite zone	Low to barren (< 1.0 g/t Au)	0.9 to 0.3[1, 3]	anhydrite, quartz, calcite, biotite, K-feldspar ± vermiculite ± magnetite ± chlorite ± epidote	Vertically and horizontally extensive basal unit; lateral and lower limits undefined	Porphyry-style potassic	Extensive anhydrite dissemination and veins from early porphyry-stage[1, 2, 4]

References: [1] = Davies and Ballantyne (1987); [2] = Moyle et al. (1990); [3] = Rytuba et al. (1993); [4] = Carman (1994).

3.1), however, thermal resetting of radiometric ratios has been questioned due to the modern high-temperature geothermal system.

The three alteration zones overprint each other at their basal contacts, and are conventionally interpreted to record distinct stages in the evolution of the magmatic-hydrothermal system (Davies and Ballantyne, 1987; Moyle et al., 1990; Carman, 1994). The lower anhydrite zone records an early porphyry-style magmatic-hydrothermal stage (~ 0.9 to 0.3 Ma), the sulfide – adularia zone represents a transition to an epithermal environment (~ 0.61 to 0.19 Ma), whereas the surficial zone of intense clay alteration is a product of the modern geothermal system (~ 0.15 Ma to Present; Table 3.1; Figure 3.4; Davies and Ballantyne, 1987; Moyle et al., 1990; Carman, 1994). Episodic volcanism has occurred during the modern geothermal-stage, with the emplacement of several volcanic-hydrothermal (diatreme) breccia bodies (> 0.06 Ma; Lawlis, in prep.), which cross-cut both anhydrite- and sulfide – adularia-dominant alteration domains.

There is significant heterogeneity within these broad, simplified alteration zones. Only the geothermal-stage, encompassed by the clay zone, is a relatively uniform layer (Figure 3.4A–D). Within porphyry- and epithermal-stage zones, there is considerable variability, both in terms of gold grades (Figure 3.4A–B), and the distribution of anhydrite veins, breccias and disseminations (Figure 3.4C–D; Carman, 1994).

3.4.1: Porphyry-stage: anhydrite zone

Anhydrite is an abundant mineral at Lihir, particularly in the lower-levels (Figure 3.4C–D). Although the anhydrite zone is defined by the presence of anhydrite, it is important to note that the mineral is not unique to this zone. Relatively minor concentrations occur within both the sulfide – adularia zone (e.g., where anhydrite is remnant and/or bladed), and as part of the modern geothermal system (e.g., where it precipitates as scales). This anhydrite zone is also referred to as the ‘anhydrite seal’ by mine personnel,

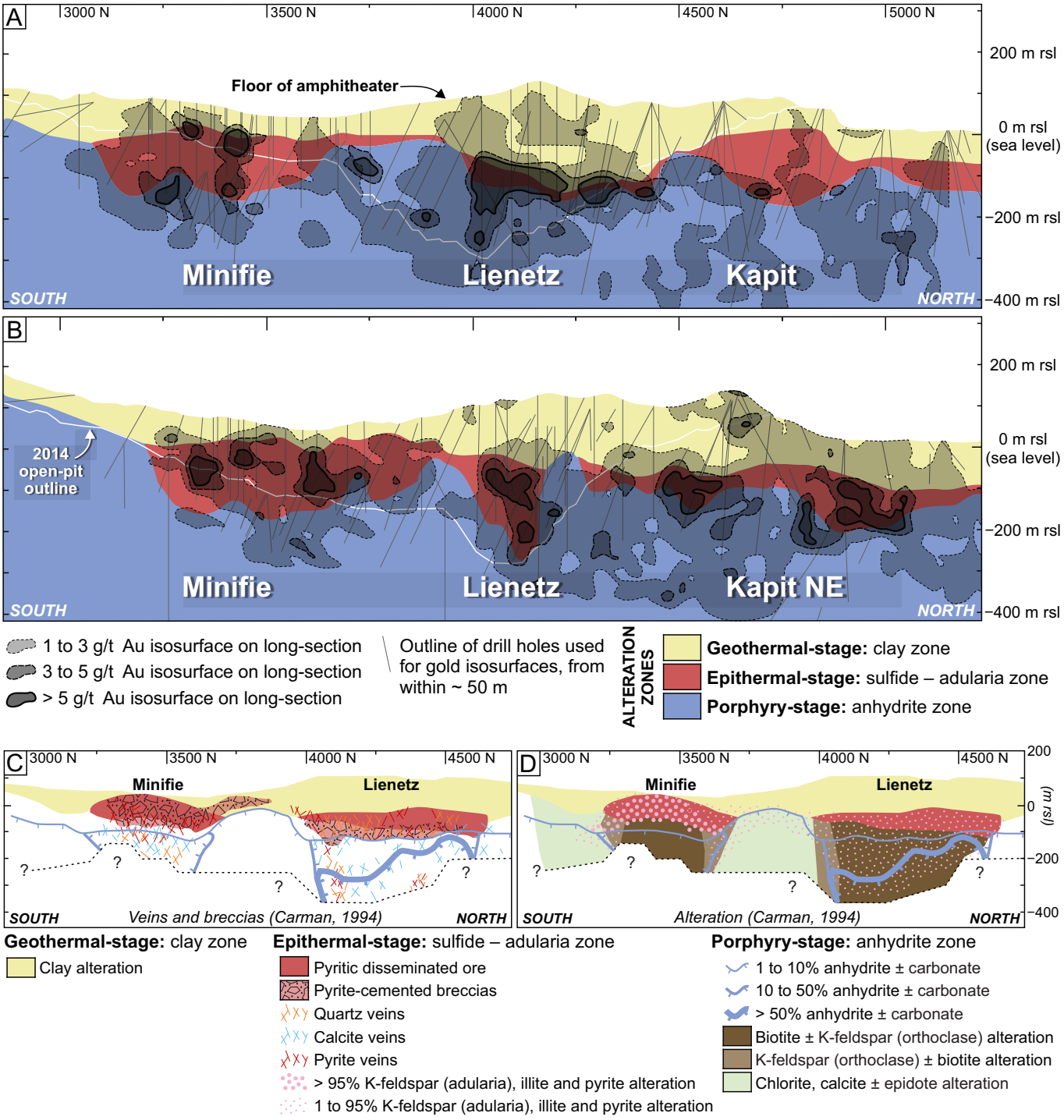

Figure 3.4: Alteration zones and gold grades within the Minifie, Lienetz, Kapit and Kapit NE orebodies. South to north long-sections, looking west, of the Lihir gold deposit along mine-grid easting of **A)** 9300 E and **B)** 9600 E. **C)** Carman (1994)'s long-sections, looking west, of the Minifie and Lienetz orebodies showing distribution of porphyry-, epithermal- and geothermal-stage features including veins, breccias, pyritic ore, anhydrite and **D)** alteration. Location is shown in Figure 3.1B.

however, the name is colloquial, deriving from the geometrically analogous impermeable seal in the modern geothermal system (discussed further below). Results of this study indicate that anhydrite precipitation was multistage throughout Lihir's hydrothermal history. Its paragenesis, and characteristics that allow discrimination of growth stages, will be examined in subsequent chapters.

The upper surface of the anhydrite zone occurs at elevations between −150 and −200 m rsl, directly below the sulfide – adularia zone in ore-bearing domains (Figure 3.4A–B). It approaches the surface in unmineralized areas, where it underlies the clay-dominant alteration zone, and has as-yet undetermined lower limits (Figure 3.4A–B; Davies and Ballantyne, 1987).

The anhydrite zone is defined by the presence of > 1% anhydrite ± calcite ± quartz occurring as veins, breccia cement and/or intergranular disseminations within wall rocks (Table 3.1; Figure 3.4C–D; Davies and Ballantyne, 1987). Locally the volume of anhydrite is > 50% within the intrusive and volcanic host rocks, and lateral variation corresponds to changes in alteration (Figure 3.4A–D). There is an association of 10 to > 50% anhydrite ± carbonate with strong biotite and K-feldspar alteration, focused in the orebodies, and peripherally there is an association of 1 to < 10% anhydrite ± carbonate with chlorite, calcite ± epidote alteration (Figure 3.4D; Carman, 1994). Carman (2003)'s stable isotope and fluid inclusion studies of anhydrite from the anhydrite zone, and related biotite (i.e., phlogopite), were consistent with a magmatic source (i.e., $\delta^{18}O_{H2O}$ = 6 ‰, and fluid inclusion salinities of 5 to > 40 eq. wt. % NaCl). The anhydrite zone has therefore been interpreted as a product of porphyry-style potassic and/or propylitic alteration (Figure 3.4; Davies and Ballantyne, 1987; Carman, 1994, 2003), although it is atypical of calc-alkalic porphyries in terms of lacking well-developed quartz stockwork veining (e.g., Sillitoe, 2010).

The anhydrite zone typically marks the lower extent of high-grade (> 3 g/t Au) mineralization (Figure 3.4A–B; Davies and Ballantyne, 1987; Moyle et al., 1990; Carman, 1994). Gold grades on the order of 1 – 3 g/t (and more sporadic > 3 g/t Au zones) occur mainly within the upper part of the anhydrite zone, and share similar lateral extent with that of overlying high-grade gold mineralization in the sulfide – adularia zone (Figure 3.4A–B). There is sparse information of gold grades at depth, but on average, low-grades (~ 1 g/t Au) appear to be generally associated with the porphyry-style potassic alteration (Figure 3.4A–B, D).

3.4.2: Epithermal-stage: sulfide – adularia zone

The sulfide – adularia zone is defined by pyrite-cemented breccias, abundant adularia alteration and disseminated pyrite in altered wall rocks (Table 3.1; Figure 3.4A–D; Davies and Ballantyne, 1987). Intense adularia – pyrite ± illite-altered rocks dominates this zone, typically > 95 vol. % total replacement of primary minerals (Carman, 2003). Anhydrite is present locally in low abundances (< 1%), with the mineral occurring along with quartz and calcite as bladed anhydrite filling cavities. The lower parts of the sulfide – adularia zone transitions gradationally into the biotite- and K-feldspar-altered rocks of the anhydrite zone. The upper parts are typically more adularia ± illite-altered (e.g., Figure 3.4C–D; Davies and Ballantyne, 1987; Carman, 1994). Carman (2003)'s fluid inclusion studies of this sulfide – adularia zone were consistent with a mixed magmatic and meteoric ground water source (i.e., $\delta^{18}O_{H2O}$ = < 0 ‰ mixed with ~ 6 ‰ which correlated to estimated temperature of ~ 200°C, and fluid inclusion salinities of ~ 2 to 7 eq. wt. % NaCl).

This sulfide – adularia zone typically is host to high-grades (> 3 g/t Au), in the form of refractory sulfide ore (Table 3.1). While high-grade gold mineralization is more uniform in this zone, it is not ubiquitous.

A combination of adularia and illite alteration with high-grade refractory sulfide ore, along with low

salinity fluid inclusions, has been interpreted to indicate that the sulfide – adularia zone corresponds to low-sulfidation epithermal-style alteration and mineralization (Davies and Ballantyne, 1987; Carman, 1994, 2003). The sulfide – adularia zone has been colloquially referred to as the 'boiling zone' by mine personnel. The term is not used here as it has genetic connotations, implying an episode of phase separation and boiling as the system decompressed, evolving from porphyry-style to epithermal conditions (Davies and Ballantyne, 1987; Moyle et al., 1990; Carman, 1994; Corbett et al., 2001).

3.4.3: Volcanic-hydrothermal diatreme breccias

Cross-cutting the anhydrite and sulfide – adularia zones, and coinciding with or forming the margins of the orebodies, are a series of matrix-rich, polymictic breccia bodies, interpreted to have formed by phreatomagmatic eruptions (Figure 3.5A–C; Blackwell, 2010; Lawlis et al., 2015). These volcanic-hydrothermal (diatreme) breccias consist of at least seven large, north- to northeast-trending (Figure 3.5C), coalescing, downward tapering, elliptical pipes (Figure 3.5A). They are both spatially and genetically linked to small (~ 10 m wide) sub-vertical andesite dikes, interpreted to be the magmatic triggers for eruption (Lawlis et al., 2015). Clasts are contained within a fine-grained, rock-flour matrix, and include charcoal, internally stratified or juvenile volcanic components, as well as anhydrite-, pyrite-kaolinite-dickite- and pyrite-altered clasts (Lawlis et al., 2015). The diatreme breccias rarely contain mineralized clasts and are comparatively low-grade (i.e., average ~ 0.8 g/t Au), but locally have complex relationships with mineralization, particularly in Kapit NE where quartz – calcite – pyrite – adularia veins cross-cut the diatreme breccia near its contact (Lawlis et al., 2015). As such, these phreatomagmatic eruptions occurred after the high-grade and main stage of gold mineralization, but not the conclusion of mineralization (Lawlis et al., 2015).

3.4.4: Geothermal-stage: clay zone and modern geothermal system

Throughout the upper levels (i.e., above −100 m rsl) of the Lihir gold deposit, a modern geothermal system has, and still continues to, alter most of the rocks to clay, defining the clay zone, or in mine terminology, the 'clay blanket' (Figure 3.4A–B). The clay zone is expressed beneath the floor of the Luise amphitheater as a weakly to unmineralized, ~ 250 m thick sub-horizontal layer of clay-altered material (Table 3.1; Figures 3.4A–B, 3.6). Previous workers have unanimously concluded that the zone formed by steam-heated processes (i.e., condensation of steam and H_2S separated from underlying boiling fluids, and sulfide oxidization to sulfate near the surface generating acidity resulting in advance argillic alteration; Table 3.1; Browne, 1978; Moyle et al., 1990; Carman, 1994; Corbett, unpublished data, 2001; Jansen, unpublished data, 2013).

Modern geothermal activity is most extensive at the northern end of the Lihir gold deposit, near the

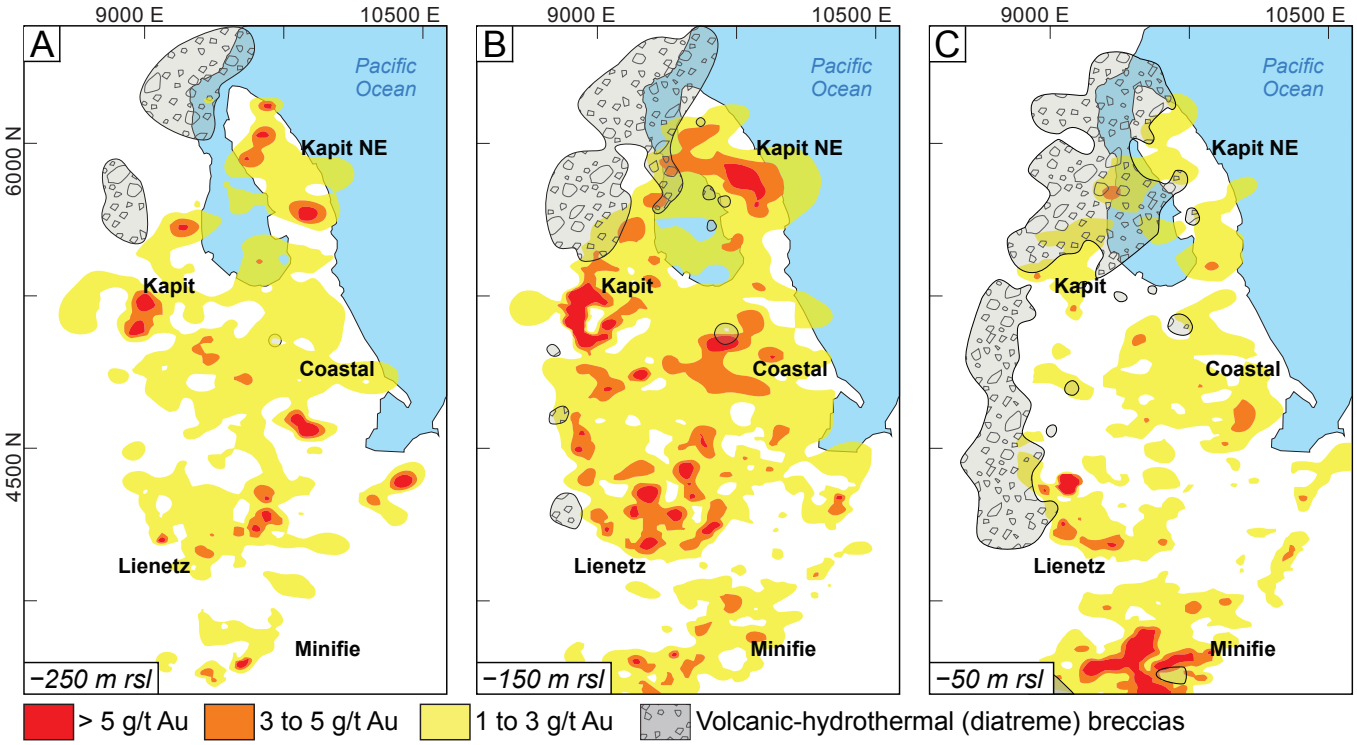

Figure 3.5: Volcanic-hydrothermal (diatreme) breccias and their relationship with the gold orebodies at Lihir. Modified from Lawlis et al. (2015). Plan view horizontal slices are at **A)** −250 m rsl, **B)** −150 m rsl, and **C)** −50 m rsl.

Kapit orebody (Williamson, 1983), along northeast and east-northeast structures (Vogwill et al., 2009; this study), and within the Luise Harbour, where it is depositing auriferous pyrite and marcasite within seafloor sediments (Pichler et al., 1999). The geothermal system is zoned vertically (Figure 3.6). It consists of a deep liquid reservoir, a two-phase liquid and gas reservoir, a shallow gas reservoir and shallow liquid reservoir (Table 3.2; Figure 3.6; SKM, unpublished data, 2007; Johnstone et al., 2007). Below −300 m rsl the geothermal reservoir has temperatures of ~ 230 to 270°C, and chemical compositions reflective of near-neutral to alkaline, oxidized conditions (Table 3.2; Figure 3.6). Fluids are sulfate-rich (> 30,000 ppm SO_4^{2-}) with high concentrations of dissolved salts, and have deuterium and oxygen isotopic signatures consistent with magmatic ± meteoric origins (Table 3.2; Wallace et al., 1983; Williamson, 1983; Geothermex, unpublished

Table 3.2: Geothermal system at the Lihir gold mine

Depth (m)	Reservoir type	Information	Temperature (°C)
0	**Shallow liquid reservoir**	Mixture of meteoric, seawater and groundwater; shallow, near-neutral chloride springs contain < 1.5 ppb Au	100°
−200	**Shallow gas reservoir**	Acidic (pH 1.6 to 2.8), sulfate-rich low-chloride fluids	150°
−400	**Two-phase liquid – gas reservoir**		200°
−600	**Deep liquid reservoir**	Near-neutral to alkaline, oxidized, sulfate-rich (~ 30,000 ppm SO_4), high chloride and bicarbonate (~ 20,000 ppm Cl), high TSD (> 100,000 ppm), high Na/K, low H_2S (~ 6 × 10^{-4} mol/kg) and H_2 (~ 1 × 10^{-6} mol/kg) saline fluids with isotopic evidence for a magmatic origin; deep sulfate-chlorite brines contain 13 to 16 ppb Au ± Ag, Cu, Mo, Zn and As	250°
−800			300°
−1000			

References: Wallace et al. (1983); Williamson (1983); Geothermex (unpublished data, 1987); Müller et al. (2002b); White et al. (2004); Brown and Bixley (2005); Simmons and Brown (2006); Johnstone et al. (2007); SKM (unpublished report, 2007); Vogwill et al. (2009); Mejorada and Hermoso (unpublished report, 2011).

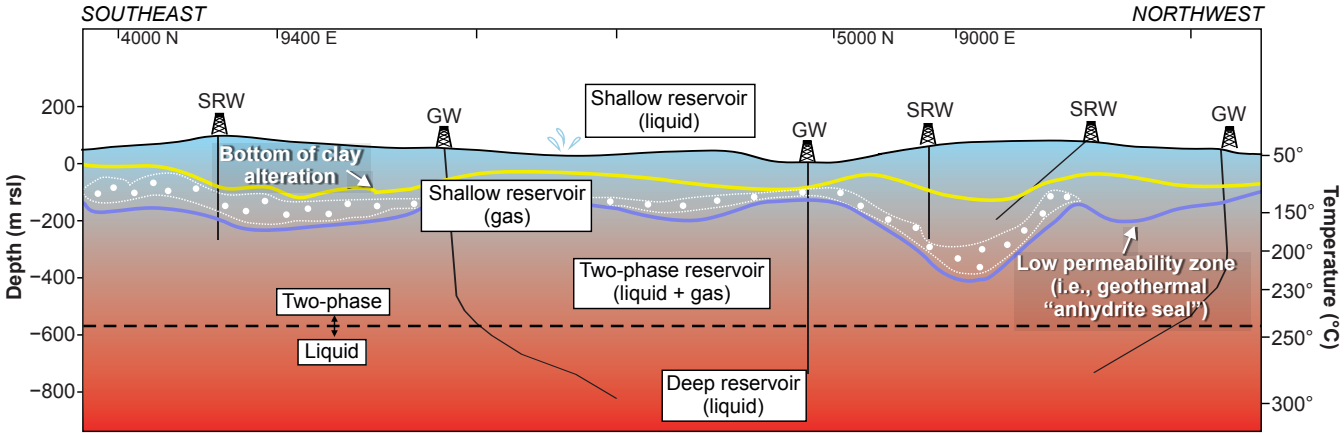

Figure 3.6: Schematic cross-section of the geothermal system at the Lihir gold mine (modified after Blackwell, 2010, and references therein). Refer to Table 3.2 and text for details.

data, 1989; Müller et al., 2002b; Brown and Bixley, 2005; Simmons and Brown, 2006). Deep geothermal fluids also contain high concentration of trace metals, including up to 16 ppb Au, as well as significant concentrations of Ag, Cu, Mo, Zn and As (Table 3.2; Brown and Bixley, 2005; Simmons and Brown, 2006). The deep geothermal reservoir discharges at the surface and within the Lienetz open pit as boiling springs, steaming ground, hot mud pools, with local rock temperatures > 60°C. The geothermal fluids undergo phase-separation and mix with meteoric waters during their ascent, so that at the surface the discharged hybrid geothermal fluids are a mixture of the deep, variably gas-saturated, magmatic-dominated waters, together with shallow meteoric groundwater and seawater (Table 3.2). These surface discharge waters are classified as mixed acid sulfate-chloride or acid-sulfate types (Table 3.2; Wallace et al., 1983; Williamson, 1983; Müller et al., 2002b). A zone of low permeability, colloquially referred to as the "anhydrite seal", separates the deep two-phase reservoir from the upper reservoirs (Figure 3.6; Johnstone et al., 2007).

The connection of the geothermal system within the Lihir gold mine to the sea is evident at shallow levels, where the geothermal resource and the sea are balanced at about −150 m rsl (White et al., 2004). However, below −150 m rsl the sea is isolated from the geothermal resource (White et al., 2004). This poor connection has been attributed to low permeability of the rock due to prior accumulation of anhydrite (White et al., 2004). Heated seawater can precipitate anhydrite and carbonate due to their retrograde solubilities (cf. Blount and Dickson, 1969), and therefore may prevent widespread seawater penetration in a hydrothermal system. An example of where this occurs is the active geothermal system in the core of the White Island andesite-dacite volcano in New Zealand. Previous isotopic studies have failed to identify presence of seawater in that hydrothermal system, even though White Island is surrounded by the sea (Giggenbach, 1987; Giggenbach et al., 1989; Hedenquist et al., 1993). This is thought to be due to the development of a chemical seal of anhydrite and calcite that precipitated from conductively heated seawater, thus preventing further incursion of seawater into the magmatic-hydrothermal system (Giggenbach, 1987; Giggenbach et al., 1989). A similar scenario may be preventing deep incursion of seawater into the modern-day geothermal

system at Lihir. Previous isotopic studies by Carman (1994) and Müller et al. (2002b) have inferred dominantly magmatic signatures for anhydrite at Lihir, however, their sample distribution was limited and new isotopic studies, presented in Chapter 7, will investigate further the possibility of a seawater input.

3.5: Summary

Lihir Island is composed of volcanic lavas, volcaniclastic deposits and fringing limestone reef deposits (Wallace et al., 1983). Only gentle uplift has occurred during the Quaternary (Wallace et al., 1983). Five presently inactive volcanic centers have been identified on the island, and the Luise volcanic center contains the northeast-elongated Luise amphitheater that hosts the Lihir gold deposit. Seafloor mapping adjacent to the Luise amphitheater has identified hummocky topography and marginal levees, which are considered to be the offshore debris avalanche deposits of the sector collapse event(s) that formed the Luise amphitheater (Herzig et al., 1998; Blackwell, 2010; White et al., 2010).

The Luise amphitheater consists of volcano-sedimentary strata and intrusions that comprise pre-ore, constructional volcanism facies. The Lihir gold deposit is nested within the Luise amphitheater and consists of several adjacent and partly overlapping orebodies. Intense alteration from the early porphyry-style, late epithermal, and modern high-temperature geothermal system has obscured many of the primary rock types, and extends beyond the orebodies both vertically and lateral, with poorly constrained limits. The main geological model used for mining at Lihir is based on a three-fold alteration architecture, the components of which broadly correspond to distinct phases in a transition from porphyry-style to epithermal-style mineralization (Davies and Ballantyne, 1987; Moyle et al., 1990; Carman, 1994). The alteration zones include: (1) a low-grade to barren near-surface steam-heated clay blanket; (2) a high-grade, refractory sulfide zone; and (3) a zone of intensely developed anhydrite veins and cemented breccias. Late-stage volcanic-hydrothermal (diatreme) brecciation occurred after main stage mineralization (Lawlis et al., 2015), but prior to the modern geothermal system. The geothermal system remains active and continues to discharge throughout the Lihir gold deposit, altering rocks, causing brecciation and depositing gold (Pichler et al., 1999; Simmons and Brown, 2006).

CHAPTER 4: VEINS AND HYDROTHERMAL BRECCIAS

4.1: Introduction

The aims of this chapter are to document and interpret veins and hydrothermal breccias at Lienetz, and to develop a paragenetic sequence for the porphyry- and epithermal-stages at Lihir. This has been achieved by open-pit mapping, drill-core logging and photo logging, with emphasis on examination of veins, breccias, alteration assemblages and cross-cutting relationships. Field samples were subjected to textural, petrographical and geochemical analyses at the University of Tasmania in order to characterize mineralogy and relative timing relationships.

4.2: Classification scheme for veins and breccias

Hydrothermal breccias and veins are abundant within the Lienetz orebody. There is a textural and morphological continuum of these features, such that differentiation between veins and breccias is not always straightforward. Nomenclature and classification schemes for dealing with breccias in hydrothermal systems, are complex and can be contradictory (e.g., Sillitoe, 1985; Laznicka, 1988; Corbett and Leach, 1998; Jebrak 1997; Woodcock and Mort, 2008; Davies et al., 2008). In this chapter a descriptive, non-genetic classification is used to separate veins and breccias (Table 4.1; Figure 4.1). The scheme is modified from that of Woodcock and Mort (2008), and is underpinned by structural geology and cave-collapse literature. Table 4.1 provides a list of definitions for the terms used in Figure 4.1, as well as definitions of genetic breccia names that will used for interpretations in the following sections.

Veins and hydrothermal breccias were distinguished principally based on their composition and textures, associated alteration halos, and cross-cutting relationships. These relationships were obscured in many veins due to multistage reactivation that occurred under diverse chemical and physical conditions. Vein stages were assigned a number which corresponds to the relative timing of each stage. Complexities caused by reactivation of veins have been accounted for in the classification scheme by assigning vein stages with an "M" subscript to denote vein modification after formation (e.g., recrystallized mineral textures, non-euhedral growth bands, etc.). This nomenclature is introduced early to aid the description of vein development, but supported throughout both this chapter and Chapter 5 with textural and geometrical evidence.

Classification of breccias is based here on components: clasts, cement and matrix (Table 4.1; Figure 4.1). Not included in Figure 4.1 is a fourth competent, open space. A spectrum of terms from crackle to chaotic breccia reflects the decreasing percentage of the clast component and the increasing amount of disaggregated wall-rock material (Figure 4.1; Woodcock and Mort, 2008). Cement-rich (i.e., hydrothermal pre-

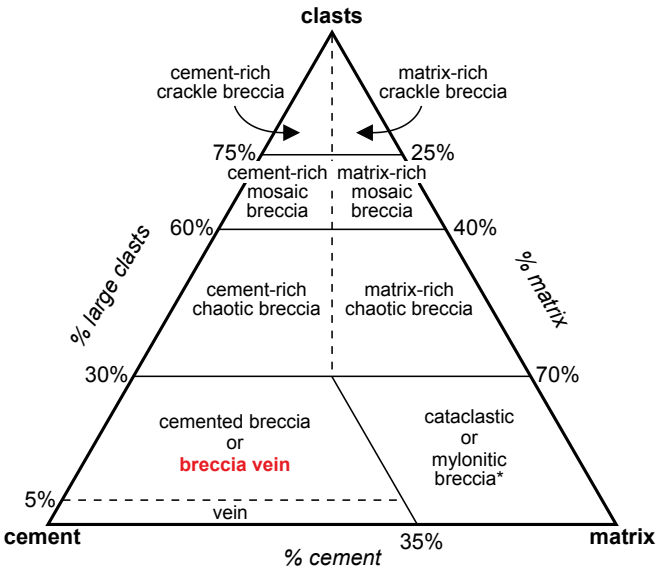

Figure 4.1: Ternary diagram of descriptive breccia classification. Modified after Woodcock and Mort (2008). Refer to Table 4.1 for definitions of terms. *Breccias in this field are usually classified as cataclastic or mylonitic breccias (cf. Woodcock and Mort, 2008), however, these genetic names should be used with caution in descriptive classification.

cipitate) or matrix-rich components (i.e., ground-up rock) will be the dominant infill (Figure 4.1). If the breccia has a cement component of > 70%, relative to clasts, and its geometry is semi-tabular, or sheet-like, the term 'breccia vein' is applied. These structures can in some cases be described as veins, particularity if the cement component is > 95% relative to clasts (Table 4.1; Figure 4.1). The classification scheme of Figure 4.1 is used as a general first-order basis, and more sufficient information is then added to describe, and eventually interpret, breccias (i.e., geometry, grain size, alteration; e.g., Davies, 2002).

4.3: Methods

Open-pit mapping and drill-core logging of the Lienetz orebody was undertaken in two field seasons: August – September, 2013, and February – March, 2014, with ~ 230 samples collected. All sample locations are in Appendix 1. Details of instruments used and UV light photographs are in Appendix 2. Analytical methods used to identify minerals and textures of veins and hydrothermal breccias were conducted at the ARC Centre for Excellence in Ore Deposits (CODES) and Central Science Laboratory (CSL), University of Tasmania, Tasmania, Australia. These included: (1) thin-section petrography (plane-polarized, cross-polarized and reflected light) for mineral identification and paragenetic relationships; (2) etching with HF^- and staining with $Na_3Co(NO_2)_6$ for K-feldspar identification; (3) scanning electron microscopy (SEM), including field emission SEM, secondary (SE) and backscattered (BSE) election imaging, for elemental compositions to aid in mineral identification in thin sections and mounts; (4) short-wave infrared (SWIR) for identification of OH^- and H_2O-bearing minerals in hand samples; and (5) ultraviolet (UV) light fluorescence of carbonate and sulfate minerals to aid in identification in hand samples. Pink K-feldspar (orthoclase) is associated with brown biotite alteration. Light grey adularia (i.e., a polymorph of K-feldspar), could easily be mistaken for quartz alteration in the field, but staining of hand samples with HF^- has confirmed the presence of K-feldspar alteration. Petrography has also revealed characteristic rhombic-form adularia in thin-section.

A plan map of the Lienetz and Minifie open pit was drafted from open-pit mapping and compilation of results from previous studies, particularly Blackwell (2010). Four cross-sections through Lienetz were drafted based partly on results from open-pit mapping, but mostly from photographs of ~ 180 unoriented drillholes. This was due to portions of geological interest within the Lienetz open pit being inaccessible due to safety reasons, and/or missing or degraded drill core. Projected onto the cross-sections are 2-D represen-

Table 4.1: Key terms and definitions for breccias and veins in this study and in Figure 4.1

Term	Definition
Clasts	Large (> 0.2 cm) fragments of material (e.g., rocks)
Matrix	Small (< 0.2 cm) fragments of material (e.g., rocks) produced by local fragmentation of larger particles or by introduction of exotic material
Cement	Crystalline material that binds together clasts and/or matrix, grown in situ from hydrothermal or magmatic-hydrothermal fluids, either as infill or void space or as replacement of clasts and/or matrix
Breccia	A rock made up of > 5% angular clasts with varying proportions of cement and/or matrix and/or void space
Vein	A sheet-like fracture with > 95% cement
Breccia vein	A cemented breccia with > 70% cement and a vein-like geometry (i.e., semi-tabular or sheet-like)
Genetic interpretation breccia names	
Cataclastic breccia	A matrix-rich breccia composed of fragments < 0.2 cm, with structural fabric produced by brittle processes (e.g., mechanical crushing and/or fracturing)
Mylonitic breccia	A foliated, matrix-rich breccia composed of minerals and/or fragments < 0.2 cm, with a structural fabric produced by ductile processes (e.g., metamorphic deformation)
Hydrothermal breccia	A breccia that forms from fragmentation due to interaction with hydrothermal fluids (i.e., solutions of water, volatile and soluble chemical components)
Magmatic-hydrothermal breccia	A breccia that forms when a hydrous igneous intrusion undergoes catastrophic brittle failure ($P_h > P_l + \tau$) and exsolves fluids (i.e., solutions of water, volatile and soluble chemical components)
Dissolution breccia	A breccia that forms by corrosion ± gravitational collapse (e.g., karsts)
Volcaniclastic breccia	A breccia that is composed predominantly of volcanic clasts
Volcanic-hydrothermal (diatreme) breccia	The downward-tapering, inverted cone-shaped breccia body of a maar volcano that forms from a phreatomagmatic eruption trigged by a dike intruding into an active geothermal system

tations of isosurfaces, modeled in Leapfrog™, of significant intervals of anhydrite ± carbonate (i.e., > 0.3 m thick) and core-loss (i.e., < 75% recovery from drill core). Thick intervals of anhydrite were identified and modeled as isosurfaces over an area larger than Lienetz, from photographs of ~ 410 drillholes. Core-loss was modeled from Lihir's geotechnical database of ~ 1050 drillholes, as well as Lihir's geothermal database of open-space cavities encountered during mining. The Leapfrog™ model is available in Appendix 2.

Gold grades within vein stages were determined from samples collected during open-pit mapping and core logging. Selected samples were assayed for gold using a fire assay method on-site at the Lihir gold mine, or using a fire assay, 30 g charge (FA301) method at Newcrest Laboratory Services, Orange, New South Wales, Australia. Gold assays (i.e., on-site fire assays) of specific drill-core intervals were acquired from the historic drilling database of the Lihir mine. A subset of samples was additionally analyzed for multi-element geochemical data using 4-acid digest and ICP-OES (MEAD4OES) at Newcrest Laboratory Services. All sample assay results are listed in Appendix 1.

4.4: Veins and breccia veins in Lienetz

Eight stages of veins and breccia veins have been distinguished at Lienetz (Figure 4.2). These are summarized in Table 4.2, where they are also compared to Carman (1994)'s paragenetic scheme. Veins have distinctive mineral assemblages (Table 4.2), textures (Figure 4.3), and cross-cutting relationships (Figure 4.4).

Table 4.2: Vein stage paragenesis with hydrothermal mineral infill, alteration and gold mineralization

Vein stage	Correlated veins[1]	Vein form[2]	Mineral textures	Vein infill[3]	Vein hydrothermal alteration halo[3]	Sulfides and mean ($\bar{x}$) and standard deviation (σ) gold grade[4]
$V1_{bio}$	IA	Veins and breccia veins with planar margins	Massive ± tabular	anh + ba ± cal ± bio ± phl ± ksp (or) ± cel ± py ± cpy ± mo ± gn ± mag ± tell ± *trem*	bio + phl ± ksp (or) ± chl ± anh ± mag ± alb ± white mica ± trem ± act ± tour ± ap	$\bar{x}$ = 0.5, σ = 0.5 g/t Au (*n = 14*); trace sulfides in veins and wall rock disseminations
$V1_{chl–epi}$	IA_{distal}	Veinlets with planar margins	Massive	cal + chl ± py ± mag ± act ± cpy ± epi ± gn	chl + epi + cal + py ± act ± anh ± mag ± alb ± ksp ± bio ± rt ± sphe	$\bar{x}$ = 0.2 g/t Au (*n = 1*); sulfides in veins ± wall rock disseminations
$V1_{ksp}$	IB	Veins with planar margins	Massive ± tabular	anh ± qtz ± cal ± py ± *rt* ± *phl* ± *ap* ± *chl* ± *vrm* ± *mo* ± *cpy*	ksp (or) + bio + K-mica + anh + py ± epi ± chl + alb + rt	$\bar{x}$ = 0.2, σ = 0.1 g/t Au (*n = 6*); sulfides in vein ± wall rock disseminations
$V1_{M1}$	II	Veins and breccia veins with irregular diffuse margins	Recrystallized ± stylolitic ± micaceous ± semi-dissolved ± tabular	anh + cel + ba + py + bio + phl + chl + gn ± sph ± cpy ± mo ± qtz ± mag ± cal ± Mg-rieb ± orbran ± *ksp* ± *mrc* ± *rt* ± *po* ± *vrm*	bio ± phl ± chl ± ksp ± py ± cal	$\bar{x}$ = 0.3, σ = 0.5 g/t Au (*n = 37*); sulfides in veins ± stylolites ± wall rock disseminations
$V2_{py}$		Veinlets and veins with planar margins	Massive ± recrystallized	anh + py ± chl ± act ± qtz ± white mica	chl + py ± white mica ± ksp ± qtz ± bio	$\bar{x}$ = 0.7, σ = 0.6 g/t Au (*n = 8*); sulfides in veins
$V3_{adu}$	$III_{brassy-py}$	Veins and breccia veins with planar to irregular margins	Massive ± vuggy ± acicular ± cockade ± crustiform	py + mrc + adu ± apy ± cpy ± qtz ± cal ± chal ± tell ± mag ± mo ± ill ± *ba* ± *cel* ± *vrm* ± *po* ± *sph* ± *tennt* ± *tethd* ± *elc* ± *gn*	adu + py + qtz + white mica ± cal ± ill ± rt ± alb ± anh ± ap	$\bar{x}$ = 5.9, σ = 4.1 g/t Au (*n = 98*); sulfides (> 15%) in veins, wall rock disseminations and breccia cement of $Bx3_{py–adu}$
$V4_{qtz}$	$III_{blue-grey\ qtz}$	Veins, breccia veins and vug-fill with irregular margins	Thickly bladed ± crustiform ± cavities ± vugs	qtz + anh + py ± chal ± mrc ± mo ± elc ± tell ± adu ± cal ± cpy ± sph ±ill ± gn ± apy ± *musc* ± *ba* ± *cel* ± *rt* ± *tethd* ± *tennt* ± *vrm* ± *argt* ± *po*	qtz + adu ± musc ± py ± anh ± cal ± clays	$\bar{x}$ = 5.4, σ = 5.4 g/t Au (*n = 16*); sulfides (5 to 15%) in veins, vug-fill and wall rock disseminations
$V1_{M2}$	$III_{qtz-cal}$ $III_{anh\ vugs}$	Veins and breccia veins with planar to irregular margins	Crustiform ± cockade ± cavities ± vugs ± thinly bladed ± massive	cal + anh + qtz + adu + py ± dol ± cpy ± sph ± gn ± ill ± *vrm* ± *rt* ± *mrc*	adu + qtz + cal + musc ± py ± bio (residual)	$\bar{x}$ = 3.7, σ = 8.9 g/t Au (*n = 30*); sulfides (< 5%) in veins ± wall rock disseminations

Abbreviations: act = actinolite, adu = adularia, alb = albite, anh = anhydrite, ap = apatite, apy = arsenopyrite, argt = argentite, ba = barite, bio = biotite, cal = calcite, cel = celestine, chal = chalcedony, chl = chlorite, cpy = chalcopyrite, dol = dolomite, elc = electrum, epi = epidote, gn = galena, ill = illite, ksp = K-feldspar, mag = magnetite, mrc = marcasite, mo = molybdenite, musc = muscovite, or = orthoclase, orbran = orthobrannerite, phl = phlogopite, po = pyrrhotite, py = pyrite, qtz = quartz, rieb = riebeckite, rt = rutile, sph = sphalerite, sphe = sphene, tell = telluride minerals, tennt = tennantite, tethd = tetrahedrite, tour = tourmaline, trem = tremolite, vrm = vermiculite.

Stages are listed top to bottom, from oldest to youngest.

[1] = correlated vein stages from Carman (1994).

[2] = vein form: veinlet = < 0.5 cm, vein = > 0.5 cm, breccia vein = > 70% cement relative to clasts and semi-tabular and sheet-like geometry (i.e., Table 4.1, Figure 4.1).

[3] = minerals in *italics* were observed by Carman (1994), but not identified in this study.

[4] = gold grades: values from fire assay largely from hand samples collected in the current study, with vein >> wall-rock material. Assays and sample locations are listed in Appendix 1. n = number of samples (grab and drill core).

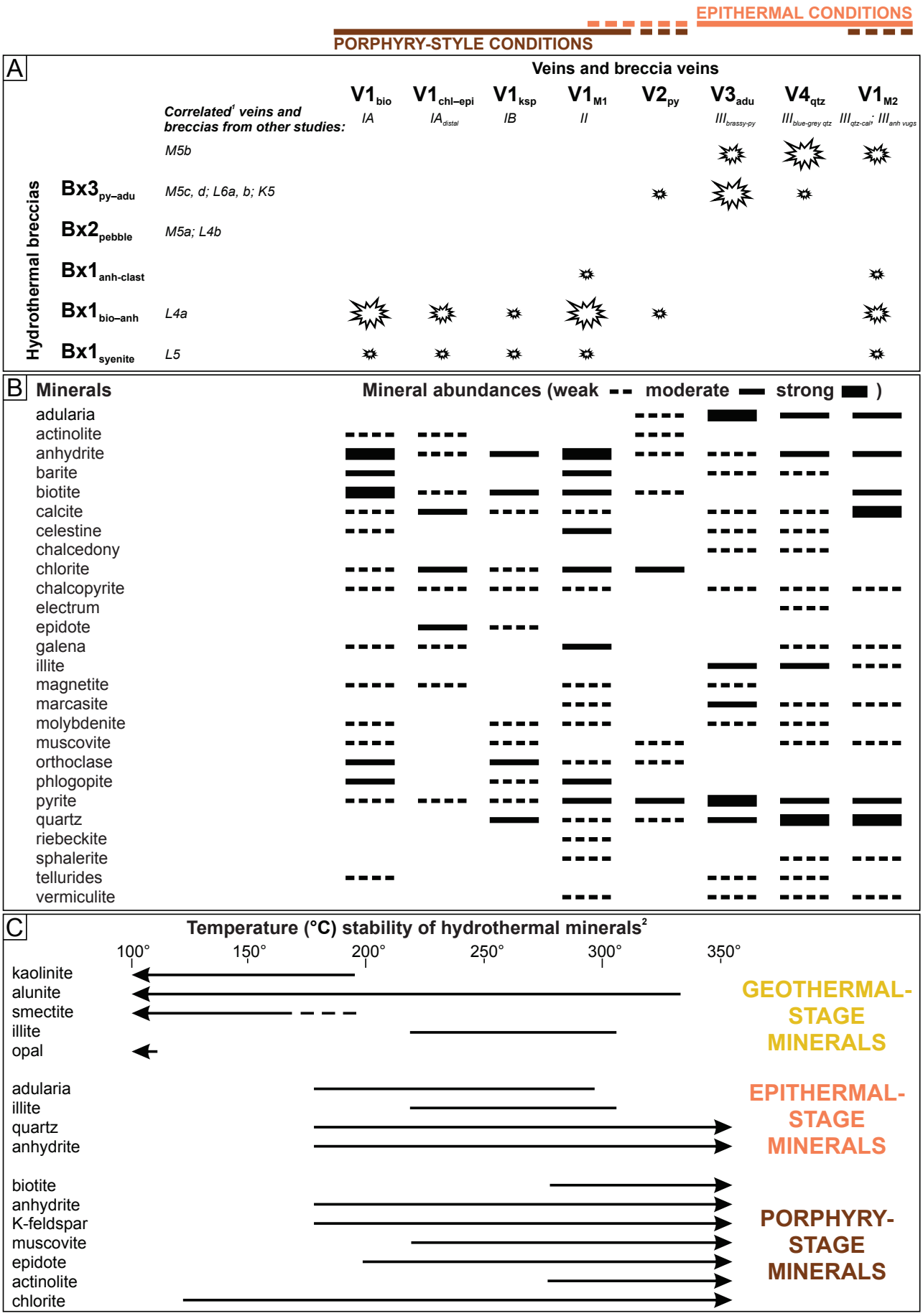

Figure 4.2: Relationships between veins and hydrothermal breccias, and inferred depositional conditions. A) Relationship between veins and breccia veins (V) emplacement and hydrothermal breccias (Bx). Interpreted porphyry-style and epithermal conditions are shown relative to vein stages. [1] = correlated vein stages from Carman (1994), and correlated breccia facies in Lienetz (L), Minifie (M) and Kapit (K) from Blackwell (2010) and Ageneau (2012). **B)** Qualitative abundances of minerals within vein stages. **C)** Mineral assemblages typical of the interpreted geothermal-, epithermal- and porphyry-stages at Lihir (e.g., Table 3.1). [2] = temperature stability of hydrothermal minerals deduced from active geothermal systems and experimental modeling (modified after Hemley et al., 1980; Reyes, 1990; Masterman, 2003; Pass, 2010 and references therein).

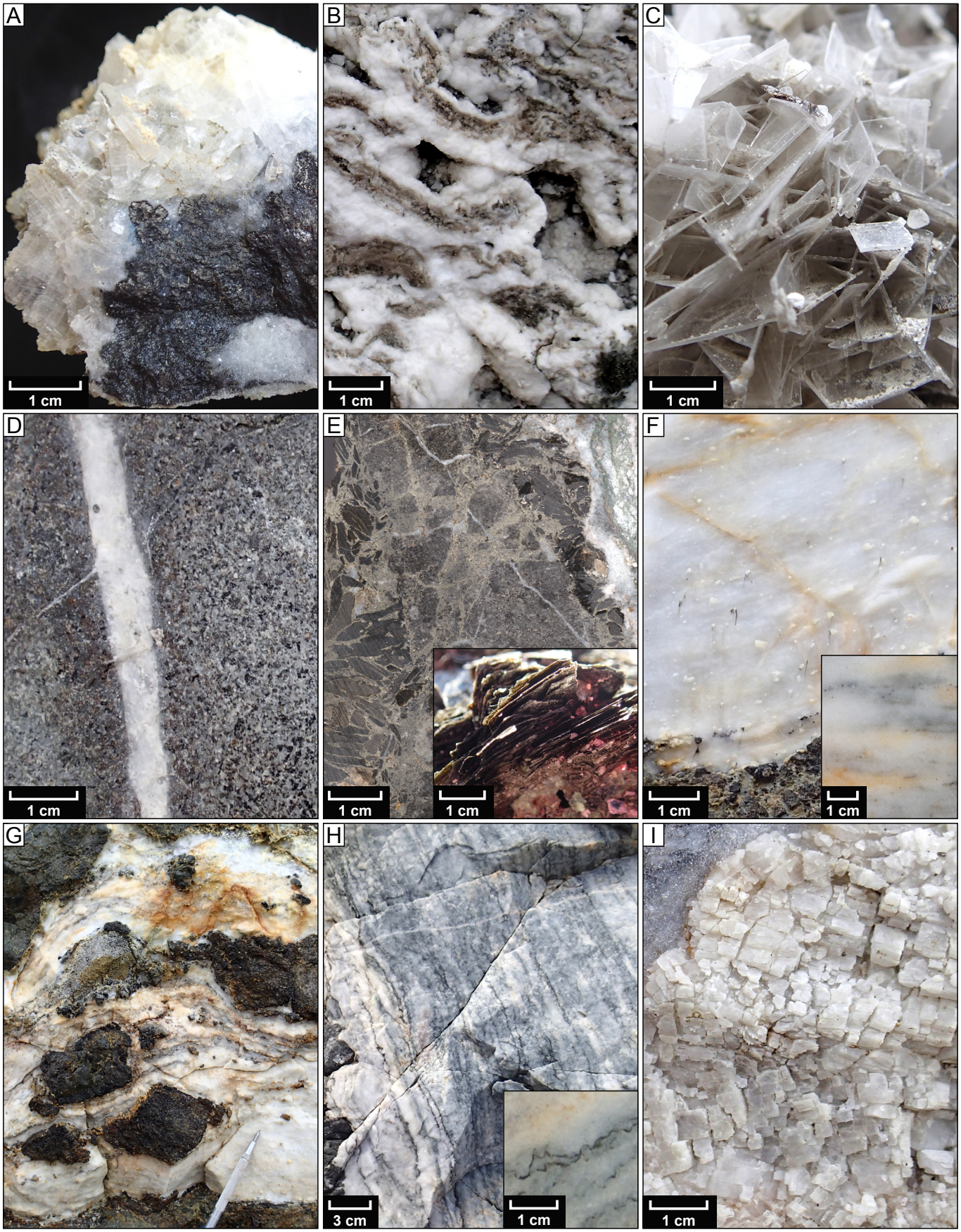

Figure 4.3: Textures of veins and breccia veins at Lienetz. A) Thickly bladed (1:4 aspect) anhydrite with quartz, pyrite and marcasite ($V4_{qtz}$; LH14SS075). **B)** Cockade banded anhydrite, calcite and quartz around K-feldspar- and quartz-altered wall-rock fragments ($V1_{M2}$; LH13SS031). **C)** Vug with projecting crystals of thinly bladed (1:16 aspect) anhydrite ($V1_{M2}$; LH13SS056). **D)** Massive-textured anhydrite vein with a selectively pervasive biotite alteration halo ($V1_{bio}$; LH13SS052). **E)** Large biotite and phlogopite books with disseminated pyrite as a halo to an anhydrite vein ($V1_{M1}$; LH13SS068), inset = biotite books. **F)** Recrystallized, sugary anhydrite ($V1_{M1}$; LH13SS059), inset = recrystallized texture. **G)** Serrated, irregular and partly dissolved wall-rock fragments in recrystallized-textured anhydrite vein ($V1_{M2}$; LH14SS042). Grey < 2 mm thick bands are asymmetrically developed about wall-rock fragments, exhibiting partial stylolitization and apparent non-coaxial shearing. **H)** Stylolites of phyllosilicates, sulfides and other less-soluble minerals within recrystallized anhydrite ± celestine ± barite ($V1_{M1}$; LH13SS082), inset = stylolites. **I)** Tabular anhydrite crystals ($V1_{M1}$; LH13SS061).

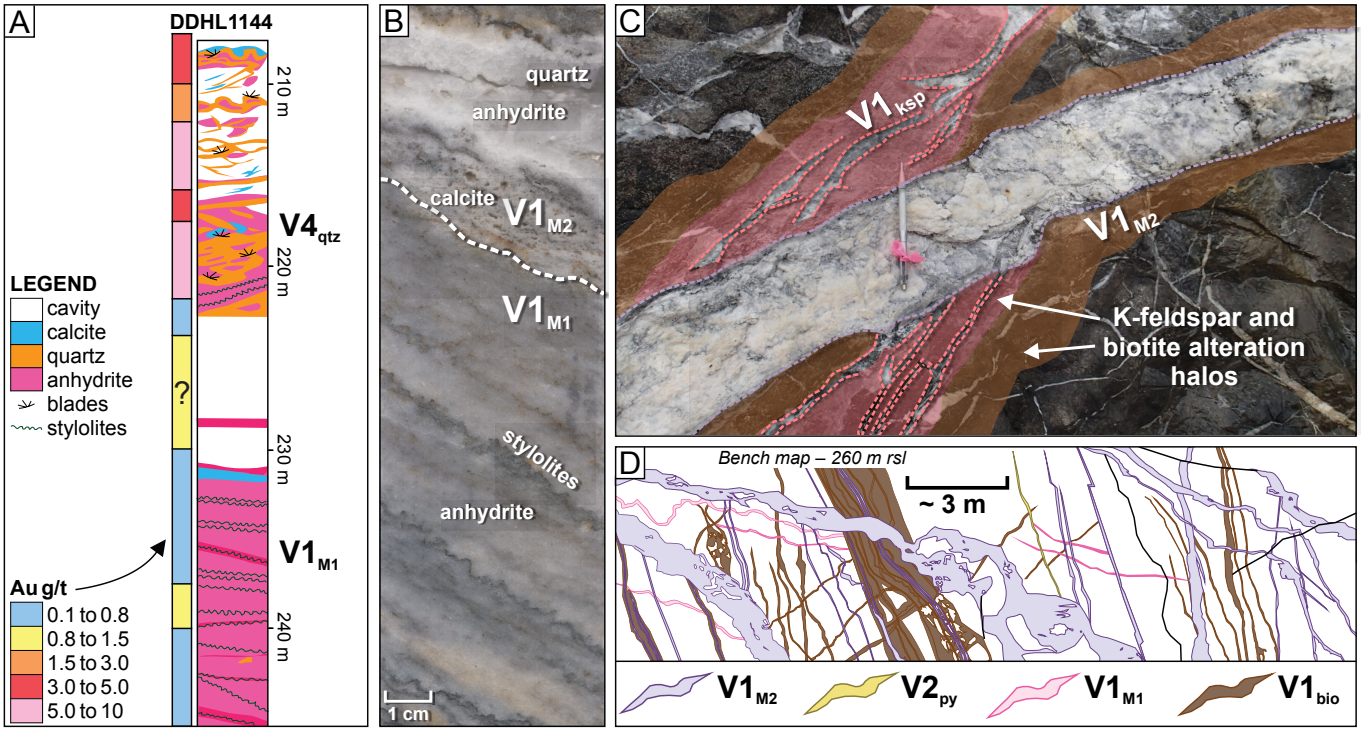

Figure 4.4: Vein examples and cross-cutting relationships. A) Annotated drill core DDHL1144 from 208 to 244 m, with two meter fire assay gold values in left column. **B)** Drill core DDHL0791 from 199 m, showing $V1_{M2}$ vein cross-cutting and overprinting stylolitic $V1_{M1}$ vein. **C)** $V1_{ksp}$ vein cross-cut by $V1_{M2}$ vein in Lienetz open pit at −284 m rsl. **D)** Annotated map of a bench in Lienetz (−260 m rsl) illustrating overprinting relationships between $V1_{bio}$, $V2_{py}$, $V1_{M1}$ and $V1_{M2}$ veins and breccia veins.

Interpretations for each vein stage are summarized in Figure 4.2A–B. Figure 4.2C also shows the temperature stability ranges of minerals, as determined from active geothermal systems and experimental modeling (e.g., Hemley et al., 1980; Reyes, 1990; Masterman, 2003; Pass, 2010 and references therein). Highlighted in Figure 4.2C are mineral assemblages typical of porphyry-, epithermal- and geothermal-stages at Lihir (e.g., Table 3.1; Davies and Ballantyne, 1987; Moyle et al., 1990; Carman, 1994).

Gold grades vary significantly within vein stages (Table 4.2). Fire assay gold results of veins ± wall-rock alteration halos reveal $V1_{bio}$, $V1_{chl–epi}$, $V1_{ksp}$ are generally low, with mean ($\overline{x}$) values of ~ 0.2 to 0.5 g/t Au (Table 4.2). The volumetrically dominant $V1_{M1}$ veins and breccia veins are also typically low-grade ($\overline{x}$ = 0.3 g/t Au). The highest gold grades belong to $V3_{adu}$ and $V4_{qtz}$, with $\overline{x}$ = 5.9 and 5.4 g/t Au, respectively. The standard deviation (σ) in gold grades is higher for these vein stages, particularly $V4_{qtz}$ with σ = 5.4. $V1_{M2}$ veins and breccia veins have moderate- to high-grades of $\overline{x}$ = 3.7 g/t Au, but grades are the most erratic, with σ = 8.9 (Table 4.2).

4.4.1: Anhydrite – biotite veins ($V1_{bio}$)

Anhydrite veins with biotite halos ($V1_{bio}$) are the earliest-formed veins in Lienetz (Table 4.2). Individual veins are on average < 1 cm thick, but locally up to 20 cm thick, with minor crackle to mosaic wall-rock fragments along edges. The distinguishing characteristic of $V1_{bio}$ veins are moderately to intensely developed alteration halos of biotite ± phlogopite (Figure 4.3D). The vein halos are 0.3 to 15 cm wide. There has

been little modification of primary vein textures in $V1_{bio}$ veins (e.g., Figure 4.3D). Pyrite has selectively replaced primary mafic minerals within the surrounding wall rock, and only occurs as trace to < 1% within veins (Table 4.2).

4.4.2: Anhydrite – chlorite ± epidote veins ($V1_{chl–epi}$)

A weakly developed set of thin (< 0.5 cm wide) wispy veinlets compose $V1_{chl–epi}$ (Table 4.2). These veinlets are infilled by chlorite, calcite ± epidote, and have compositionally similar alteration halos that are up to 0.5 cm wide. There is a predominance of chalcopyrite over pyrite, with trace amounts of galena, although sulfides typically compose trace to < 1% of the veinlets (Table 4.2).

4.4.3: Anhydrite – K-feldspar veins ($V1_{ksp}$)

$V1_{ksp}$ veins contain anhydrite and quartz, and are < 0.5 to 5 cm thick with planar margins (Table 4.2). Distinct pink to grey K-feldspar alteration halos, up to 3 cm wide, are characteristic of this vein stage. $V1_{ksp}$ veins have cross-cut or re-opened $V1_{bio}$ veins (Table 4.2; Figure 4.4C).

4.4.4: Irregular anhydrite veins and breccia veins ($V1_{M1}$)

The $V1_{M1}$ veins and breccia veins are one of the most volumetrically significant hydrothermal stages at Lienetz. They vary from 3 cm to 30 m thick. They probably originated as $V1_{bio}$ or $V1_{ksp}$ veins, but have experienced modification that led to a variety of textures and irregular forms due to significant anhydrite volume changes. $V1_{M1}$ consist chiefly of recrystallized anhydrite, with lesser celestine, barite, phyllosilicates and sulfides (Table 4.2; Figures 4.3E–I; 4.4A–B). Fragments of wall rock material in anhydrite are common (i.e., ~ 15 to 30%; e.g., Figure 4.3G). $V1_{M1}$ veins have irregular, diffuse and serrated margins with the surrounding wall rock and internal wall-rock fragments (Figure 4.3G). Variable, but typically intense, alteration halos of cryptocrystalline K-feldspar and biotite are common, with local coarse biotite and phlogopite crystals up to 2 cm in diameter (Figure 4.3E).

$V1_{M1}$ veins and breccia veins commonly contain < 0.01 to 0.03 cm thick, crenulated seams with dark green-grey accumulations of least-soluble wall-rock material (Figures 4.3H, 4.5A–B). These are interpreted herein as dissolution seams or stylolites. Their origins are discussed in Chapters 4 and 5. Anhydrite, with lesser inclusions of celestine, surround the stylolites and display recrystallized grain boundaries (Figure 4.5A–B). Stylolites and dissolution seams are composed of wall-rock inclusions, chlorite, biotite, magnesio-oriebeckite, celestine and barite with trace amounts of pyrite, galena, monazite, molybdenite, orthobrannerite and sphalerite (Figure 4.5A–E). Celestine, orthobrannerite and molybdenite are common along the edges

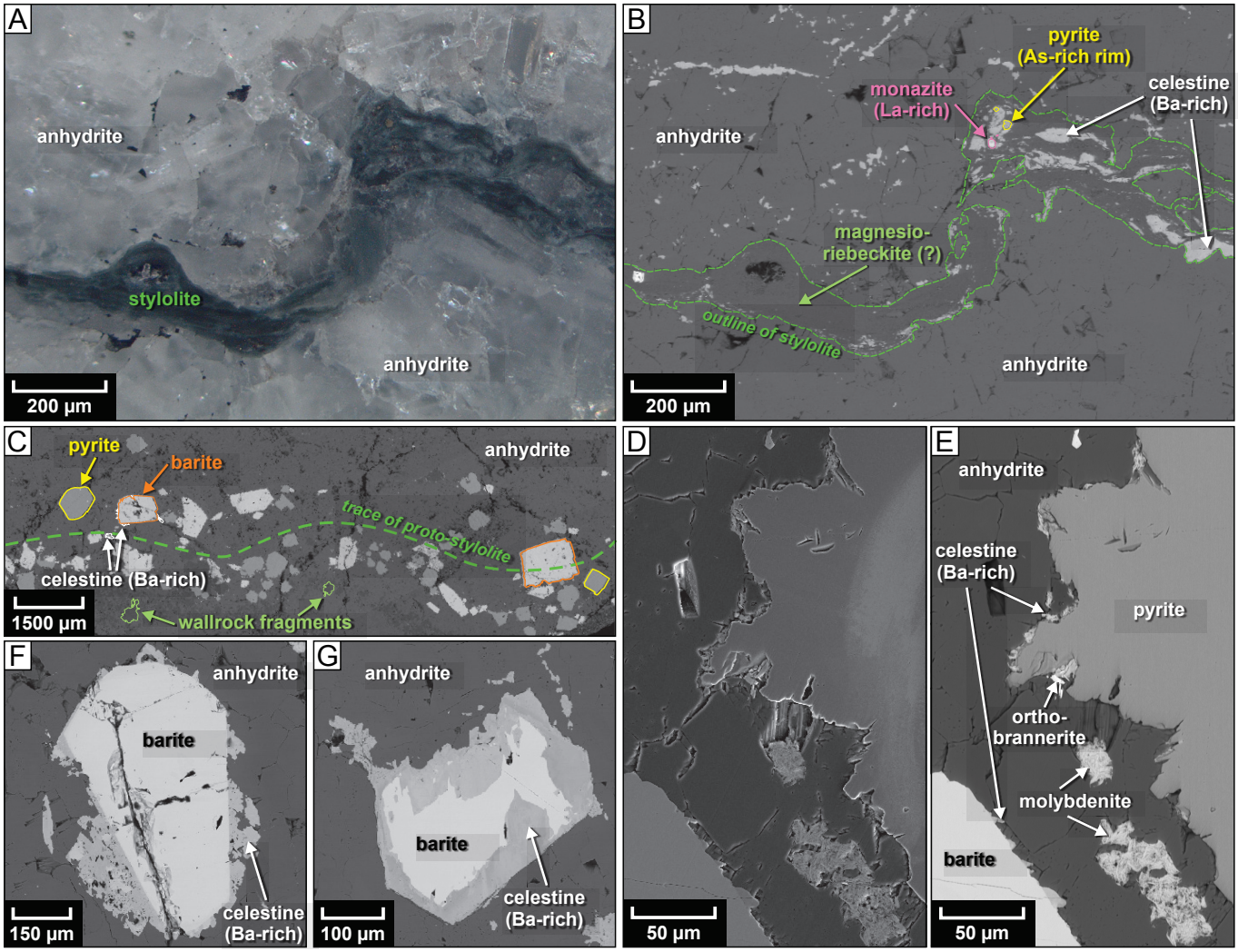

Figure 4.5: Features of stylolities. A) Photograph of polished face of anhydrite vein with stylolite ($V1_{M1}$; LH13SS082). **B)** BSE image of same stylolite as (A). Stylolites consists of magnesioriebeckite(?) as well celestine and trace amounts of monazite and pyrite. Anhydrite surrounds stylolites and is interbedded with minor amounts of celestine. **C)** BSE image showing trail of pyrite, barite ± celestine, and wall-rock material along a dissolution seam, interpreted to be a proto-stylolite ($V1_{M1}$; LH13SS073). **D)** SE image and **E)** BSE image of edge of pyrite and barite grain in sample LH13SS073. Note the celestine, orthobrannerite and molybdenite are along the edges of the serrated-textured pyrite. **F)** BSE image of barite and celestine from LH13SS073 and **G)** LH13SS082. The barite grain in (G) is from the well-developed stylolite in (B), and shows celestine >> barite.

of the serrated-textured pyrite grains (Figure 4.5D–E). Pyrite, barite ± celestine, and wall-rock material comprise bands in samples that have weakly developed stylolites (Figure 4.5C). In more well-developed stylolites (i.e., more intense textural destruction of original material in seams and greater density of seams), a solid-solution series of celestine and barite is apparent (Figure 4.5F–G). Celestine is Ba-rich (i.e., 10 to 30 wt. % Ba) and occurs along the margins of euhedral to subhedral barite crystals (Figure 4.5F). In well-developed stylolites celestine replaces barite crystals and is more abundant (Figure 4.5G).

4.4.5: Pyrite – anhydrite veins ($V2_{py}$)

The $V2_{py}$ stage comprises thin (< 0.5 cm wide), wispy veins, rich in pyrite both internally and in alteration halos (Table 4.2). They contain pyrite, anhydrite, chlorite ± muscovite ± K-feldspar ± quartz ± biotite. This stage is not well-developed at Lienetz, but enough examples were observed to permit temporal relationships to be constrained with earlier vein stages (Figure 4.4D).

4.4.6: Adularia – pyrite veins and breccia veins ($V3_{adu}$)

$V3_{adu}$ are irregular veins and breccia veins that are transitional and equivalent to hydrothermal cemented breccias (i.e., $Bx3_{py–adu}$; Figure 4.2). As such, they are classified here as veins, breccia veins and related hydrothermal breccias. $V3_{adu}$ typically is composed of > 15% pyrite, and is porous with > 10% open space (Table 4.2). Intensely developed adularia ± quartz ± illite alteration is also associated with $V3_{adu}$ (Table 4.2).

4.4.7: Quartz – anhydrite veins, breccia veins and vug-fill ($V4_{qtz}$)

$V4_{qtz}$ veins and breccia veins have irregular geometries, and $V4_{qtz}$ material has also partly filled vugs above a large breccia complex (i.e., Bx1). Within $V4_{qtz}$, quartz is the most abundant component, followed by anhydrite that is characterized by distinct thickly bladed textures (Figure 4.3A). $V4_{qtz}$ also contains chalcedony, adularia, pyrite, and marcasite. $V4_{qtz}$ veins are cross-cut only by $V1_{M2}$. $V4_{qtz}$ veins have strongly developed, pervasive adularia and quartz alteration and contain ± free gold ± tellurides (Table 4.2).

4.4.8: Calcite – anhydrite – quartz veins and breccia veins ($V1_{M2}$)

$V1_{M2}$ is the final stage of veins and breccia veins at Lienetz (Table 4.2; Figure 4.2), and is also one of the most voluminous vein stages. As with $V1_{M1}$, $V1_{M2}$ veins and breccia veins probably started as $V1_{bio}$,$V1_{ksp}$ or $V1_{M1}$ veins and breccia veins. They subsequently experienced modification, leading to a variety of textural changes and volume increase due to significant mineral precipitation of calcite, quartz, anhydrite and adularia. $V1_{M2}$ are largely breccia veins, ranging from 1 cm to 35 m thick, with angular, lenticular to blocky wall-rock inclusions. $V1_{M2}$ veins and breccia veins vary along strike, both in terms of their internal textures and thickness (Figure 4.4D), and cross-cut all previous vein stages (Figure 4.4B–D). They are composed of calcite, anhydrite and quartz ± adularia ± pyrite (Table 4.2). Inner adularia and outer biotite alteration halos are typical of $V1_{M2}$ veins (Table 4.2). Textures include massive and cockscomb banded calcite, anhydrite and quartz ± adularia (Figure 4.3B). Banding occurs as irregular discontinuous laminae, defined by aligned K-feldspar-altered and sulfide-rich (i.e., pyrite, chalcopyrite, galena) wall-rock fragments typically at oblique angles to the vein-wall rock margin (Figure 4.3B). Internal porosity is high (locally 5 to 15%), with local examples infilled by 0.3 to 3 cm long, euhedral crystals of anhydrite (thinly bladed), calcite and quartz (Figure 4.3C). The calcite has distinctive long-wave UV fluorescence (Appendix 2).

4.5: Hydrothermal breccias in Lienetz

A series of large hydrothermal breccia bodies are abundant within the Lienetz orebody (Figures 4.6, 4.7, 4.8), and to a lesser degree within the Minifie orebody (Figure 4.6; Blackwell, 2010). Hydrothermal

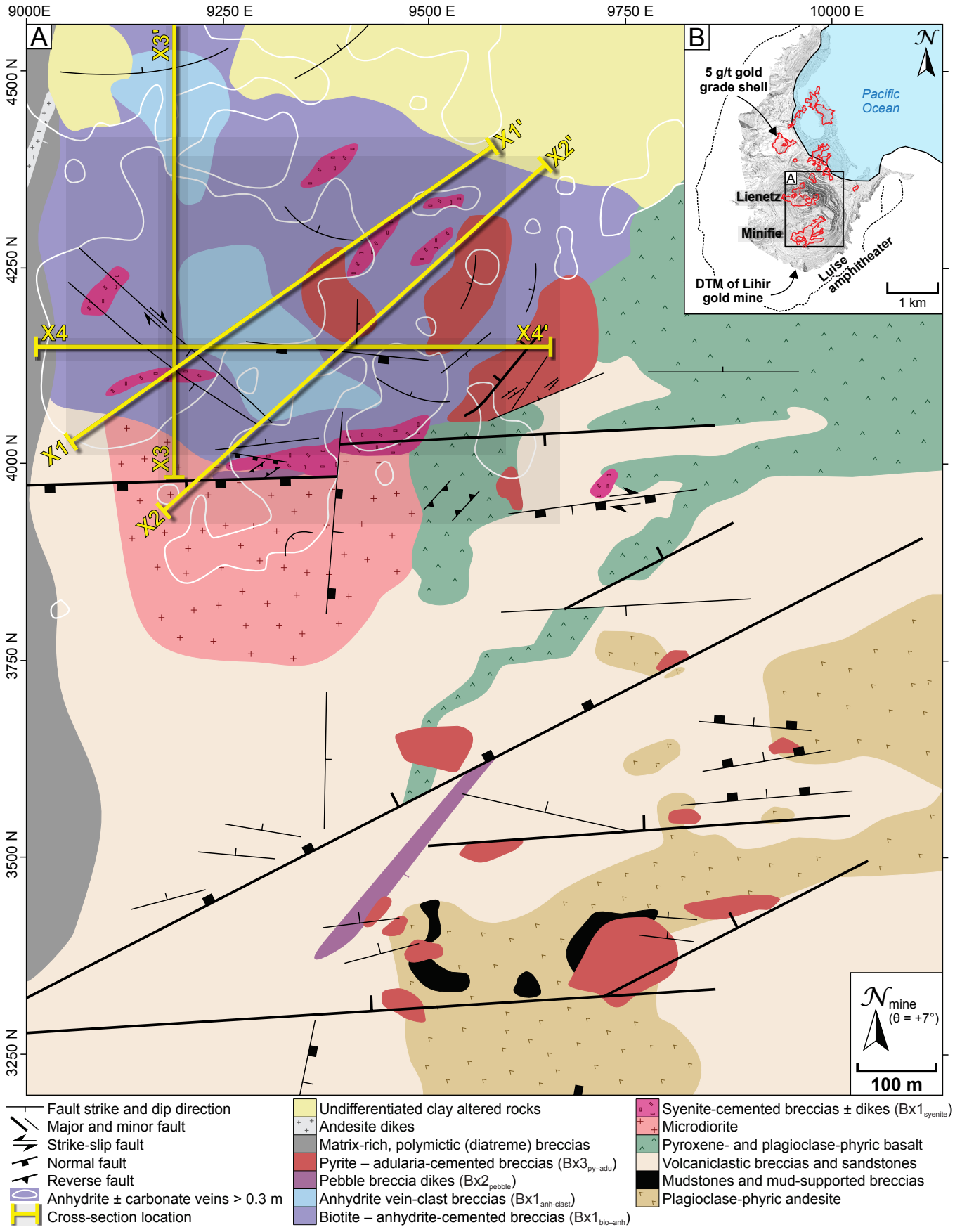

Figure 4.6: Geological plan map of Lienetz and Minifie. A) Simplified geological map of Lienetz and Minifie on an approximately −150 to −100 m rsl elevation slice. Locations of cross-sections X1, X2, X3 and X4 are shown in yellow. **B)** Insert of the DTM of the Lihir gold mine, with 5 g/t Au isosurface projected to 100 m rsl. Location of (A) is outlined in black box.

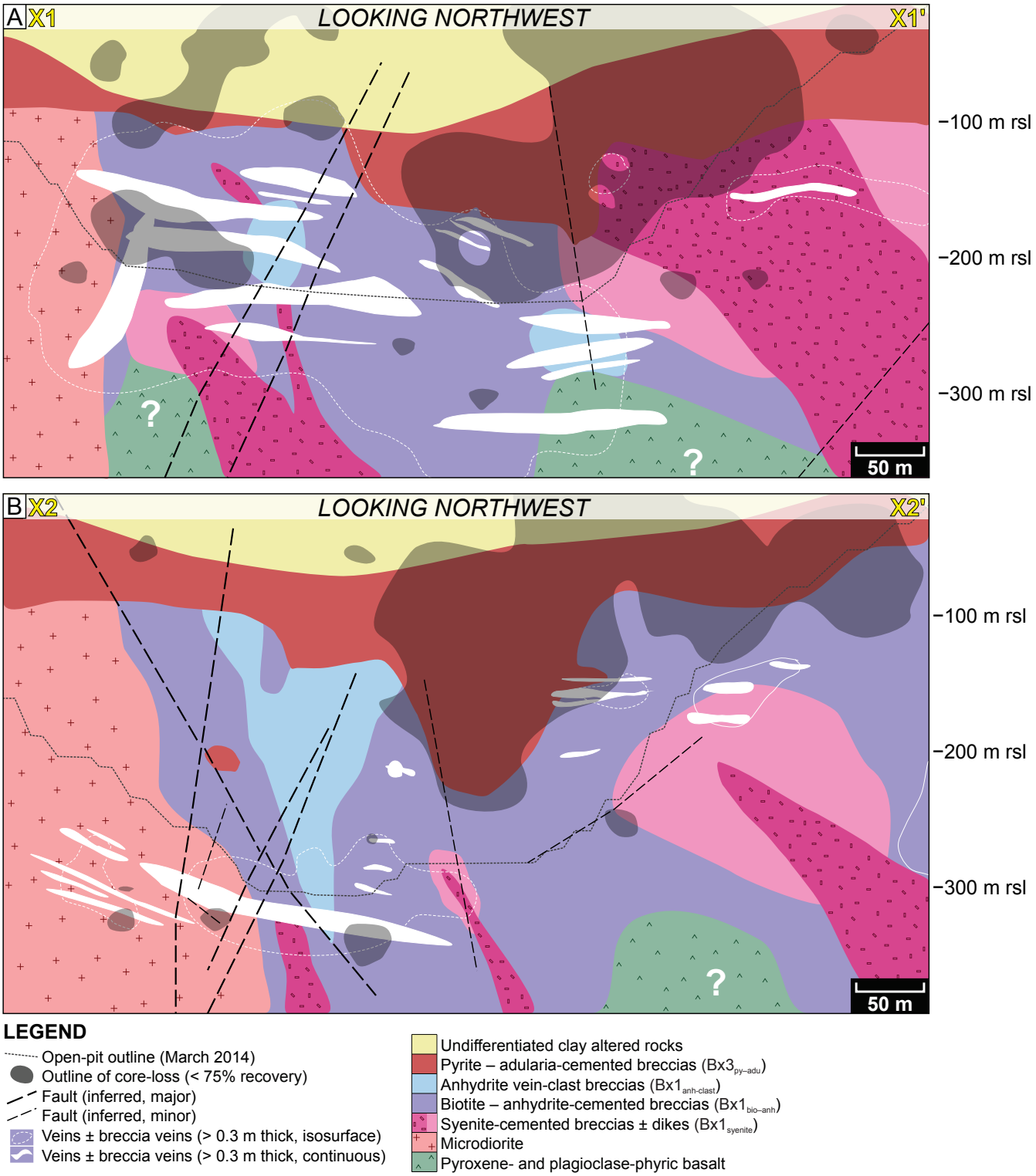

Figure 4.7: Cross-sections X1 and X2 of the Lienetz orebody. A) Northwest-looking cross-section (azimuth 055°), from X1 to X1'. **B)** Northwest-looking cross-section (azimuth 048°), from X2 to X2'. Data are projected from ~ 25 m on each side of sections. Locations of cross-sections are shown in Figure 4.6A.

breccias cross-cut the volcaniclastic breccias, mudstones, and basaltic to andesitic lavas and shallow intrusions (Figure 4.6A). Hydrothermal breccias have pre-, syn- to post-mineralization timing relationships. There are three main breccia facies (i.e., Bx1, Bx2 and Bx3), which are composed of five distinct subfacies, including: (1) syenite-cemented breccias ± dikes ($Bx1_{syenite}$); (2) biotite – anhydrite-cemented breccias ($Bx1_{bio–anh}$); (3) anhydrite vein-clast breccias ($Bx1_{anh-clast}$); (4) pebble breccia dikes ($Bx2_{pebble}$); and (5) pyrite –

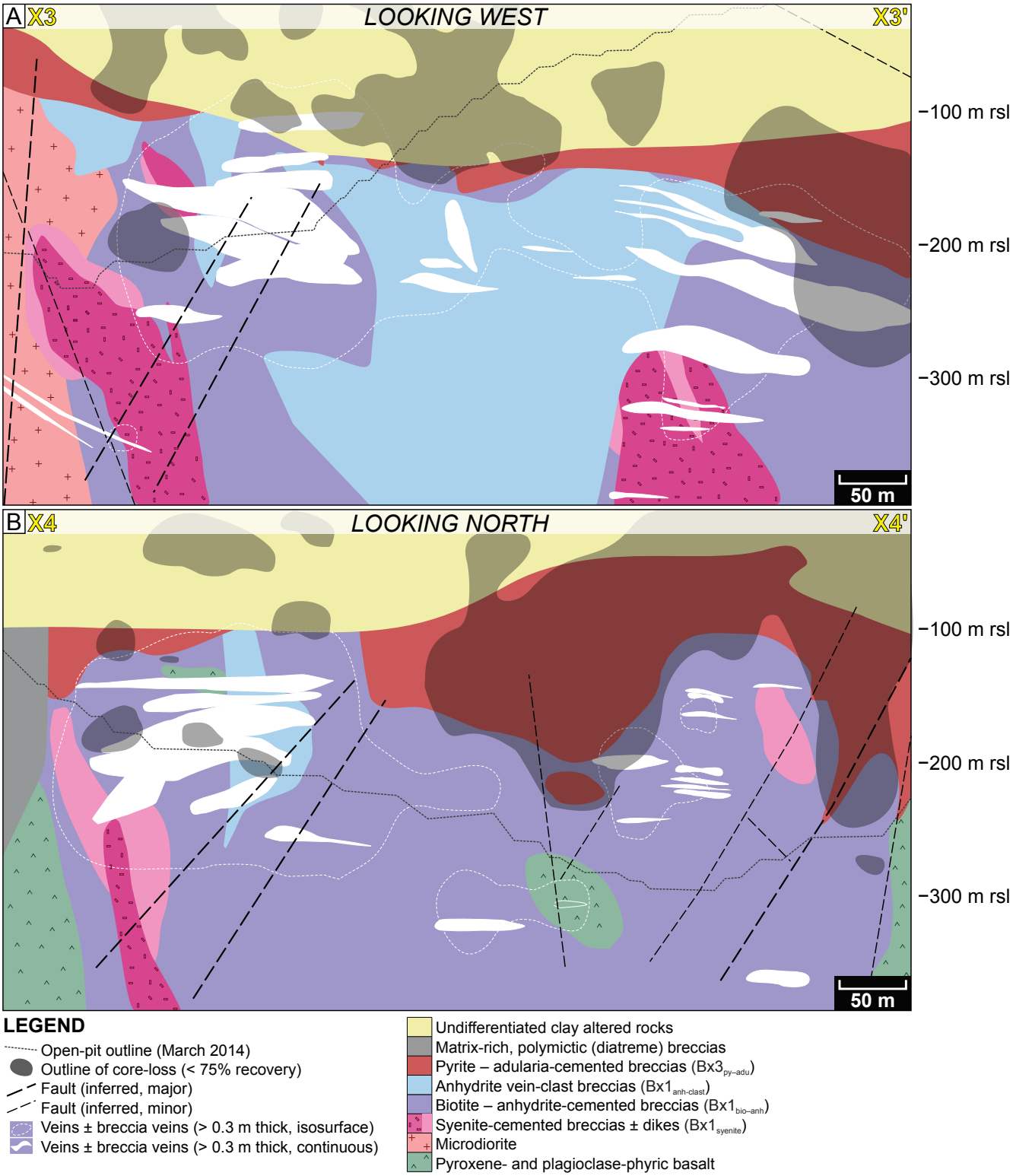

Figure 4.8: Cross-sections X3 and X4 of the Lienetz orebody. A) West-looking cross-section (azimuth 000°) from X3 to X3'. **B)** North-looking cross-section (azimuth 090°) from X4 to X4'. Data are projected from ~ 25 m on each side of sections. Locations of cross-sections are shown in Figure 4.6A.

adularia-cemented breccias ($Bx3_{py–adu}$). Hydrothermal breccia facies Bx1, Bx2 and Bx3 are related to veins on the basis of cross-cutting relationships, if present, spatial distribution and similar mineral assemblages and textures (i.e., Figure 4.2). Figure 4.2 correlates the hydrothermal breccias investigated in this study with those described by Blackwell (2010) and Ageneau (2012) from the Lienetz, Minifie and Kapit orebodies.

Gold grades within hydrothermal breccias are highly variable. Fire assay results of breccias reveal that $Bx1_{syenite}$ and $Bx1_{bio–anh}$, of the Bx1 facies, are low- to moderate-grade with $\bar{x}$ = 0.4 g/t Au (σ = 0.3, n = 7) and 1.3 g/t Au (σ = 1.0, n = 6), respectively. No specific gold assays were available for $Bx1_{anh\text{-}clast}$. The volumetrically insignificant Bx2 is low-grade, with $\bar{x}$ = 0.9 g/t Au (σ = 0.7, n = 2). The highest, yet most erratic, gold grades came from the Bx3 facies with $\bar{x}$ = 6.9 g/t Au (σ = 4.1, n = 94). Copper was also assayed, with similar average values of $\bar{x}$ = 590 ppm for breccias of the Bx1 facies. The Bx2 and Bx3 facies had slightly lower copper values, with $\bar{x}$ = 140 and 380 ppm Cu, respectively (Appendix 1).

4.5.1: Syenite-cemented breccias ± dikes ($Bx1_{syenite}$)

Syenite-cemented breccias ± dikes ($Bx1_{syenite}$; Figure 4.9) occur as discrete features within deep levels of the Lienetz orebody: below −300 m in open-pit exposures and below −300 m rsl in drill core from northeastern and northern areas of Lienetz (Figures 4.6A, 4.7A–B, 4.8A–B). The two components of $Bx1_{syenite}$ are intimately related, with breccias as coronal halos about coherent to brecciated porphyritic syenite dikes (Figures 4.7A–B, 4.8A–B). The composite bodies have elliptical form, with widths of < 50 m, northeast- to east-northeast-elongation, and high-angle dips (Figures 4.6A, 4.7A–B, 4.8A–B, 4.9C).

$Bx1_{syenite}$ are cement-rich, mosaic to chaotic breccias (cf. Figure 4.1). Cement is composed of both igneous (i.e., syenite) and hydrothermal material (i.e., anhydrite, biotite and K-feldspar; Figure 4.9A, D). The igneous cement (and related dikes) commonly have phenocrysts of K-feldspar (~ 0.1 to 0.5 cm) and biotite (~ 0.05 to 0.1 cm), set within a pink aphanitic groundmass (Figure 4.9B). Plagioclase, titanite and trace amount of nepheline and apatite are present. Chalcopyrite, pyrite and trace molybdenite are typically present in trace amounts, but in some cases comprise up to 2%, occurring as disseminations and in veinlets (Figure 4.9B).

4.5.2: Biotite – anhydrite-cemented breccias ($Bx1_{bio–anh}$)

Biotite – anhydrite-cemented breccias ($Bx1_{bio–anh}$; Figure 4.10) are the dominant unit in the deeper levels of the Lienetz open pit (Figures 4.6A, 4.7A–B, 4.8A–B). The $Bx1_{bio–anh}$ breccia body is ~ 750 m wide and > 300 m in vertical extent (maximum depth as-yet undetermined), and has a steeply dipping geometry (Figures 4.6, 4.7A–B, 4.8A–B). $Bx1_{bio–anh}$ locally cross-cuts, and is cross-cut by, $Bx1_{syenite}$.

$Bx1_{bio–anh}$ are cement- to matrix-rich, chaotic breccias (cf. Figure 4.1). Clasts account for ~ 30 to 50% of the rock mass, are poorly sorted, angular to sub-rounded, ranging ~ 0.2 cm to > 150 cm in diameter. They are polymictic and polyphase, comprising pre-ore volcano-sedimentary strata, intrusive rocks, $Bx1_{syenite}$, $Bx1_{bio–anh}$, and include clasts with truncated $V1_{bio}$, $V1_{chl–epi}$, $V1_{ksp}$, and $V1_{M1}$ veins (e.g., Figure 4.10A, E).

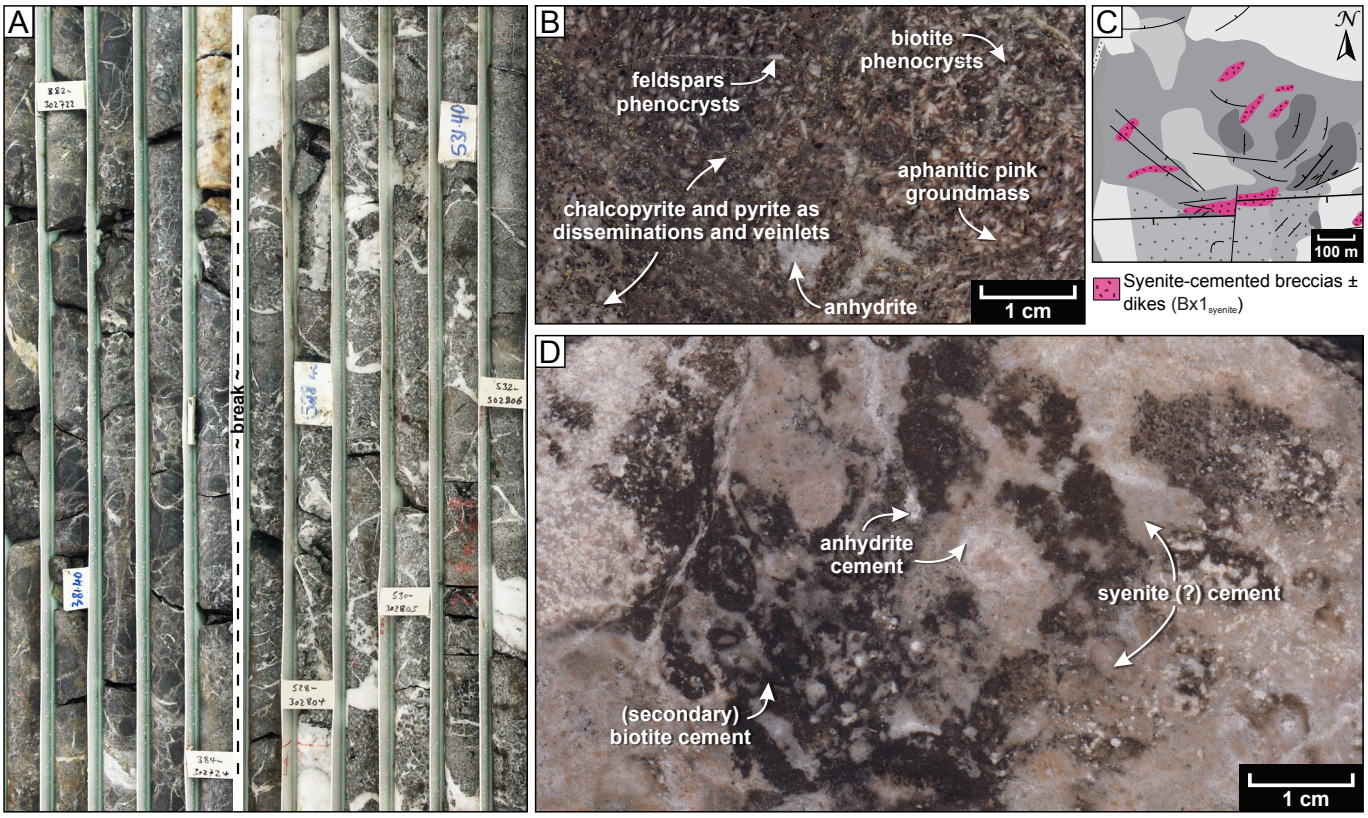

Figure 4.9: Examples of syenite-cemented breccias ± dikes ($Bx1_{syenite}$). A) Intervals of the $Bx1_{syenite}$ in drill core (DDHL1991 from 381 to 385 m and 527 to 533 m; 36 m rsl, 9654702 N, 459175 E). **B)** Cut hand-sample specimen of $Bx1_{syenite}$ (LH14SS077; −230 m rsl, 9654210 N, 459316 E). **C)** Grey-scale plan map of Lienetz orebody, with coloured unit of interest. **D)** Cut hand-sample specimen of $Bx1_{syenite}$ showing hydrothermal biotite cement intergrown with anhydrite, K-feldspar and an igneous (syenite?) cement (LH14SS021; −305 m rsl, 9654045 N, 459481 E).

Large clasts of $V1_{M1}$ anhydrite veins, locally with distinct pre-fragmental dissolution seams and stylolites, are also common (Figure 4.10D). Many clast margins, in particular vein-clasts of $V1_{M1}$ origin, are irregular and serrated (Figure 4.10A, D). The matrix component ranges from ~ 10 to 70% by volume, and consists of fine-grained (< 0.2 cm) rock and vein fragments that are weakly to moderately biotite-altered. Overall, weak to strong biotite and K-feldspar alteration is common throughout the breccia clasts and matrix. Cement and open space account for ~ 1 to 30% and ~ 1 to 5% of the rock volume, respectively. Anhydrite and biotite are the major cement minerals. Anhydrite cement is intergranular and massive-textured (Figure 4.10B), with local weakly developed dark-coloured dissolution seams (Figure 4.10A). Biotite cement is predominantly fine-grained and shreddy-textured, but locally coarse-grained elongated biotite books are present (Figure 4.10A). Disseminated pyrite ± chalcopyrite constitutes trace amounts to 1% of the rock volume.

4.5.3: Anhydrite vein-clast breccias ($Bx1_{anh\text{-}clast}$)

Anhydrite vein-clast breccias ($Bx1_{anh\text{-}clast}$; Figure 4.11) are spatial and compositionally associated with $Bx1_{bio–anh}$ (Figure 4.2). They crop out in the center and northwest of Lienetz, and occur enclosed within bodies of $Bx1_{bio–anh}$, with an apparent northwest-elongation in plan view (Figures 4.6A, 4.7B, 4.8A, 4.11C).

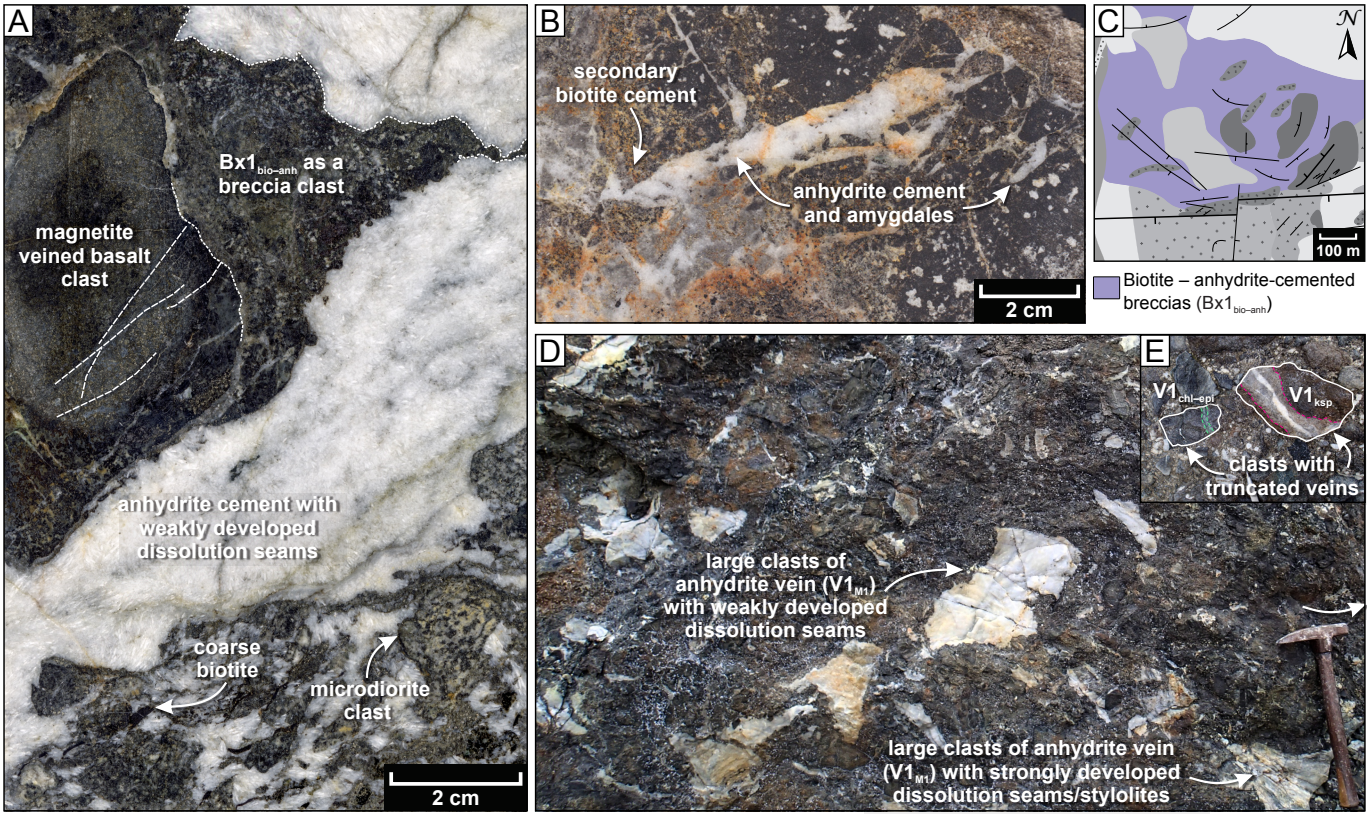

Figure 4.10: Examples of biotite – anhydrite-cemented breccias ($Bx1_{bio–anh}$). A) Cut drill-core specimen of $Bx1_{bio–anh}$ with clasts of $Bx1_{bio–anh}$ and magnetite-veined basalt. Clast margins and magnetite veins are outlined in dashed white lines. Weakly developed dissolution seams are the irregular dark lines in anhydrite-cement (sample 166 m in DDHL0791, located at 44 m, 9654196 N, 459133 E). **B)** Cut hand-sample specimen of $Bx1_{bio–anh}$ (LH14SS086, located at −185 m, 9654197 N, 459113 E). **C)** Grey-scale plan map of Lienetz orebody, with coloured unit of interest. **D)** Bench outcrop of $Bx1_{bio–anh}$ showing large clasts of anhydrite veins with weakly to strongly developed dissolution seams. Note the irregular serrated edges of anhydrite clasts. Hammer in bottom right corner for scale (location: −272 m rsl, 9654150 N, 459542 E). **E)** Bench outcrop of $Bx1_{bio–anh}$ showing clasts with truncated veins of $V1_{ksp}$ and $V1_{chl–epi}$. Scribe in bottom image for scale (location: −257 m rsl, 9654150 N, 459313 E).

The $Bx1_{anh\text{-}clast}$ bodies are variable in size, ranging from 5 to 150 m wide, with sharply bounded, downward tapering pipe-like geometries (Figures 4.6A, 4.7B, 4.8A).

$Bx1_{anh\text{-}clast}$ are matrix-rich, chaotic breccias (cf. Figure 4.1). Clasts comprise ~ 10 to 30% of the rock mass, are poorly sorted, angular to sub-rounded and polymictic, however, they are characteristically composed of anhydrite vein-clasts (Figures 4.11A–B, D–E). The anhydrite vein-clasts have weakly to strongly developed dissolution seams and stylolites (Figure 4.11A, D), features characteristic of $V1_{M1}$ veins. In addition to its distinctive anhydrite-vein clast assemblage, $Bx1_{anh\text{-}clast}$ consists of ~ 30 to 70% matrix, ~ 1 to 15% cement and ~ 1 to 8% open space. The cement and matrix compositions are also similar to $Bx1_{bio–anh}$, however, the cement is less abundant and rock and vein fragments are more common (Figure 4.11B). Weak to moderate biotite alteration has also affected the breccia clasts and matrix (Figure 4.11B), and trace disseminated pyrite is present.

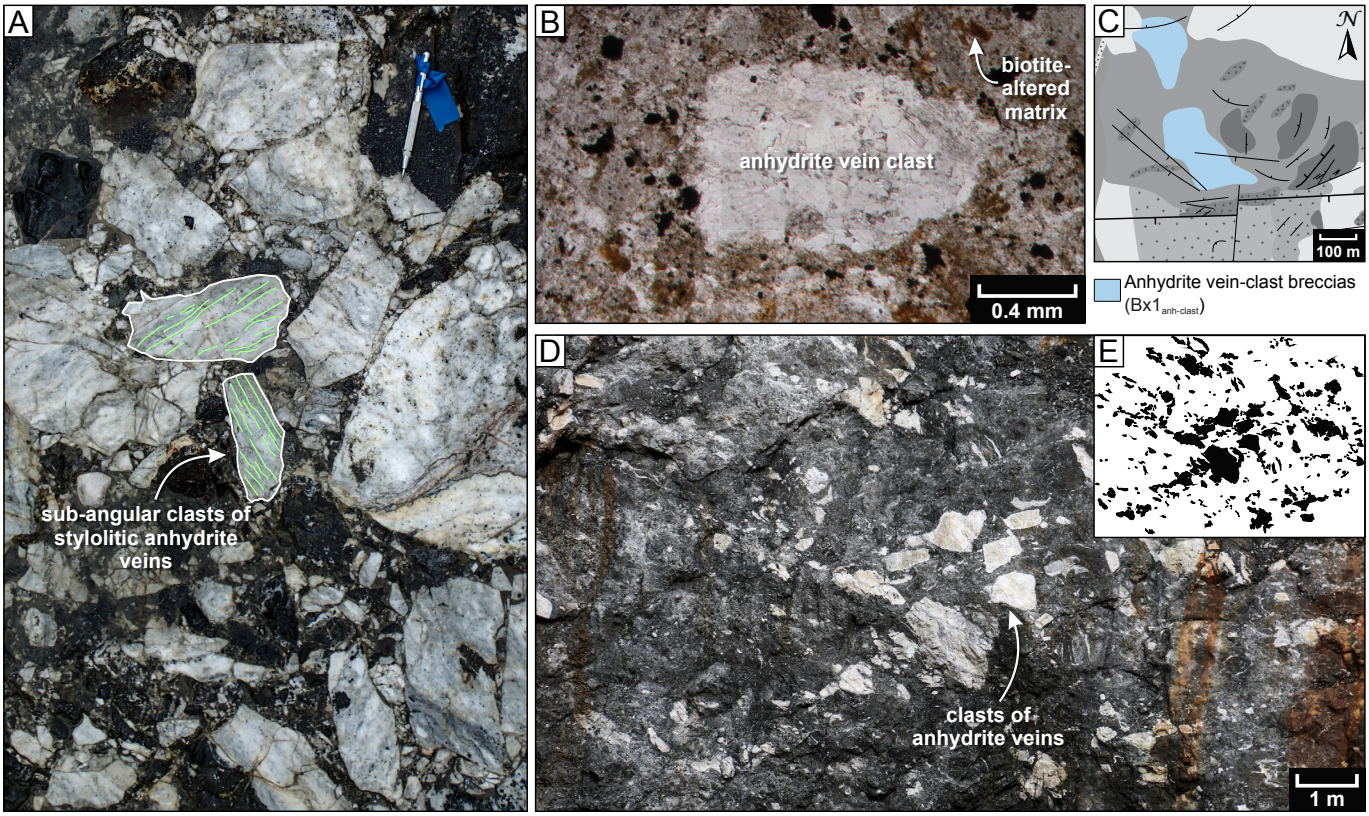

Figure 4.11: Examples of anhydrite vein-clast breccias ($Bx1_{anh\text{-}clast}$). A) Bench outcrop of $Bx1_{anh\text{-}clast}$ showing anhydrite veins ($V1_{M1}$) with strongly developed stylolites. Note the random orientation of clasts in regards to stylolites (location: −192 m rsl, 9654187 N, 459196 E). **B)** Microscope photo of $Bx1_{anh\text{-}clast}$ under plane polarized light showing small anhydrite vein-clasts in biotite-altered matrix (LH14SS081; −254 m rsl, 9654019 N, 459236 E). **C)** Grey-scale plan map of Lienetz orebody, with coloured unit of interest. **D)** Bench outcrop of $Bx1_{anh\text{-}clast}$ showing the anhydrite vein-clasts (location: −296 m rsl, 9654000 N, 459310 E). **E)** Illustrated version of (D), highlighting the anhydrite vein-clast components (~ 20% in this case) as black silhouettes.

4.5.4: Bx1 facies: relationships with V1 veins

Bx1 facies breccias are temporally and genetically associated with V1 veins (Figure 4.2A). Clasts of truncated $V1_{bio}$, $V1_{chl\text{–}epi}$, $V1_{ksp}$ and $V1_{M1}$ veins in $Bx1_{bio\text{–}anh}$ imply that veins formed prior to or synchronous with prolonged Bx1 brecciation. $V1_{M1}$ and $V1_{M2}$ veins variably cross-cut $Bx1_{bio\text{–}anh}$, implying that veins formed syn- to post-brecciation. Within, but not limited to, Bx1 breccias are significant continuous intervals (i.e., up to 35 m thick) of anhydrite ± carbonate veins and breccia veins, dominantly belonging to $V1_{M1}$ and $V1_{M2}$ (Figure 4.12). There is an apparent spatial relationship with these veins, cavities and core-loss (Figure 4.12). Increased core-loss was noted consistently during logging above veins (Figures 4.4A, 4.12A, F–G), and also in areas within thick anhydrite ± carbonate veins (Figure 4.12B, F–G).

4.5.5: Pebble breccia dikes ($Bx2_{pebble}$)

Pebble breccia dikes ($Bx2_{pebble}$; Figure 4.13) are volumetrically insignificant, appearing to be restricted to the southwestern part of Lienetz. They have also been reported at Minifie (Figure 4.6A; Blackwell, 2010). $Bx2_{pebble}$ are matrix-rich, chaotic breccias (cf. Figure 4.1). Clasts account for ~ 10 to 40% of the rock

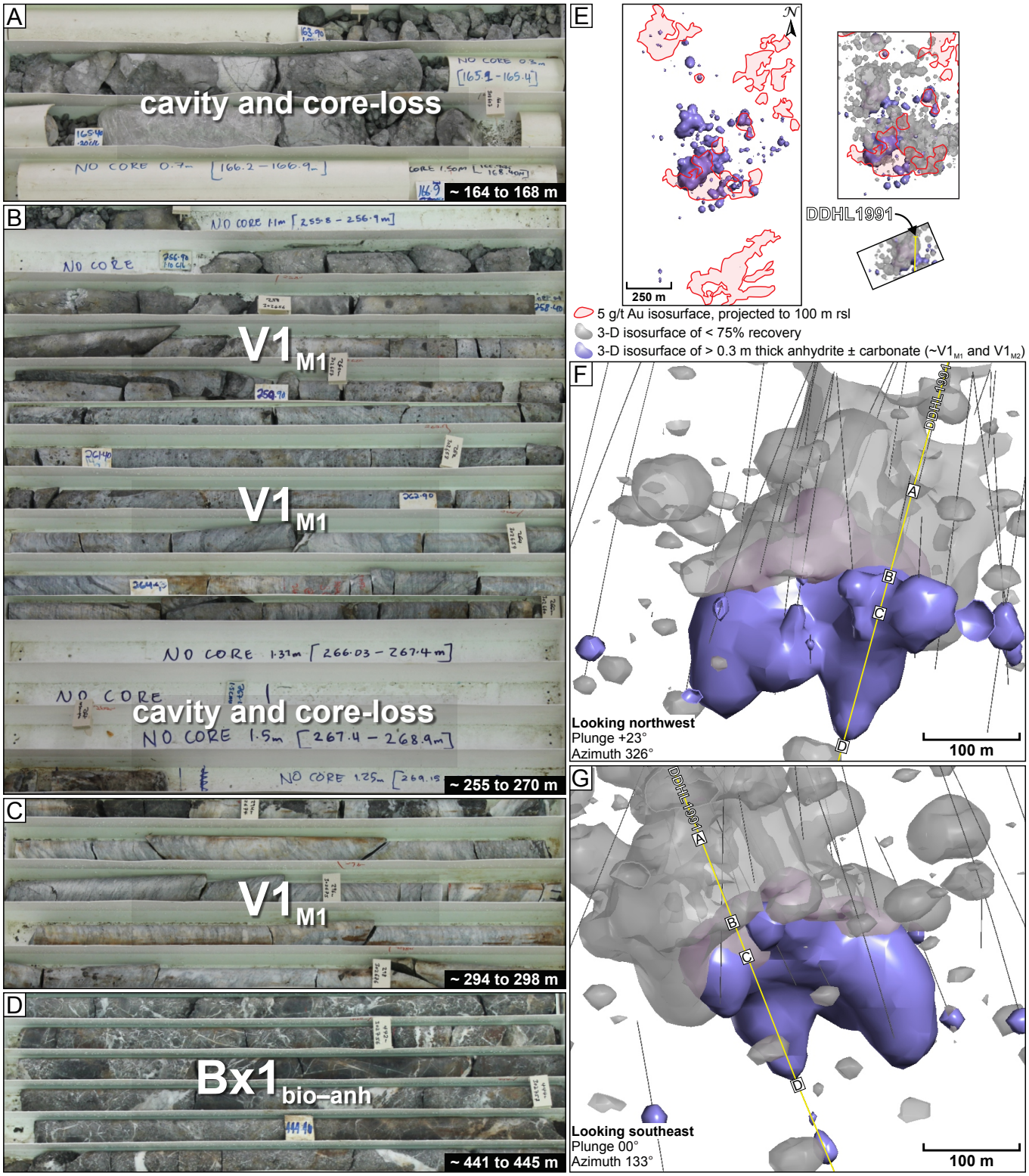

Figure 4.12: Examples of drill core and 3-D model of large anhydrite ± carbonate veins (i.e., ~ $V1_{M1}$ and $V1_{M2}$), as well as and relationship to core-loss and cavities. **A)** DDHL1991 (164 to 168 m) drill core with significant core-loss. **B)** DDHL1991 (255 to 270 m) drill core with large intervals of anhydrite intermixed with significant intervals of core-loss. **C)** DDHL1991 (294 to 298 m) drill core with significant intervals of continuous anhydrite veins. Within this significant anhydrite vein interval is a large cavity/core-loss interval. **D)** DDHL1991 (441 to 445m) drill core of $Bx1_{bio–anh}$. **E)** Legend and plan maps showing the extent of the 3-D modeled thick anhydrite ± carbonate veins and core-loss (i.e., < 75% recovery) isosurfaces. High-grade (5 g/t Au) isosurfaces are also projected on plan maps. **F–G)** Cross-sections with data projected from ~ 140 m on each side, showing the 3-D model of anhydrite ± carbonate (purple) and core-loss (grey). Locations of (A), (B), (C) and (D) are also shown.

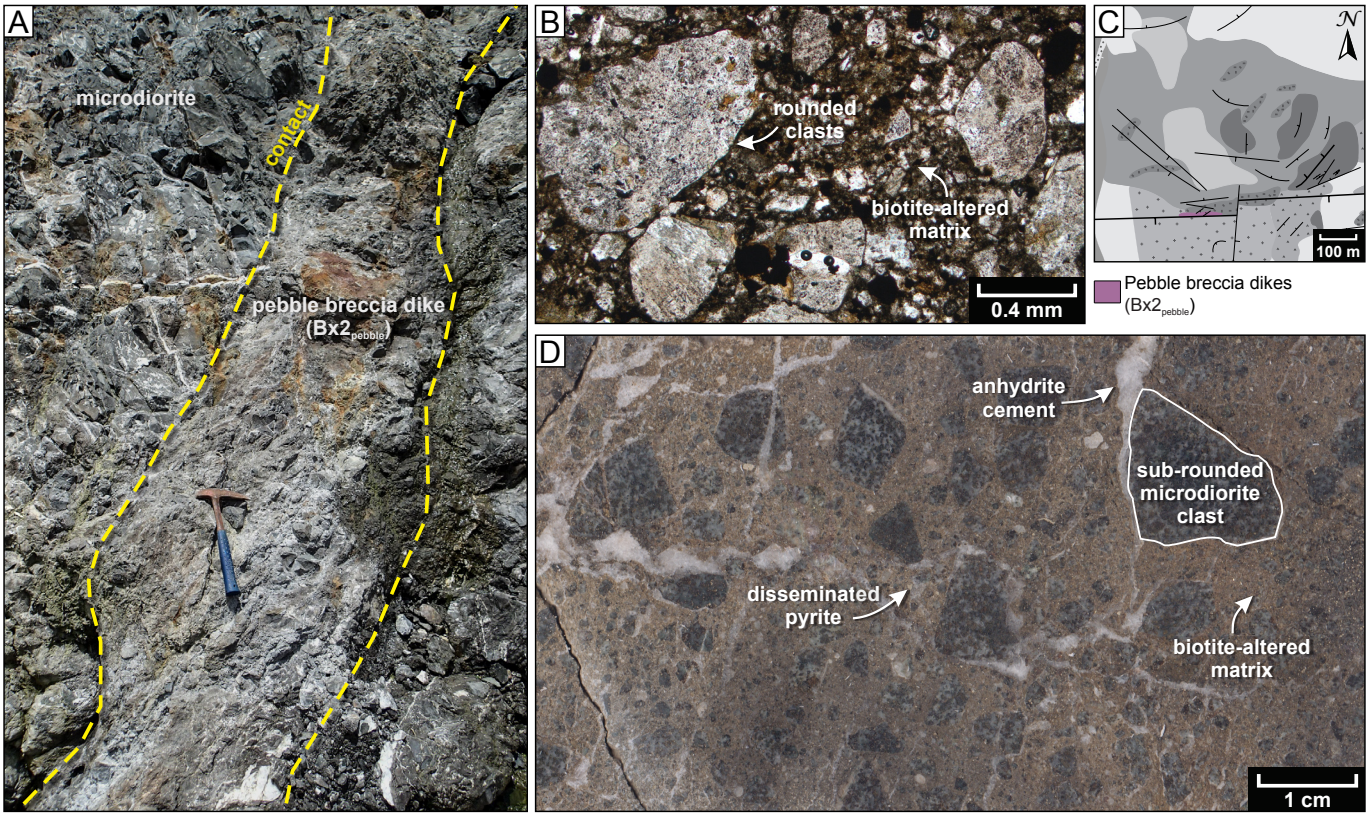

Figure 4.13: Examples of pebble breccia dikes ($Bx2_{pebble}$). A) Bench outcrop of $Bx2_{pebble}$ with sharp, steeply dipping contacts (location: −254 m rsl, 9654036 N, 459228 E). **B)** Microscope photo of clasts and matrix of the $Bx2_{pebble}$ under plane polarized light, showing the rounded nature of clasts and the biotite-altered matrix (sample 230 m in DDHL1174, located at 49 m, 9654121 N, 459283 E). **C)** Grey-scale plan map of Lienetz orebody, with coloured unit of interest. **D)** Cut drill-core sample of $Bx2_{pebble}$ showing sub-rounded microdiorite clasts, matrix, cement and disseminated pyrite (sample 230 m in DDHL1174, located at 49 m, 9654121 N, 459283 E).

volume, are moderately sorted, sub-rounded to rounded, ~ 0.2 to 2 cm wide, and polymictic but dominantly composed of microdiorite (Figure 4.13B, D). The matrix comprises ~ 35 to 80% of the rock mass, cement ~ 1 to 10%, and open space ~ 0 to 1%. The cement and matrix compositions are similar to $Bx1_{bio–anh}$, with moderate biotite-altered matrix and clasts (Figure 4.13B). Trace disseminated pyrite is present (Figure 4.13D). A single outcrop of $Bx2_{pebble}$ was observed with narrow (~ 2 to 6 m wide), east-northeast-striking, steeply dipping form, proximal to the contact of the microdiorite and $Bx1_{syenite}$ (Figures 4.6A, 4.13A, C). It is most likely that $Bx2_{pebble}$ breccias may be more abundant, but are hard to identify in drill core, either directly or from photographs. There is no synchronous relationship between Bx2 facies and any vein stage.

4.5.6: Pyrite – adularia-cemented breccias ($Bx3_{py–adu}$)

Pyrite – adularia-cemented breccias ($Bx3_{py–adu}$; Figure 4.14) typically form extensive sub-horizontal bodies, the bottoms of which occur above – 100 m rsl (Figures 4.7A–B, 4.8A–B). However, they locally extend to depths of −250 m rsl as downward-tapering bodies (e.g., Figures 4.7B, 4.8B). The roots of $Bx3_{py–adu}$ breccias appear to be bounded by steep, northeast-striking faults that link into higher level tabular $Bx3_{py–adu}$ zones (Figures 4.8B, 4.14B). $Bx3_{py–adu}$ cross-cuts Bx1 and Bx2 breccia facies.

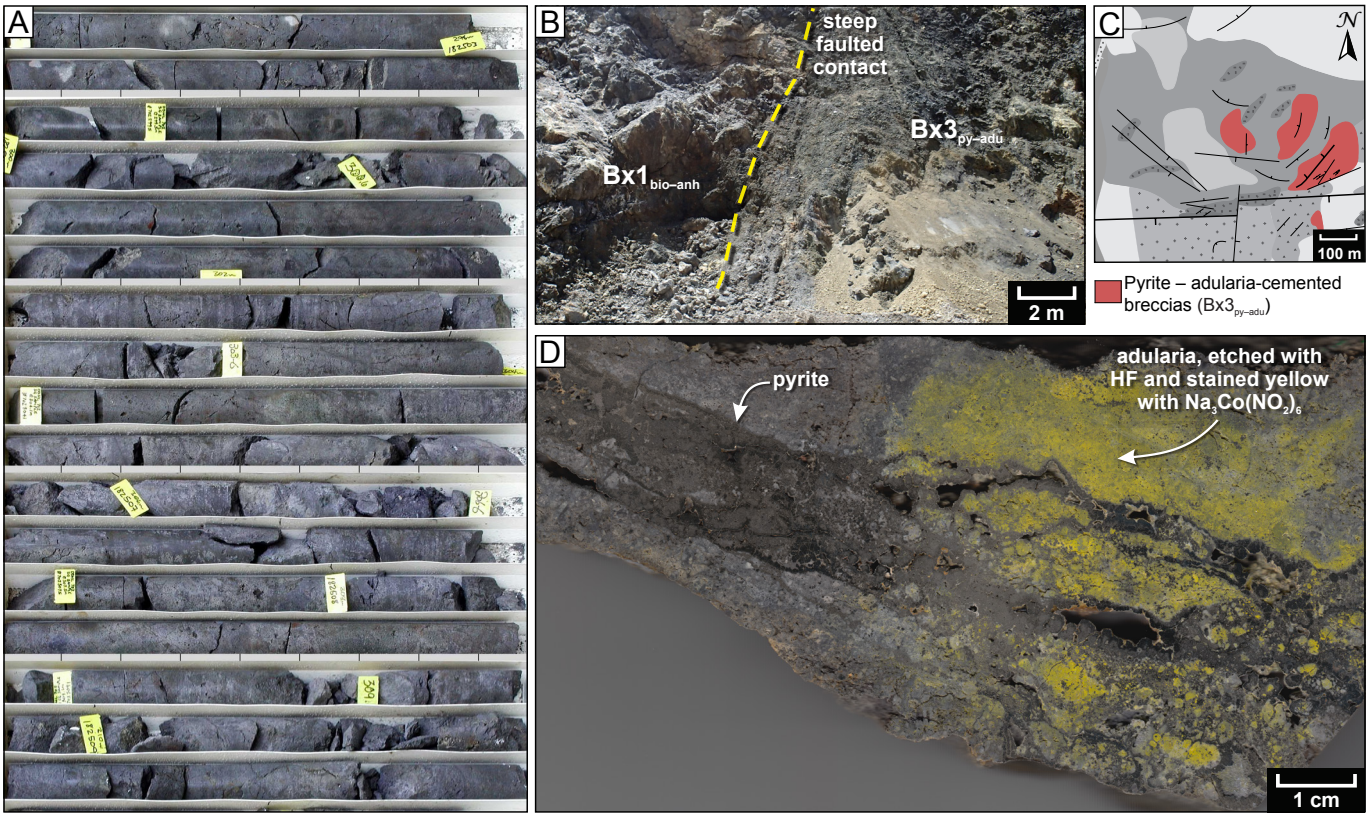

Figure 4.14: Examples of pyrite – adularia-cemented breccias ($Bx3_{py–adu}$). A) Drill core photograph of $Bx3_{py–adu}$ showing characteristic adularia alteration (i.e., light-grey colour), disseminated pyrite (i.e., sooty black colour), and porous nature (i.e., small holes). Photograph from 295 to 311 m in DDHL0702, located at 70 m rsl, 9654308 N, 459665 E. **B)** Bench outcrop of $Bx3_{py–adu}$ showing steeply dipping faulted contact with $Bx1_{bio–anh}$. Photograph from location of −272 m rsl, 9654126 N, 459615 E. **C)** Grey-scale plan map of Lienetz orebody, with coloured unit of interest. **D)** Cut hand-sample specimen of $Bx3_{py–adu}$ etched with HF acid and stained with $Na_3Co(NO_2)_6$ dye that reacts with and turns potassium bright yellow, interpreted here to be adularia. Photograph from sample LI12EL00A, located at −202 m rsl, 9654200 N, 459683 E).

$Bx3_{py–adu}$ are cement-rich, mosaic to chaotic breccias (cf. Figure 4.1). Clasts account for ~ 20 to 50% of the rock volume, are moderately to poorly sorted, angular to sub-rounded and apparently polymictic. The matrix comprises ~ 1 to 20% of the rock mass, whereas the cement ranges ~ 5 to 60% and is typically abundant. A distinctive assemblage of pyrite and marcasite ± quartz ± adularia defines the cement (Figure 4.14A, D). Cement textures include cockade, crustiform and acicular pyrite and marcasite, which have locally overgrown magnetite. Open spaces are common, ranging from 5 to 25% of the rock volume (Figure 4.14A). Although adularia is typically a minor cement component, it is a significant replacement or overgrowth product in clasts, leading to obliteration of primary textures and a pervasive light grey colour (Figure 4.14A, D).

Breccias of the Bx3 facies are temporally and genetically associated with $V3_{adu}$ and $V4_{qtz}$ veins, breccia veins and vug-fill (Figure 4.2). $Bx3_{py–adu}$ is also spatially related to areas of significant core-loss and cavities (i.e., < 75% recovery; e.g., Figures 4.7A–B, 4.8A–B).

4.6: Discussion

Hydrothermal breccias and veins are closely associated at Lienetz, and record various stages in the porphyry-epithermal transition. A combination of several compositional and textural features common to veins and breccia veins and hydrothermal breccias are used to indicate the prevailing conditions during their formation, as either porphyry-style (i.e., > 300°C; Lowell and Guilbert, 1970; Beane, 1974; Beane and Titley, 1981; Henley and Ellis, 1983; Reyes, 1990; Giggenbach, 1997; Corbett and Leach, 1998; Sillitoe, 2010), or epithermal (i.e., < 300°C; Buchanan, 1981; Heald et al., 1987; White and Hedenquist, 1990; Corbett and Leach, 1998; Cooke and Simmons, 2000; Simmons et al., 2005).

4.6.1: Veins and hydrothermal breccias that formed under porphyry-style conditions

V1 veins (apart from $V1_{chl–epi}$), and Bx1 breccias are interpreted have formed under porphyry-style potassic alteration conditions (Figure 4.2). Evidence supporting this interpretation includes: (1) the presence of hydrothermal biotite and K-feldspar as alteration halos of veins and alteration of breccia matrix and clast margins; (2) vein infill and breccia cement assemblages of anhydrite and biotite ± K-feldspar ± chalcopyrite ± magnetite; (3) local spatial association with porphyritic syenite dikes ± syenite-cemented breccias of similar composition (i.e., $Bx1_{syenite}$); and (4) high salinity (5 to > 40 eq. wt. % NaCl) fluid inclusions in related vein stages documented by Carman (2003; Table 4.2; Figure 4.2A–C). In addition, $V1_{chl–epi}$ veins are interpreted to have formed under porphyry-style propylitic alteration conditions related to the potassic-altered veins and breccias at Lihir.

The Bx1 facies is interpreted to be a magmatic-hydrothermal breccia complex (e.g., Table 4.1; Sillitoe, 1985). The high-angle dip of the edges of Bx1 permit a depth extent of > 1 km rsl. Thus, the Bx1 facies exposed at Lienetz may be only the upper part of a much larger breccia complex sourced from an intrusion located below the limits of the current drilling. Anhydrite – biotite-rich breccias and associated igneous-cemented breccias and porphyritic dikes have been reported from many porphyry Cu ± Au ± Mo deposits, where they are typically interpreted to be high-temperature magmatic-hydrothermal breccia complexes, based on mineralogy, fluid inclusions and isotopic data (e.g., El Teniente, Rio Blanco – Los Bronces and others; Sillitoe, 1985; Warnaars et al., 1985; Skewes et al., 2002; Candela and Piccoli, 2005; Cannell et al., 2005; Frikken et al., 2005).

The Bx2 facies is interpreted to be a pebble dike. It most likely formed under porphyry-style conditions, as a late-stage hydrothermal (phreatic) breccia produced by steam explosions (cf. Sillitoe, 1985). A gas-charged slurry of rock fragments would have migrated along faults and fractures. This interpretation is supported by: (1) rounded and moderate- to well-sorted clasts; (2) sand-sized clastic matrix; (3) sharp contacts and steeply dipping geometry; and (4) biotite alteration. Pebble dikes have been reported in other

magmatic-hydrothermal ore deposits (e.g., Tintic, Bisbee, Cuajone, El Salvador and Mt. Morgan; Farmin, 1934; Bryner, 1961; Sillitoe, 1985).

Although Lihir is commonly referred to as an alkalic epithermal deposit (e.g., Carman, 1994, 2003), the volume of relatively early porphyry-related veins and breccias is significant, particularly at depths. A paucity of typical A- and B-type quartz veins is atypical of calc-alkalic porphyry Cu ± Mo deposits, but is consistent with more silica-undersaturated alkalic porphyry Cu ± Au deposits (e.g., Richards, 1995; Sillitoe, 2000; Sillitoe, 2010; Bissig and Cooke, 2014).

4.6.2: Modification of veins and breccias that formed under porphyry-style conditions

Stage $V1_{M1}$ veins and breccia veins, and parts of the Bx1 breccia facies, are interpreted to have been modified after initial formation under porphyry-style conditions, likely during the transition to epithermal-style conditions (Figure 4.2). This event reopened and modified some V1 veins, producing $V1_{M1}$ veins (Figure 4.2). Evidence for vein modification includes: (1) $V1_{M1}$ veins having hydrothermal biotite and K-feldspar alteration halos; (2) assemblages of anhydrite and biotite ± K-feldspar ± chalcopyrite ± magnetite; (3) dissolution seams; (4) stylolites; (5) irregular and partly dissolved anhydrite-wall rock boundaries; (6) irregular and partly dissolved wall-rock inclusions in anhydrite-rich veins and breccia veins, (7) variable contents and textures of barite, celestine and anhydrite; and (8) high salinity (5 to > 40 eq. wt. % NaCl) fluid inclusions documented by Carman (2003; Table 4.2; Figure 4.2A–C). Additionally, fluid inclusions from Ageneau (2012)'s vein stage 2A/B, which are correlated with stage $V1_{M1}$ veins at Lienetz, support porphyry-style to transitional conditions, with variable salinities and temperatures of homogenization (i.e., temperatures from ~ 215 to 350°C, and salinities from ~ 1 to 20 eq. wt. % NaCl; Figure 4.15). Fluid inclusions homogenisation temperatures measured from anhydrite must always be treated with caution, however, because of the possibility of post-entrapment modification of the fluid inclusion by stretching or deformation (e.g., Cooke and Bloom, 1990).

$V1_{M1}$ textural modifications were facilitated by anhydrite dissolution and recrystallization, probably due to changing temperatures ± pressures ± salinities. Anhydrite, as well as celestine, has retrograde solubility at < 350°C (Blount and Dickson, 1969; Hanor, 2000), whereas barite has prograde solubility when temperature is < 350°C (Hanor, 2000). Therefore lower temperature conditions will most likely facilitate anhydrite dissolution by cool groundwater. Anhydrite has been shown to recrystallize at ~ 120°C (possible as low as 80°C), and flow readily at 150° to 180°C, with strain rates of 10^{-14}/s (Müller et al., 1981; Schreiber and Helman, 2005, and references therein). Therefore, anhydrite can also be affected significantly by low to moderate degrees of stress, resulting in significant preferential dissolution (i.e., preferential to less soluble minerals), as well as recrystallization. This can result in mylonitic-like foliation and flow tex-

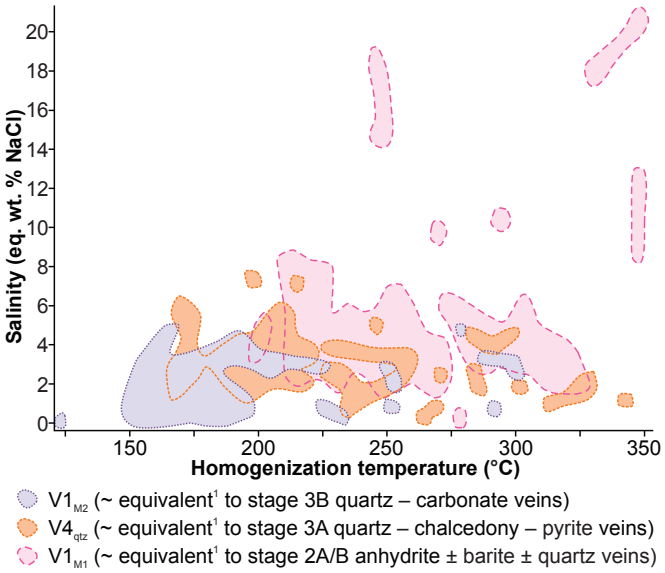

Figure 4.15: Salinities and homogenization temperatures from Ageneau (2012)'s fluid inclusion studies. [1] = polygons encompass data from Ageneau (2012)'s vein stages 2A/2B, 3A and 3B, which are approximately equivalent to this study's $V1_{M1}$, $V4_{qtz}$ and $V1_{M2}$, respectively.

tures within anhydrite, as opposed to surrounding competent rock layers that will exhibit more brittle deformation (Schreiber and Helman, 2005). Brittle components of wall rocks can be incorporated into anhydrite, breaking up, disintegrating, rotating and fracturing into smaller pieces, leaving behind a trail of broken, fine-grained residue along the shear plane (e.g., Schreiber and Helman, 2005). These textures are analogous to the textures observed in $V1_{M1}$. The presence of stylolites, which are interpreted to form by pressure-driven dissolution and recrystallization, also implies reduction of porosity and permeability in the $V1_{M1}$ veins and breccia veins (e.g., Nenna and Aydin, 2011).

The same modification event that affected $V1_{M1}$ also resulted in parts of $Bx1_{bio–anh}$ and most of $Bx1_{anh\text{-}clast}$ undergoing partial dissolution, leading to local volume loss and local collapse. The modified breccias are interpreted to be dissolution breccias (e.g., Table 4.1). This is evident by: (1) serrated margins of anhydrite and wall-rock clasts; (2) dissolution seams in cement; (3) randomly oriented vein-clast fragments; and (4) open-space cavities in the upper-levels of the breccias and associated veins. At least partial dissolution occurred prior to fragmentation, since clasts of vein material with strong dissolution fabrics (e.g., stylolitic $V1_{M1}$ veins) occur within $Bx1_{bio–anh}$ and $Bx1_{anh\text{-}clast}$.

4.6.3: Veins and hydrothermal breccias that formed under epithermal-style conditions

V3 and V4 (and possibly V2) veins, and Bx3 breccia facies are interpreted to have formed under epithermal conditions (Figure 4.2). Evidence for this includes: (1) the presence of hydrothermal adularia and illite alteration; (2) vein assemblages, and breccia cement, of pyrite and marcasite ± adularia ± quartz ± anhydrite (bladed); and (3) low salinity (2 to 7 eq. wt. % NaCl) fluid inclusions (Carman, 2003; Table 4.2; Figure 4.2A–C). Fluid inclusions from Ageneau (2012)'s vein stage 3A, which is correlated with stage $V4_{qtz}$ veins at Lienetz, provide additional evidence for epithermal conditions, with the mean values of homogenization temperatures and salinities around ~ 175 to 250°C and 2 to 5 eq. wt. % NaCl; Figure 4.15).

The upper levels of $Bx3_{py–adu}$ breccias at least in part formed by cementing the partly dissolved upper-levels of $Bx1_{bio–anh}$ and $Bx1_{anh\text{-}clast}$ breccias. Void space created by prior, or synchronous, partial leaching and dissolution of anhydrite formed open-space cavities and permeable and porous zones. These conduits

were then infiltrated by epithermal-style auriferous hydrothermal fluids that partly sealed areas and deposited Bx3. While the broad upper zone of Bx3 formed by re-cementation, deeper roots of Bx3 facies have some structural control due to their apparent narrowing at depth. These structural controls will be expanded upon in Chapter 5.

4.6.4: Continued preferential modification under epithermal-style conditions

$V1_{M2}$ is interpreted to be the second modification event, which preferentially reactivated and modified V1 veins during late-stage hydrothermal activity under epithermal conditions. This is evidenced by: (1) the presence of inner illite and adularia alteration assemblages in the wall rocks around $V1_{M2}$ veins that overprint broader biotite alteration halos; (2) assemblages of massive and cockscomb banded calcite, quartz and anhydrite (thinly bladed) ± pyrite ± adularia; and (3) low salinity (2 to 7 eq. wt. % NaCl) fluid inclusions (Carman, 2003; Table 4.2; Figure 4.2). It is most likely that the pre-existing V1 veins and breccia veins localized hydrothermal fluid flow, allowing cooler, carbonate – silica-rich, sulfate-poor fluids to precipitate the $V1_{M2}$ mineral assemblages. Additionally, fluid inclusions from Ageneau (2012)'s vein stage 3B, which are correlated with stage $V1_{M2}$, support epithermal conditions (i.e., mean values of homogenization temperatures and salinities cluster around ~ 150 to 200°C and 0 to 4 eq. wt. % NaCl; Figure 4.15).

4.6.5: Veins and hydrothermal breccias relationships with gold mineralization

The highest gold grades in Lienetz (i.e., > 5 g/t Au) are typically associated with the late epithermal-style Bx3 breccia and associated $V3_{adu}$ and $V4_{qtz}$ veins, breccia veins and vug-fill (Table 4.2; Appendix 1). Lower gold grades (i.e., < 1 g/t Au) ± low copper grades (i.e., < 0.1 wt. % Cu) occur within porphyry-stage Bx1 and Bx2 breccias and associated $V1_{bio}$ and $V1_{ksp}$ veins (Table 4.2; Appendix 1). This implies that the early porphyry-style hydrothermal activity was moderately auriferous. Although porphyry-related gold grades are meager relative to the late stage epithermal-style gold mineralization at Lihir, they rank favorably compared to known porphyry Au deposits globally (e.g., Sillitoe, 2000; Sinclair, 2007). Lihir can therefore more appropriately be classified as a hybrid alkalic porphyry and low-sulfidation epithermal gold deposit.

4.7: Conclusions

The early porphyry-style environment in Lienetz resulted in a magmatic-hydrothermal breccia complex and associated veins and breccia veins, most of which are rich in anhydrite. Early low-grade gold ± copper was associated with these events.

Evidence of modification of anhydrite-rich veins and breccias is widespread, indicating fundamental changes in physicochemical conditions during the porphyry-epithermal transition, which in turn appear to have influenced permeability and porosity evolution at the deposit scale. Dissolution seams and stylolites provide evidence for pressure solution and volume reduction. Further volume loss is indicated by the extensive areas of core-loss and open-space cavities, typically above or within large masses of recrystallized ± stylolite-bearing anhydrite. This was largely facilitated by the solubility of anhydrite via changing temperatures ± pressures ± salinities. With changing conditions, anhydrite dissolved and recrystallized, particularly along the edges and surfaces, but also within anhydrite. While dissolution of anhydrite is typically not reported in ore deposit studies, anhydrite karst systems are not uncommon (e.g., Carlsbed Caverns karst systems in Mexico – Hill, 1987; tunnels in Switzerland – Gysel, 2002).

The late epithermal environment in Lienetz resulted in hydrothermal breccias, veins, breccia veins and vug-fill with high-grade gold mineralization. This was partly facilitated by preconditioning from the porphyry-stage events. Continued hydrothermal activity in the ancient to modern epithermal environment led to further modification by reactivation of veins and breccia veins.

CHAPTER 5: STRUCTURAL GEOLOGY

5.1: Introduction

Widespread overprinting of epithermal-style features upon the porphyry-related veins and breccias, within the relatively well-preserved dissected volcanic edifice at Lihir, provides a rare opportunity to understand the physical evolution of magmatic-hydrothermal activity in a giant alkalic gold deposit. This chapter focuses on the structural processes that operated throughout the porphyry-epithermal transition, by examining the formation and evolution of spectacular vein arrays in the deeper levels of Lienetz, largely within the anhydrite-rich zone. The geometric and kinematic features of various vein stages are used to provide constraints on the relative roles of tectonic, magmatic, hydrothermal and gravitational forces that led to broad-scale permeability and porosity development. The deposit-scale structural template is used to examine the distribution of gold within the anhydrite-rich zone in Lienetz, and to place constraints on gold introduction, remobilization, and precipitation throughout the evolution from porphyry- to epithermal-style conditions.

5.2: Previous structural studies at Lihir

Mapping and identifying faults on Lihir Island has been hindered by the island's poor exposure, tropical rainforest cover, and rugged terrain. Work by the Geological Survey of Papua New Guinea (Wallace et al., 1983), and subsequent unpublished consultant reports (e.g., Pridmore, unpublished report to Kennecott Exploration Ltd., 1991), relied heavily on interpreting aerial photography, with supplementary sideways looking radar, and airborne geophysical datasets to produce basic lineament maps (Figure 5.1A). Of the geometrically distinct lineament sets, those with east-northeast and northeast trends are most prevalent and coincide with aligned offshore islands, aeromagnetic features and elongation of inferred volcanoes and intrusions (Figure 5.1A). By contrast, north, northwest and west-northwest trending elements are less common, but are also defined by magnetic lineaments and truncations. The combination of each set contributes to the overall wedge-shaped, southward-tapering form of the island (Figure 5.1A).

Further structural analyses of the Luise amphitheater, largely presented in unpublished reports to Lihir mining operations, integrated aerial and ground geophysical surveys, aerial photography, synthetic aperture radar images, photogrammetry, borehole temperature maps, drill-core geotechnical data and limited surface mapping to define similar trending lineaments (Figure 5.1B, Williamson, 1983; Moyle et al., 1990; Corbett et al., 2001; Müller et al., 2002b; Haneberg et al., 2005; Vogwill et al., 2009). Lineaments within the amphitheater have been proposed to define a complex array of faults (e.g., Moyle et al., 1990; Corbett et al., 2001), but these inferred structures have poor kinematic constraints and imprecise positions, with only the east-northeast- and northeast-striking lineaments relatable to mappable faults. Additionally, east-northeast,

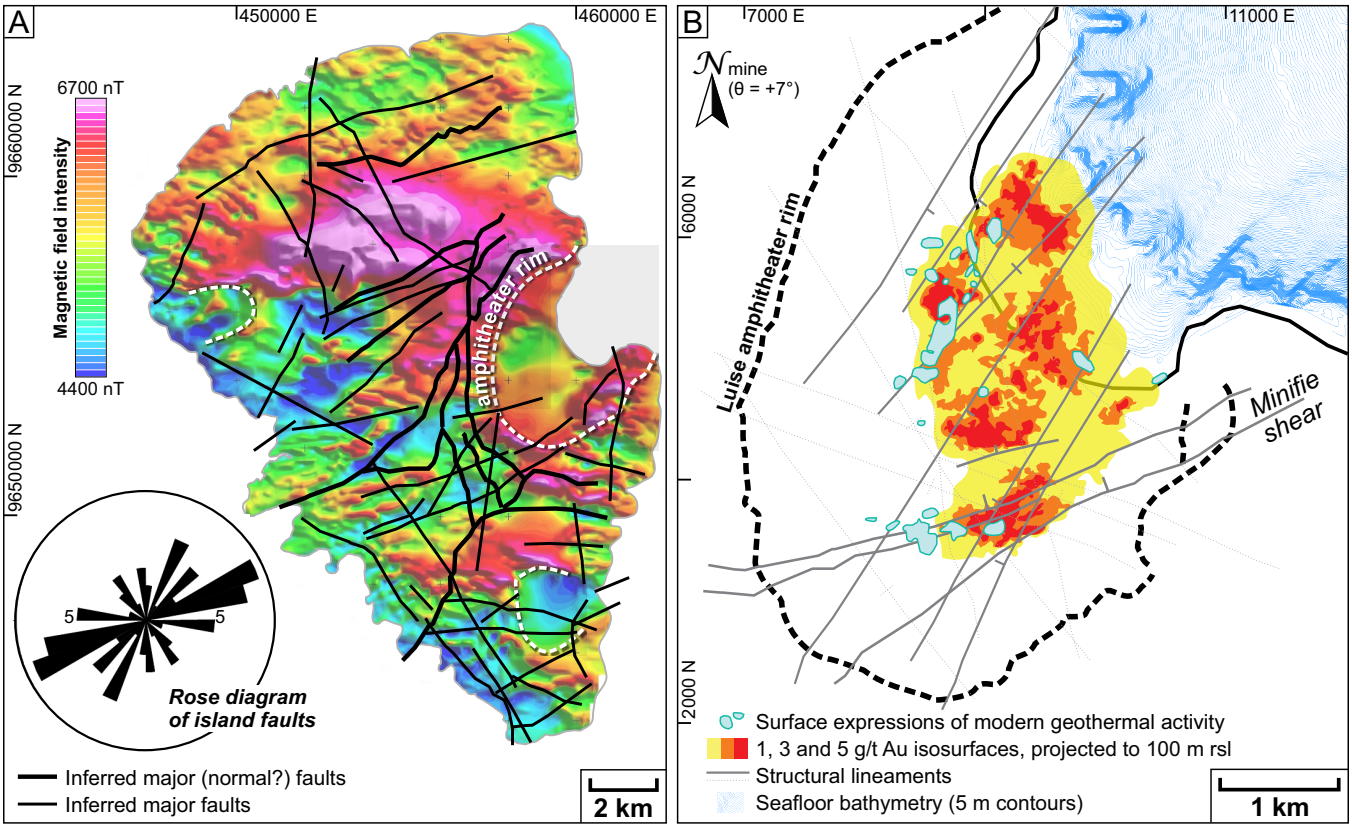

Figure 5.1: Structures interpreted on Lihir Island and within the Luise amphitheater. A) Airborne magnetic data reduced to pole of Lihir Island, with inferred faults (Wallace et al., 1983; Pridmore, unpublished report to Kennecott, 1991; Komyshan, unpublished report to Lihir Mining Ltd., 1999; Reid and Eade, unpublished report to Lihir Mining Ltd., 2010). **B)** Amphitheater-scale structural lineaments, recognized from previous workers and consultants at Lihir mine, and surface expressions of high-temperature geothermal activity (Williamson, 1983; Vogwill et al., 2009).

northeast and northwest trends conform to boundaries, or long-axes, of high-grade gold isosurfaces that define orebodies (Figure 5.1B). The most notable example is the east-northeast-striking, steeply to moderately northward-dipping Minifie shear, which marks the southern margin of the Minifie orebody (Figure 5.1B). Both the east-northeast and northeast lineaments are loci for the presently active high-temperature geothermal system (Figure 5.1B). The northeast-striking lineaments also parallel the steep bathymetric ridges of the Luise amphitheater that project offshore (Figure 5.1B).

5.3: Methods

Data were collected primarily through open-pit mapping of the deepest levels of the Lienetz orebody. Although exposure of the vein array is excellent, working in areas of active mining and geothermal outflow presented a number of logistical hazards. Average bench heights are approximately 12 m with steep faces (i.e., 65 to 80°), resulting in overhanging and unstable rocks. The modern high-temperature geothermal system has surficial discharge points in the bottom and walls of the Lienetz open pit, resulting in areas of potential geothermal outbursts with boiling springs and steaming ground, hot mud pools, and local rock temperatures > 60°C. In the current study, inaccessible areas were mapped remotely with the aid of spatially referenced high-resolution photographs, and supplemented with drill-core data. The drill cores are unorient-

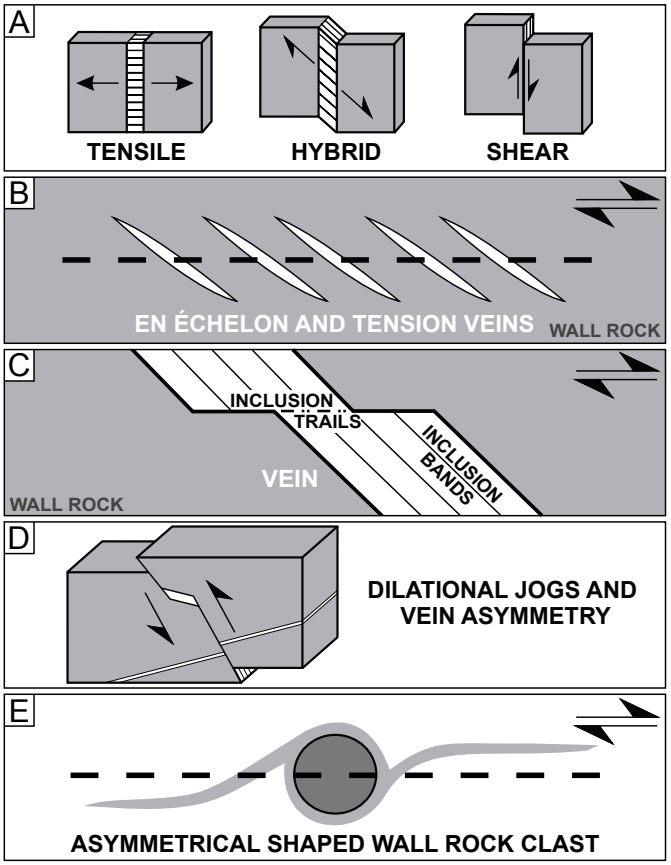

Figure 5.2: Kinematic indicators for veins. A) Tensile, hybrid and shear failure modes of vein opening (e.g., Anderson, 1951; Phillips, 1972; Cosgrove, 1995). **B)** En échelon vein arrays (e.g., Beach, 1975; Olson and Pollard, 1991). **C)** Inclusion bands and trails (e.g., Ramsay, 1980; Cox and Etheridge, 1983; Ramsay and Huber, 1983; Cox, 1987; Urai et al., 1991; Koehn and Passchier, 2000). **D)** Vein asymmetry and cross-cutting relationships (e.g., Atkinson, 1987). **E)** Wall-rock clast with asymmetrical shape symmetry, similar to δ-porphyoclast systems (e.g., Passchier and Simpson, 1986).

ed, but the very substantial thicknesses (> 10 m) and distinct textures of certain vein arrays has permitted correlation across the Lienetz orebody. All structural measurements are listed in Appendix 1, as well as an example of a raw bench map.

To examine relationships between structural elements in the Lienetz open pit and gold mineralization, high-grade gold isosurfaces from gold assay composites (i.e., a blend of blasthole and drillhole fire Au assays) were constructed for depths below −100 m rsl. Data were modeled using interpolants in Leapfrog™, and subdivided into a suite of geometrically, and to a lesser extent spatially, distinct ellipsoidal isosurfaces (Appendix 2). Mineralized high-grade isosurfaces are defined by > 1.5 g/t Au. Geometric data were generated by digitizing 'structural disks' on the margins of ellipsoidal isosurfaces, and are shown in stereograms.

Vein stages were distinguished principally by their composition and textures, associated alteration halos, and cross-cutting relationships (e.g., Table 4.2; Figure 4.2). Vein opening mechanisms and interpretations of their kinematic significance were partly determined from internal fabric elements, including vein fibers and inclusion bands where present (Figure 5.2A, C; e.g., Cox and Etheridge, 1983; Ramsay and Huber, 1983; Cox, 1987; Urai et al., 1991). The form of vein arrays, and geometric relationships with non-mineralized fractures, provided additional kinematic constraints (Figure 5.2B, D). Veins locally possess folded internal fabrics. Local inclusions of wall rocks with asymmetric tails, similar to porphyroclasts in shear zones (Figure 5.2E), were also used to define relative wall rock displacement histories.

5.4: Structure and kinematic domain analysis

Figure 5.3 shows a plan map of rock types and faults in Lienetz and Minifie. Figures 5.4 and 5.5 show unrolled profiles maps of the Lienetz open pit. Geometric and kinematic analysis of structures in the Lienetz open pit has been conducted in four broadly lithologically homogeneous domains (Figure 5.3B), three of which are highlighted in Figures 5.4 and 5.5.

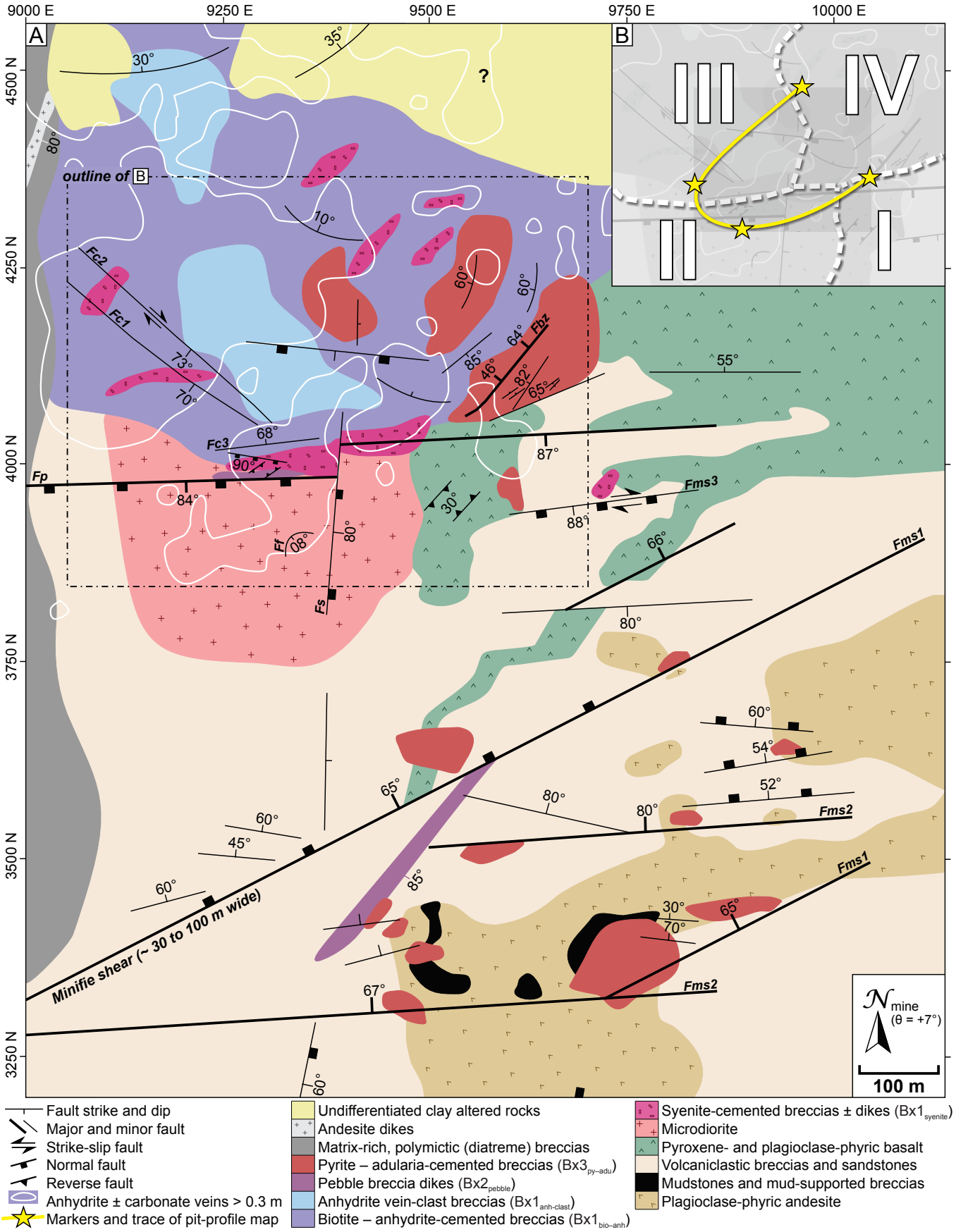

Figure 5.3: Lienetz and Minifie geological plan map with structures and outline of domains. A) Simplified geological map of Lienetz and Minifie orebodies with data projected from ~ 25 m on each side of a −125 m rsl elevation slice. **B)** Insert of the Lienetz open pit showing the four domains analyzed in this study, and the trace and markers (i.e., yellow line and stars) for the pit-profile map of Figures 5.4 and 5.5.

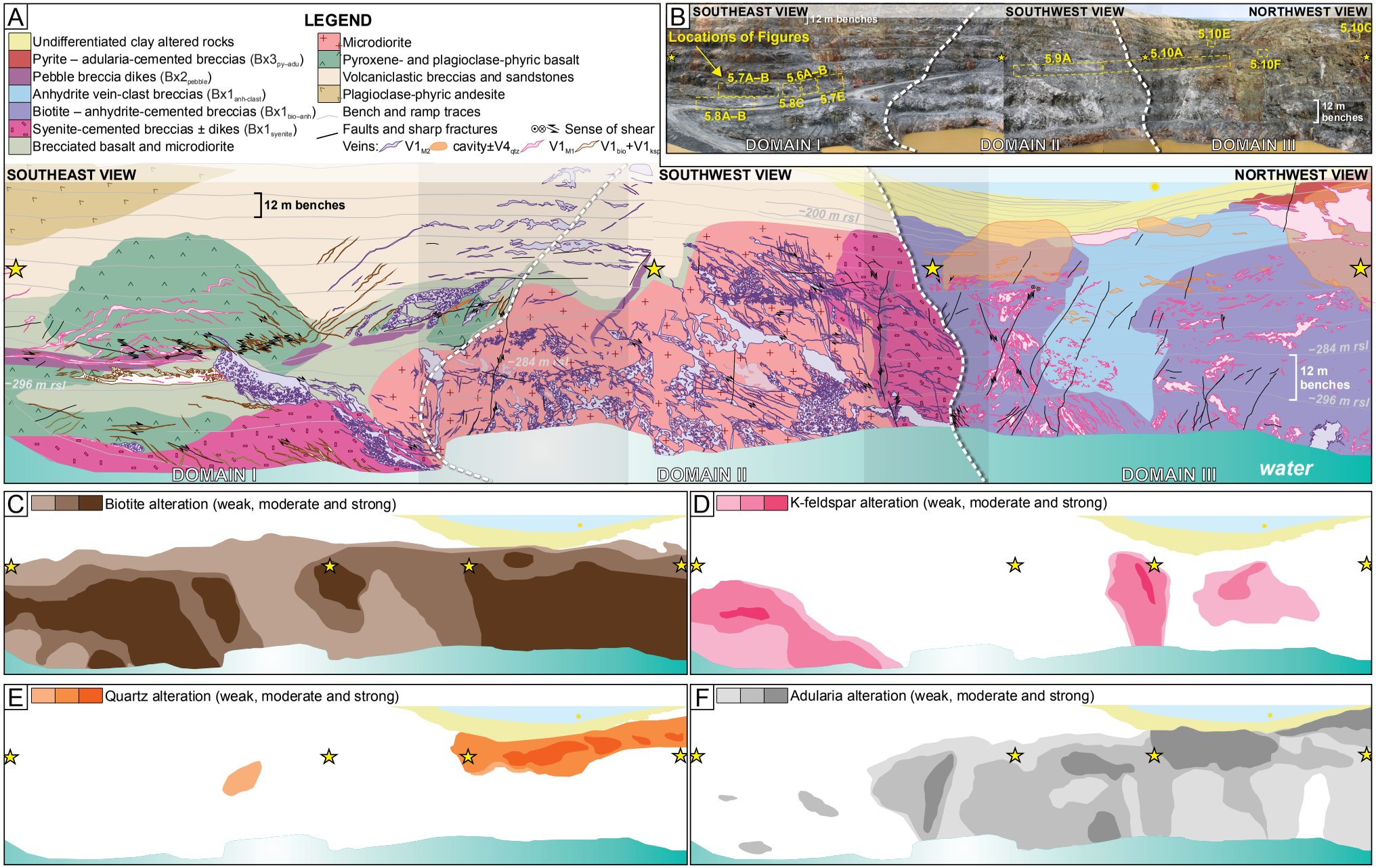

Figure 5.4: Lienetz open-pit profile geological map. A) Unrolled profile the Lienetz open pit with draped geological features. Rock types, veins and structures were compiled from bench mapping and supplemented by spatially referenced photos. Yellow stars are fixed orientation points. White dashes are boundaries to analyzed structural domains (Figure 5.3B). **B)** A ~ 180° photo panorama of the open pit. Yellow boxes indicate locations of figures. **C)** to **F)** Distribution and intensity of hydrothermal alteration of **C)** biotite, **D)** K-feldspar (orthoclase), **E)** quartz and, **F)** adularia.

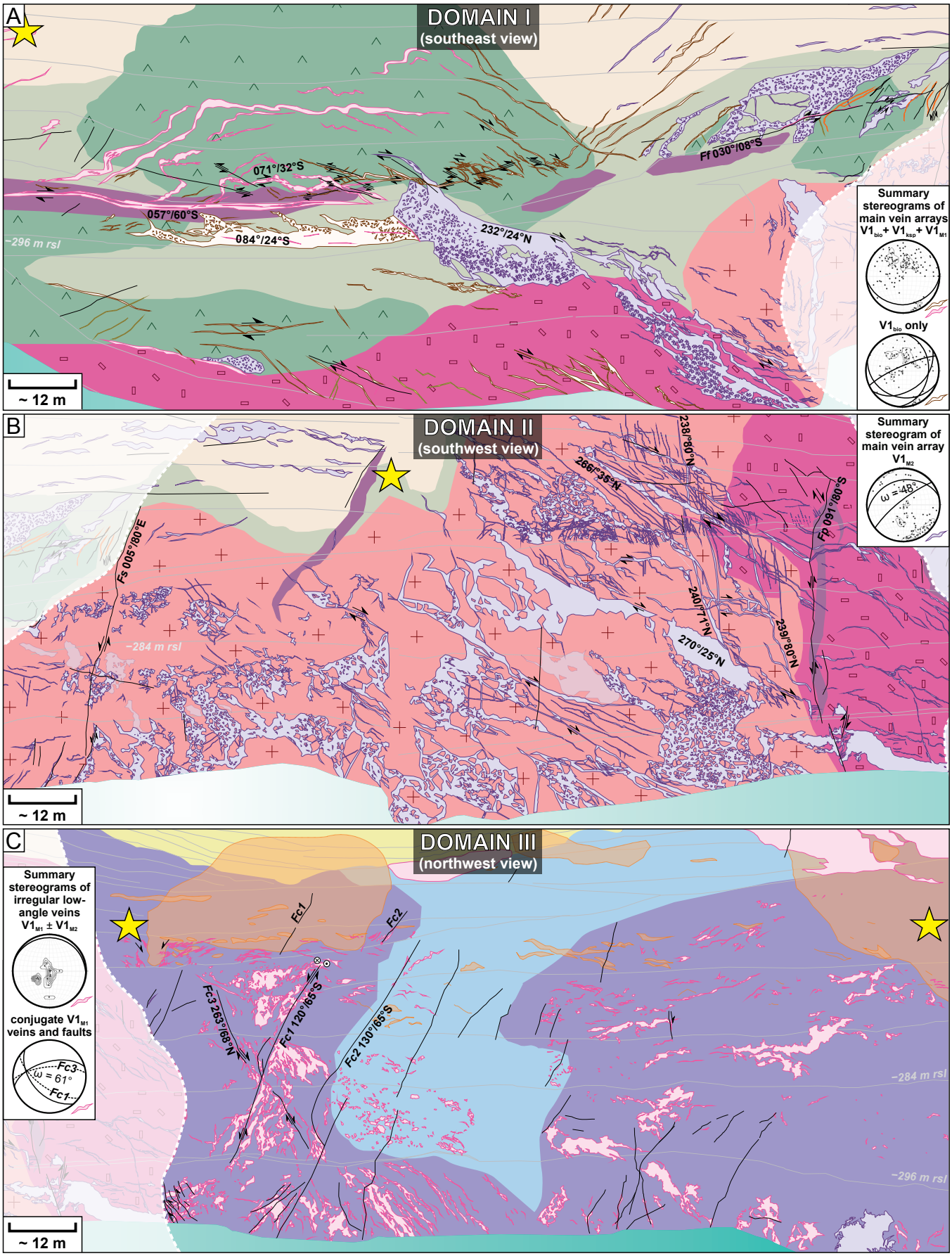

Figure 5.5: Domains of the Lienetz open-pit profile map and summary stereograms. Legend is depicted in Figure 5.4A. All stereograms are equal-area and show the mean plane ± contoured poles. **A)** Domain I, looking to the southeast. Inserts are stereograms of $V1_{bio}$, $V1_{ksp}$ and $V1_{M1}$ veins (i.e, ~ 85% of all veins in domain I; n = 160) showing overall low-angle dips to the south, and stereogram of the relatively unmodified $V1_{bio}$ veins with four geometric clusters (n = 98). **B)** Domain II, looking to the southwest. Insert is stereogram of $V1_{M2}$ veins and breccia veins (n = 117) that represent the majority of veins in domain II, and consist of thick veins with low-angle dips (~ 30°) to the north, linked with a series thinner veins and breccia veins with high-angle dips (~ 70°) to the northwest. Local rhombic forms and dilational jogs containing large breccia veins are also evident. **C)** Domain III, looking northwest. Inserts are stereograms of the majority of veins: $V1_{M1} \pm V1_{M2}$ veins. Veins have with low-angle to sub-horizontal dips (n = 14), however, a subset of veins are related to conjugate faults and have high-angle dips (n = 4).

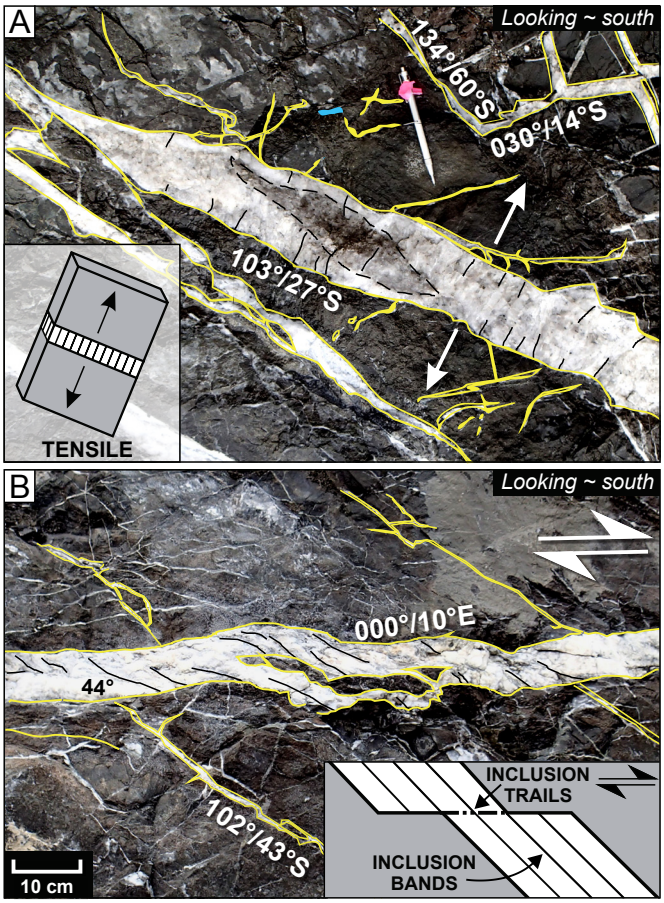

Figure 5.6: Kinematics of $V1_{bio}$ veins in domain I. A) Tensile $V1_{bio}$ vein with low-angle dip (27°) to the south, kinematics evident by anhydrite crystal elongation at high-angles (85°) to the vein-wall rock margin. **B)** Oblique (44°) inclusion bands of sulfides and wall rock fragments, and vein off-sets, indicative of top-block to the west-northwest (i.e., to the right) sense of shear.

5.4.1: Domain I

Domain I, located in the southeast of the Lienetz open pit (Figures 5.3B, 5.4A–B, 5.5A) consists primarily of basalts and volcaniclastic breccias and sandstones. These rock types are cross-cut by faults and $V1_{bio}$, $V1_{chl–epi}$, $V1_{ksp}$, $V1_{M1}$ and $V1_{M2}$ veins (Figures 5.4A, 5.5A).

The majority (~ 85%) of veins in domain I are the earliest stages, $V1_{bio}$, $V1_{ksp} \pm V1_{M1}$, with typical low-angle dips (~ 25°) to the south (Figure 5.5A). However, least modified $V1_{bio}$ veins define four distinct populations with low- to high-angle dips to the southwest, southeast, east and north-northwest (Figure 5.5A). Vein opening modes and kinematic indicators, deduced from blocky anhydrite crystal elongation (Figure 5.6A), inclusion bands, inclusion trails and wall-rock fragments (Figure 5.6B), reveal both tensile and hybrid failure modes, and a general top-block to the west-northwest sense of shear.

A fault array with low-angle dips (~ 5 to 35°) to the southeast and northwest is evident in domain I (Figures 5.5A, 5.7A–C). Along these fault planes, evidence for local drag of $V1_{M1}$ and $V1_{bio}$ veins is apparent (Figure 5.7A–B, D). A conjugate tensile vein array of $V1_{bio}$ is linked to the faults with low-angle dips (Figure 5.7E). Stress conditions deduced from the conjugate fault-tensile vein relationships are consistent with a southeast and/or northwest hanging wall transport direction (Figure 5.7E). The en échelon vein array with local vein drag along fault planes is therefore interpreted to indicate local compression and an approximately sub-horizontal maximum principal stress (σ_1), with top-block up to the southeast and/or northwest sense of shear of the conjugate faults with low-angle dips (Figure 5.7F; e.g., Beach, 1975; Rickard and Rixon, 1983).

A subset of $V1_{M1}$ veins in domain I have moderate-angle dips (~ 50°) to the south with internal modification fabrics, defined by dissolution seams (Figure 5.8A–B). The dissolution seams within these $V1_{M1}$ veins have moderate-angle dips to the south (Figure 5.8B). Initial kinematics are indeterminable for this modified vein set, however, the geometry of veins and dissolution seams implies an oblique σ_1 orientation.

The youngest veins in domain I are thick $V1_{M2}$ veins with low-angle dips (~ 25°) to the northwest (Fig-

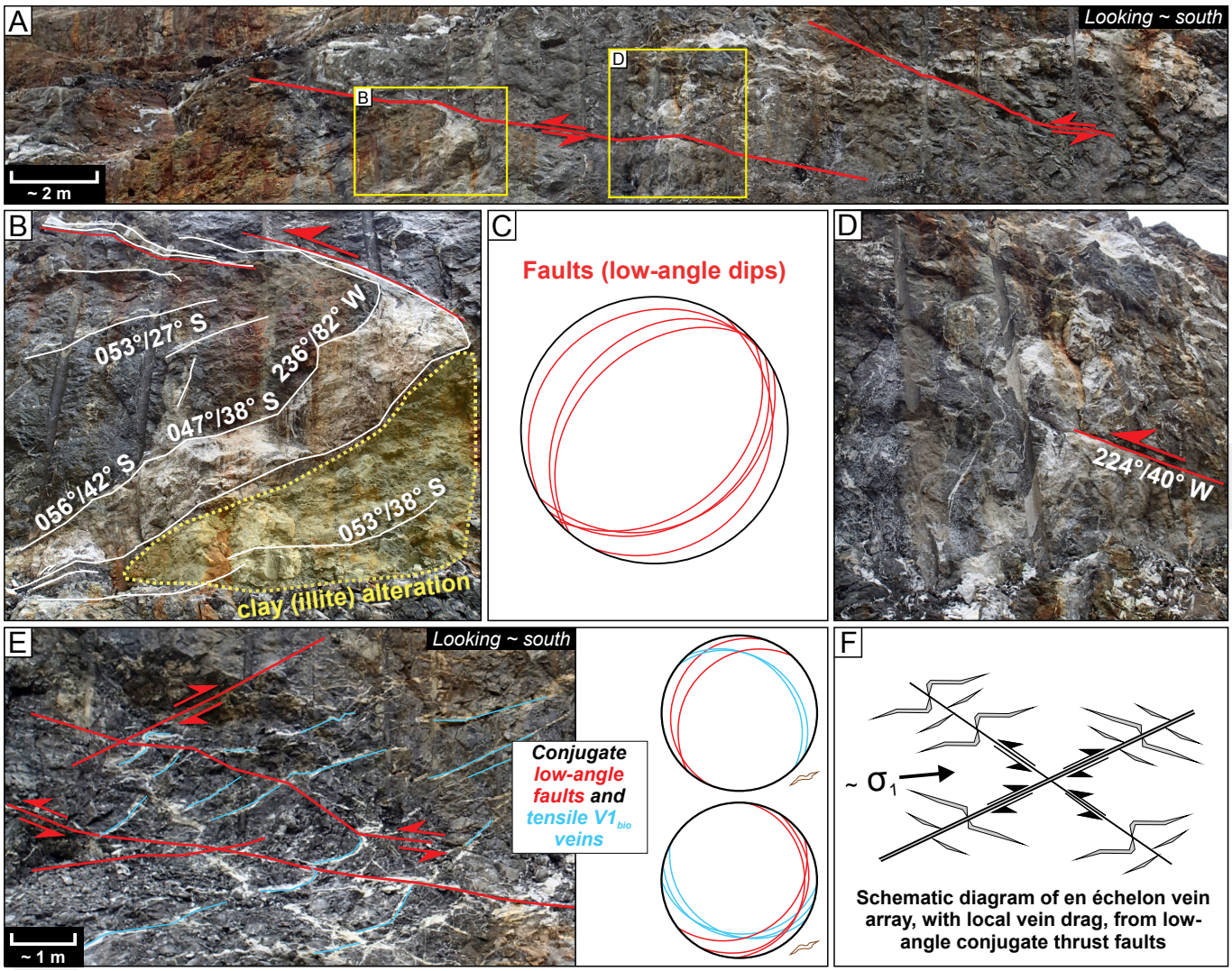

Figure 5.7: Conjugate thrust faults and veins with low-angle dips and vein drag in domain I. A) Bench −272 m rsl, looking approximately south, with large $V1_{M1}$ veins. **B)** Close-up of $V1_{M1}$ vein with moderate-angle dips to the south, showing attenuation and drag along faults with low-angle dips and top-block up to the southeast sense of shear. Vein dip is steeper toward the fault plane, as well as attenuated and less dilatant. **C)** Stereogram of thrust faults with low-angle dips (n = 7). **D)** Thrust fault with low-angle dips to the northwest, with local vein drag. **E)** Conjugate faults and tensile $V1_{bio}$ vein array with low-angle dips. Stereograms represent the fault-tensile vein relationship which is indicative of northwest and/or southeast hanging wall transport. **F)** Schematic diagram of en échelon vein array with local vein drag, from conjugate thrust faults with low-angle dips.

ure 5.8C). $V1_{M2}$ veins have contorted internal textures and are hybrid veins, with a top-block down to the northwest sense of shear (Figure 5.8C). This is in contrast to the neighboring $V1_{bio}$ veins, which are tensile veins with prominent rhombic geometries (Figure 5.8C).

5.4.2: Domain II

Domain II, located in the southwest of the Lienetz open pit (Figures 5.3B, 5.4A–B, 5.5B) consists primarily of a microdiorite intrusion that has brecciated contacts, proximal to faults with high-angle dips. The northern contact of the microdiorite is proximal to a normal fault with a high-angle dip (~ 80°) to the south (i.e., fault Fp on Figures 5.3A, 5.5B). The eastern contact is brecciated, with clasts of basalt units cemented by microdiorite. There is a fault 0 to 30 m from the contact (i.e., fault Fs on Figures 5.3A, 5.5B). The northern contact is highly brecciated, with K-feldspar-altered syenite-cemented breccias ± dikes ($Bx1_{syenite}$;

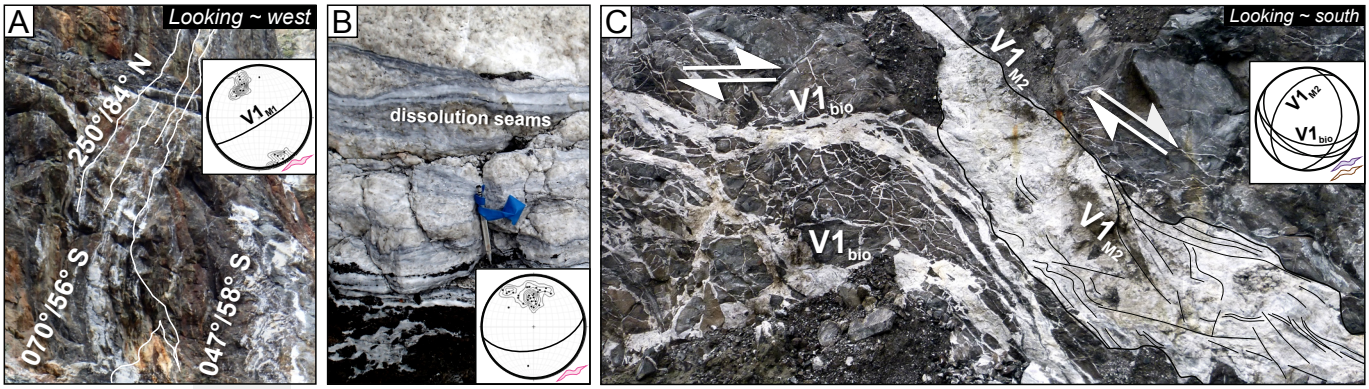

Figure 5.8: South-dipping veins, modification fabrics and late cross-cutting and reactivated vein in domain I. A) $V1_{M1}$ veins with moderate-angle dips to the south, and summary stereogram (n = 37). **B)** Vein stage $V1_{M1}$ modification fabrics, define by dissolution seam, and summary stereogram (n = 38). **C)** $V1_{bio}$ vein with rhombic tensile geometry and top-block to the west (i.e., to the right) sense of shear. $V1_{M2}$ hybrid vein with contorted internal fabrics, low-angle dips to the northwest, and top-block down to the west-northwest sense of shear.

Figures 5.3A, 5.4C, 5.5B). Along the northern contact, the $Bx1_{syenite}$, and a late pebble dike ($Bx2_{pebble}$), have eastward-elongation with high-angle dips, similar to the Fp fault (Figures 5.3A, 5.5B).

The competent and broadly isotropic character of the microdiorite has contributed to the development and preservation of an extensive and systematic anhydrite-bearing vein array, which has experienced little macroscopic-scale modification compared to the anhydrite veins in neighboring breccia-hosted domains (Figure 5.5B). At the macroscopic (open pit) scale, it is evident that the main vein array dominantly consists of thick veins with low-angle dips (~ 30°) to the north, linked with a series of thinner veins and breccia veins with high-angle dips (~ 70°) to the northwest (angular relationship ω = 48°; Figure 5.5B). In local areas, this vein array has rhombic forms, and amplifies to large linking dilational jogs of breccia veins (Figure 5.5B). The variable compositions, geometries and kinematic indicators of veins in domain II are illustrated in detail with the aid of a bench map (Figure 5.9), located along the −260 m rsl bench in domain II (i.e., Figure 5.4B).

Veins in Figure 5.9A account for ~ 40% of the exposed bench face. Most veins have brown biotite alteration halos that range from 1 to 10 cm in width. Evidence of vein reactivation under illite and adularia stable conditions is widespread, with the majority of veins having narrow (~ 3 cm wide) grey adularia alteration halos, ascribed to the $V1_{M2}$ stage.

Earliest vein stages include $V1_{bio}$ with high-angle dips (~ 75°) to the northwest, with lesser-developed $V2_{py}$ veins with high-angle dips (~ 85°) to the south, and $V1_{M1}$ veins with sub-horizontal dips (Figure 5.9B). Later vein stages include the volumetrically dominant $V1_{M2}$ veins and breccia veins (Figure 5.9B). $V1_{M2}$ has two geometric subsets: (1) 1 to 50 cm wide veins and breccia veins with high-angle dips (~ 75°) to the northwest (Figure 5.9A–B); and (2) 20 to 300 cm wide veins and breccia veins with low-angle dips (~ 35°) to the north (Figure 5.9A–B). These $V1_{M2}$ vein sets are interconnected at both macro- and mesoscopic-scales, resulting in a consistent, and probably synchronously developed, rhombic fracture pattern that is evident in

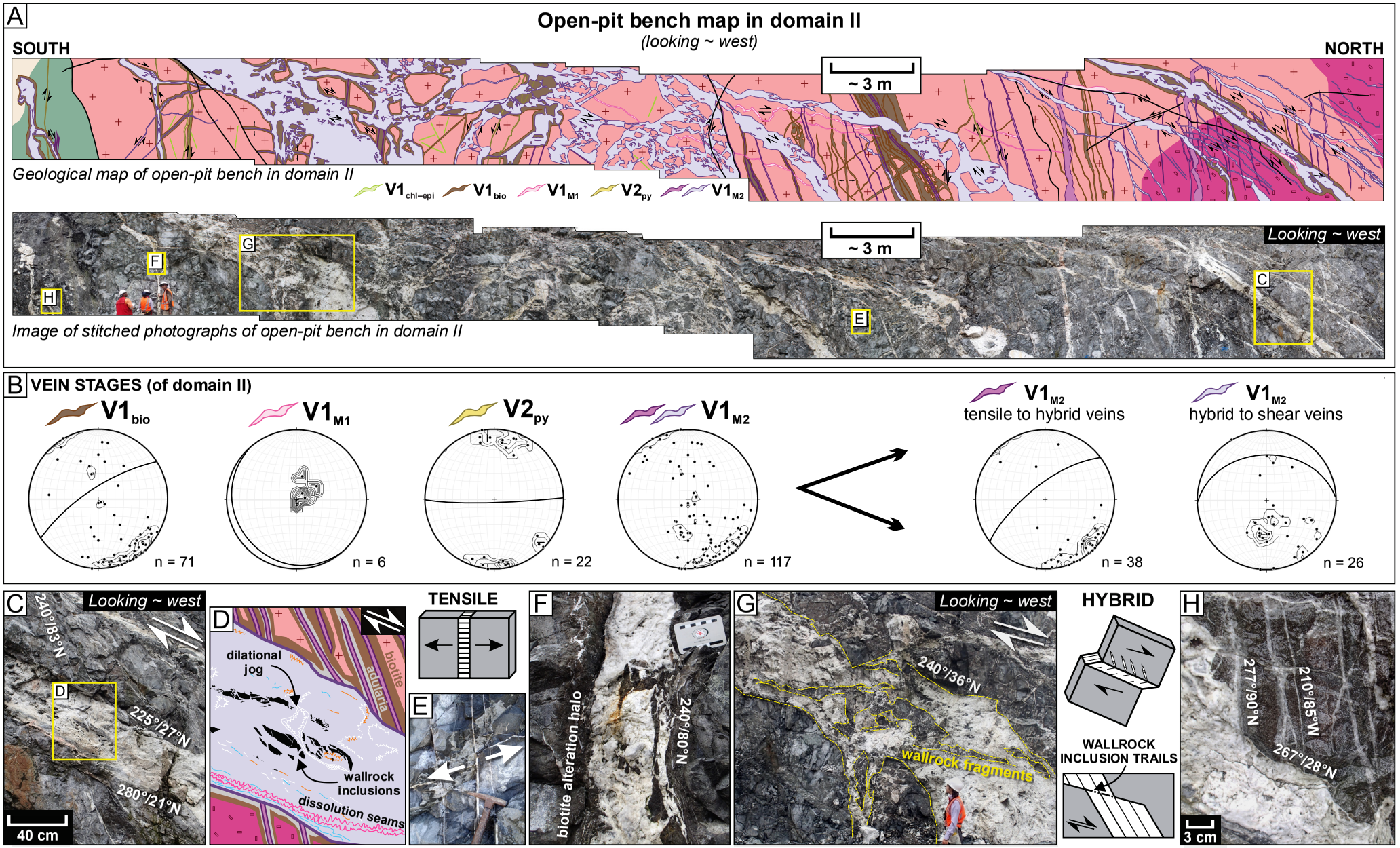
A
Open-pit bench map in domain II
(looking ~ west)
SOUTH
NORTH
~ 3 m
Geological map of open-pit bench in domain II
V1chl–epi
V1bio
V1M1
V2py
V1M2
~ 3 m
Looking ~ west
F
G
H
C
E
Image of stitched photographs of open-pit bench in domain II
B
VEIN STAGES (of domain II)
V1bio
n = 71
V1M1
n = 6
V2py
n = 22
V1M2
n = 117
V1M2
tensile to hybrid veins
n = 38
V1M2
hybrid to shear veins
n = 26
C
Looking ~ west
240°/83°N
D
225°/27°N
280°/21°N
40 cm
D
dilational jog
biotite
actinolite
wallrock inclusions
dissolution seams
TENSILE
E
F
biotite alteration halo
240°/80°N
G
Looking ~ west
240°/36°N
wallrock fragments
HYBRID
WALLROCK INCLUSION TRAILS
H
277°/90°
210°/85°W
267°/28°N
3 cm

Figure 5.9: Bench map with geometries and kinematics of veins in domain II. A) Geological map, and image of stitched photographs, of open-pit bench (−260 m rsl) in domain II. Geometries and kinematics of vein stages are highlighted, with colours corresponding to symbols beside stereograms in (B). Geological map legend is depicted in Figure 5.4A. Yellow boxes on stitched photograph image indicate locations of subsequent figures (C) to (H). **B)** Equal-area stereograms (contoured poles and a mean plane) of veins in domain II, largely represented in the bench map (A). **C)** Multi-stage (i.e., reactivated) $V1_{M2}$ hybrid vein with a low-angle dip to the north. The hanging wall consists of tensile veins with high-angle dips to the northwest. **D)** Annotated example of the reactivated $V1_{M2}$ vein with top-block down to north sense of shear. Vein contains lenticular, dragged wall-rock clasts, anhydrite (thinly bladed)-filled vugs and dilational jogs parallel to the vein strike, as well as dissolution seams near the lower vein-wall rock contact. Broader outer biotite (brown) alteration halos have been overprinted by narrower adularia (grey) alteration halos. **E)** $V1_{bio}$ veins with high-angle dips and biotite alteration halos. A subset of $V1_{bio}$ veins have little internal modification and are indicative of tensile failure modes. **F)** $V1_{M2}$ tensile to hybrid vein with broad biotite alteration halo and high-angle dip to the north. Within vein are plucked and rotated lenticular wall rock fragments. **G)** Large $V1_{M2}$ hybrid to shear breccia vein with dragged-out wall rock inclusions, indicative of top-block down to north-northwest sense of shear. **H)** Array of $V1_{M2}$ tensile veins in the hanging wall of a $V1_{M2}$ hybrid vein with a low-angle dip to the north, indicative of a synchronous relationship and top-block down to the north sense of shear.

Figure 5.5B. In the northern half of the bench map (Figure 5.9A), low-angle $V1_{M2}$ veins have locally overprinted and cross-cut $V1_{M2}$ and $V1_{bio}$ vein sets with high-angle dips, indicating preferential reactivation of the veins with low-angle dips (Figure 5.9A).

The dominant vein stage (i.e., $V1_{M2}$) in domain II preserves evidence of complex multi-stage reactivation histories (Figures 5.5B, 5.9A). As such, kinematic indicators for early vein formation have been obscured by overprinting and modification events. This is exemplified by the complex $V1_{M2}$ vein in Figure 5.9C–D. This vein formed initially as a $V1_{bio}$ (evident by outer biotite alteration halos), and then experienced some modification, producing dissolution seams similar to those in $V1_{M1}$. Subsequent $V1_{M2}$ reactivation is evidenced by inner adularia and illite alteration halos, and vein infill of calcite – quartz – anhydrite (thinly bladed; Figure 5.9D).

Although this complex history of multi-stage vein reactivation is dominant, some sparsely preserved examples of original crystal elongations in the earliest $V1_{bio}$ veins with high-angle dips (~ 80°) to the northwest indicate a tensile failure mode under an approximately sub-vertical σ_1 (Figure 5.9E). The $V1_{M1}$ veins locally contain sub-horizontal dissolution seams, and in areas, low-amplitude stylolites, indicating a flattening fabric parallel to the dominantly sub-horizontal boundaries of the veins, possibly indicative of a sub-vertical σ_1. $V1_{M2}$ veins and breccia veins, have intricate internal fabrics (e.g., Figure 5.9D). The arrangement of wall rock inclusions becomes progressively more complex from the margins to the centers of veins. Clasts located near the vein-wall rock contact typically have a crackle to mosaic arrangement, with fragments elongated sub-parallel to the vein margins, whereas inclusions within the central parts exhibit evidence for rotation (Figure 5.9F). $V1_{M2}$ veins with low-angle dips contain large, lenticular, locally spalled out and sheared wall rock fragments which occur at oblique angles to the wall rock margin (Figure 5.9D, G). Veins also locally contain internal rhombic dilational jogs, filled with thinly bladed anhydrite, that parallel the vein's strike (Figure 5.9D). These configurations are interpreted to indicate that the veins are not simply tensile fractures, but record variable components of shear, and as such are interpreted to be hybrid to shear veins (Figure 5.9B; e.g., Cox, 1987; Fowler, 1996; Jébrak, 1997). Kinematic indicators, coupled with an

association of thin, planar, steeply northwest-dipping tensile veins projecting from the margins of the low angle sets (Figure 5.9D, H), are interpreted to indicate top-block down to the northwest sense of shear. The $V1_{M2}$ veins with high-angle dips contain similar hybrid features. Some $V1_{M2}$ veins have crystal elongations perpendicular to the wall-rock margins and less shear fabrics than the $V1_{M2}$ veins with low-angle dips, indicating a more tensile to hybrid failure mode for the steeply dipping vein set (Figure 5.9B). The relationship of both hybrid to shear failure modes of $V1_{M2}$ vein with low-angle dips, and tensile to hybrid failure modes of $V1_{M2}$ veins with high-angle dips, are consistent σ_1 oriented sub-vertically (Figure 5.9B).

5.4.3: Domain III

Domain III, located in the northwest of the Lienetz open pit (Figures 5.3B, 5.4A–B, 5.5C) consists primarily of $Bx1_{bio–anh}$ and $Bx1_{anh\text{-}clast}$ breccias. Veins in domain III are not as well-developed as in the neighboring domains (I and II). Many veins have irregular and/or discontinuous boundaries (Figures 5.5C, 5.10A). Most veins in domain III belong to stages $V1_{M1}$ or $V4_{qtz}$ (Figure 5.5C).

The first geometrically distinct set of veins in domain III is an array of $V1_{M1}$ veins, ~ 2 to 5 m thick, with moderate-angle dips (~ 55°) to the north and southwest (Figure 5.5C). They have been partly offset and attenuated by conjugate faults with high-angle dips to the north and south ($\omega = 61°$; Figure 5.5C). Although there are no measurable kinematic indicators for this vein set, the observed geometric relationships are consistent with a conjugate normal hybrid vein array that would have formed under a sub-vertical σ_1 (e.g., Rickard and Rixon, 1983; Sibson, 1996; Belayneh and Cosgrove, 2010).

The second geometrically distinct set is 1 to 30 m thick $V1_{M1}$ veins with sub-horizontal dips, located largely in the northern and upper levels (i.e., above −240 m rsl) of domain III (Figures 5.5C, 5.10B–C). $V1_{M2}$ veins are also locally present in these upper levels of domain III (Figure 5.10D), where they appear to have overprinted and/or reopened the $V1_{M1}$ veins. While most of these veins were outside of the open-pit mapping area, the distinctive textural characteristics of $V1_{M1}$, and to a lesser extent $V1_{M2}$, allowed these veins to be readily identified in drill-core photographs (e.g., Figure 5.10C–D). Analysis of ~ 150 drillholes within the Lienetz orebody indicates a fairly restricted distribution of $V1_{M1} \pm V1_{M2}$ veins in the upper northwest section. The modeled continuous shells of these veins have sub-horizontal to low-angle dips (~ 15°) to the north (Figures 5.5C, 5.10B). This is similar to the dips of $V1_{M1}$ veins located on the −260 m rsl bench in domain III (Figure 5.10A–B).

The $V1_{M1}$ with sub-horizontal dips have moderate- to well-developed stylolites, also with sub-horizontal to low-angle dips (Figure 5.10B–C). The stylolites are separated by recrystallized anhydrite ± celestine ± barite (e.g., Figure 4.5). In veins where stylolites are not well-developed, larger wall-rock fragments exhibit serrated, irregular and corroded boundaries that are locally bounded by dissolution seams, and have asym-

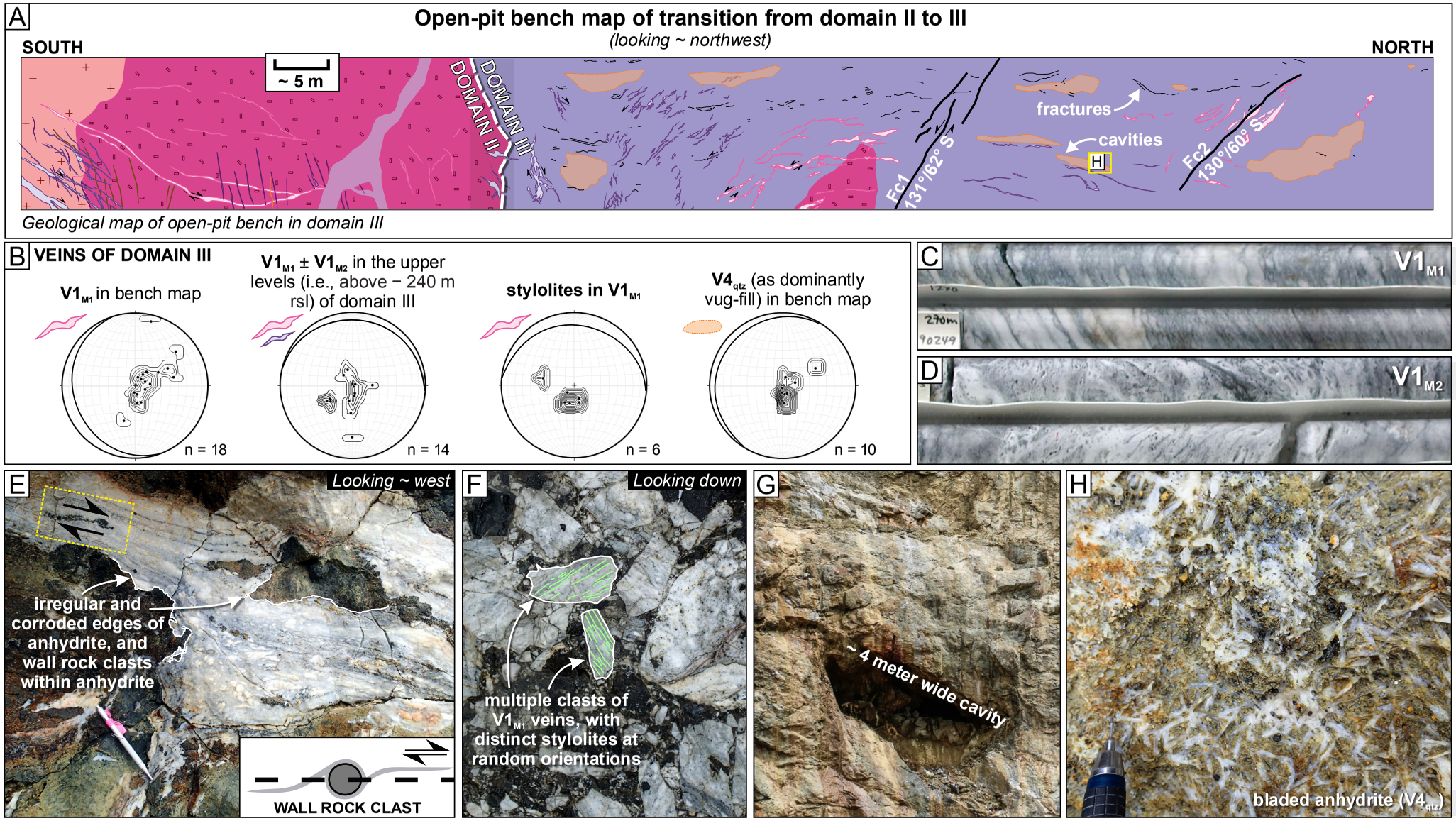
A
Open-pit bench map of transition from domain II to III
(looking ~ northwest)
SOUTH
NORTH
~ 5 m
DOMAIN II
DOMAIN III
fractures
cavities
H
Fc1
131°/62° S
Fc2
130°/60° S
Geological map of open-pit bench in domain III
B
VEINS OF DOMAIN III
V1M1 in bench map
n = 18
V1M1 ± V1M2 in the upper levels (i.e., above − 240 m rsl) of domain III
n = 14
stylolites in V1M1
n = 6
V4qtz (as dominantly vug-fill) in bench map
n = 10
C
V1M1
D
V1M2
E
Looking ~ west
irregular and corroded edges of anhydrite, and wall rock clasts within anhydrite
WALL ROCK CLAST
F
Looking down
multiple clasts of V1M1 veins, with distinct stylolites at random orientations
G
~ 4 meter wide cavity
H
bladed anhydrite (V4qtz)

Figure 5.10: Bench map of transition from domain II to III, with geometries, kinematics and photographs of veins in domain III. A) Geological map of open-pit bench (−248 m rsl) at the transition from domain II to III. Geometries and kinematics of vein stages are highlighted, with colours corresponding to symbols beside stereograms in (B). Geological map legend is depicted in Figure 5.4A. Yellow boxes indicate locations of (H). Locations of (E) to (G) are shown in Figure 5.4B. **B)** Equal-area stereograms (contoured poles and a mean plane) of dominant veins in domain III. **C)** Photograph of $V1_{M1}$ vein in drill core, exhibiting dissolution seams and stylolites with low-angle dips (i.e., < 30° from horizontal), all within massive recrystallized anhydrite (from 270 m in drillhole DDHL0771, azimuth 180°, dip 71°). **D)** Photograph of $V1_{M2}$ vein in drill core, exhibiting low- to moderate-angle (< 50° from horizontal) contorted cockade calcite – anhydrite – quartz ± adularia bands (from 210 m in drillhole DDHL1169, azimuth 183°, dip 67°). **E)** Example of a $V1_{M1}$ vein in outcrop, with irregular and corroded edges at the vein-wall rock contact, as well as around wall-rock clasts within the vein. Dissolution seams and asymmetrical textures are similar to shear-related porphyroclasts systems, indicative here of a top-block down to the north sense of shear. **F)** Photograph of outcrop of anhydrite vein-clast breccia ($Bx1_{anh\text{-}clast}$) with randomly oriented clasts of $V1_{M1}$ anhydrite veins with stylolites. **G)** Photograph of a large open-space cavities (bench −224 m rsl; e.g., Figure 5.4B). **H)** Vug-fill of quartz – pyrite – anhydrite (thickly bladed), belonging to the $V4_{qtz}$ stage, in an area proximal to abundant open-space cavities (e.g., Figure 5.4B).

metrical textures similar to shear-related porphyroclasts (Figure 5.10E). These features imply that some dissolution and strain localization occurred during vein modification. Stylolites and syn-modification shear sense is consistent with mostly sub-vertical σ_1 ± top-block down to the north sense of shear. At deeper levels in the open pit (i.e., below −250 m rsl), the stylolitic $V1_{M1}$ veins occur as randomly oriented clasts, in the anhydrite vein-clast breccia (i.e., $Bx1_{anh\text{-}clast}$; Figures 5.5C, 5.10F).

This is an anhydrite-poor sub-horizontal area with flat-lying cavities and $V4_{qtz}$ veins in the upper-levels of the Lienetz open pit (Figure 5.5C). The open-space cavities are large (i.e., ~ 4 m wide, Figure 5.10G), and locally contain $V4_{qtz}$ vein minerals (i.e., anhydrite (thickly bladed) – quartz – pyrite) as partial vug-fill (Figure 5.10H), and are spatially associated with strong quartz ± adularia alteration (Figure 5.4E–F). Similar cavities are ubiquitous above most preserved intervals of $V1_{M1}$ veins in drill core (e.g., Figure 4.4A). This indicates that the irregular $V4_{qtz}$ vug-fill are spatially, and temporally, related to areas where partial dissolution of $V1_{M1}$ veins and breccia veins had occurred.

5.4.4: Domain IV

Domain IV, located in the northeast corner of the open pit (Figure 5.3B), consists primarily of $Bx3_{py\text{–}adu}$ breccias (Figure 5.11A–B). $Bx3_{py\text{–}adu}$ breccias correspond compositionally and temporally to $V3_{adu}$ veins and breccia veins (e.g., Figure 4.2). The lower extents of $Bx3_{py\text{–}adu}$ breccia/$V3_{adu}$ veins and breccia veins are apparently bounded by faults that have sharp contacts with the $Bx1_{bio\text{–}anh}$ (Figure 5.11A). Faults in domain IV have moderate-angle dips (~ 65°) to the northwest (Figure 5.11A). Some faults have minor listric splays, while some of the larger faults flare upward to undetermined extents (Figure 5.11A).

5.5: Spatial relationships between structures and mineralization at Lienetz

Gold grades vary significantly with vein stages and breccias facies (e.g., Table 4.2). In order to evaluate structural controls of grade distribution, gold assay composites (i.e., a blend gold fire assay values

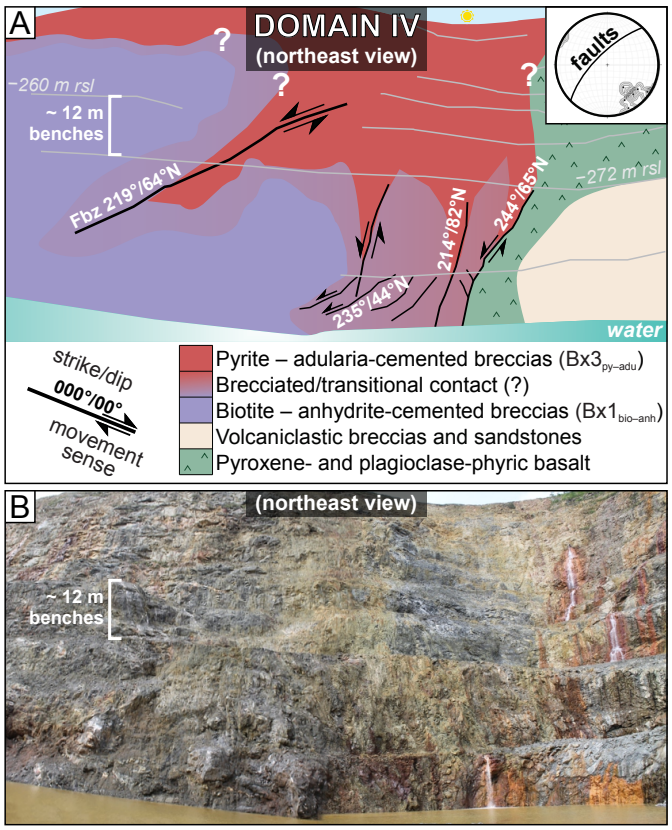

Figure 5.11: Bench map of northeast corner in domain IV. A) Geological map and, **B)** image of stitched photographs, of domain IV. Faults have moderate- to high-angle dips to the northwest, and are summarized in an equal-area stereogram with a mean plan (n = 8). $Bx3_{py–adu}$ breccias correspond compositionally and temporally to the $V3_{adu}$ veins and breccia veins. Uncertainty increases in the upper-levels due to inaccessible mapping areas and poor exposures on open-pit benches.

from 10 m intervals of bench-face blast holes, and 2 m intervals of surface-collared drillholes), were compiled into polygons and projected onto domain II and III's open-pit exposures (Figure 5.12A). Macroscopic patterns were examined in order to assess geometrical relationships and spatial distributions of high-grade gold across both Lienetz and Minifie (Figure 5.12B, D). A number of discrete, ellipsoidal high-grade (> 1.5 g/t Au) isosurfaces were defined geometrically in Leapfrog™ (i.e., Figure 5.12B, D). The geometries (i.e., strikes and dips) of ellipsoidal isosurfaces were then extracted to be represented via stereograms, as shown in Figure 5.12C. Of these, four ellipsoidal isosurfaces were defined: (1) two tabular ellipsoidal isosurfaces with high-angle dips and prominent east-northeast and northeast strikes (i.e., Au1 and Au2; Figure 5.12C); and (2) two broader ellipsoidal isosurfaces with low-angle dips (i.e., Au3 and Au4; Figure 5.12C).

Moderate gold-grades (~ 0.8 to 1.5 g/t Au) characterize most of breccia-hosted domains III and IV. The basalt- and microdiorite-hosted domains I and II have lower average grades (~ 0.1 to 0.8 g/t Au), implying that porosity and permeability of host rocks influenced gold grades at Lienetz (Figure 5.12A, D).

High-grade gold (i.e., > 1.5 g/t Au) within Lienetz has several structural controls. In domain II there is a strong correlation of 1.5 to 3.0 g/t Au and 3.0 to 5.0 g/t Au polygons with the $V1_{M2}$ vein array (Figure 5.12A). In particular, the northeast-striking, tensile to hybrid $V1_{M2}$ with high-angle dips to the northwest, and the dilational jogs of breccia veins, control gold distribution within this more competent domain (Figure 5.12A). This is notable near the boundary of domains II and III, as well as the steeply dipping, east-northeast-striking Fp fault (Figure 5.12A). On the macroscopic scale this high-grade zone corresponds spatially and geometrically with Au1 and Au2 ellipsoidal isosurfaces (i.e., Figure 5.12B–D). The east-northeast-striking, steeply dipping ellipsoids that comprise Au1 project across, and are apparent on multiple levels, in the Lienetz and Minifie open pits (Figure 5.12B, D). One of the Au1 ellipsoids corresponds to the Minifie shear zone (Figure 5.12D). Northeast-striking Au2 ellipsoids are more prominent in domain IV (Figure 5.12B, D). Au2 correlates with northeast-striking, moderately to steeply dipping faults that controlled the distribution of $V3_{adu}$ veins and breccia veins and $Bx3_{py–adu}$ breccias in the deeper levels of Lienetz (e.g., Figure 5.11).

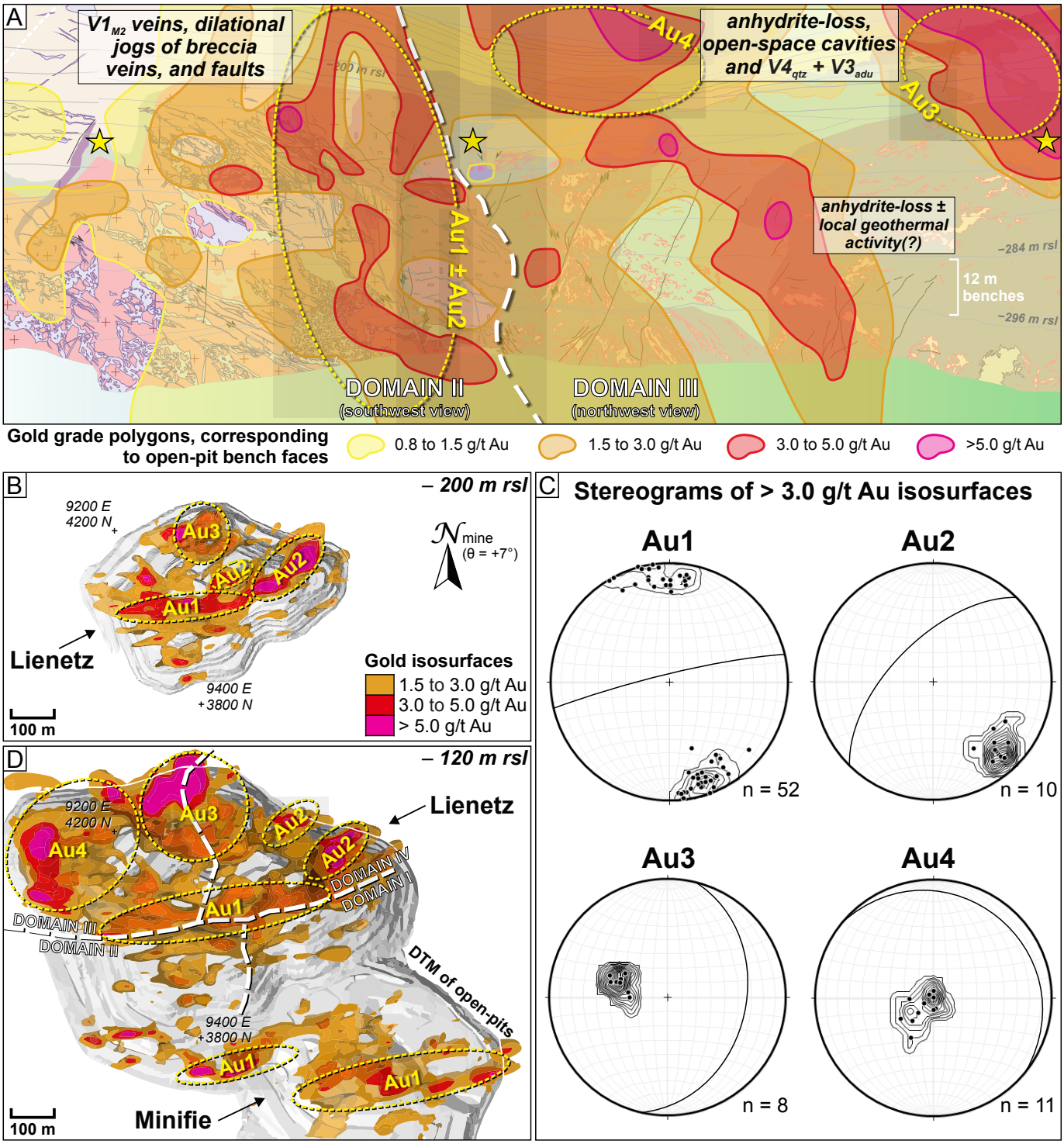

Figure 5.12: High-grade gold distribution in Lienetz and Minifie. A) Open-pit profile map of domain II and III (i.e., Figure 5.5), with projected polygons of 0.8 to 1.5 g/t Au, 1.5 to 3.0 g/t Au, 3.0 to 5.0 g/t Au and > 5.0 g/t Au, from composite 10 m blast-hole Au assays obtained along benches from current mining. **B)** Plan map of −200 m rsl elevation slice with high-grade gold ellipsoidal isosurfaces projected on slice. Light grey background is digital terrain model (DTM) of the open pits. **C)** Equal-area stereograms (contoured poles and a mean plane) representing the four geometrically distinct high-grade gold ellipsoidal isosurfaces: Au1, Au2, Au3 and Au4. **D)** Same map at (B) but on a −120 m rsl elevation slice. Dashed yellow circles in (A), (B) and (D) outline the spatial distribution of the four distinct high-grade gold ellipsoidal isosurfaces Au1 to Au4.

In domain III, high-grade 3.0 to 5.0 g/t Au and > 5.0 g/t Au polygons correlate with the anhydrite-poor, broadly sub-horizontal area with flat-lying cavities (Figure 5.12A). They also correlated with $V4_{qtz} \pm V3_{adu}$ irregular veins and vug-fill that are in upper-levels of $Bx1_{bio–anh}$ and $Bx1_{anh-clast}$ breccias (Figure 5.12A). At the macroscopic scale, these high-grade polygons correspond spatially and geometrically with the Au3 and Au4 ellipsoidal isosurfaces (Figure 5.12B–D). The high-grade Au3 and Au4 isosurfaces have low-angle to

sub-horizontal dips, and are more laterally continuous in the upper levels (i.e., above −120 m rsl) of Lienetz (Figure 5.12C). As such, these broad ellipsoid isosurfaces most likely relate to $Bx3_{py–adu}$, which crops out above the mapped area (e.g., Figures 4.7, 4.8).

There is a local area containing 1.5 to 5.0 g/t Au in domain III (Figure 5.12A). This high-grade area is interpreted to relate to a more permeable area at the contact of the $Bx1_{anh\text{-}clast}$. It is an area that lacks anhydrite veins and vein-clasts. There are, however, multiple small fractures, along which recent geothermal activity has caused jarosite staining (Figure 5.12A).

5.6: Discussion

Structural mapping in the Lienetz orebody has revealed multiple stages of veins, together with evidence for structural controls of their emplacement. Many veins were reactivated, but with grossly similar geometries and kinematic histories. Overall, sets of veins record a history of early compression and protracted, or multistage, northwest-directed extension, with predominant east-northeast and northeast strikes for both veins and faults (Figure 5.13A). The best kinematic and geometric relationships of veins and breccia veins are preserved within the lithologically competent domains I and II, whereas domains III and IV had poorer preservation of kinematic and geometric relationships, partly due to the less competent nature of the host breccias and the considerable amount of anhydrite dissolution.

5.6.1: Initial vein formation, geometries and kinematics

V1 stage veins formed under porphyry-style conditions, based predominantly on high-temperature minerals (e.g., Figure 4.2). They have both high- and low-angle dips throughout all domains (Figure 5.13A). Kinematic indicators of the least-modified $V1_{bio} \pm V1_{ksp}$ tensile vein arrays in domains I and II provide evidence of early northwest and/or southeast-directed compression (Figure 5.13A–B). Evidence for early extension in the form of top-block to the west-northwest displacement is also apparent (Figure 5.13A–C). These early tensile vein arrays, with both sub-vertical and sub-horizontal dips, are compositionally and temporally similar. The vein geometries and kinematic indicators are therefore consistent with formation under a dynamic stress regime where σ_1 was oscillating between sub-vertical and sub-horizontal (Figure 5.13A–C).

5.6.2: Vein modification, dissolution, solution collapse and block rotation

Early V1 porphyry-style veins underwent partial dissolution and recrystallization in all domains, but particularly in domain III (Figure 5.13D). Dissolution fabrics are typically oriented sub-horizontally, par-

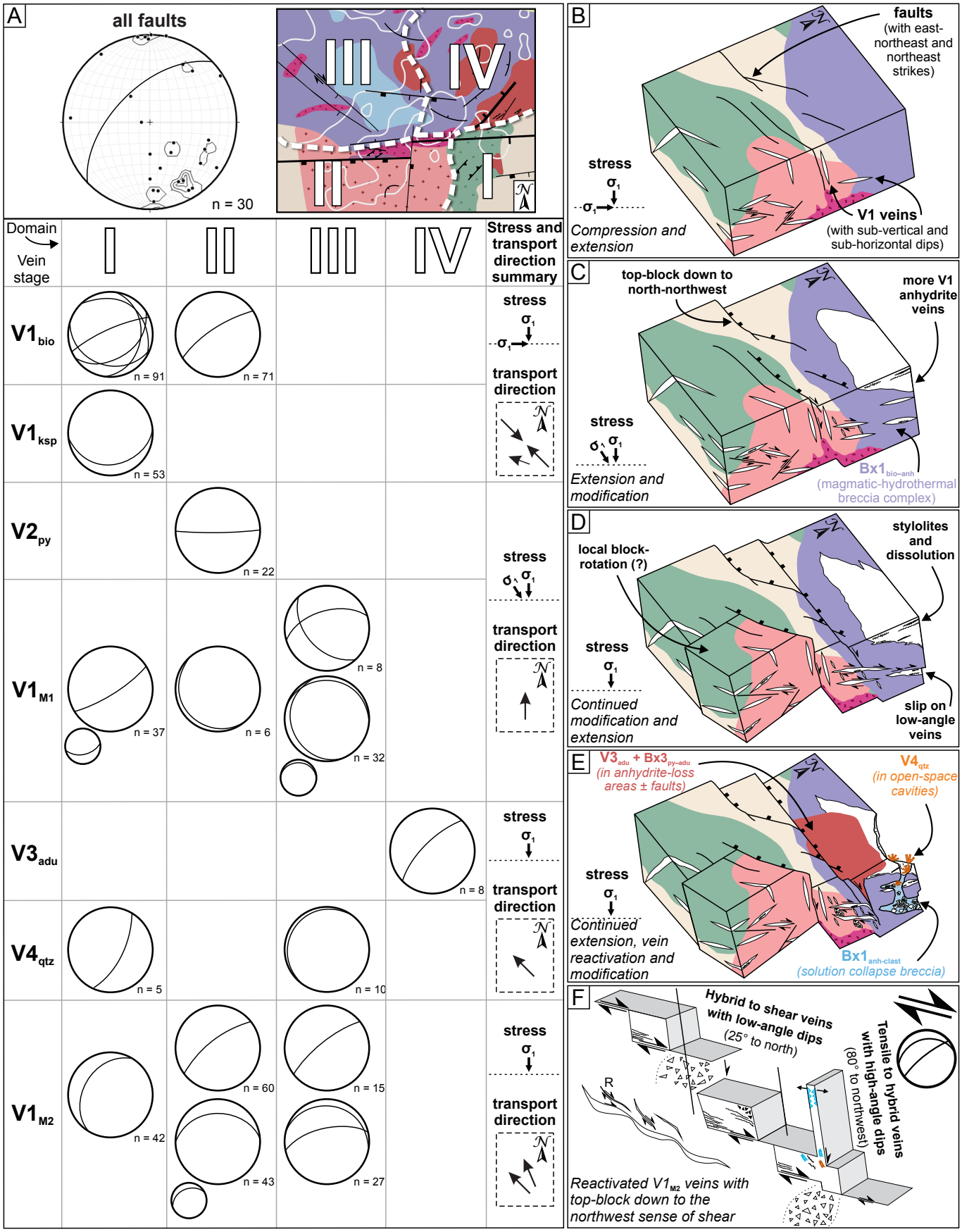

Figure 5.13: Structural evolution of Lienetz, with summary stereograms, stresses, transport directions and schematic block diagrams. A) Stereogram of all major faults within Lienetz ± Minifie, insert of plan map showing domains I to IV (i.e., Figure 5.3B), and table with summary stereograms of vein stages, summary stress (σ_1) and transport directions for each structural domain. All stereograms are equal-area with a mean plane, and small companion stereograms represent modification fabrics in veins. Summary σ_1 is shown relative to the Earth's surface (dashed black line), and summary transport direction is shown in plan-view looking down at the Earth's surface. **B)** to **E)** Schematic block diagrams of the structural evolution of the anhydrite zone in Lienetz. See text for details. **F)** Schematic diagram of reactivated $V1_{M2}$ veins with top-block down to the northwest sense of shear along a system of interconnected veins. Shear related dilation of some veins created irregular to rhombic voids and jogs. Preferential slip on veins with low-angle dips was combined with mineral sealing, leading to variable elevated fluid pressures, further promoting slip on misoriented fractures and resulting in tensile veins and breccia veins, locally within dilational jogs.

allel to the vein-wall rock boundary, except in domain I where they have moderate-angle dips to the south within a subset of southward-dipping $V1_{M1}$ veins (Figure 5.13A). In domain III, the moderately north- and southwest-dipping conjugate $V1_{M1}$ hybrid veins, and sub-horizontal stylolites in $V1_{M1}$ are consistent with conditions where σ_1 was, at least temporarily, sub-vertical (Figure 5.13A, C). Shear-related modification fabrics of $V1_{M1}$ within domain III indicate top-block down to the north transport (Figure 5.13A, C). During $V1_{M1}$ modification, local block rotation occurred in domain I, with back rotation to the south-southeast (Figure 5.13D). Continued anhydrite dissolution occurred in domains III and IV leading to the formation of solution collapse breccias ($Bx1_{anh\text{-}clast}$; Figure 5.13E). Local block rotation in domain I can explain the $V1_{M1}$ veins that have the same sense of shear as veins with low-angle dips in other domains, but with different dip directions (Figure 5.13A, D). Solution collapse brecciation can explain the randomly oriented $V1_{M1}$ anhydrite vein-clasts with stylolites, which were mapped in situ in the upper-levels with dominantly sub-horizontal orientations (Figure 5.13A, E).

5.6.3: Epithermal-style gold and faults

$V3_{adu}$ and $V4_{qtz}$ veins, breccia veins and vug-fill are interpreted to have formed under epithermal conditions (e.g., Figure 4.2). They are common in the upper levels of the $Bx1_{bio–anh}$. They also occur in the lower levels of $Bx1_{bio–anh}$ along northeast and east-northeast-striking faults with moderate- to high-angle dips (Figure 5.13E). Anhydrite dissolution led to solution collapse and formed open-space cavities and sub-horizontal, highly permeable and porous zones (Figure 5.13E). These provided conduits for auriferous hydrothermal fluids that partly sealed areas and deposited $V3_{adu}$ and $V4_{qtz}$, with high to bonanza gold grades (Figure 5.13E). These events occurred under a regime of northwest-directed extension with σ_1 dominantly sub-vertical (Figure 5.13A, E).

5.6.4: Late-stage vein reactivation and modification

Many veins, particularly those with low-angle dips to the north, were preferentially reactivated and modified during $V1_{M2}$. Kinematic indicators in $V1_{M2}$ veins provide evidence for continued northwest to north-northwest-directed extension (Figure 5.13E–F). This is illustrated by the two geometric subsets of $V1_{M2}$ veins and breccia veins: (1) tensile to hybrid veins and breccia veins with high-angle dips to the northwest; and (2) hybrid to shear veins and breccia veins with low-angle dips to the north (Figure 5.13F). The $V1_{M2}$ vein array records protracted or multistage extension and top-block down to the northwest to north-northwest sense of shear along a system of interconnected veins with low-angle dips to the north (Figure 5.13A, F). Shear-related preferential slip and dilation of veins with low-angle dips, combined with sealing by anhydrite ± carbonate, created irregular to rhombic voids and dilational jogs. This allowed influx

of late-stage epithermal-style fluids along V1 veins, which produced crustiform and cockade bands of calcite – quartz ± adularia ± anhydrite (thinly bladed), and linking steeply dipping breccia vein arrays, all with variable localized high-grade gold (Figure 5.13F).

With the transition to an epithermal environment, a hydrostatically pressured regime was most likely dominant. This would explain the reactivation and modification of $V1_{M2}$ veins, as these pre-existing structures would have strongly influenced hydrothermal fluid flow (Figure 5.13F).

5.6.5: Pressure conditions during vein development

Fluid movements were controlled by pressure gradients and permeability pathways. In the epithermal environment fluid pressures can vary from hydrostatic to lithostatic, but dominantly are hydrodynamic (i.e., 10% to 40% greater than hydrostatic; Hedenquist and Henley, 1985). In porphyry-style environments fluid pressures are typically near-lithostatic, which aids in the formation of abundant stockwork veins (Fournier, 1999).

Constraints on pressures and depths of vein formation at Lienetz can be estimated, given the well-preserved volcanic setting in which the veins reside, and the fact that most of the anhydrite veins formed in a porphyry-style environment. An approximate age of initial porphyry-style alteration is ~ 0.9 Ma (Table 3.1; Davies and Ballantyne, 1987), and only gentle uplift has occurred along the Tabar-Lihir-Tanga-Feni island chain over the past ~ 1 m.y. (Wallace et al., 1983). Anhydrite ± carbonate veins within the Lienetz orebody occur from −50 to depths greater than −350 m rsl. They potentially formed approximately 1150 to 1450 m below the original ~ 1100 m volcanic cone, a height determined by extrapolating the dip of the amphitheater walls and assuming a symmetrical cone shape (Wallace et al., 1983; Blackwell, 2010). V1 veins are interpreted to have formed prior to sector collapse, as they have porphyry-style alteration halos and a close spatial and temporal associated with magmatic-hydrothermal breccias and dikes. The lithostatic (P_l) and/or hydrostatic (P_h) pressures at the depth of formation (h) can therefore be roughly estimated assuming the volume of a cone (V), area of a circle (πr^2) and density (ρ) of andesite rock and water, via equation 5.1:

$$P = F/A = \rho g V/\pi r^2 = \rho g h/3 \quad (5.1)$$

$$= 99.7 \text{ to } 126 \text{ bars } (P_l) \text{ or } 37.6 \text{ to } 47.4 \text{ bars } (P_h)$$

where, $\rho_l = 2.65$ g/cm^3 $\rho_h = 1.00$ g/cm^3

$g = 9.81$ m/s^2

$h = 1150$ to 1450 m

Using equation 5.1, pressures beneath the original volcanic edifice are estimated to have been 99.7 to 126 bars (lithostatic) or 37.6 to 47.4 bars (hydrostatic) during vein formation under porphyry-style potassic conditions. Lithostatic and hydrostatic pressure estimates are slightly lower than what would be expected for a porphyry deposit at ~ 1 km depth (e.g., $P_l \sim 260$ bars and $P_h \sim 100$ bars; e.g., Fournier, 1999). The calculated pressures are comparable to the ~ 150 and 90 bars estimates obtained via microthermometry by Carman (1994) from veins correlated to $V1_{M1}$ (e.g., Table 4.2).

Temporarily elevated fluid-pressures (i.e., $P_f > P_l + \tau$) (where τ = tensile strength) of early magmatic-hydrothermal fluids prior to sector collapse, coupled with local compression under very low differential stress, could explain the formation of tensile to hybrid V1 veins with both low- and high-angle dips in domains I and II, which formed in the porphyry-style environment at ~ 1 to 1.5 km depth. Due to the relatively shallow depth and low pressures calculated from equation 5.1 and Carman (1994)'s fluid inclusion studies, it appears that lithostatic fluid pressures would have been difficult to maintain. The rocks probably became less permeable due to anhydrite ± carbonate precipitation, causing pore fluid pressures to increase and thus temporarily elevating fluid-pressures above the rock tensile strength and $\sigma_3 \pm \sigma_1$ during porphyry-style vein formation (e.g., Sibson et al., 1988; Cosgrove, 1995; Cox, 1995; Sibson, 1996; Fournier, 1999).

A similar example of veins with low-angle dips that formed where σ_1 was sub-horizontal and fluid pressures were elevated transiently (i.e., $P_f > P_l$) are the mineralized 'flat-makes' at the Emperor low-sulfidation epithermal Au vein deposit in Fiji (Begg, 1996; Begg and Gray, 2002). Extensional veins with low- and high-angle dips have been documented in other ore deposits, attributed therein to local pressure perturbations triggered by exsolution of magmatic-hydrothermal fluids (e.g., Panasqueira, Portugal – Kelly and Rye, 1979; Bingham Canyon, USA – Gruen et al., 2010; Cadia East, Australia – Fox et al., 2015). Exploitation of existing lithological weaknesses facilitated the formation of flat-makes at Emperor (Begg, 1996), as well as the tensile vein sets with low-angle dips at Panasqueira (Kelly and Rye, 1979). Other documented examples of magmatic-hydrothermal induced extension include quartz stockwork veins in felsic magmatic systems that formed at depths of 2 to 6 km (Burnham and Ohmoto, 1980; Fournier, 1999).

5.6.6: Mechanisms of hybrid to shear failure on veins with low-angle dips

Lienetz contains a number of normal faults with high-angle dips (> 60°) and a relatively small population of similarly oriented veins that record components of tensile and hybrid failure modes (e.g., Figure 5.13). However, most of the vein arrays define hybrid fracture systems with low-angle dips. This includes the association of thick hybrid to shear veins with low-angle dips to the north, and relatively thin tensile to hybrid veins with high-angle dips to the northwest (e.g., Figure 5.13F). There are also broader breccia veins, commonly linked to the thick hybrid to shear veins with low-angle dips, that together produce rhombic

dilational jog configurations (e.g., Figure 5.13F). The thick veins with low-angle dips record a progressive history of modification via dissolution, flattening, and continued top-block down to the northwest sense of shear, which is consistent with a sub-vertically oriented σ_1 (Figure 5.13).

The physics of friction of isotropic rocks ($\mu \approx 0.6$ to 0.85) should limit extensional normal faults on surfaces dipping < 65° to 70° in the upper 1 km of the brittle crust when σ_1 is vertical (Anderson, 1951). However, the presence of minerals with weak rheological properties such as talc, calcite, anhydrite, serpentine and phyllosilicates can allow frictional slip to occur at low-angle dips (< 30°) in the brittle regime (e.g., Holdsworth, 2004; Numelin et al., 2007; Abers, 2009; Collettini et al., 2009; Collettini, 2011). At Lienetz, the accumulation of frictionally weak bands of anhydrite ± carbonates ± phyllosilicates promoted decoupling and shear at low-angle dips (Figure 5.13F). Continuous weakening was induced by dissolution and subsequent re-precipitation of anhydrite, possibly coupled with variable periods of hydrothermal mineral sealing. This potentially led to elevated fluid pressures (i.e., $P_f >> \sigma_3$; with $P_f \approx \sigma_1$), promoting slip on misoriented fractures, including reactivated fractures and veins that formed via early compression under low differential stress and temporarily elevated fluid-pressures.

5.6.7: Sector collapse at Lihir: influence of faults and veins

Veins and faults exposed at depth in the anhydrite-rich zone of Lienetz may have preserved evidence for some of the geometries and kinematics related to the sector collapse event(s) that were vital to the formation of the bulk mineable resource at Lihir (e.g., Sillitoe, 1994). Volcanoes are generally internally unstable, deforming under their own weight plastically, and/or via catastrophic sector collapse (Dieterich, 1988; Borgia et al., 2000; Byrne et al., 2013). Edifice failure via collapse can impact significantly on a potential ore-forming system, as rapid decreases in confining pressure, and ingress of meteoric and/or seawater to the magmatic-hydrothermal environment can occur rapidly and may induce hydrothermal brecciation, boiling and epithermal-style gold precipitation (e.g., Sillitoe, 1994; Carman, 2003). The mass-wasting event(s) that shaped the Luise amphitheater most likely had a basal surface above the present-day exposures in the floor of the amphitheater. The basal slip plane was most likely removed by erosion and/or masked by texturally destructive clay alteration, because it has not been identified during this or any previous study. The detachment surface may have been localized along a hydrothermally clay-altered zone of low shear strength, as has been observed in other edifices (e.g., López and Williams, 1993; Voight and Elsworth, 1997; Reid et al., 2001). However, given that the intense clay alteration that affects the upper levels of Lihir is interpreted to be a product of post-sector collapse (Moyle et al., 1990), modern high-temperature geothermal activity is likely to have been superimposed on and below the detachment surface, rather than being a causative feature. If the collapse was progressive or multistage, there may have been earlier-formed clay alteration areas positioned above the present-day steam-heated clay alteration zone, that facilitated sector collapse.

Alternatively, edifice weakening could have been in part, at least, facilitated by dissolution of, and/or shear along, thick anhydrite veins similar to those preserved at depth in Lienetz. $V1_{M1}$ veins have the appropriate low-angle to sub-horizontal dips for a décollement surface. Local textures of $V1_{M1}$ veins are consistent with strain localization and other features common to deformed anhydrite, such as the textures produced around décollement surfaces in evaporites (e.g., Davis and Engelder, 1985; Schreiber and Helman, 2005). However, the kinematics recorded by $V1_{M1} \pm V1_{M2}$ veins and breccia veins at Lienetz do not coincide with the northeast-direction of the sector collapse. Instead, they provide evidence for a history of more north to northwest-directed extension. Therefore the anhydrite veins and breccia veins are not kinematically linked to the collapse event(s). Nonetheless, they still may have had some control on the geometry of, and lubrication for, sector collapse. If this was the case, it would seem more likely that the sector collapse was at least in part incremental, rather than catastrophic.

The northeast-elongated geometry of the Lihir amphitheater, and the sector collapse event(s), may have been inherited and triggered from an underlying, deep-seated, tectonically generated northeast to east-northeast-striking structural array. Studies of other sector-collapsed volcanoes have demonstrated that movement along inherited faults can tectonic trigger volcano edifice instabilities (e.g., Iriga, Philippines, and Mt. St. Helens, USA – Lagmay et al., 2000; Mathieu and van Wyk de Vries, 2011; Mathieu et al., 2011). Additionally, regional differential stress and/or pre-existing fractures will favor construction of elongated volcanic edifices, which in turn have steeper and unstable flanks, making them more susceptible to sector collapse (e.g., Mathieu et al., 2011; Sielfeld et al., 2017). Even though Lihir Island's, and indeed the entire Tabar-Lihir-Tanga-Feni island chain's, formation is still enigmatic, there seems to have been important roles for the faults that contributed to the elongate form of each of the islands and their offshore ridges, and faults that are at acute angles (clockwise) to the island's long-axes. Kinematic indicators of faults associated specifically with the sector collapse at Lihir cannot be studied as they have been eroded, however, it is suspected that the northeast-elongated geometry of the amphitheater and collapse were inherited from the pre-existing northeast- to east-northeast-striking structural grain, as expressed in both Lienetz and Minifie (e.g., Figures 5.1, 5.3, 5.5, 5.9, 5.11–5.13).

5.7: Conclusions

Veins in Lienetz, broadly encompassed within the anhydrite-rich zone, record a dynamic structural evolution that spans early porphyry-style alteration, subsequent vein modification and dissolution, and overprinting by late-stage epithermal-style mineralization and alteration.

Early northwest and/or southeast-directed compression and west-northwest-directed extension was linked with vein formation during early porphyry-style alteration, under low differential stress, an oscillat-

ing sub-horizontal to sub-vertical σ_1, and temporarily elevated fluid-pressures from mineral sealing. Protracted, or multistage, northwest-directed extension with a mostly sub-vertical σ_1 was dominant for the rest of the porphyry- to epithermal-stage vein paragenesis at Lienetz. This is most evident in the principal vein array that consists of hybrid to shear veins with low-angle dips to the north, linked with thinner tensile to hybrid veins, or broader breccia veins, with high-angle dips to the northwest (e.g., Figure 5.5B).

Initial vein formation was followed by modification via anhydrite dissolution, along with some block-rotation and collapse brecciation. Modified veins localized some shear, and their sub-horizontal to low-angle northward-dipping orientations may have had some control on the geometry of, and lubrication for, sector collapse event(s). However, structures appear not to be kinematically linked to the northeast-directed collapse event(s) due to their top-block to the northwest or north-northwest sense of shear.

High-grade epithermal-style gold mineralization was post-sector collapse(s). Mineralization was partly facilitated by permeable and porous open spaces and cavities that were created by the dissolving of anhydrite (e.g., Figures 5.5, 5.10, 5.12, 5.13), as well as localized at depth by northeast-striking faults (e.g., Figures 5.11, 5.12, 5.13).

Continued extension with top-block down to the northwest preferentially reactivated the large vein array with low-angle dips to the north at Lienetz. Veins were modified during epithermal mineralization due to reactivation under extensional conditions (e.g., Figure 5.13F). Reactivation produced northeast-striking tensile to hybrid veins and breccia veins with high-angle dips and rhombic dilational jog that localized high-grade gold.

The northeast to east-northeast-striking faults, evident at both the island scale and the deposit scale, were inherited from a tectonically generated structural grain. The faults were reactivated throughout the evolution of Lienetz. Similarly oriented deep-seated faults are considered to have contributed to the northeast-elongation of the volcanic amphitheater, and provided fundamental structural controls on vein formation and gold mineralization.

Chapter 6: Pyrite trace element compositions

6.1: Introduction

Superimposed epithermal-style mineralization upon porphyry-style alteration makes Lihir one of the best examples of a telescoped ore deposit (Carman, 1994; Sillitoe, 1994). However, while telescoping led to a large bulk mineable resource at Lihir, it also created complexity with regards to mineral processing. Gold at Lihir predominantly occurs in the form of refractory pyrite (i.e., gold contained within pyrite), as is common in all Carlin-type, and in some epithermal-style and VHMS gold deposits (e.g., Fleet et al., 1993; Richards and Kerrich, 1993; Cline, 2001; Cline et al., 2005; Reich et al., 2005; Large et al., 2009; Deditius et al., 2014; Belousov et al., 2016). Gold also occurs locally in the form of gold tellurides and as inclusions of native gold within pyrite, which is common in many porphyry Cu-Au deposits (e.g., Deditius et al., 2009; Gregory et al., 2013; Reich et al., 2013). Previous work has identified variations in pyrite forms and textures at Lihir and linked them to various gold content (Carman, 1994; Wightman, unpublished data, 2004; Ageneau, 2012; Thomas, et al., unpublished data, 2014). Most of the refractory gold at Lihir is associated with As-rich pyrite [$Fe(S,As)_2$] or marcasite, with colloform and acicular forms typically containing the highest gold grades (Ageneau, 2012). Gold ore at Lihir is treated using pressure oxidation followed by conventional cyanidation and electrowinning (Latti et al., 2001; Newcrest Mining Ltd., 2016). Therefore, knowing how much of the gold resides as inclusions or in the crystal lattice of pyrite, and where the gold resides within that pyrite grain, is important with regards to optimizing mineral processing.

This chapter reports a subset of spatially and paragenetically constrained pyrite-bearing samples from the Lienetz orebody. Samples have been assigned to either porphyry- or epithermal-stages based on the constrained vein paragenesis (e.g., Figure 4.2). Using LA-ICP-MS trace element images of pyrite grains, coupled with NaOCl etching, the trace element zonation and metal contents of pyrite from each paragenetic event have been documented. This improved understanding of trace element association with gold, and of the overall gold deportment at Lihir, is used to provide insights to the genesis of the gigantic Lihir gold deposit, and to highlight implications for mineral processing.

6.2: Methods and analytical techniques

Paragenetically constrained vein samples were collected during open-pit mapping. A total of 31 polished 2.5 cm wide circular pucks set in epoxy were made for in situ analysis of pyrite by laser ablation – inductively coupled plasma – mass spectrometry (LA-ICP-MS) at CODES, University of Tasmania, Australia (e.g., Danyushevsky et al., 2011). Thirty-one pyrite grains were chosen for quantitative and qualitative analyses by ablating the surface of each pyrite grain and compiling trace element images from parallel laser

lines, following the methods outlined in Large et al. (2009), Danyushevsky et al. (2011) and Gregory et al. (2013). Imaging was conducted using a set of parallel lines with spacing equaling the laser beam size, thus covering the entire area of interest. Each line was pre-ablated to remove surface deposition and other surface contaminants. The memory effects and instrumental drift sensitivities were controlled by regular measurements of the background and calibration standards. Square, rather than round, beam shapes were used to maximize signal without increasing spot size and obtain representative sampling during line ablations. The beam size was determined by size of grains of interest and ranged from 13 to 20 μm. Lines were ablated at 10 Hz and a constant speed covering the size of the beam in 1 sec. Counts per second (cps) were converted to concentrations (ppm) by using average Fe content of a section of a line across pyrite and calculating the Fe content using the expected stoichiometric content for pyrite (i.e., 465,000 ppm Fe). Concentrations of lithophile elements (Na, Mg, Al, Si, K, Ca, Ti, V, Cr, Zr, In, Ba, Gd, Hf, Ta, U) were calculated via an in-house standard (GSD). Chalcophile elements (S, W, Pt, Au, Hg, Tl, Pb, Bi, Th, Sn, Sb, Te, Mo, Ag, Cd, Mn, Fe, Co, Ni, Cu, Zn, As, Se) were calculated via an in-house lithium-borate glass standard (STDGL-2b2). Only 13 significant elements in pyrite are highlighted in this chapter (i.e., Co, Ni, Cu, Zn, As, Se, Mo, Ag, Sb, Te, Au, Tl and Pb), as these elements were consistently above detection limit and had significant variability within different pyrite grains. Full elemental suites are listed in Appendix 3. Coordinates for all samples can be found in Appendix 1. The error on average, estimated from the standards, is < 5%, with the notable exception of sulfur, which is strongly affected by the instrumental drift and fractionation. The majority of elements hosted by pyrite show orders of magnitude variations and the corresponding uncertainty on averages are also large. Therefore, the analytical uncertainty was considered insignificant in comparison with heterogeneity of the sample. The detection capability was estimated from noise-on-gas background (Longerich et al., 1996), and the measurements below the crucial values (Appendix 3) were replaced by half of the critical value for calculations of averages and plotting. The details of the equipment and setting for the LA-ICP-MS analyses are as follows: Agilent 7700 ICP-MS with 0.95 (Ar) and 0.70 (He) L min-1 carrier gas flow rates; the ICP-MS was coupled to a Resolution (Australian Scientific Instruments) S155 193 nm excimer laser ablation system using 2.3 to 2.7 J cm^{-2} fluence, Pt cones, 1200 W RF power, < 0.25% (ThO/Th) oxides, 24 to 95 mJ energy.

Pyrite grains were etched using commercially available bleach (sodium hypochlorite solution, 6 – 14% w/v active chlorine; NaOCl) to reveal internal textures. Drops of NaOCl were applied to the sample surface and left for periods of 30 to 120 seconds, until noticeable color change of the pyrite occurred. Samples were then rinsed immediately with cold tap water and allowed to dry. Most of the tarnishing occurs during drying. The NaOCl acts as an oxidant for the pyrite, and discoloration patches and zones reflect compositional differences within the grains and the intensity of the tarnish varies according to mineral compositions, crystal lattice orientation and duration of the etch (e.g., Fleet et al. 1993; Peterson and Mavrogenes 2014).

A subset of polished pucks were analyzed with a scanning electron microscope (SEM). There, back-scattered electron (BSE) images and secondary electron (SE) images were used to identify chemical zoning and pyrite form. Details of instrument settings are in Appendix 2.

Pyrite LA-ICP-MS trace element images were analyzed in the geochemical software ioGAS™. Only minerals identified as pyrite (i.e., pixels that had characteristic elemental ratios and compositions of pyrite (FeS_2)) were queried from each full image and line sample. Out of the ~ 224,000 data points from the 31 pyrite images, 33,100 pyrite-only measurements were isolated. A minor amount of small inclusions within the pyrite grains (i.e., < 10 µm diameter) were too small to be isolated from the analyses, therefore, micro- and nano-sized inclusions as well as lattice-bound elements contribute to the total trace element concentrations. The LA-ICP-MS images of pyrite grains highlight trace element distributions within grains. By comparing pyrite laser images with detailed petrographic microscope photos, the cores and rims of pyrite grains were categorized and isolated in ioGAS™. The mean, median, geometric mean, minimum and maximum trace element concentrations for each pyrite grain's core, rim and entire grain was then extracted into an Excel™ database and compared between vein stages using weighted averages that take into account the number of pixels (each representing an analysis) for each pyrite image multiplied by the trace element concentration (Appendix 3). Grains from individual vein stages were further grouped into porphyry- or epithermal-stages and subdivided into cores and rims, again using weighted averages for each vein stage in order to achieve an unbiased average (Appendix 3). Gold deportment was calculated by multiplying the count number of each mineral identified with their mean Au concentrations (Appendix 3). Similar to trace element calculations, samples were then combined using weighted averages to obtain a representative percent Au per mineral (Appendix 3). Porphyry-stage pyrite grains include those found in $V1_{bio}$, $V1_{ksp}$, the cores of $V1_{M1}$, $V2_{py}$ and $V1_{M2}$, and two samples of pyrite in the mafic minerals from biotite-altered basalts, associated with the porphyry-style alteration event (e.g., Table 4.2). Epithermal-stage pyrite grains include $V3_{adu}$ and $V4_{qtz}$ (e.g., Table 4.2; Figure 4.2). Compositions of both cores and rims were calculated for $V1_{M1}$ and $V1_{M2}$ pyrite grains, and also for several additional samples from $V1_{bio}$, $V1_{ksp}$ and $V2_{py}$ veins where cores and rims were obvious visually.

6.3: Pyrite forms and internal textures

Pyrite forms and textures vary between different vein stages (Table 6.1; Figure 6.1). Pyrite grains from the least-modified V1 stages (i.e., $V1_{bio}$ and $V1_{ksp}$) are typically medium- to coarse-grained (100 to 1000 µm) with sub-angular to sub-rounded edges (Table 6.1; Figure 6.1A, C). V1 pyrite grains are typically inclusion-free with minor cavities (Table 6.1; Figure 6.1C). Etching with NaOCl revealed little to no internal textures (Figure 6.1C), or a patchy irregular pattern (Figure 6.1B). The patchy texture was best-developed in pyrite grains that have selectively replaced mafic minerals, as opposed to the pyrite grains that occur in

Table 6.1: Pyrite grain forms and NaOCl etched textures

Vein stage	Pyrite grain shape	Pyrite grain size	NaOCl reaction strength	Textures revealed by NaOCl etching	Comments
$V1_{bio}$ + $V1_{ksp}$	Sub-angular to rounded edges	Medium to large (100 to 1000 µm)	Weak to moderate	± patchy; ± wispy banded rims	Interstitial cpy ± mag
$V1_{M1}$	Angular to very rounded edges; irregular corroded edges; cavities	Small (< 10 to 300 µm)	Moderate to strong	Wispy zoned rims; ± oscillatory zonation	Overgrowth locally of euhedral py on rims; py over corroded mag; ± interstitial cpy, gn
$V3_{adu}$	Very angular to sub-rounded edges; inclusions	Medium (100 to 300 µm)	Strong	Oscillatory zonation; ± sector zonation; ± radiating crystals; ± colloform banded	Multiple generation of py and mrc overgrowth on rims; ± interstitial gn
$V4_{qtz}$	Very angular to rounded edges; irregular corroded edges; cavities; inclusions	Small (< 5 to 150 µm)	Strong	Oscillatory zonation; ± radiating crystals	Interstitial cpy, gn, sph; overgrowth locally of euhedral py on rims
$V1_{M2}$	Angular to sub-rounded edges; irregular corroded edges; cavities; inclusions	Medium – large (100 to 1000 µm)	Moderate	Wispy zoned rims; discolouration blots; ± oscillatory zonation; ± patchy	Interstitial cpy, sph; overgrowth locally of py over corroded mag

Abbreviations: cpy = chalcopyrite, gn = galena, mag = magnetite, mrc = marcasite, py = pyrite, sph = sphalerite.

veins. Wispy zoned rims are absent or only weakly developed in $V1_{bio}$ and $V1_{ksp}$ pyrite grains.

$V3_{adu}$ and $V4_{qtz}$ pyrite grains range from < 5 to 300 µm, with very angular to rounded edges, and locally contain inclusions and cavities (Table 6.1; Figure 6.1D–F). Etching with NaOCl revealed strong discoloration, oscillatory zonation, sector zonation and radiating textures (Figure 6.1E–F).

$V1_{M1}$ and $V1_{M2}$ pyrite grains range from < 10 to 1000 µm in diameter, have angular to very rounded edges, and contain abundant inclusions (including glauberite, anhydrite, wall rocks, etc.) and cavities (Table 6.1; Figure 6.1G–I). The edges of these pyrite grains typically have corroded-like textures (Figure 6.1H–I). Etching with NaOCl revealed discolored wispy zoned rims along most $V1_{M1}$ and $V1_{M2}$ pyrite grains (Figure 6.1H–I). The wispy zoned rims have locally been truncated along the edges of pyrite grains (Figure 6.1H).

6.4: Trace element deportment

Many of the pyrite grains analyzed have distinct trace element assemblages and concentrations (Table 6.2; Figure 6.2). Overall, the epithermal-stage pyrite grains have orders of magnitude higher trace element concentrations than porphyry-stage pyrites (Table 6.2 and 6.3; Figure 6.2). The trace elements in most pyrite grains define distinct zonation patterns, with trace element-poor cores and trace element-rich rims (Table 6.2 and 6.3; Figure 6.2). However, the end-member porphyry- and epithermal-stage pyrite grains have little to no clearly defined trace element rims.

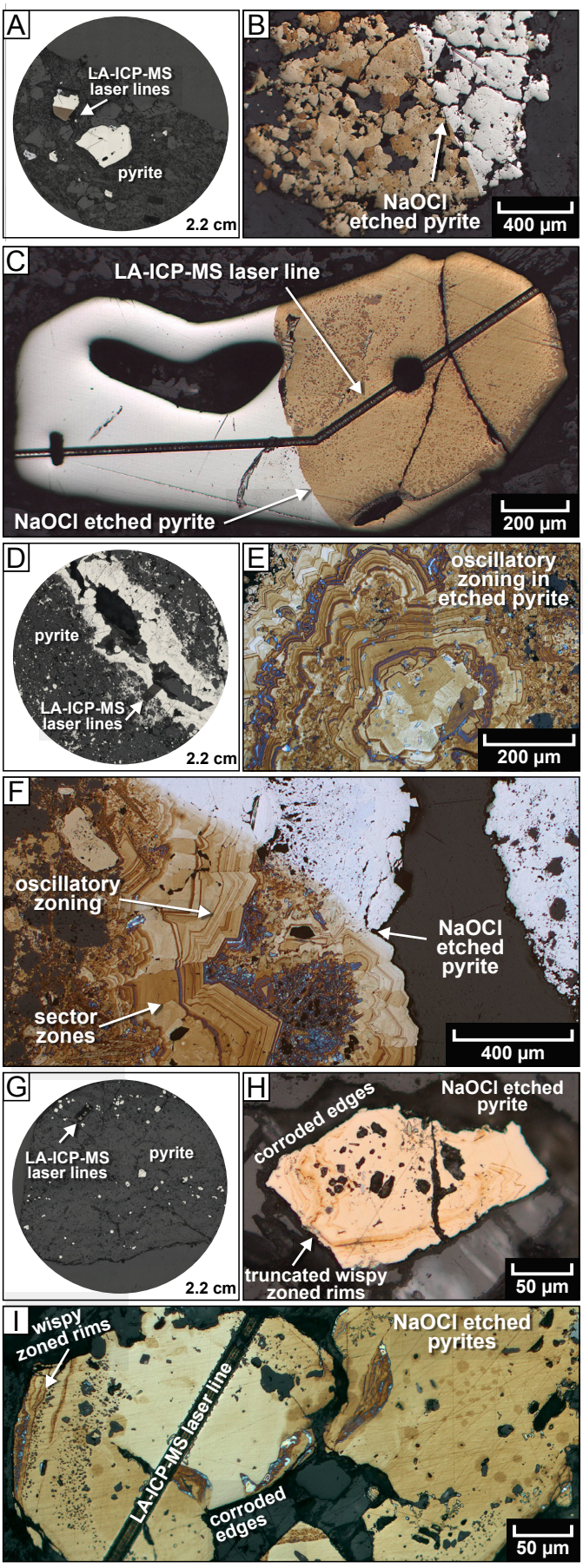

Figure 6.1: Pyrite form and NaOCl etched textures (e.g., Table 6.1). **A)** Reflected-light microscope photo of sample from $V1_{bio}$ vein (LH14SS051-1) exhibiting large grain size of pyrites. **B)** Reflected-light microscope photo of porphyry-stage pyrite grain (GW47-1122m) half-etched with NaOCl, exhibiting patchy textures. **C)** Reflected-light microscope photo of porphyry-stage pyrite grain (LH14SS051-2) half-etched with NaOCl, exhibiting no textures. **D)** Reflected-light microscope photo of sample from $V3_{adu}$ vein (LI12EL002B). **E)** Reflected-light microscope photo of epithermal-stage pyrite grain (LI12EL002A) fully etched with NaOCl, exhibiting oscillatory zoning. **F)** Reflected-light microscope photo of epithermal-stage pyrite grain (LI12EL002B) half-etched with NaOCl exhibiting oscillatory zoning and sector zones. **G)** Reflected-light photograph of sample from stage $V1_{M1}$ (LH13SS077) exhibiting small but variable pyrite grain sizes. **H)** Reflected-light microscope photo of composite pyrite grain (LH13SS069) fully etched with NaOCl, exhibiting truncated wispy zoned rims and corroded edges. **I)** Reflected-light microscope photo of composite pyrite grain (LH13SS069) fully etched with NaOCl, exhibiting wispy zoned rims and corroded edges.

Table 6.2: Pyrite trace element values in ppm

Element	Porphyry-stage pyrite grains	Epithermal-stage pyrite grains	Composite pyrite grains			
			Cores	Rims	$V1_{M1}$ only rims	$V1_{M2}$ only rims
Co						
median	190	53.3	215	55.9	20.0	99.6
geometric mean	131	52.0	136	47.3	17.8	79.5
Ni						
median	202	10.7	55.7	34.2	20.4	13.0
geometric mean	163	9.70	47.3	26.3	15.1	10.9
Cu						
median	65.1	113	36.0	68.4	142	9.18
geometric mean	52.1	98.1	24.6	46.5	85.9	9.94
Zn						
median	6.08	11.5	2.56	14.4	31.8	1.88
geometric mean	6.01	11.2	2.72	10.7	22.2	2.73
As						
median	168	10200	77.7	1150	2440	182
geometric mean	169	9480	78.0	757	1560	145
Se						
median	136	92.0	153	79.2	44.9	165
geometric mean	125	95.9	141	54.8	45.5	85.7
Mo						
median	0.687	384	0.620	4.17	8.60	1.92
geometric mean	0.712	324	0.700	4.06	7.88	2.36
Ag						
median	1.94	27.9	1.08	3.75	8.46	0.536
geometric mean	1.77	19.6	0.966	2.78	5.96	0.756
Sb						
median	2.19	71.7	1.22	13.1	29.5	1.69
geometric mean	2.08	52.7	1.30	7.55	16.1	1.87
Te						
median	10.6	12.3	11.3	14.4	20.9	14.6
geometric mean	11.6	11.9	11.8	13.5	18.2	12.6
Au						
median	0.561	10.8	0.213	2.98	5.94	0.360
geometric mean	0.539	10.1	0.253	1.64	3.24	0.390
Tl						
median	0.210	165	0.099	1.22	2.86	0.063
geometric mean	0.195	137	0.103	0.719	1.60	0.108
Pb						
median	32.1	85.0	17.7	125	281	13.3
geometric mean	29.8	70.0	16.9	122	274	13.1

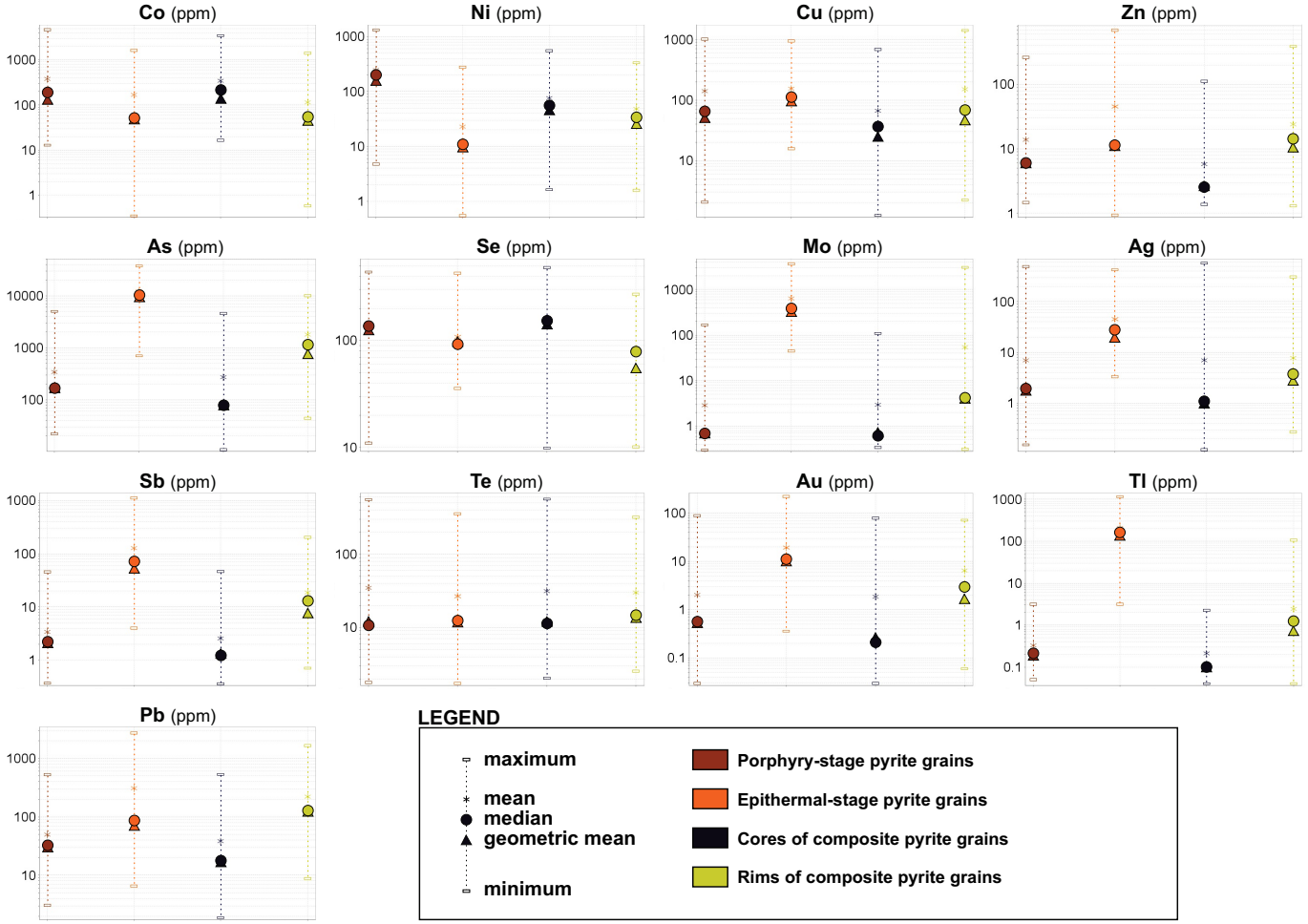

Figure 6.2: Trace element graphs of pyrites. Maximum, mean, median, geometric mean and minimum trace element concentrations for porphyry-stage and epithermal-stage pyrite grains, as well as cores and rims of composite pyrite grains.

Table 6.3: Percent change (%) of median and geometric mean trace element values for different pyrite generations

Element	median (R − C)/C	geometric mean (R − C)/C	median (E − P)/P	geometric mean (E − P)/P	median (R − P)/P	geometric mean (R − P)/P
Co	−74%	−65%	−72%	−60%	−71%	−64%
Ni	−39%	−45%	−95%	−94%	−83%	−84%
Cu	90%	89%	74%	88%	5%	−11%
Zn	460%	290%	88%	86%	140%	78%
As	1400%	870%	5900%	5500%	590%	350%
Se	−48%	−61%	−32%	−23%	−42%	−56%
Mo	570%	480%	56,000%	45,000%	510%	470%
Ag	250%	190%	1300%	1000%	93%	57%
Sb	970%	480%	3200%	2400%	500%	260%
Te	27%	15%	16%	2%	35%	16%
Au	1300%	550%	1800%	1800%	430%	210%
Tl	1100%	600%	78,000%	70,000%	480%	270%
Pb	610%	620%	170%	140%	290%	310%

Colour codes represent positive (green) and negative (red) percent change of element within pyrite grains.
Abbreviations: **C** = cores of composite pyrite grains; **E** = epithermal-stage pyrite grains ($V3_{adu}$, $V4_{qtz}$); **P** = porphyry-stage pyrite grains (V1); **R** = rims of composite pyrite grains.

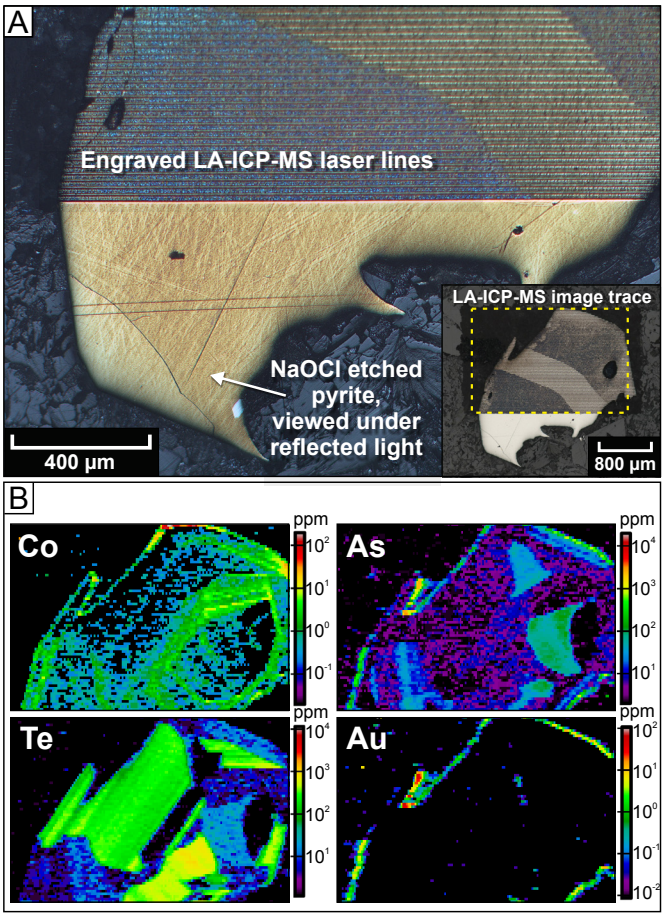

Figure 6.3: Porphyry-stage pyrite grains and corresponding LA-ICP-MS images. **A)** Reflected-light image of NaOCl etched pyrite from $V1_{bio}$ (LH14SS051-1). **B)** LA-ICP-MS images for Co, As, Te and Au.

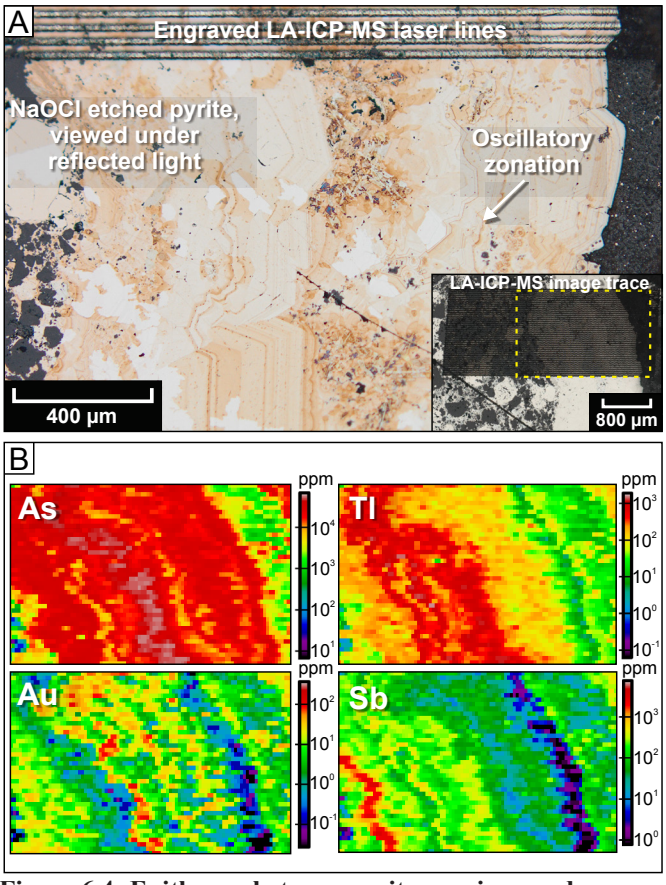

Figure 6.4: Epithermal-stage pyrite grains and corresponding LA-ICP-MS images. A) Reflected-light image of NaOCl etched pyrite from $V3_{adu}$ (LI12EL002B). **B)** LA-ICP-MS images for As, Tl, Au and Sb.

6.4.1: Porphyry- versus epithermal-stage pyrite

Pyrite grains that formed during porphyry-style hydrothermal activity at Lienetz have > 100 ppm (median and geometric mean) concentrations of Co, Ni, As and Se, and > 5 ppm (median and geometric mean) concentrations of Cu, Zn, Te and Pb (Table 6.2; Figure 6.2). There is typically minor zonation of most trace elements within porphyry-stage pyrite grains (Figure 6.3A–B). There is, however, an antithetic sector zonation of Te and As, and a concentric zonation of Co ± Ni that mimics the shape of the larger pyrite grains (Figure 6.3B). Both the sector and concentric zones were rarely visible after being etched with NaOCl. The patchy texture, revealed by NaOCl etching, was only observed in a few porphyry-stage pyrite grains (e.g., Figure 6.1B). This texture corresponds to an amalgamation of pyrite sub-grains with enriched concentrations of Co and Ni and/or different crystal orientations of individual pyrite grains on the polished puck.

Pyrite grains that formed during epithermal conditions at Lienetz have > 100 ppm (median and geometric mean) concentrations of As, Mo and Tl, and > 10 ppm (median and geometric mean) concentrations of Co, Ni, Cu, Zn, Se, Ag, Sb, Te, Au and Pb (Table 6.2; Figure 6.2). Trace element zonation patterns are well-developed within epithermal-stage pyrite grains and typically correlate with oscillatory zones, visible under reflected light after being etched with NaOCl (Figures 6.1E–F, 6.4A). Some trace elements are concentrated in patches within the pyrite grains or in fine-grained radial marcasite pseudomorphs of pyrite grains (Figure 6.4A–B). The darker coloured oscillatory zones correspond to

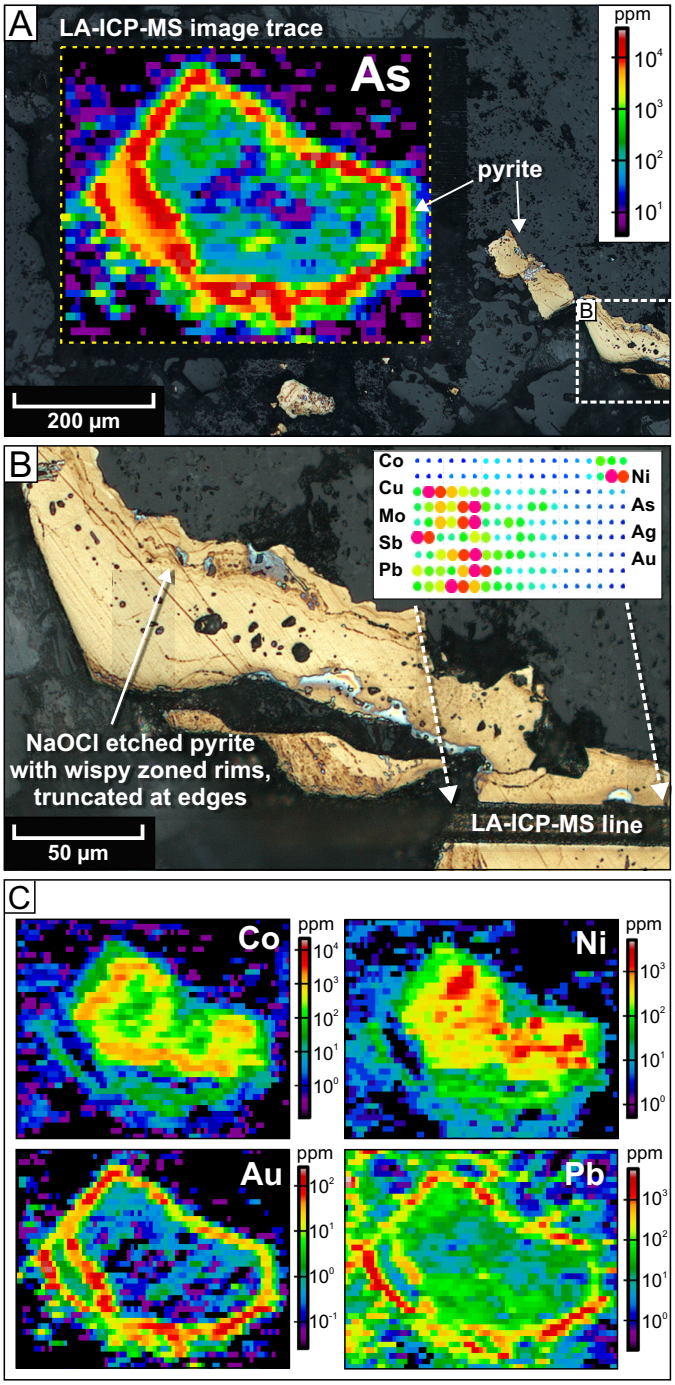

Figure 6.5: Composite pyrite grains ($V1_{M1}$) and corresponding LA-ICP-MS images. A) Reflected-light microscope photo of NaOCl etched pyrite from $V1_{M1}$ (LH13SS069). LA-ICP-MS image of As overlain on pyrite. **B)** Close up view of rim of pyrite highlighting wispy zoned rims, partly truncated at edges. Insert shows schematic of higher values of trace elements (i.e., larger circles with hotter colours), along a LA-ICP-MS laser line. **C)** LA-ICP-MS images for Co, Ni, Au and Pb.

high As concentrations, and to other trace elements such as Sb, Tl and Au (Figure 6.4A–B). Some pyrite grains have replaced and overgrown corroded magnetite and pre-existing pyrites, but generally the epithermal-stage pyrites appear to have not overgrown pre-existing sulfides.

Table 6.3 compares the median and geometric mean trace element concentrations for epithermal-stage pyrite grains to porphyry-stage pyrite grains. When the two pyrite generations are compared, epithermal-stage pyrites are have > 1000% positive change in As, Mo, Ag, Sb, Au and Tl, and > 10% positive change in Cu, Zn, Te and Pb (Table 6.3). On the other hand, porphyry-stage pyrites have > 10% positive change in Co, Ni and Se, compared to the epithermal-stage pyrite grains (Table 6.3).

6.4.2: Pyrite cores versus rims

Compositionally distinct core and rims of pyrite grains were revealed with NaOCl etching, largely from $V1_{M1}$ and $V1_{M2}$ stages, and have been highlighted with trace element images obtained by LA-ICP-MS (Figures 6.5, 6.6). Most of the pyrite grains are composite grains, with distinct trace element zonation patterns, with trace element-rich rims, and relatively trace element-poor cores (Table 6.2; Figure 6.2). The cores and rims of pyrite grains have significant differences in their trace element concentrations (Table 6.3). Overall, cores of pyrite grains have > 100 ppm (median and geometric mean) concentrations of Co and Se, and > 5 ppm (median and geometric mean) concentrations of Ni, Cu, As, Te and Pb (Table 6.2). Concentric zonation of Co ± Ni and Se is typical with trace element images of some of the larger pyrite grains, but the zonation is rarely visible with NaOCl etching (Figure 6.5C, 6.6C). Rims of pyrite grains have > 100 ppm (median and geometric mean) concentrations of As and Pb, and > 2 ppm (median and geometric mean) concentrations of Co, Ni, Cu, Zn, Se, Mo, Ag, Sb, Te and Au (Table 6.2). Trace element-rich rims are irregular, but define multiple discrete growth

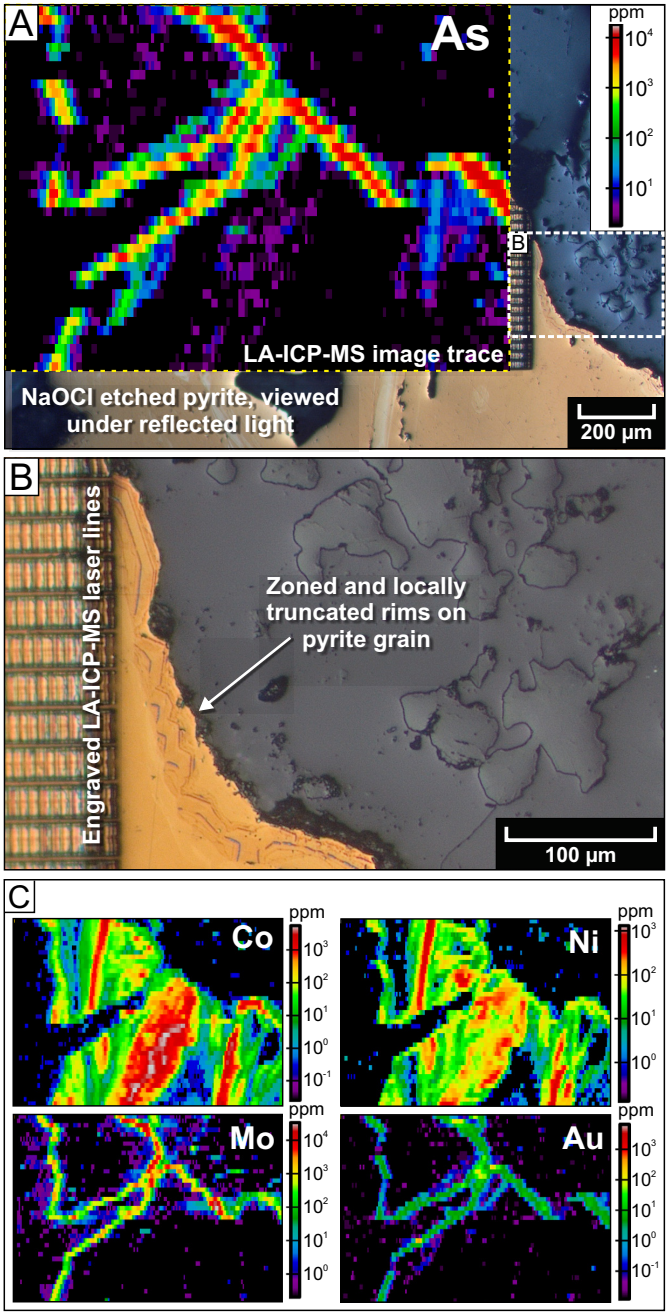

Figure 6.6: Composite pyrite grains ($V1_{M2}$) and corresponding LA-ICP-MS images. A) Reflected-light microscope photo of NaOCl etched pyrite from $V1_{M2}$ (LH13SS003). LA-ICP-MS image of As overlain on pyrite. **B)** Close up view of rim of pyrite highlighting bright oscillatory zoned rims with irregular and partly truncated contacts on both the inner edge to the pyrite grain and outer edge to calcite. **C)** LA-ICP-MS images for Co, Ni, Mo and Au.

bands around the cores (Figures 6.5, 6.6). The trace element-rich rims (e.g., Figure 6.6B) are similar to the oscillatory zones, observed in some epithermal-stage pyrite grains (e.g., Figure 6.4A), however they are generally more irregular, and have locally been truncated along both their inner and outer edges (e.g., Figure 6.5B).

When the median and geometric mean trace element concentrations from pyrite rims are compared to pyrite cores (Table 6.3), the rims have > 500% positive change in As, Mo, Sb, Au, Tl and Pb, and > 10% positive change in Cu, Zn, Ag and Te (Table 6.3). On the other hand, pyrite cores have > 10 % positive change in Co, Ni and Se, compared to pyrite rims (Table 6.3).

6.4.3: Rims compared to epithermal-stage pyrite

The rims of composite pyrite grains were compared to epithermal-stage pyrite grains in order to investigate if the modification event(s) that produced trace element-rich rims have similar trace element enrichment or depletion patterns (Table 6.3). Thus, as with epithermal-stage pyrite grains, the percent change of composite pyrite rims was calculated relative to porphyry-stage pyrite grains (Table 6.3).

When the median and geometric mean trace element concentrations for rims are compared to porphyry-stage pyrite grains, the rims have > 100% positive change in Zn, As, Mo, Sb, Te, Au, Tl and Pb, and > 10% positive change in Ag and Te (± Cu). On the other hand, rims have > 10% negative change in Co, Ni and Se (± Cu) compared to porphyry-stage pyrite grains (Table 6.3).

6.5: Gold deportment

The high As concentrations detected from pyrite grains analyzed in this study (Table 6.2; Figures 6.2, 6.4B, 6.5A, 6.6A) are consistent with previous reports on the high As content of pyrite at Lihir (e.g., Moyle et al., 1990; Fortune, unpublished data, 2010; Ageneau, 2012). This positive correlation of As and Au is common – it has been reported in other ore deposit studies (e.g., Fleet et al., 1993). Reich et al. (2005) identified a strong positive Au – As correlation in pyrite from Carlin-type and epithermal ore deposits and determined that the maximum amount of gold that can be contained within the pyrite lattice depends on the arsenic content. This can be represented as a gold saturation line on a Au versus As plot, described by the equation $C_{Au} = 0.02 \times C_{As} + 4 \times 10^{-5}$ (Reich et al., 2005).

When the total amount of gold within different minerals was calculated from all minerals identified/analyzed in the LA-ICP-MS images, ~ 75% of the gold was identified as hosted in pyrite (Table 6.4). When plotted on a Au versus As diagram ~ 81% of data fall below the Reich et al. (2005) gold saturation line, and thus is inferred to be within the crystal lattice of the pyrite (Table 6.4). In only the epithermal-stage pyrite

Table 6.4: Gold deportment (i.e., % Au present as a trace element within minerals)

Mineral	Au (all samples)	Au (epithermal-stage samples)	Au (porphyry-stage and composite samples)
anhydrite	5%	2%	7%
arsenopyrite	0%	0%	0%
barite	1%	1%	1%
biotite	3%	6%	3%
chalcopyrite	1%	0%	2%
epidote	1%	1%	1%
ferroactinolite	0%	1%	0%
ferrohornblende	1%	0%	1%
galena	1%	0%	2%
magnesiohornblende	3%	0%	4%
magnetite	0%	0%	1%
molybdenite	2%	3%	1%
orthoclase	1%	2%	1%
pyrite	**61%**	**67%**	**59%**
inclusions in pyrite grain rims	**5%**	**0%**	**6%**
inclusions in pyrite grain cores	**7%**	**10%**	**6%**
tellurides (large inclusions)	**1%**	**6%**	**0%**
quartz	1%	1%	1%
sphalerite	2%	1%	2%
Total % Au in other minerals	24%	17%	28%
Total % Au as inclusions in pyrite	14%	15%	12%
Total % Au in crystal lattice of pyrite	61%	67%	59%
Total % Au in pyrite	**75%**	**82%**	**70%**
as Au inclusions in pyrite[1]	**19%**	**18%**	**17%**
as Au in crystal lattice of pyrite[1]	**81%**	**82%**	**83%**

[1] = according to the gold saturation line defined by $C_{Au} = 0.02 \times C_{As} + 4 \times 10^{-5}$ (Reich et al., 2005)

Correlation with Au	
Co	−0.00
Ni	−0.00
Cu	+0.05
Zn	+0.02
As	+0.01
Se	+0.01
Mo	+0.01
Ag	+0.88
Sb	+0.02
Te	+0.98
Au	+1.00
Tl	+0.01
Pb	+0.00

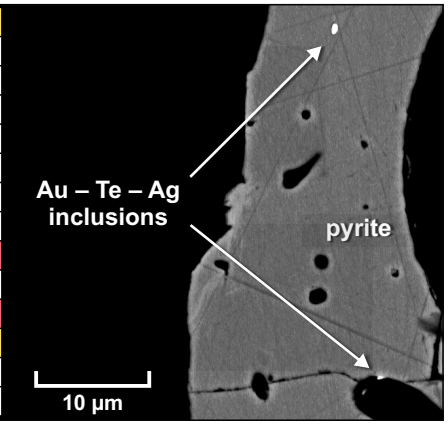

Figure 6.7: Gold inclusions in pyrite. Principal component analysis correlation of Au with other elements, and a BSE-SEM photo of a pyrite grain (i.e., $V1_{M1}$ LH13SS069), with micro- to nano-size bright Au − Te − Ag inclusions.

grains (i.e., $V3_{adu}$ and $V4_{qtz}$), ~ 82% of the gold was identified as hosted in pyrite, and of that ~ 82% of data fall below the gold saturation line (Table 6.4). In only the porphyry-stage and composite pyrite grains (i.e., $V1_{-}$), ~ 70% of the gold was identified in pyrite, and of that ~ 83% of data fall below the gold saturation line (Table 6.4). The remainder percent of gold above the gold saturation line in all pyrite grains is inferred to be gold as micro- to nano-sized inclusions (Table 6.4). These were sparsely identified as Au – Ag – Te inclusions (Figure 6.7). Principal component analysis of all inclusions in pyrite further show this strong correlation with Au – Ag – Te (Figure 6.7), of which some of these are likely petzite (Ag_3AuTe_2).

6.6: Discussion

There are marked differences in the trace element contents of pyrite grains from porphyry- to epithermal-stage vein assemblages at Lihir, with strong enrichment of trace elements characterizing the delicately textured rims of composite pyrite grains (Table 6.3). These changes in trace element concentrations suggests changes in fluid compositions, possibly due to processes such as fluid mixing, boiling, oxidation or acidification, and/or successive pulses of hydrothermal fluids with distinct fluid compositions (e.g., Spycher and Reed, 1986; Spycher and Reed, 1989; Cooke and McPhail, 2001; Kouzmanov et al., 2010) during the epithermal-stage. The highly variable gold concentrations and trace element suites within pyrite at Lihir has important implications both for ore genesis and processing.

6.6.1: Porphyry- versus epithermal-stage pyrite grains

Large (100 to 1000 µm) porphyry-stage pyrite grains from V1 veins have > 100 ppm concentrations of Co, Ni, As and Se, but have low overall trace element concentrations compared to later pyrite generations (Figure 6.8A). Cobalt, Ni ± Se are enriched in growth zones in the core of the pyrite grains, and antithetic Te and As zones appear to reflect discrete sector partitioning in particular facets during pyrite growth.

The relatively low concentrations of trace elements in porphyry-stage pyrites, and the large grain sizes, are consistent with pyrite crystallizing slowly in a higher temperature environment at Lihir (e.g., up to 410°C; Carman, 1994; Ageneau, 2012). Under these conditions many trace elements are soluble and not incorporated into the structure of pyrite, except for Co and Ni which have been shown to stoichiometrically substitute for Fe at 400°C (Klemm, 1965), and possibly Se and Te substituting for S (Huston et al., 1995).

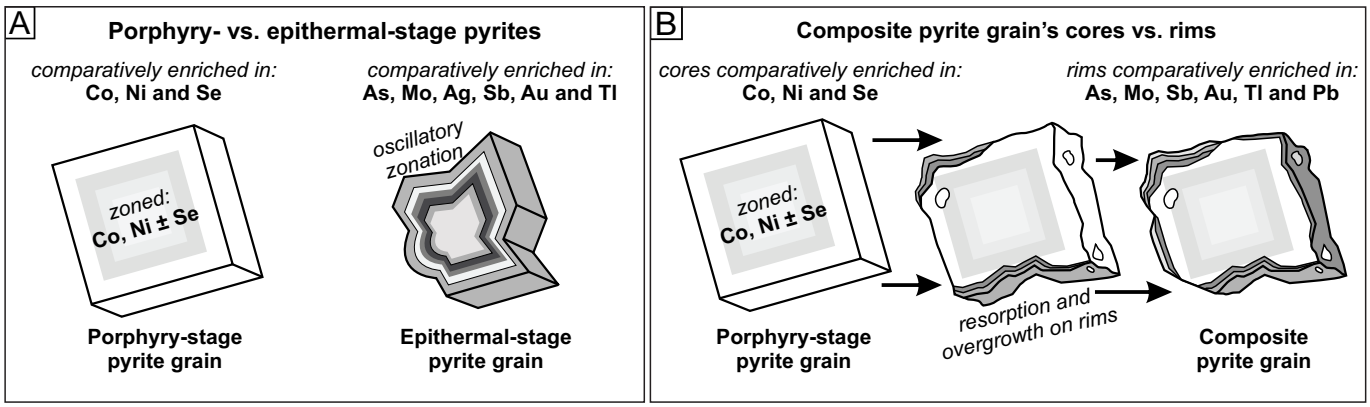

Figure 6.8: Schematic summary diagram of comparative trace element enrichment in pyrite from the Lienetz orebody, Lihir gold deposit (i.e., Table 6.2). **A)** Porphyry-stage pyrite grains compared to epithermal-stage pyrite grains. Porphyry-stage pyrite grains have distinct zoned cores and epithermal-stage pyrite grains have distinct oscillatory zones. **B)** Composite porphyry-stage pyrite grain cores compared to rims, illustrating the progression from an initial large euhedral porphyry-stage pyrite grain, which was partly dissolved and followed by overgrowth to produce rims enriched in trace elements.

The Co- and Ni-rich pyrite grains that formed under porphyry-style conditions at Lihir are consistent with other studies of pyrite that formed in relatively higher temperature environments. Studies of pyrite grains from porphyry Cu-Au deposits have reported Co- and Ni-rich pyrites (e.g., Hanley and MacKenzie, 2009; Gregory et al., 2013; Reich et al., 2013). Reich et al. (2013) found that Cu, As, Au ± Ni and Co were the most abundant trace elements analyzed within pyrite grains at the Dexing porphyry deposit, China. Hanley and MacKenzie (2009) reported pyrites with high Co and Ni concentrations, as well as Pt and Pd, from alkalic porphyry Cu-Au deposits in the Canadian Cordillera. Similar Co- and Ni-zoned pyrite grains were reported from the Sudbury-district nickel sulfide deposit Craig in Ontario, Canada (Craig and Solberg, 1999). In that deposit Co-, and to a lesser degree, Ni-enriched zones have sharp boundaries and were interpreted to represent multiple periods of pyrite growth, rather than diffusion (Craig and Solberg, 1999). Cobalt has also been found to be high in pyrite grains from the Cu-rich, higher temperature assemblages of VHMS deposits (e.g., Green et al., 1981; Walshe and Solomon, 1981; Huston et al., 1995).

Pyrite grains formed during epithermal-stages $V3_{adu}$ and $V4_{qtz}$ at Lihir have > 100 ppm concentrations of As, Mo and Tl, and are significantly enriched in As, Mo, Ag, Sb, Au and Tl, when compared to V1 porphyry-stage pyrite grains (Figure 6.8A). Trace element LA-ICP-MS images and NaOCl etching has revealed strong oscillatory zones that corresponds to variations in trace element contents (Figure 6.8A). This suite of trace elements, particularly As, Tl, Au and Mo, can be incorporated into pyrite by non-stoichiometric substitution in the pyrite lattice, or possible in the case with As, as a coupled substitution $[AsS]^{3-}$ with S (Cook and Chryssoulis, 1990; Huston et al., 1995), or as a metastable solid-solution of the type $Fe(S, As)_2$ (Fleet et al., 1993). The extreme concentrations of As and other trace elements detected in these epithermal-stage pyrite grains probably requires disequilibrium precipitation of pyrite, that is enhanced under conditions of rapid precipitation (e.g., Huston et al., 1995; and reference therein; Peterson and Mavrogenes, 2014).

The sharp textural features (i.e., oscillatory zones, colloform bands, etc.) and corresponding trace element enrichments (i.e., As, Au, Mo, Tl, etc.) of epithermal-stage $V3_{adu}$ and $V4_{qtz}$ pyrite grains are interpreted to represent episodic fluctuation in fluid composition during crystal growth and rapid deposition (e.g., Fleet et al., 1989). Studies comparing trace elements and sulfur isotopes of pyrite from epithermal deposits (e.g., Yanacocha, Pueblo Viejo, and Porgera) that have shown similar sharp colloform and oscillatory Au-, As- and chalcophile-rich bands, with a formation attributed to rapid decompression simultaneous with extreme chemical changes associated with volatile exsolution (Fleet et al., 1989; Deditius et al., 2009; Peterson and Mavrogenes, 2014).

6.6.2: Trace element-rich rims via dissolution and overgrowth

Trace element-rich rims have overgrown on trace element-poor cores in most of the pyrite grains analyzed (Figure 6.8B). These are particularly well-developed in $V1_{M1}$ and $V1_{M2}$. Only Se, Co and Ni are depleted in the rims, whereas the rims themselves are significantly enriched in As, Mo, Sb, Au, Tl and Pb, compared to their cores (Figure 6.8B). This trace element enrichment assemblage is similar to, although generally an order of magnitude less than, epithermal-stage pyrite grains (e.g., Figure 6.8A). The trace element-rich rims have delicate banded textures that relate to enriched trace element concentrations, similar to the oscillatory zones in $V3_{adu}$ and $V4_{qtz}$ pyrites (e.g., Figure 6.8A). Many of the rims appear to have overgrown on irregular and corroded pyrite grains (e.g., Figures 6.1H–I, 6.5B, 6.6B). Some of the rims are truncated by grain boundaries (e.g., Figure 6.1H), consistent with partial dissolution of pyrite (e.g., Cook et al., 2009). Similar textures of dissolution are evident at mesoscopic- and macroscopic-scales within Lienetz, where anhydrite, and entrained fragments of wall rocks, have been dissolved, resulting in solution collapse breccias and large, several meter wide, open-space cavities (e.g., Figures 4.3G, 4.10–11, 5.10). Observations across several scales are therefore consistent with interpretation of mineral dissolution and re-precipitation during hydrothermal activity at Lihir. Although the two minerals (i.e., anhydrite and pyrite) have contrasting solubilities, and therefore factors controlling the dissolution of each would have been different, they still support a dynamic ore-forming environment. For example, mineral solubilities would be affected by episodic periods of heating and cooling, as well as changing pressures due to mineral precipitation (e.g., Sander and Einaudi, 1990).

The diffusion of trace elements along the edges of pyrite grains producing the trace element enriched rims is unlikely given the textural evidence for truncation of growth bands and the sharp zonation boundaries between compositional bands. Similar studies of other types of gold deposits (e.g., Carlin and Bendigo) have found similar Au- and As-rich and Co-depleted rims of pyrite grains, with the processes attributed to overgrowth on pre-existing pyrite by later hydrothermal events (Deditius et al., 2008; Deditius et al., 2009; Large et al., 2009; Deditius et al., 2011).

6.6.3: Occurrence of gold in pyrite and implications for metallurgical processing

The median concentration of gold in porphyry-stage pyrite grains is ~ 0.5 ppm, considerably lower than the median of ~ 10 ppm for gold in epithermal-stage pyrite grains (Table 6.2). Rims of composite pyrite grains have a median of ~ 3 ppm Au. Fire assayed gold concentrations of veins ± wall-rocks alteration halos from samples that formed during porphyry-style conditions within Lienetz are approximately 0.2 to 0.5 g/t for $V1_{bio}$ and $V1_{ksp}$, and 0.3 and 3.7 g/t for modification stages $V1_{M1}$ and $V1_{M2}$, respectively (e.g., Table 4.2). Gold concentrations in epithermal-stage veins ($V3_{adu}$ and $V4_{qtz}$) are 5.9 and 5.4 g/t (Table 4.2). Because the epithermal-stage $V3_{adu}$ and $V4_{qtz}$ veins contain abundant sulfides (i.e., > 15% volume; Table 4.2), and ~ 80% of the gold occurs within the pyrite from this study's samples (e.g., Table 6.4), most of the gold is interpreted to occur in pyrite, as either lattice-bound gold or micro- to nano-sized inclusions of dominantly Au – Ag – Te inclusions in pyrite. In the composite pyrite grains from largely $V1_{M1}$ and $V1_{M2}$ veins > 70% of the gold occurs in the pyrite, and mostly in the rims of pyrite grains, as either lattice-bound pyrite or micro- to nano-sized inclusions of dominantly Au – Ag – Te inclusions. Some gold may occur in other mineral phases (e.g., Table 6.4), and the average gold grades in bulk rock samples are likely to have been affected by local gold micro-nuggets. A dedicated gold deportment study is recommended for future work in order to quantify which minerals besides pyrite host the majority of gold inclusions.

Overall, the epithermal-stage pyrite grains and the rims of composite pyrite grains have very high As and Au concentrations, and can be classified as refractory pyrite in the sense of metallurgical processing. Pyrite with high As concentrations (i.e., arsenian pyrite > 500 ppm As) is common in hydrothermal ore deposits, particularly epithermal and Carlin-type Au deposits (Fleet et al., 1993; Richards and Kerrich, 1993; Cline, 2001; Cline et al., 2005; Reich et al., 2005; Large et al., 2009; Deditius et al., 2014; Peterson and Mavrogenes, 2014). For metallurgical processing, an opportunity exists to reduce the level of oxidation when extracting gold from the composite pyrite grains, due to the fact that they have only As- and Au-rich rims, as opposed to the epithermal-stage pyrite grains which are As- and Au-rich throughout. Composite pyrite grains should therefore require a shorter oxidation and leaching time, as it is only necessary to liberate gold from the pyrite grain rims in order to liberate most of the gold.

6.6.4: Pyrite associated with porphyry-style biotite alteration

In the Lienetz orebody, most of the samples were taken within a broad zone of secondary biotite alteration, interpreted as potassic alteration relating to the early porphyry-stage at Lihir (e.g., Figure 5.4C; Carman, 1994). Potassic alteration, defined by either biotite or K-feldspar ± magnetite ± anhydrite ± quartz, is the most proximal alteration assemblage encompassing mineralized porphyry Cu ± Au ± Mo deposits and associated porphyritic intrusions, in a generalized model (Lowell and Guilbert, 1970; Beane and Titley, 1981; Sillitoe, 2000; Seedorff et al., 2005; Sillitoe, 2010). In mafic host rocks (i.e., rocks with significant

Fe and Mg), biotite alteration is dominant over K-feldspar alteration (Sinclair, 2007). Typically the potassic alteration zone in the core of porphyry deposits is associated with low total sulfide minerals, and a predominance of Cu-sulfide minerals (e.g., bornite and chalcopyrite) over Fe-sulfide minerals (e.g., pyrite and marcasite; Lowell and Guilbert, 1970; Sillitoe, 2000). The potassic alteration zone in Lienetz has an unusually profuse amount of pyrite and only a minute amount of Cu-sulfide minerals. This conundrum of pyrite with biotite alteration could be attributed to overprinting of epithermal mineralization upon early formed porphyry-style alteration, where pyrite nucleated on and/or replaced chalcopyrite and/or magnetite. The abundance of pyrite grains with large sizes and relatively trace element-poor concentrations, however, makes this scenario unlikely; these pyrite grains are interpreted to have formed under early porphyry-style conditions. Another possibility is that the magmatic-hydrothermal fluids associated with the early porphyry-style potassic alteration were only rich in Fe, S and As, and lacked Cu. This is common in alkalic porphyry Au deposits with little or no Cu (Richards, 1995). A third possibility is that Cu-sulfide minerals may be deeper within the deposit, and Lienetz is only the top of a much broader zone of potassic alteration relating to a large porphyry Au ± Cu deposit at depth. Potassic alteration zones can be greater than 1 km wide and 1 km high with only a relatively small mineralized core (e.g., Seedorff et al., 2005), and it is common in porphyry Cu deposits to have zoning with Au/Cu ratios increasing upward and outward (Richards, 1995; Sillitoe, 2000).

6.7: Conclusions

Pyrite crystals from the anhydrite zone at the Lienetz orebody of Lihir gold deposit display strong textural and geochemical variations that relate to their conditions of formation and subsequent modification events. The LA-ICP-MS imaging combined with NaOCl staining appears to be powerful method of investigation of pyrite zonation. The features revealed by these methods provide insights into the nature of the mineralizing fluids. Early generations of pyrite grains (i.e., V1) formed under higher temperature porphyry-style conditions. These pyrite grains are relatively large and uniform in zoning. Later generations of pyrite grains (i.e., $V3_{adu}$ and $V4_{qtz}$) formed under lower temperature epithermal conditions, and vary in form but commonly display spectacular oscillatory zones. Comparative to one another, epithermal-stage pyrite grains are enriched in As, Mo, Ag, Sb, Au and Tl, whereas porphyry-stage pyrite grains are depleted in most trace elements, except for Co, Ni and Se.

Composite, relatively coarse-grained pyrites are the most common within the anhydrite zone at Lienetz. These composite pyrite grains are interpreted to be porphyry-stage pyrite grains that were modified during the subsequent evolution of the Lihir gold deposit. They commonly have corroded and dissolved rims and central cavities, textures indicative of dissolution, followed by epithermal-style pyrite overgrowth. Rim on these pyrite grains, compared to their cores, are enriched in As, Mo, Sb, Au, Tl and Pb.

Because most (i.e., ~ 80%) of the gold occurs within pyrite at Lihir, the effected extraction of gold during mineral processing is strongly dependent on paragenetically and texturally controlled gold deportment. The composite pyrite grains have gold and other trace elements only enriched in rims with local Au – Ag – Te inclusions, whereas epithermal-stage pyrites are enriched in gold throughout their lattice and contain Au – Ag – Te inclusions. The composite pyrite grains can be subjected to a shorter period of oxidation and leaching to liberate most of their gold from the rims. For areas dominated by epithermal-stage mineralization, pyrite grains need to be fully oxidized in order to liberate the gold from their entire crystal lattice. This has not only important implications for the Lihir gold deposit, but also for porphyry Au ± Cu deposits and associated epithermal gold deposits worldwide, where overprinting by subsequent hydrothermal fluid may enrich only the rims of sulfide minerals with gold.

CHAPTER 7: SULFUR AND STRONTIUM ISOTOPES

7.1: Introduction

Although the Lihir gold deposit has many features of a low-sulfidation, alkalic, epithermal Au deposit, there is evidence of an early magmatic-hydrothermal (i.e., porphyry-style) component during its evolution, characterized by biotite – K-feldspar alteration (Carman, 1994). Lihir formed adjacent to the Pacific Ocean, and the widely accepted model for the formation of Lihir involves seaward-directed sector collapse (e.g., Sillitoe, 1994). It is therefore possible that the ingress of seawater, either catastrophically or incrementally, could help to explain the abundant anhydrite and/or pyrite at Lihir (e.g., Carman, 2003; Gemmell et al., 2004).

This chapter reports new sulfur isotope data for sulfate and sulfide samples from the Lienetz orebody, and the broader Lihir gold deposit. The new data are discussed in the context of all previous work on sulfur and strontium isotopes. The aims are to investigate the source(s) of sulfur for sulfate and sulfide minerals, and if mineralizing fluids evolved isotopically from porphyry-style to epithermal conditions.

7.2: Sulfur in magmatic-hydrothermal ore deposits

Sulfur in magmatic-hydrothermal ore systems is commonly derived from an igneous source (e.g., Wilson et al., 2007). In some cases, however, a component of sulfur may be obtained by leaching of sulfur-bearing wall rocks (e.g., Ohmoto and Rye, 1979). In contrast, a seawater sulfur source can be significant for rocks deposited in submarine settings (e.g., volcanic-hosted massive sulfide deposits; Ohmoto and Rye, 1979; Ohmoto and Skinner, 1983). Sulfur derived from an igneous source (i.e., magma), may be transported as volatile sulfur species such as sulfur dioxide (SO_2) or hydrogen sulfide (H_2S; Ohmoto and Rye, 1979; Carroll and Webster, 1994). The dominant sulfur species in magmatic-hydrothermal fluids will therefore be predominantly in the form of oxidized sulfate (e.g., SO_4^{2-}) or reduced sulfide (e.g., H_2S^{2-}). These sulfur species can coexist in hydrothermal fluids, with the ratio of sulfide to sulfate largely depending on the oxidation state, although temperature and pressure are also factors (Katsura and Nagashima, 1974; Burnham, 1979; Ohmoto and Rye, 1979; Whitney, 1984; Ohmoto, 1986; Carroll and Rutherford, 1987; Carroll and Webster, 1994; Symonds et al., 1994). As magmatic-hydrothermal fluids cool and/or magmatic volatiles ascend towards the brittle-ductile transition zone (i.e., < 400°C; Fournier, 1999), SO_2 can react with H_2O, via reaction 7.1 and disproportionate to H_2S and H_2SO_4 (Holland, 1965; Burnham, 1979):

$$4\ SO_{2(g)} + 4\ H_2O_{(l)} \leftrightarrow 3\ H_2SO_{4(aq)} + H_2S_{(aq)} \qquad (7.1)$$

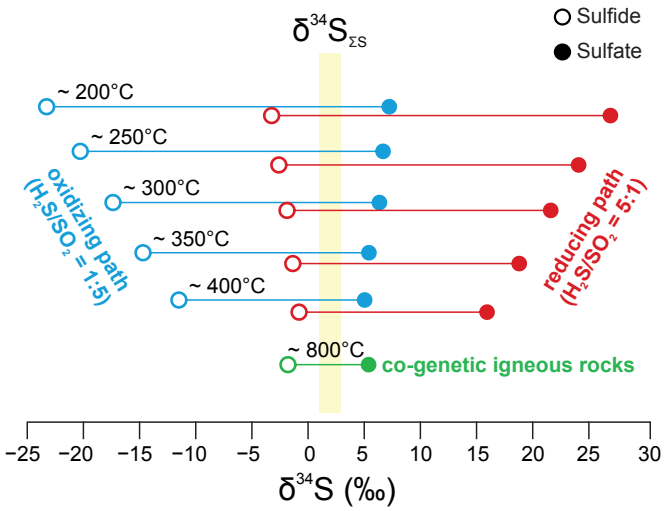

Figure 7.1: Idealized $\delta^{34}S$ of co-existing sulfides and sulfate minerals, modified from Rye (1993). Diagram reflects a disproportionation of magmatic fluid with initial $H_2S/SO_2 = 1$, under more reducing and oxidizing paths. Bulk sulfur ($\delta^{34}S_{\Sigma S}$) is derived from co-genetic igneous rocks, and is assumed to remain constant.

Any H_2SO_4 formed by reaction 7.1 can react with plagioclase and other Ca-bearing minerals in the wall rocks to precipitate anhydrite. The H_2S formed by reaction 7.1 can react with iron and/or cause aqueous metal chloride species to dissociate, resulting in the precipitation of pyrite and other metal-sulfides (Holland, 1965). Disproportionation will result in enrichment of ^{34}S in H_2SO_4 which will react to from sulfate minerals. The lighter ^{32}S isotope partitions into H_2S, which can react to form sulfide minerals (Ohmoto and Rye, 1979). Fractionation between sulfate and sulfide increases with decreasing temperatures, and is dependent on the oxidation state of the fluid (Figure 7.1; Ohmoto and Rye, 1979; Rye, 1993). Assuming constant bulk sulfur (e.g., magmatic sulfur 0 ± 5 ‰ $\delta^{34}S$), variations within sulfur isotopes will reflect only changes in temperature and oxidation state of fluids after their exsolution from the magma (Figure 7.1; Ohmoto and Rye, 1979). Typically $\delta^{34}S$ values of sulfide (i.e., $\delta^{34}S_{sulfide}$) decrease markedly when precipitated form a cooling oxidizing (sulfate-predominant) fluid, whereas $\delta^{34}S$ values of sulfate (i.e., $\delta^{34}S_{sulfate}$) values will only increase slightly with cooling (Figure 7.1; Rye, 1993). The opposite occurs where deposition occurs from a reducing, H_2S-predominant fluid (Figure 7.1). However, if one sulfur species was produced from the other by oxidation or reduction, or if both species were produced from another compound (e.g., dissolution of pyrite), then the isotopic relationship will be controlled by kinetic isotopic effects, because the chemical reactions are mass dependent, such that the lighter isotope will react faster (Ohmoto and Rye, 1979).

In studies of magmatic-hydrothermal ore deposits such as porphyry Cu deposits, the sulfur source is typically igneous, and $\delta^{34}S$ of sulfides and sulfates generally have $\delta^{34}S_{sulfide}$ values of −3 to +1 ‰ and $\delta^{34}S_{sulfate}$ values of +8 to +15 ‰ (Ohmoto and Rye, 1979). Notable deviations from the trend include more negative $\delta^{34}S_{sulfide}$ values with wider ranges for systems that formed under more oxidizing conditions, such as alkalic porphyry Cu ± Au deposits (e.g., Cadia – Wilson et al., 2007; Galore Creek – Micko, 2010; Mount Polley – Pass et al., 2014). In contrast, deposits that formed under more reducing conditions can have positive $\delta^{34}S_{sulfide}$ values with a narrower range (e.g., deposits in the Baguio district – Cooke et al., 2011). If an evaporitic or seawater source is involved, then both $\delta^{34}S_{sulfide}$ and $\delta^{34}S_{sulfate}$ values can be higher (e.g., Morococha; Petersen, 1972), as is typical of submarine volcanic-hosted massive sulfide deposits (Rye and Ohmoto, 1974).

7.3: Previous work

Previous isotopic studies of sulfide and sulfate minerals at the Lihir gold deposit includes 147 $\delta^{34}S$ analyses and 7 $^{87}Sr/^{86}Sr$ analyses (Table 7.1) The historic data set includes 76 $\delta^{34}S$ analyses of pyrite, marcasite and anhydrite from Carman (1994), 17 $\delta^{34}S$ analyses of anhydrite, pyrite and native sulfur, and five $^{87}Sr/^{86}Sr$ analyses of anhydrite from Hannington (unpublished data from Gemmell et al., 2004), 12 $\delta^{34}S$ analyses of anhydrite from Blackwell (unpublished data from Blackwell, 2010), 31 $\delta^{34}S$ analyses of pyrite and anhydrite from Müller et al. (2002a), two $^{87}Sr/^{86}Sr$ analyses of anhydrite from Müller et al. (2002b), 8 $\delta^{34}S$ analyses of pyrite from Gemmell et al. (2004), and three $\delta^{34}S$ analyses of alunite from Jansen (unpublished data, 2012). All previous studies used the conventional technique described below, with the exception of Carman (1994). Details on Carman (1994)'s two different techniques (i.e., combustion laser ablation and SHRIMP; Table 7.1), are provided in Carman (1994). All of the isotopic results from previous studies have been combined with new results, shown below. All previous isotopic results, together with detailed descriptions and locations (if possible), are provided in Appendix 4 and summarized in Table 7.1.

Table 7.1: Compilation and techniques of all sulfur isotope studies from the Lihir gold deposit

Source	Mineral	Number of samples	Technique	Spot size (mm)	average $\delta^{34}S_{CDT}$ (‰)	Average precision (‰)
Carman (1994)	anh	3	SHRIMP[1]	0.030	13	2
Hannington (unpublished data from Gemmell et al. (2004))	anh	10	Conventional	1 to 2	12.7	0.1 to 0.3
Müller et al. (2002a)	anh	3	Conventional	1 to 2	9.4	0.1 to 0.3
Blackwell (unpublished data, 2008)	anh	12	Conventional	1 to 2	12.5	0.1 to 0.3
This study, plus samples from Carman (1994), Ageneau (2012) and Lawlis (in prep.)	anh	47	Conventional	1 to 2	9.7	0.1 to 0.3
Carman (1994)	py ± mrc	62	Combustion laser ablation	0.10 to 0.25	−2.8	0.2 to 0.5
Carman (1994)	py ± mrc	11	SHRIMP[1]	0.030	−6.3	2
Gemmell et al. (2004)	py	8	Conventional	1 to 2	−6.3	0.1 to 0.3
Hannington (unpublished data from Gemmell et al. (2004))	py ± mrc	4	Conventional	1 to 2	−7.4	0.1 to 0.3
Müller et al. (2002a)	py	28	Conventional	1 to 2	−3.9	0.1 to 0.3
This study, plus samples from Herrmann (unpublished data, 2003), Blackwell (2010), Ageneau (2012) and Lawlis (in prep.)	py	21	Conventional	1 to 2	−6.8	0.1 to 0.3
This study	py	6	LA-ICP-MS	0.043	−5.4	1.4
This study	py	16	SHRIMP[2]	0.025	−3.2	0.2
This study	ba	1	Conventional	1 to 2	9.7	0.1 to 0.3
Jansen (unpublished. report, 2012)	alu	3	Conventional	1 to 2	−1.2	0.1 to 0.3
Hannington (unpublished data from Gemmell et al. (2004)	native S	3	Conventional	1 to 2	−6.5	0.1 to 0.3

Superscript numbers represent different SHRIMP methods, explained in [1] = Eldrige et al. (1987) and [2] = Ireland et al. (2008).

7.4: Methods

A total of 91 $\delta^{34}S$ analyses of sulfate and sulfide minerals were performed in this study (Table 7.1). This included 63 analyses of paragenetically constrained samples from Lienetz as part of the current study, and 28 analyses of samples from previous worker's collections: one sample from Carman (1994)'s collection; three samples from Herrmann (unpublished data, 2003); two samples from Blackwell (2010); six samples from Ageneau (2012), and; 16 samples from Lawlis (in prep.; Table 7.1). All sample locations are provided in Appendix 4. Sulfur isotopes analyses were obtained by one of the following techniques: (1) Conventional combustion (n = 69); (2) LA-ICP-MS (n = 6); or (3) SHRIMP (n = 16). Isotopic data are reported as $\delta^{34}S_{CDT}$ values (per mil ‰) relative to the Canyon Diablo Troilite (CDT) standard (Thode et al., 1961), as shown in equation 7.2.

$$\partial^{34}S_{CDT}\ (‰) = [((^{34}S/^{32}S)_{sample}/(^{34}S/^{32}S)_{V\text{-}CDT} - 1) \times 1000] \qquad (7.2)$$

Conventional analyses of $\delta^{34}S$ were completed at the Central Science Laboratory, University of Tasmania, Australia. Sulfur isotopes were analyzed from 36 sulfate samples (i.e., 35 anhydrite and one barite), and 11 sulfide samples (i.e., pyrite ± marcasite) from paragenetically constrained samples obtained during mapping and/or core logging of the Lienetz orebody (e.g., Table 4.2). An additional 12 sulfate samples (i.e., anhydrite) and 16 sulfide samples (i.e., pyrite ± marcasite) were analyzed conventionally from historic samples of Carman (1994), Herrmann (unpublished report, 2003), Ageneau (2012), and Lawlis (in prep.). For conventional analysis, anhydrite or pyrite was extracted from fist-sized hand samples and drill-core slabs using a small (~ 1 mm diameter) dental drill. Approximately 1 g of powder was collected and weighed into calibrated tin cups. The samples were then flash burnt to produce SO_2 gas. The technique used a NCS combustion schematic and "purge and trap" technique. An IsoPrime100 IRMS was used to measure the SO_2 gas signal and $\delta^{34}S$ isotope ratios. Individual conventional analyses had a precision of 0.1 to 0.3 ‰. More details on the analytical technique are provided in Robinson and Kusakabe (1975).

Due to the small grain sizes of pyrite, and geochemical evidence for significant variation in trace element compositions of composite pyrite grains, microscopical techniques were used to obtain $\delta^{34}S_{sulfide}$ values from growth zones within pyrite grains. Pyrite grains from six samples were analyzed for both cores and rims, using either the LA-ICP-MS or SHRIMP methods.

Six in situ analyses for $\delta^{34}S_{sulfide}$ were completed for four samples by laser ablation-inductively coupled plasma-mass spectrometry (LA-ICP-MS) at CODES, University of Tasmania, Australia. Samples were placed on a 2.5 cm wide circular puck. Each pyrite grain analysis consisted of eight laser spots. Two pyrite grain analyses were in relatively homogeneous regions of pyrite grains, interpreted to be representatives of end-member porphyry- and epithermal-stages. The cores and rims of four pyrite grains were analyzed to assess within-grain isotopic variability. The details of the equipment and setting for the LA-ICP-MS analyses

are as follows, Agilent 7700 ICP-MS using 10% Xe in He mix collision cell gas at 0.5 ml min-1 flow rate, and tuned so that all ^{32}S signals were measured in pulse mode. The ICP-MS was coupled to a Resolution (Australian Scientific Instruments) S155 193 nm excimer laser ablation system using 2.7 J cm^{-2} fluence, pulse rate of 10 Hz and beam size was 43 μm. The interface tubing between the laser sample chamber and the ICP-MS consisted of a 'squid', a glass bulb (~ 6 cm^3) and a coil of small diameter Tygon tubing. This combination provided the most signal smoothing for improved precision and fastest washout of sulfur between analyses. Each laser spot measurement consisted of background measurements for 30 seconds, laser signal collection for 60 seconds and 60 seconds of wait between analyses for background sulfur to washout. The primary standard for mass bias correction was Peru Pyrite, and secondary standards were 660 and C50 pyrites (Gilbert et al., 2014). Individual LA-ICP-MS analyses had an average precision of 1.4 ‰ (2σ, i.e., 95% confidence interval). For more information on this technique and operational procedures, see Gilbert et al. (2014).

Results are reported as weighted mean $\delta^{34}S$, 2σ error and MSWD. The MSWD is a statistical comparison between the variation in the samples and the individual errors bars. If MSWD < 1 then the error bars cover the range of data and the sample is homogeneous. If MSWD > 1 then the variation between analyses is larger than the errors bars and the sample is heterogeneous or bimodal.

The cores and rims of eight composite pyrite grains from two samples were additionally analyzed in situ for $\delta^{34}S_{sulfide}$ (i.e., total of 16 analyses) using the sensitive high resolution ion microprobe (SHRIMP) at the Australian National University, Canberra, Australia. Samples were placed in a 2.5 cm wide circular puck. This was coated with 0.01 μm of gold prior to analysis in order to dissipate charge build-up and provide ~ 10 kV of energy to ensure the ablated ions have the correct potential. The beam spot size was 25 μm with a Cs+ beam source (10 keV). Average count rates were 630 MHz (^{32}S) and 28 MHz (^{34}S). Each measurement consisted of 10 cycles with 10 seconds of data acquisition in each cycle. S-isotopes were detected and measured using multiple Faraday cups (e.g., Ireland et al., 2008). Pre-ablation of the samples was run for 120 seconds prior to analysis. Standards were analyzed twice every ~ seven analyses, using Balmat pyrite as the primary standard (Crowe and Vaughan, 1996; Williford et al., 2011) and an in-house pyrite standard from New Zealand ($\delta^{34}S_{sulfide}$ ~ 4 ± 0.1 ‰). Individual SHRIMP-SI analyses had a precision of 0.2 ‰ (2σ). For more information on this technique and operation procedures, see Ireland et al. (2008).

No geothermometry was done of sulfide-sulfate pairs due to one or more of the follow requirements not being met: (1) both mineral phases were formed in equilibrium; (2) no isotopic exchange took place between the mineral phases or between mineral phases and a fluid phase after the formation of the mineral (i.e., original isotopic composition was frozen in); (3) pure mineral phases were separated for isotopic analysis (Ohmoto and Rye, 1979).

7.5: Results

A total of 47 $\delta^{34}S_{sulfate}$ analyses of anhydrite from paragenetically constrained vein stages from Lienetz (n = 35), together with samples from Carman (1994), Ageneau (2012) and Lawlis (in prep.)'s collections (n = 12), are shown in Table 7.2 and Figure 7.2A. Overall $\delta^{34}S_{sulfate}$ has a narrow range, from 7.2 to 13.0 ‰, with a median of 9.8 ‰ and 1σ = 1.3 ‰ (Table 7.2, Figure 7.2A). Figure 7.2B shows only the paragenetically constrained sample from this study (n = 35). There is a moderate +1.3 ‰ enrichment of $\delta^{34}S_{sulfate}$ in vein stages $V3_{adu}$, $V4_{qtz}$ and $V1_{M2}$, relative to stages $V1_{bio}$, $V1_{ksp}$ and $V1_{M1}$ (Table 7.2, Figure 7.2B).

A total of 27 $\delta^{34}S_{sulfide}$ analyses of pyrite ± marcasite of paragenetically constrained vein samples from Lienetz is shown in Figure 7.3. Overall, the $\delta^{34}S_{sulfide}$ values have a large range, from −1.6 to −8.9 ‰ (Figure 7.3). The duplicate conventional and LA-ICP-MS analyses of one pyrite grain from $V1_{bio}$ overlap within error with $\delta^{34}S_{sulfide}$ values of −8.7 ± 0.4 ‰ and −8.0 ± 1.0 ‰ (Figure 7.3). The core of the composite pyrite grain from $V1_{M2}$ has a similar $\delta^{34}S_{sulfide}$ value of −7.8 ± 1.0 ‰ (Figure 7.3).

Duplicate conventional and LA-ICP-MS analyses of one pyrite grain from $V3_{adu}$ had $\delta^{34}S_{sulfide}$ values inconsistent with one another (−8.9 ± 0.4 ‰, −6.0 ± 1.0 ‰; Figure 7.3). A pyrite grain from $V4_{qtz}$ also was different from the $V3_{adu}$ values, with −3.5 ± 0.4 ‰ (Figure 7.3).

Composite pyrite grain's cores and rims from $V1_{M1}$ and $V1_{M2}$ stages have the widest range of $\delta^{34}S_{sulfide}$ values, from −1.6 to −7.8 ‰ (Figure 7.3). The median $\delta^{34}S_{sulfide}$ value is −3.6 ‰, with the most precise median $\delta^{34}S_{sulfide}$ value obtained from the SHRIMP analyses of −3.1 ± 0.3 ‰ (Figure 7.3). A significant variation from the core to rim was detected in one $V1_{M2}$ sample (i.e., "d"; Figure 7.3). The core's $\delta^{34}S_{sulfide}$ value was −7.8 ± 1.0 ‰ (MSWD = 1.2) and the rim was −1.6 ± 1.1 ‰ (MSWD = 1.2). In contrast, one sample of $V1_{M1}$ had a smaller core-rim variation from −4.8 ± 2.6 ‰ (MSWD = 4.7) to −4.3 ± 1.9 ‰ (MSWD = 2.8; Figure 7.3). Both the error and MSWD were significantly larger within this sample, implying that it has a heterogeneous or bimodal composition, which is consistent with the pyrite grain's irregular form (e.g., Figure 6.1H–I). Two additional samples of $V1_{M2}$ yielded 16 core and rim values, summarized as core and rim pairs with a mean ($\bar{x}$) and 1σ calculate from the variance (Figure 7.3). Overall there is small variation in $\delta^{34}S_{sulfide}$ values for these cores and rims, averaging −0.1 ‰ difference (Figure 7.3). These samples have similar irregular pyrite grain forms (e.g., Figure 6.1H–I).

Table 7.2: Statistics of $\delta^{34}S_{sulfate}$ values (‰) from all anhydrite analyzed in this study

$\delta^{34}S_{sulfate}$ (‰)	all	$V1_{bio}$ and $V1_{ksp}$	$V1_{M1}$	$V3_{adu}$ + $V4_{qtz}$	$V1_{M2}$
Number of samples	47	8	18	7	2
Minimum	7.2	7.2	7.6	9.0	9.8
Maximum	13.0	10.5	11.0	12.2	10.1
Median	9.8	8.8	9.0	10.4	9.9
Mean	9.7	9.0	9.2	10.5	9.9
Standard deviation (1σ)	1.3	1.0	0.9	1.1	0.2

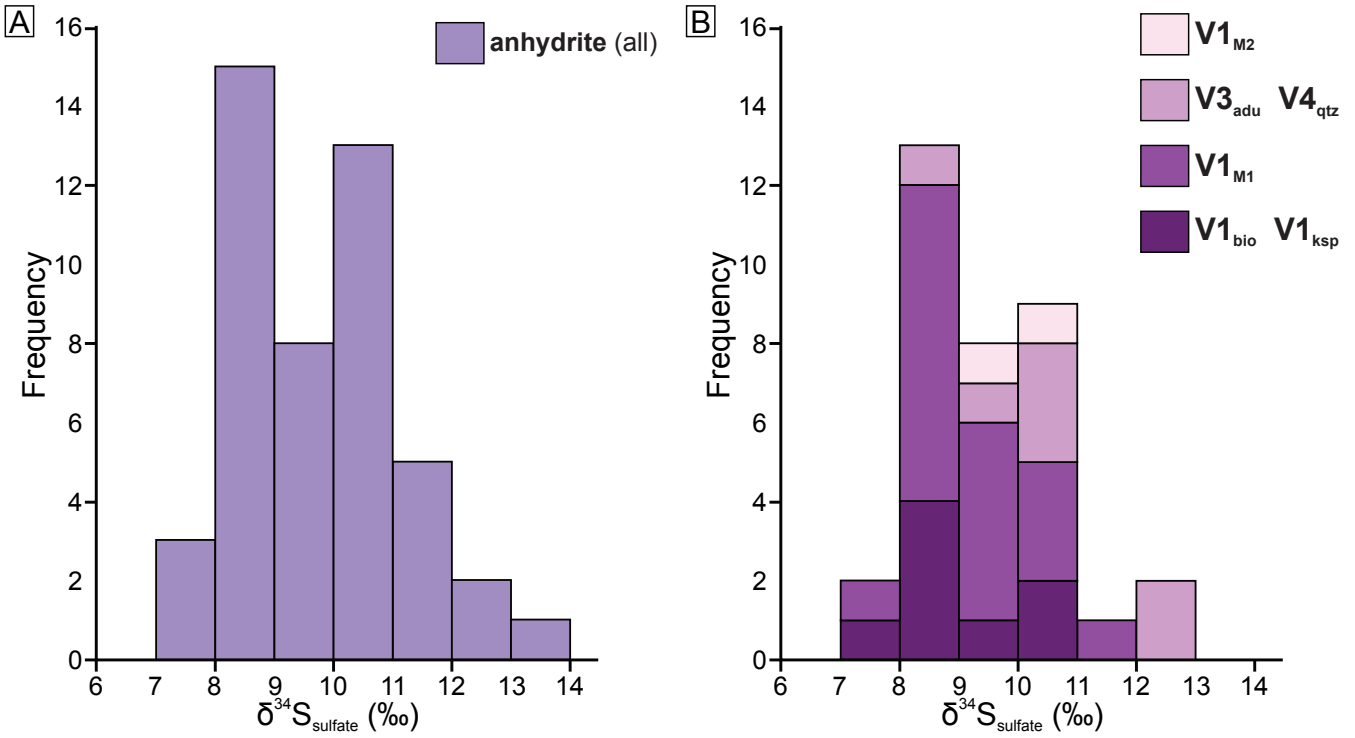

Figure 7.2: Histograms of $\delta^{34}S_{sulfate}$ values (‰) of anhydrite from this study. A) $\delta^{34}S_{sulfate}$ values of anhydrite from Lienetz, Minifie, Kapit and Kapit NE orebodies, including 35 samples collected in this study, and 12 historic samples from Carman (1994), Ageneau (2012) and Lawlis (in prep.). **B)** $\delta^{34}S_{sulfate}$ values of anhydrite from samples collected in this study, subdivided by paragenetic stage.

The combined $\delta^{34}S_{sulfide}$ and $\delta^{34}S_{sulfate}$ values from the Lihir gold deposit (n = 238) are shown in Table 7.3 and Figure 7.4. The $\delta^{34}S_{sulfide}$ values vary from −13.0 to 3.6 ‰, with a median of −3.9 ‰ (Table 7.3, Figure 7.4). The $\delta^{34}S_{sulfate}$ values have a narrow range from 7.2 to 13.6 ‰ (within 3σ), with a median of 10.4 ‰ (Table 7.3, Figure 7.4).

The spatial variations in plan view of $\delta^{34}S$ values of sulfides and sulfates throughout the various orebodies of the Lihir gold deposit is shown in Figure 7.5. For $\delta^{34}S_{sulfate}$ the consistently higher values are from the Minifie and Coastal orebodies, whereas consistently lower $\delta^{34}S_{sulfate}$ values are largely from Lienetz, and possibly also from the northwest area of the amphitheater (Figure 7.5A). High $\delta^{34}S_{sulfate}$ values, however, are locally present at Lienetz (Figure 7.5A). For $\delta^{34}S_{sulfide}$, trends are less evident, although consistently lower values appear to be more common around Borefields and Kapit NE (Figure 7.5B). Overall, lower values of

Table 7.3: Statistics of $\delta^{34}S$ values (‰) from sulfates, sulfides and native sulfur of the Lihir gold deposit

	anhydrite[1, 2, 4, 5, 7]	pyrite ± marcasite[1, 2, 3, 4 , 7]	alunite[6]	barite[7]	native sulfur[4]
Number of samples	75	156	3	1	3
Minimum	7.2	−13.0	−3.0	9.7	−7.3
Maximum	21.4	3.6	0.0	9.7	−5.0
Median	10.4	−3.9	−0.5	9.7	−7.2
Mean	10.7	−4.2	−1.2	9.7	−6.5
Standard deviation (1σ)	2.4	3.2	1.3	0.0	1.1

Compiled samples from: [1] = Carman (1994), [2] = Müller et al. (2002a), [3] = Gemmell et al. (2004), [4] = Hannington (unpublished data from Gemmell et al., 2004), [5] = Blackwell (unpublished data from Blackwell, 2010), [6] = Jansen (unpublished data, 2012) and [7] = this study.

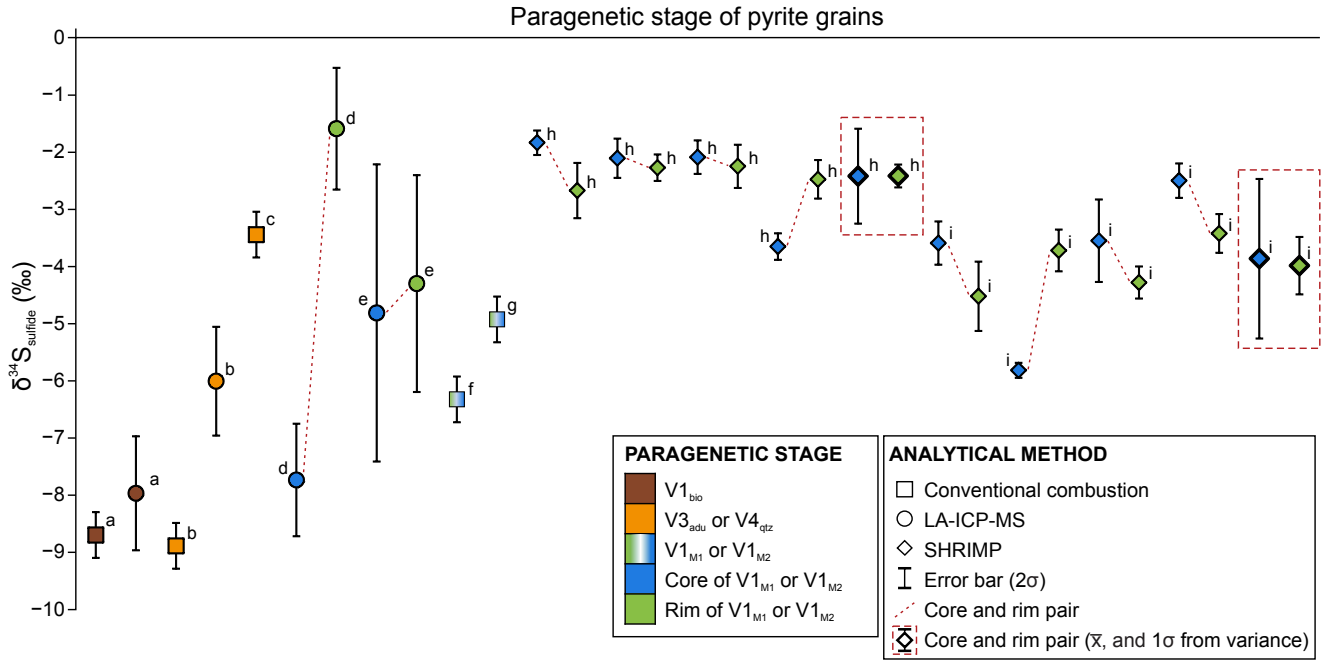

Figure 7.3: Graph of $\delta^{34}S_{sulfide}$ values (‰) of pyrite as a function of paragenetic stage. This figure also compares the three different analytical methods used to generate $\delta^{34}S_{sulfide}$ data (i.e., conventional combustion, LA-ICP-MS and SHRIMP). Superscript letters represent samples as follows: [a]LH14SS051, [b]LI12EL002B, [c]DDHL1174_286.7m, [d]LH13SS003, [e]LH13SS069, [f]LH14SS035, [g]LH14SS094, [h]LH13SS050, [i]LH13SS031.

$\delta^{34}S_{sulfide}$ characterize the high-grade gold areas at Lienetz, with high values in the periphery (Figure 7.5B). Although some trends are evident in $\delta^{34}S_{sulfate}$ and $\delta^{34}S_{sulfide}$ values within different orebodies, paragenetic stages could not be broken out from this vast historic data. The complexity of overprinting porphyry- and epithermal-stages may therefore have obscured any spatial trends in the data.

7.6: Discussion

Overall $\delta^{34}S_{sulfate}$ values of 7.2 to 13.6 ‰ (within 3σ) at Lihir are consistent with those from alkalic porphyry Cu-Au deposits ± porphyry Cu deposits (Figure 7.4). The $\delta^{34}S_{sulfide}$ values of −13.0 to 3.6 ‰ are most consistent with alkalic porphyry Cu-Au deposits and alkalic-type epithermal Au deposits (Figure 7.4). The results are consistent with the classification of Lihir as a hybrid alkalic porphyry and epithermal deposit. They also have significant implications for fluid sources.

In general, previous interpretations by Carman (1994, 2003) and Müller et al. (2002b) of $\delta^{34}S_{sulfide}$ and $\delta^{34}S_{sulfate}$ values, combined with results from $\delta^{18}O_{H2O}$ and $^{87}Sr/^{86}Sr$ values, suggested a magmatic-dominant, oxidized fluid source. However, two $\delta^{34}S_{sulfate}$ values reported in Gemmell et al. (2004) raised the possibility of a seawater component for the source of sulfur. Carman (2003) also documented a decrease in $\delta^{34}S_{sulfide}$ values from the porphyry- to epithermal-stage pyrite grains at Lihir, and interpreted this to be a change in depositional conditions and/or fluid chemistry, possibly due to increasing oxidation state or decreasing temperature or boiling.

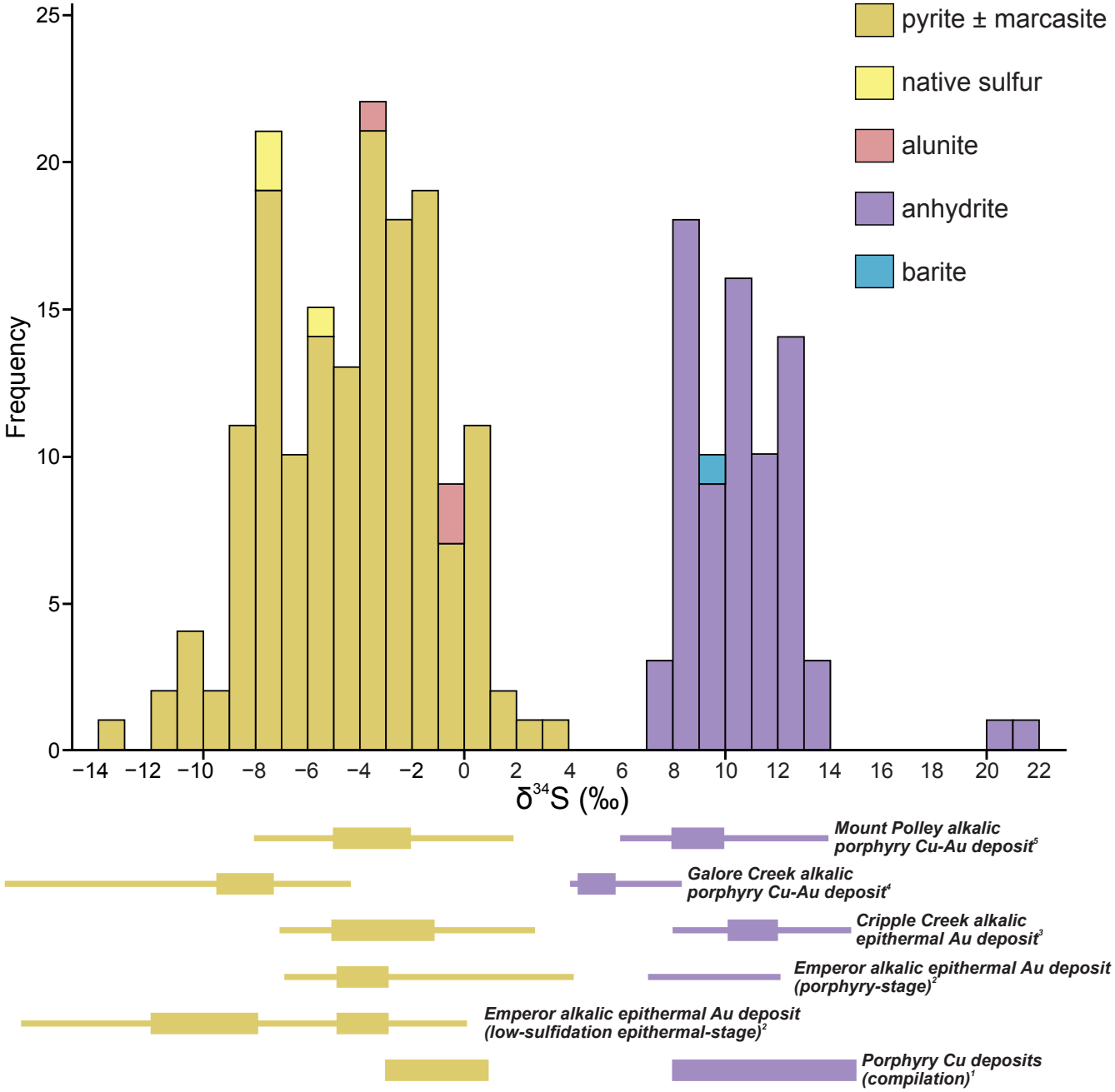

Figure 7.4: Histogram of all $\delta^{34}S$ values (‰) of sulfates, sulfides and native sulfur from the Lihir gold deposit, and comparison to other deposits. Data compiled from Carman (1994), Müller et al. (2002a), Gemmell et al. (2004), Hannington (unpublished data from Gemmell et al., 2004), Blackwell (unpublished data from Blackwell, 2010), Jansen (unpublished data, 2012) and this study. All data are listed in Appendix 4. Below the histogram are lines which represent $\delta^{34}S$ values from other ore deposits, for comparison. Superscript numbers represent data compiled from the following: [1]Ohmoto and Rye (1979), [2]Begg (1996); [3]Jensen (2003), [4]Micko (2010), and [5]Pass et al. (2014).

7.6.1: Sulfur and strontium sources

Modern seawater $\delta^{34}S$ values are 21 ‰ (Rees et al., 1978). Modern barite deposits from Holocene core-top sediments from the Atlantic, Pacific and Indian oceans are comparable with $\delta^{34}S_{sulfate}$ values ~ 21 ‰ (Paytan et al., 1998). Likewise, modern gypsum from evaporites have $\delta^{34}S_{sulfate}$ values around 20 ‰ (Thode and Monster, 1965; Claypool et al., 1980). Seawater $\delta^{34}S$ values has only varied ~ 1 ‰ since the Pliocene (e.g., Paytan et al., 1998), therefore, if sulfate at Lihir was sourced from seawater, then $\delta^{34}S_{sulfate}$ values should be close to ~ 21 ‰. Since anhydrite at Lihir has a median $\delta^{34}S_{sulfate}$ value of 10.4 ‰, it is unlikely

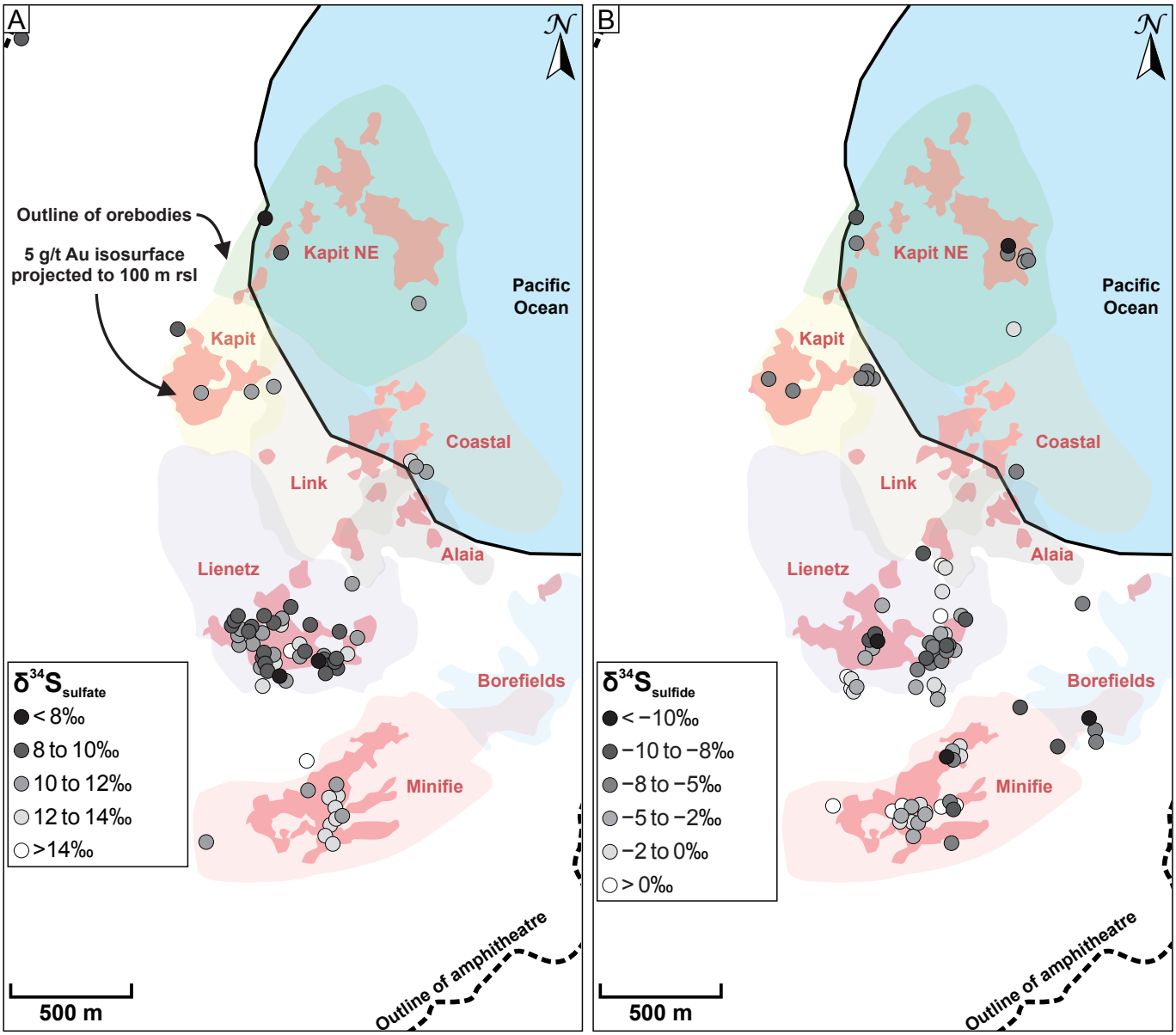

Figure 7.5: Spatial distribution of $\delta^{34}S$ values of pyrite and anhydrite from the Lihir gold deposit. Locations are from previous studies and this study. All data listed in Appendix 4. **A)** $\delta^{34}S_{sulfate}$ values of anhydrite. **B)** $\delta^{34}S_{sulfide}$ values of pyrite ± marcasite.

that seawater was the main source of sulfur. Two samples analyzed by Hannington (reported in Gemmell et al., 2004) are exceptions to this, with $\delta^{34}S_{sulfate}$ values of 20.7 and 21.4 ‰ (Figure 7.4). Assuming a normal distribution, the two values are over 4σ from the mean $\delta^{34}S_{sulfate}$ value, and therefore could be considered statistical outliers and not representative of $\delta^{34}S_{sulfate}$ values of the Lihir gold deposit. Although they are outliers, compositions are similar to $\delta^{34}S$ values of modern seawater, and imply a seawater component locally at Lihir.

Strontium isotopes can be used to trace the potential sources of hydrothermal fluids in ore deposits (e.g., Richards et al., 1991). Analysis for both $\delta^{34}S_{sulfate}$ and $^{87}Sr/^{86}Sr$ of seven anhydrite samples from Lienetz and Minifie are shown in Figure 7.6; these data are from Müller et al. (2002a), Müller et al. (2002b) and Hannington (unpublished data from Gemmell et al., 2004). Figure 7.7 compares the $^{87}Sr/^{86}Sr$ results for Lihir anhydrite with $^{87}Sr/^{86}Sr$ values from volcanic rocks in the surrounding Papua New Guinea area, an-

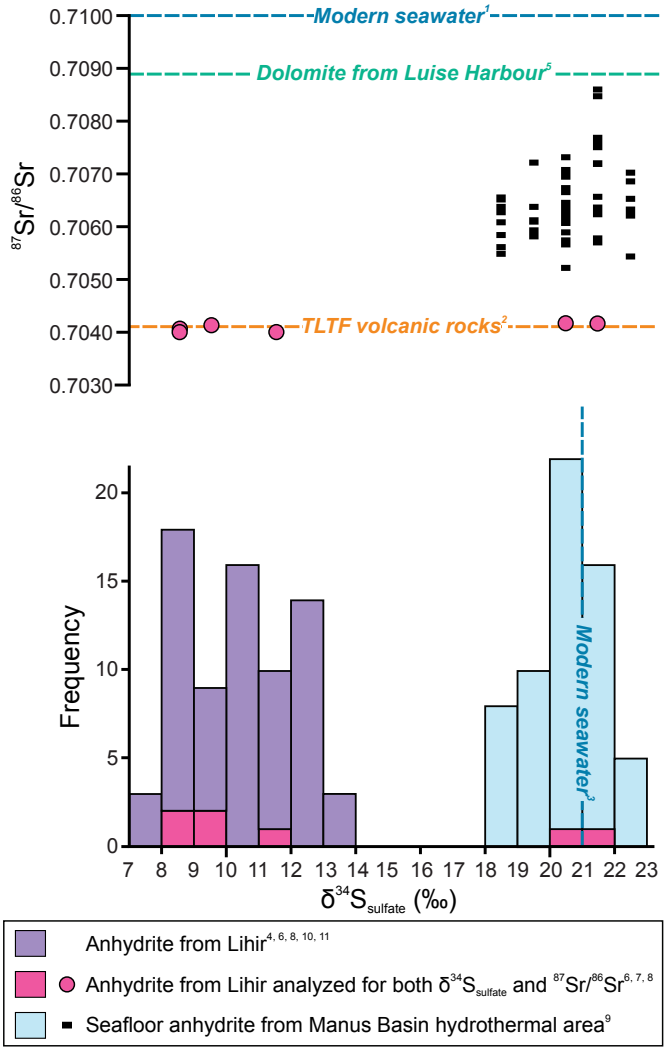

Figure 7.6: Comparison of $\delta^{34}S$ with $^{87}Sr/^{86}Sr$ values of anhydrite at the Lihir gold deposit. Plotted also are values from modern seawater, volcanic rocks, and the Manus Basin submarine hydrothermal system. Superscript numbers represent data compiled from the following: [1] = Peterman et al. (1970), [2] = Page and Johnson (1974), [3] = Rees et al. (1978), [4] = Carman (1994), [5] = Pichler et al. (1999), [6] = Müller et al. (2002a), [7] = Müller et al. (2002b), [8] = Hannington (unpublished data from Gemmell et al., 2004), [9] = Bach et al. (2007), [10] = Blackwell (unpublished data, Blackwell, 2010), [11] = this study.

hydrite from the PACMANUS hydrothermal area in the Manus Basin, and modern seawater (data from Peterman et al., 1970; Page and Johnson, 1974; Müller et al., 2002b; Hannington, unpublished data from Gemmell et al., 2004; Bach et al., 2007). The $^{87}Sr/^{86}Sr$ values of Lihir anhydrite have a narrow range, from 0.7040 to 0.7042, however, their corresponding $\delta^{34}S_{sulfate}$ values range have a wide range from 8.6 to 21.4 ‰ (Figure 7.6). Although the two high $\delta^{34}S_{sulfate}$ values are similar to modern seawater, the $^{87}Sr/^{86}Sr$ values for these samples are low (Figure 7.6). The $^{87}Sr/^{86}Sr$ values of Lihir anhydrite are similar to the volcanic rocks of the Tabar-Lihir-Tanga-Feni island chain (Figure 7.6; Page and Johnson, 1974). The results contrast markedly with data from the PACMANUS hydrothermal area in the Manus Basin, which is a submarine hydrothermal system that has progressively mixed with seawater to precipitate anhydrite (Bach et al., 2007). The anhydrite samples from the Lihir gold deposit are compositionally distinct from the mutually high $\delta^{34}S_{sulfate}$ and $^{87}Sr/^{86}Sr$ values from the Manus Basin anhydrite (Figures 7.6, 7.7). Lihir anhydrite is also distinct from the $^{87}Sr/^{86}Sr$ values of 0.70890 for dolomite (coexisting with pyrite) from the modern shallow-water hydrothermal system in the Luise Harbour (Figure 7.6; Pichler et al., 1999).

It is therefore concluded that the predominant sources of sulfur and strontium at the Lihir gold deposit are mantle-derived (i.e., 0 ± 5 ‰ $\delta^{34}S_{CDT}$; Ohmoto and Rye, 1979), and were most likely sourced from magmatic-hydrothermal fluids. This interpretation is consistent with Carman (1994) and Müller et al. (2002b)'s interpretations of a magmatic-dominant fluid source at Lihir.

7.6.2:Variation in anhydrite and pyrite with changing physicochemical conditions

The wide range of negative $\delta^{34}S_{sulfide}$ (i.e., −13.0 to 3.6 ‰) and narrow range of positive $\delta^{34}S_{sulfate}$ (i.e., 7.2 to 13.6 ‰ within 3σ) is consistent with a dominantly oxidized, magmatic source of sulfur (Ohmoto and

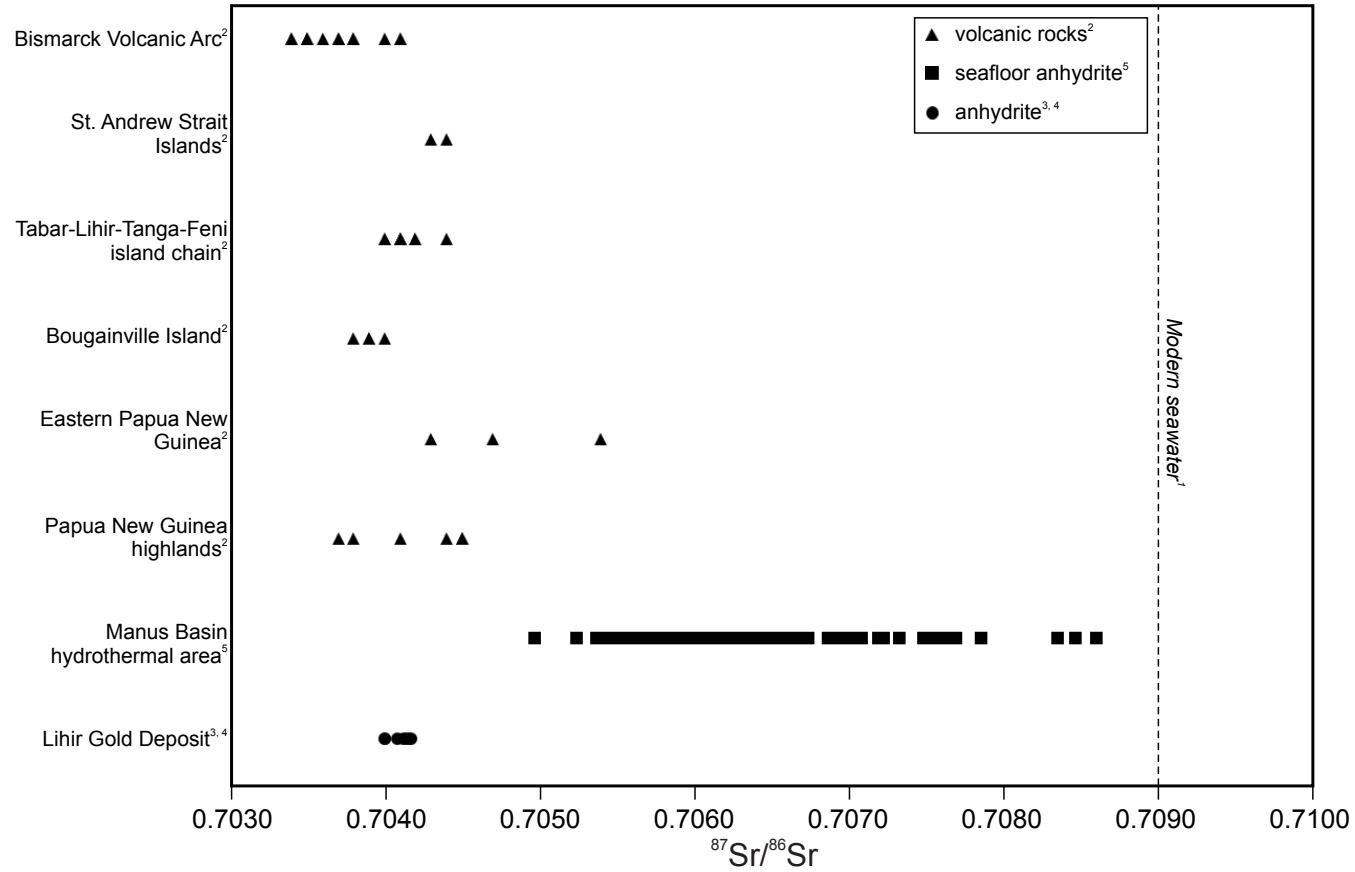

Figure 7.7: Comparison of $^{87}Sr/^{86}Sr$ values from volcanic rocks of Papua New Guinea, anhydrite of the Manus Basin submarine hydrothermal system, and anhydrite of the Lihir gold deposit. Superscript numbers represent data compiled from the following: [1] = Peterman et al. (1970), [2] = Page and Johnson (1974), [3] = Müller et al. (2002b), [4] = Hannington (unpublished data from Gemmell et al., 2004), [5] = Bach et al. (2007).

Rye, 1979; Rye, 1993). The moderate (+1.3 ‰) enrichment in $\delta^{34}S_{sulfate}$ values from the porphyry- to epithermal-stage samples is consistent with cooling of oxidized fluids with a common magmatic sulfur source (e.g., Rye, 1993). The possibility of mixing with a small component of seawater sulfur, cannot however, be totally dismissed, nor can variation in the bulk sulfur isotopic composition of the mineralizing fluid or modification due to water-wall rock interactions. Some microscopic-scale internal heterogeneity within anhydrite crystals may be present, as possible growth zones were visible under cathodoluminescence. However, overall $\delta^{34}S_{sulfate}$ values between 7.2 and 12.2 ‰ are relatively homogeneous for individual anhydrite crystals.

The small change to more positive $\delta^{34}S_{sulfate}$ in anhydrite with changing porphyry-style to epithermal conditions is consistent with the large shift to more negative $\delta^{34}S_{sulfide}$ values from porphyry- to epithermal-stage pyrite, noted by Carman (2003). Likewise, at the Emperor alkalic epithermal Au deposit, a similar progression to negative $\delta^{34}S_{sulfide}$ values was evident in the low-sulfidation epithermal stage, compared to the less negative $\delta^{34}S_{sulfide}$ values in the porphyry-stage (e.g., Figure 7.4; Begg, 1996).

Pyrite grains analyzed in this study are heterogeneous in terms of their $\delta^{34}S_{sulfide}$ values, with the largest variability in epithermal and composite pyrite grains. End-member porphyry-style pyrite grains from

$V1_{bio}$ have low $\delta^{34}S_{sulfide}$ values around −8 ‰. Epithermal pyrite grains from $V3_{adu}$ and $V4_{qtz}$, and composite pyrite grains from $V1_{M1}$ and $V1_{M2}$, have $\delta^{34}S_{sulfide}$ values varying from −1.6 to −8.9 ‰. This trend to more variability in values implies complexity either in bulk isotopic compositions of the mineralizing fluids, or water-rock interaction, as the higher temperature sulfides should be enriched in $\delta^{34}S$ relative to lower temperature pyrites of a single oxidized fluid evolved from high to low temperature (e.g., Rye, 1993; Wilson et al., 2007).

7.7: Conclusions

The $\delta^{34}S$ values of anhydrite and pyrite from the Lihir gold deposit are consistent with deposition from oxidized magmatic-hydrothermal fluids dominated by magmatic sulfur. Strontium isotopes support this interpretation, with all $^{87}Sr/^{86}Sr$ values consistent with a primitive (mantle) source. The $\delta^{34}S_{sulfate}$ values increased from porphyry-style to epithermal conditions with time. The $\delta^{34}S_{sulfide}$ values of pyrite grains vary significantly at the microscopic scale, and in time and space. While the porphyry-stage pyrite grains have fairly homogeneous $\delta^{34}S_{sulfide}$ values, the composite pyrite grains and epithermal-stage pyrites have heterogeneous or bimodal values, which is consistent with the oscillatory trace element values documented in Chapter 6.

CHAPTER 8: CONCLUSIONS

8.1: Introduction

This thesis has investigated the genesis of an enigmatic anhydrite-rich zone in the Lihir gold deposit. Its evolution was structurally controlled, with processes that operated prior to, during and after the porphyry-epithermal transition. This chapter summarizes the sequence of events that produced the Lienetz orebody. It draws together results and conclusions from the various macroscopic- to microscopic-scale studies presented in previous chapters. It places the evolution of Lienetz, as well as the entire Lihir gold deposit, into the broader geodynamic setting, highlighting the tectonic precursors relating to Lihir Island's formation and the development of the mineralized structural array. The chapter also summarizes the magmatic-hydrothermal events that formed the Lihir gold deposit. It concludes with several implications for exploration, as well as recommendations for future research.

8.2: Geodynamic evolution

Lihir Island and the Tabar-Lihir-Tanga-Feni island chain formed via a series of complex tectonic events. Oblique westward convergence of the Pacific Plate with the Australian Plate in the Paleogene led to the formation of the broad Melanesian Arc (e.g., Figure 2.1A; Gordon et al., 1978; Hall, 2002; Sharp and Clague, 2006). Subduction of oceanic crust beneath this arc caused metasomatism of the mantle wedge, leading to enrichment in lithophile and volatile elements (e.g., McInnes and Cameron, 1994; Kamenov et al., 2008). Docking of the Ontong Java Plateau with the Melanesian Trench during the Oligocene caused near-complete cessation of magmatism, and eventually led to a reversal of subduction polarity in the Miocene, forming the markedly northward-convex New Britain Trench (e.g., Figure 2.1B–C; Curtis, 1973; Falvey and Pritchard, 1982; Weissel et al., 1982; Kroenke and Rodda, 1984; Solomon, 1990; Coffin and Eldholm, 1993; Martinez and Taylor, 1996; Petterson et al., 1997; Tregoning et al., 1998; Hall, 2002; Mann and Taira, 2004; Knesel et al., 2008). Pliocene to Recent subduction along the New Britain Trench was coeval with: (1) back-arc spreading in the Manus Basin; (2) volcanism along New Britain, (3) sinistral transposition of New Ireland relative to New Britain; and (4) formation of the Tabar-Lihir-Tanga-Feni island chain (e.g., Figures 2.1C, 2.2A; Pascal, 1979; Taylor, 1979; Taylor et al., 1994; Martinez and Taylor, 1996).

The Tabar-Lihir-Tanga-Feni island lavas are shoshonitic, alkali- and volatile-rich, silica-undersaturated, and highly oxidized with elevated large-ion lithophile elements (e.g., Figure 2.9; Johnson et al., 1976; Johnson et al., 1978; Kennedy et al., 1990a; Kennedy et al., 1990b; McInnes and Cameron, 1994; Stracke and Hegner, 1998; McInnes et al., 2001; Kamenov et al., 2008). Their hybrid geochemical characteristics are consistent with partial melting of an already metasomatized, oxidized and hydrous mantle wedge origi-

nally formed by the Miocene Melanesian subduction zone (e.g., Figure 2.10; Johnson et al., 1978; Kennedy et al., 1990a; Kennedy et al., 1990b; McInnes and Cameron, 1994; Stracke and Hegner, 1998). Pliocene to Pleistocene partial melting was most likely caused by adiabatic decompression due to transtensional or extensional tectonics, or alternatively due to the development of a local deep-seated heat source (e.g., Johnson et al., 1978a; McInnes and Cameron, 1994). Volcanism occurred during progressive northwestward counterclockwise transposition and rotation of the North Bismark Plate relative to the South Bismarck Plate during the last ~ 3.5 m.y. (e.g., Figure 2.12), possibly aided by the preexisting island arc architecture associated from the paleo-Melanesian subduction zone. This scenario explains the strong statistical correlation of the Tabar-Lihir-Tanga-Feni island chain's elongation of island long-axes and the angular discordance of island long-axes from one island group to the next (e.g., Figure 2.5). It is also consistent with the apparent younging of volcanism to the southeast (e.g., Table 2.1; Figure 2.5C).

A tectonically generated northeast to east-northeast-striking structural grain underpins Lihir Island (e.g., Figure 5.1A). This is evident at both the regional- and deposit-scales (e.g., Figures 5.1, 5.3, 5.12, 5.13). Northeast- to east-northeast-striking structures localized gold mineralization, geothermal activity, and contributed to the northeast-elongation of the Luise volcanic amphitheater (e.g., Figures 5.1B, 5.12C). The fault array at Lienetz may be explained by a combination of oblique transtensional and extensional structures that were produced by transposition and counterclockwise rotation of Lihir Island during its northwestward migration over the past ~ 1 to 3 m.y. (Figure 8.1A). Dynamic movement and rotation of the island was partly facilitated by the dramatic curvature of the New Britain Trench, coupled with the sinistral transform fault that partly dissects present-day New Ireland (Figure 8.1B).

Progressive ~ 25° counterclockwise rotation led to the present day position of Lihir Island (Figure 8.1B). Steeply dipping extensional or transtensional structures rotated into the compressional field of strain, and resist modern failure. This may account for the limited number of low-magnitude compressional earthquakes along fault traces northwest of the Tabar-Lihir-Tanga-Feni island chain (e.g., Figure 2.8).

8.3: Genesis of the Lienetz orebody and Lihir gold deposit

After island-forming constructional volcanism and plutonism, an ore-forming magmatic-hydrothermal system developed under the Luise volcanic edifice (Figure 8.2). This began around ~ 0.9 Ma, based on previous radiometric studies (e.g., Tables 2.1, 3.1; Davies and Ballantyne, 1987; Rytuba et al., 1993).

The genetic evolution of the ore-forming magmatic-hydrothermal system, in regards to the anhydrite-rich Lienetz orebody, can be divided into five major events: (1) porphyry-stage; (2) transitional-stage; (3) epithermal-stage; (4) diatreme volcanism; and (5) geothermal-stage.

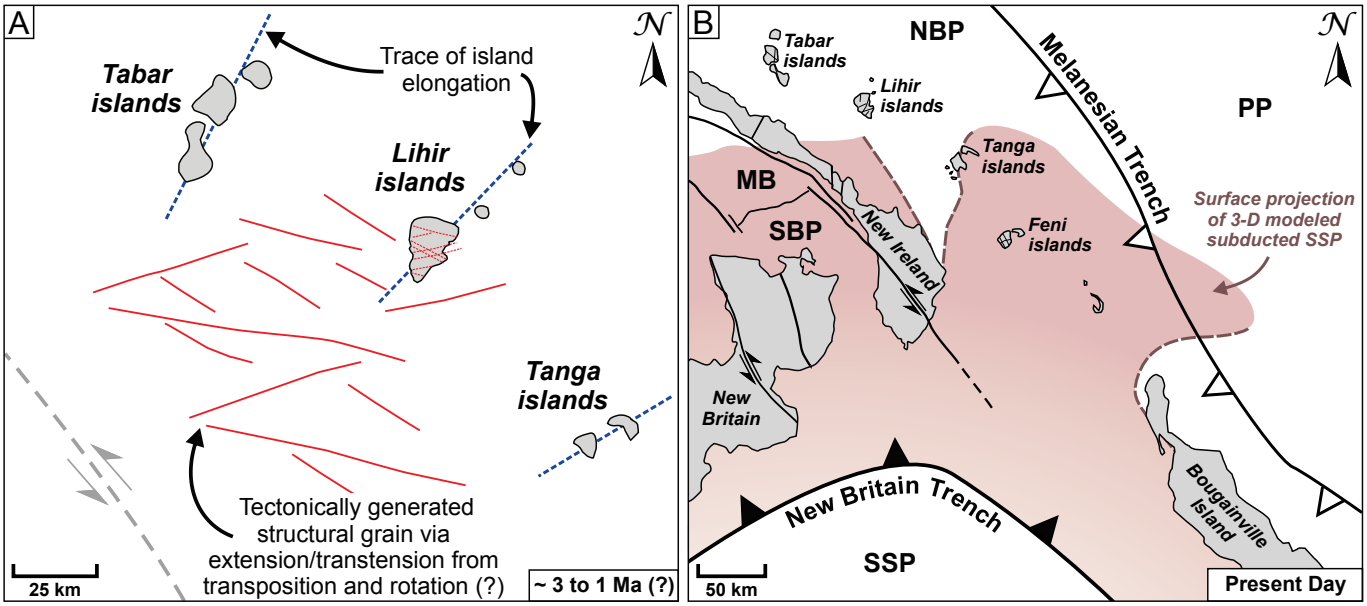

Figure 8.1: Schematic diagram of geodynamic history of Lihir Island, and generation of the prospective structural fabric. A) Schematic diagram representing Lihir Island at sometime between 3 and 1 Ma (?). Initially island groups of the Tabar-Lihir-Tanga-Feni chain formed via partial melting of the Melanesian metasomatized mantle wedge. Island groups are evenly spaced with island long-axes elongation. Island group formation may have been facilitated from perturbations in the active subducting SSP, and/or influenced by a pre-existing island arc architecture from the paleo-Melanesian subduction zone. The progressive counterclockwise rotation and relocation to the northwest, partly accommodated along the curved northwest-striking sinistral transform fault, led to a transtensional and/or extensional structural array. This was significant for localizing gold mineralization in the Lihir gold deposit. **B)** Present day position and tectonic elements of the Tabar-Lihir-Tanga-Feni island chain (modified after Taylor et al., 1994; Tregoning et al., 1998; Tregoning, 2002; O'Kane, 2008). MB: Manus basin; NBP: North Bismarck plate; PP: Pacific Plate; SBP: South Bismarck plate; SSP: Solomon Sea Plate.

8.3.1: Porphyry-stage

Porphyry-style hydrothermal activity occurred from ~ 0.9 to 0.3 Ma, within the volcano-sedimentary strata and alkalic intrusive stock substrate, under the confining pressure of the paleo-Luise volcano edifice (Figure 8.2A; Davies and Ballantyne, 1987; Rytuba et al., 1993; Carman, 1994). It produced minor anhydrite – biotite veins (V1) and a major magmatic-hydrothermal breccia complex (Bx1) that was associated with alkalic porphyritic dikes (Figure 8.2A). This was centered in northern Lienetz, and emplacement was controlled by northeast-striking faults (Figure 8.2A). The porphyry-stage breccias and veins have moderate to strong inner biotite and K-feldspar alteration halos, and distal chlorite and calcite alteration assemblages (e.g., Table 4.2; Figure 4.2A–B, 5.4C–D).

V1 veins have low- and high-angle dips to the north and northwest, and locally to the south and southeast (e.g., Figures 5.13A, 8.2A). Early northwest and/or southeast-directed compression and west-northwest-directed extension was linked with V1 vein formation under low differential stress (Figure 5.13A–B). σ_1 varied from sub-horizontal to sub-vertical, with locally increased fluid pressures due to sealing by mineral deposition.

The early porphyry-stage produced low-grade gold ± copper mineralization (Figure 8.2A), with low-grades within Bx1 and Bx2 breccias, and $V1_{bio}$ and $V1_{ksp}$ veins (i.e., < 1 g/t Au and < 0.1 wt. % Cu; e.g.,

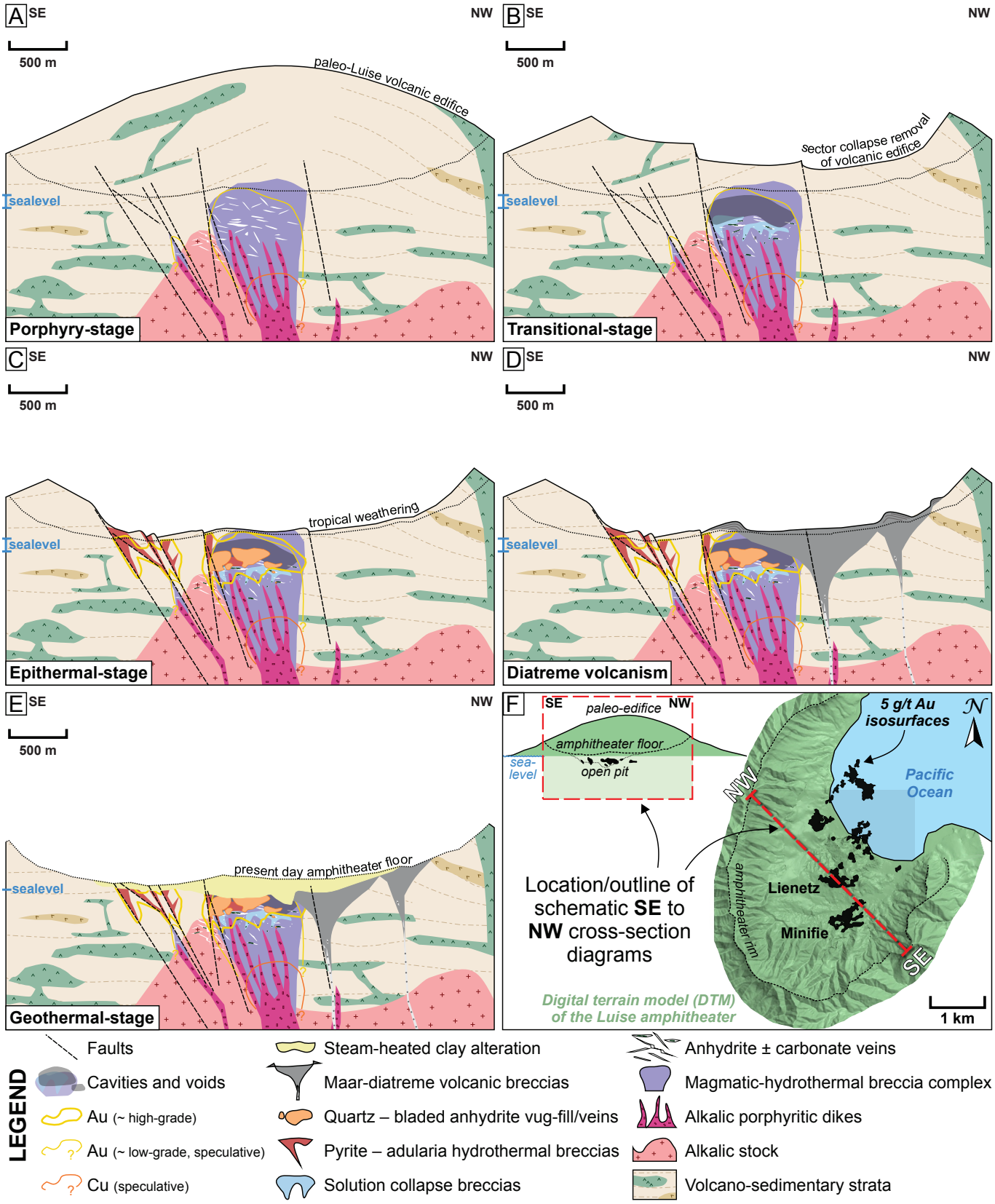

Figure 8.2: Schematic cross-section diagram of the genesis of the Lihir gold deposit, focused on Lienetz and Minifie. **A)** Porphyry-stage events produced a magmatic-hydrothermal breccia complex, alkalic porphyritic dikes and associated anhydrite-rich veins. Emplacement was controlled by northeast-striking faults, and under the original volcanic edifice with low differential stress, an oscillating sub-horizontal to sub-vertical σ_1, and temporarily elevated fluid-pressures from mineral sealing. Protracted, or multistage, northwest-directed extension with a mostly sub-vertical σ_1 was dominant for the rest of the evolution. **B)** Transitional-stage events resulted in modification of porphyry-stage veins and breccias, including solution collapse breccias, cavities and stylolites. This occurred during or after sector collapse(s) exhumed the volcanic edifice. **C)** Low-sulfidation epithermal-stage events resulted in pyrite – adularia-cemented hydrothermal breccia and quartz – bladed anhydrite vug-fills/veins. The auriferous fluids that formed these assemblages used permeable and porous cavities/voids, as well as localized at depth by steeply dipping, northeast-striking faults. **D)** Maar-diatreme volcanism occurred. Continued extension with top-block down to the northwest preferentially reactivated veins during late-stage hydrothermal activity, allowing influx of epithermal fluids. These occurred after sector collapse(s) and prolonged tropical weathering. **E)** Geothermal-stage events produced steam-heated clay alteration, and this high-temperature geothermal activity persists today. **F)** Plan view of the amphitheater, gold deposit and location of cross-section.

Table 4.2; Appendix 1). While this is considered low-grade mineralization in context of the Lihir gold mine, it is in fact a high-grade porphyry gold resource when compared to known porphyry Au deposits globally (e.g., Sillitoe, 2000; Sinclair, 2007).

Low-grade porphyry-style gold mineralization at Lienetz is associated at the mesoscopic-scale with breccias and veins. However, LA-ICP-MS analyses have shown that gold is dominantly not located within the crystal lattice of pyrite (e.g., Table 6.2; Figures 6.2, 6.3). It may be that gold occurs as micro-nuggets in V1 veins and Bx1 breccias, or in different minerals (e.g., Table 6.4). A detailed gold deportment study of porphyry-stage veins, breccias and altered rocks is recommended to resolve the mode of occurrence of porphyry-stage gold at Lienetz.

Anhydrite and pyrite in V1 and Bx1 precipitated from oxidized, magmatic hydrothermal fluids, resulting in $\delta^{34}S_{sulfate}$ values of 7.2 to 10.5‰ and $\delta^{34}S_{sulfide}$ approximately −8‰ (e.g., Table 7.2; Figures 7.2, 7.3). High salinity (5 to > 40 eq. wt. % NaCl) fluid inclusions documented by Carman (2003) are consistent with a magmatic-hydrothermal fluid and sulfur source for porphyry-stage hydrothermal activity at Lienetz.

8.3.2: Transitional-stage

Modification of porphyry-stage veins and breccias involved partial dissolution and recrystallization of anhydrite (Figure 8.2B). Age constraints are poor, but it is estimated that modification occurred during the transition from porphyry-style to epithermal conditions (i.e., between 0.9 and 0.3 Ma; Davies and Ballantyne, 1987; Rytuba et al., 1993; Carman, 1994), during which the Luise volcanic edifice experienced sector collapse(s) and was partly exhumed (Figure 8.2B).

Modification was confined to $V1_{M1}$ veins, as well as the Bx1 magmatic-hydrothermal breccia complex, and resulted in: (1) dissolution seams; (2) stylolites; (3) irregular and partly dissolved anhydrite-wall rock boundaries; (4) irregular and partly dissolved wall-rock inclusions in veins; (5) variable contents and textures of barite, celestine and anhydrite; (6) local solution collapse breccias; and (7) voids and cavities above and within thick intervals of $V1_{M1} \pm V1_{M2}$ (Figure 8.2B). Modification that created these features was most likely facilitated by anhydrite dissolution and recrystallization, most likely due to changing temperature ± pressures ± salinities.

The $V1_{M1}$ veins have dominantly low-angle to sub-horizontal dips with similarly oriented stylolites parallel to the vein margins (e.g., Figures 5.5C, 5.10B–C, 8.2B). They are consistent with sub-vertical σ_1 (e.g., Figure 5.13A, C), as is the sub-set of conjugate faults and $V1_{M1}$ veins with moderate dips (e.g., Figure 5.5C). An extension regime was dominant during the transitional-stage, with top-block down to the north to northwest, accompanied by local block rotation to the south-southeast (e.g., Figure 5.13A, C–D).

Sector collapse was a major event in the evolution from porphyry-style to epithermal conditions at Lihir (Carman, 1994; Sillitoe, 1994; White et al., 2010). It most likely occurred around the time of modification, and the two may have been linked (Figure 8.2B). Weakening of the volcanic edifice could have been, at least in part, facilitated by dissolution of, and/or shear along, the thick anhydrite veins. The $V1_{M1}$ veins have low-angle to sub-horizontal dips that could have facilitated the development of a décollement surface (e.g., Figures 5.5C, 5.10B). Their internal textures are consistent with strain localization (e.g., Figure 5.10E), and their recrystallization textures are consistent with deformation of anhydrite (e.g., décollement along evaporites; e.g., Davis and Engelder, 1985; Schreiber and Helman, 2005). However, the kinematics recorded by $V1_{M1} \pm V1_{M2}$ veins and breccia veins at Lienetz are not consistent with the northeast-direction of sector collapse into the Luise Harbour and Pacific Ocean (e.g., Figure 8.2F). Instead, they provide evidence for a history of north to northwest-directed extension (e.g., Figure 5.13A). Although modification of the anhydrite veins at Lienetz was most likely not directly linked to the collapse event(s), veins still may have influenced the geometry of, or provided lubrication for, it. If this was the case, then sector collapse event(s) may have been incremental, rather than catastrophic (Figure 8.2B).

While the thick anhydrite-rich veins and magmatic-hydrothermal breccia complex are low-grade (i.e., ~ 0.3 and ~ 1.0 g/t Au, respectively; Table 4.2; Appendix 1), modification subsequently helped facilitate overprinting by high-grade auriferous fluids. This is evident at the macroscopic-scale with areas of intense core-loss and cavities (e.g., Figures 4.7, 4.8, 4.12, 5.4, 5.10), and at the microscopic-scale where the majority of composite pyrite grains are interpreted to be porphyry-stage pyrite cores that were subjected to partial resorption and dissolution, and overgrown along the rims by gold and trace element-rich pyrite (e.g., Table 6.3; Figures 6.1, 6.2, 6.5, 6.8). This pyrite trace element assemblage is similar to, although with concentrations an order of magnitude lower than, epithermal-stage pyrite grains (e.g., Table 6.3). The limited analyses of $\delta^{34}S_{sulfide}$ (average −4 ‰) was less conclusive, showing that pyrite grains are either too heterogeneous or bimodal to distinguish core and rim isotopic variations (e.g., Figure 7.3).

Anhydrite related to the transitional-stage has the same oxidized, magmatic-hydrothermal isotopic fluid signature of porphyry-stage anhydrite (i.e., $\delta^{34}S_{sulfate}$ values of 7.6 to 11.0‰; Table 7.2; Figure 7.2B). Correlated $^{87}Sr/^{86}Sr$ values of 0.704084 from Hannington (unpublished data from Gemmell et al., 2004), as well as high salinity (5 to > 40 eq. wt. % NaCl) fluid inclusions from Carman (2003) are also consistent with a magmatic fluid source (e.g., Table 4.2; Figure 7.6).

8.3.3: Epithermal-stage

Low-sulfidation epithermal-stage hydrothermal activity was superimposed upon porphyry- and transitional-stage features after the mineralizing system was exhumed by sector collapse(s) and prolonged

tropical weathering (Figure 8.2C). This epithermal-stage may have occurred from ~ 0.6 to 0.2 Ma (e.g., Tables 2.1, 3.1; Moyle et al., 1990; Carman, 1994). Adularia ± quartz alteration are characteristic of the epithermal-stage (e.g., Figure 5.4E–F).

The epithermal-stage is characterized by pyrite – adularia-rich hydrothermal breccias and breccia veins, and quartz – bladed anhydrite vug-fill/veins, which also contain auriferous pyrite (i.e., $V3_{adu}$, $V4_{qtz}$ and $Bx3_{py–adu}$; e.g., Figures 4.2A–B, 8.2C). They formed on the partly dissolved upper-levels of the magmatic-hydrothermal breccia complex via overprinting and re-cementation (Figure 8.2C). Gold mineralization exploited voids created by anhydrite dissolution ± solution collapse (e.g., Figures 5.12, 8.2C). Auriferous fluids also were structurally localized throughout the gold deposit, creating hydrothermal breccias along northeast to east-northeast-striking faults (e.g., Figures 5.13A, E, 8.2C). The northeast- to east-northeast-striking structures were active during extension and northwest-directed transport, still under a dominantly sub-vertical σ_1 (e.g., Figure 5.13A, E).

Extension continued with top-block down to the northwest, preferentially reactivating the principal porphyry-stage vein array that has low-angle dips to the north (i.e., $V1_{M2}$; Figure 5.13F). Shear-related preferential slip and dilation of veins with low-angle dips, combined with sealing by anhydrite ± carbonate, created irregular to rhombic voids and dilational jogs. This allowed influx of late-stage epithermal-style fluids along veins, which produced crustiform and cockade bands of calcite – quartz ± adularia ± anhydrite (thinly bladed), and linking steeply dipping veins and breccia vein jogs, with variable localized high-grade gold (e.g., Figure 5.12, 5.13F).

Refractory sulfide ore associated with the epithermal-stage is characterized by pyrite with spectacular oscillatory zones enriched in As, Mo, Ag, Sb, Au and Tl (e.g., Table 6.2; Figures 6.2, 6.4, 6.8A). The extreme concentrations of As and other trace elements, and sharp textural feature (i.e., oscillatory zones, colloform bands, etc.) are interpreted to represent episodic fluctuation in fluid composition during crystal growth and rapid deposition (e.g., Fleet et al., 1989; Peterson and Mavrogenes, 2014).

The source of sulfur for auriferous pyrite ± marcasite and associated anhydrite was predominantly magmatic. These minerals precipitated from mixtures of magmatic and meteoric fluids with low salinities (i.e., 2 to 7 eq. wt. % NaCl and 0 to 4 eq. wt. % NaCl; analyzed from fluid inclusions by Carman (1994) and Ageneau (2012), respectively; e.g., Figure 4.15). This is also supported by $\delta^{34}S_{sulfate}$ values (9.0 to 12.2 ‰) from this study (e.g., Table 7.2; Figure 7.2B), and $\delta^{34}S_{sulfide}$ and $\delta^{18}O_{H2O}$ values from Carman (1994). The variability in $\delta^{34}S_{sulfide}$ values from this study, however, implies complexity either in bulk isotopic compositions of the mineralizing fluids, or water-rock interaction (e.g., Rye, 1993; Wilson et al., 2007).

8.3.4: Diatreme volcanism

Episodic volcanic processes (i.e., phreatomagmatic eruptions) occurred at Lihir after high-grade epithermal-stage mineralization (e.g., Figure 3.5A–C), but did not terminate mineralization (Figure 8.2D; Lawlis et al., 2015). Conditions were most likely similar to the modern geothermal-stage which was established at > 0.15 Ma (e.g., Table 3.1; Davies and Ballantyne, 1987). Diatreme volcanism occurred prior to 0.06 Ma (Lawlis, in prep.).

Andesite dikes, identified in drill core by Lawlis et al. (2015), are interpreted to have intruded the paleo-water table and reacted explosively, feeding phreatomagmatic eruptions that formed the diatreme breccia pipes and related maar deposits (Figure 8.2D). Phreatomagmatic eruptions lead to draw-down of organic material (e.g., carbonized tree trunks) and tephra rings from the sides (e.g., Lawlis et al., 2015, Lawlis, in prep). Eventually volcanism ceased and upper-level maar volcanic deposits were eroded away, exposing the diatreme roots at the present-day surface (Figure 8.2E).

8.3.5: Geothermal-stage

The modern high-temperature geothermal system at Lihir established itself at least 0.15 million years ago (Tables 2.1, 3.1; Davies and Ballantyne, 1987). Geothermal activity still continues to discharge throughout the Lihir gold deposit to this day, altering rocks, causing brecciation and depositing gold (e.g., Pichler et al., 1999; Simmons and Brown, 2006). It has formed the surficial clay alteration zone via steam-heated processes (Figure 8.2E; Browne, 1978; Moyle et al., 1990; Carman, 1994; Corbett, unpublished data, 2001; Jansen, unpublished data, 2013).

Below −300 m rsl, the geothermal fluids are high-temperature (~ 230 to 270°C), near-neutral to alkaline, oxidized, rich in sulfate, dissolved salts, and contain high concentrations of trace metals (e.g., Table 3.2; Figure 3.6; Wallace et al., 1983; Williamson, 1983; Geothermex, unpublished data, 1989; Müller et al., 2002b; Brown and Bixley, 2005; Simmons and Brown, 2006). As such, the geothermal system is interpreted to represent the waning ancient auriferous hydrothermal system (Williamson, 1983; Simmons and Brown, 2006).

8.4: Exploration and processing implications

This study has highlighted several implications for exploration and processing at Lihir and at similar magmatic-hydrothermal ore deposits.

- Northeast and east-northeast-striking extensional structures controlled gold mineralization, veins and faults. These orientations should be considered for brownfields and island-scale exploration campaigns.

- Reactivation of structures was significant in Lienetz, and locally aided in gold mineralization. The potential for pre-existing structures being reactivated should be considered in the exploration and understanding of other magmatic-hydrothermal ore deposits.

- Areas where anhydrite was abundant but now has been partly or completely dissolved are permeable and porous, and provided favorable sites for high-grade gold mineralization. There is abundant textural evidence for widespread anhydrite dissolution, and this influenced the distribution of high-grade gold at Lienetz. Anhydrite dissolution may have been important in other magmatic-hydrothermal ore deposits, and potentially a key factor for localizing copper and gold ore.

- Dilational jogs and steeply dipping tensile to hybrid veins and breccia veins (linked by hybrid to shear veins with low-angle dips), are all associated with high-grade gold at Lienetz. Mapping and understanding vein geometry and kinematics can help to target these favorable structures during on-going exploration.

- Physical lithological controls on low-grade gold should be considered when mining at Lienetz and other orebodies at Lihir. Specifically, low-grade gold is disseminated in breccia complexes, in contrast to more competent rock types.

- Composite pyrite grains, which were commonly observed in Bx1, $V1_{M1}$ and $V1_{M2}$, can be subjected to a shorter period of oxidation during mineral processing to liberate most of their gold from the auriferous rims. The present gold-rich rims can be easily checked with NaOCl etching, due to the high As content on rims. In contrast, for areas dominated by high-grade epithermal-stage mineralization, pyrite grains need to be fully oxidized during processing in order to liberate the gold from their entire lattice. Understanding gold deportment in similar pyrite-rich deposits is therefore essential for optimizing mineral processing, as it can impact significantly on the economics of mining these complex, hybrid ore deposits.

- If the tectonic reconstruction presented in Chapter 2 proves to be accurate, then island arcs that rotate around bends could be favorable settings for gold mineralization due to the development of oblique extensional fracture arrays.

8.5: Future research

After more than 35 years since Lihir's discovery and with several PhD and MSc theses now completed, there is still much to learn about one of the world's most interesting and complicated ore deposits. Below are a series of suggestions for future research.

- Further studies are required to confirm the prevailing tectonic environment during the formation of the Tabar-Lihir-Tanga-Feni island chain. This could include refined modeling of the plate configurations over the past 3.5 m.y, with the use of tomographic data, combined with refined models of stress and strain associated with the subducting Solomon Sea Plate. Detailed investigations of geochemical variations between the islands and better constraints of magmatic ages for each of the islands would be essential to help resolve these issues. A detailed stratigraphic mapping campaign of the island chain, combined with age dating of targeted units, is recommended.

- For Lihir Island, an island-scale geological and structural map is necessary to constrain the prevailing structures. In particular, orientations and kinematics should be recorded. This would help resolve whether early compression affected the island, or if conditions were always extensional. Combining this with syn-kinematic mineral dating would allow timing of fault movement to be quantified, and in turn related to gold mineralization.

- Radiometic age determinations for mineralization and alteration related to porphyry-, transitional- and epithermal-stages are required, but have proven elusive in part due to difficulties in dating young rocks, and thermal resetting of K–Ar and Ar–Ar radiometric ratios due to the modern high-temperature geothermal system at Lihir. Further Re–Os dating of molybdenite and U–Pb dating of zircon and possibly apatite is recommended.

- There is little geological evidence of products from the catastrophic sector collapse event(s) at Lihir. Future research could investigate this by looking for volcanic ejecta, ash-fall layers (that can be dated) and signatures of large tsunamis. The islands located immediately offshore to the northeast of the Luise amphitheater and Lihir gold deposit would be ideal places to study, as they might have preserved these distal features without high-temperature geothermal activity potentially resetting their K–Ar radiometric ages.

- Faults have been identified within the Lienetz and Minifie orebody, but they are poorly constrained outside of the orebodies, or at depth. Evaluating multi-element geochemical data from drill core assays could be used to help identify enrichment and depletion in elements associated with alteration proximal to faults, and better constrain faults in other orebodies. Additionally, multi-element geochemical data can be used to quantify alteration assemblages linked to porphyry- and epithermal-stages (e.g., Halley et al., 2015), as well as identify sulfate and sulfide minerals.

- Sulfur and strontium isotopes indicate little to no seawater influence for the formation of anhydrite at Lihir, however, the possibility of seawater involvement cannot but fully discounted. Future research could use trace elements in anhydrite to assess possible marine influence. Seawater has a very specific REE-Y pattern which can be found as an imprint in both modern and ancient marine limestones (e.g., Webb and Kamber, 2000; Kamber and Webb, 2001). Analysis of REE-Y patterns of anhydrite, barite or calcite at Lihir would be beneficial to further confirm or refute the seawater influence on the Lihir magmatic-hydrothermal system.

- Infrared (IR) imaging could potentially be used to map fluid-flow pathways of the modern high-temperature geothermal system. This can be used to better constrain faults and permeable/porous rock types.

- The characteristic long- and short-wave ultraviolet (UV) light fluorescence of anhydrite and calcite could be used to aid in mineral identification (e.g., Appendix 2). Additional, variation in fluorescence may correspond to difference elements that are activators or inhibitors (e.g., Verbeek, 1995), and potentially can be used as a vector to mineralization.

- The porphyritic syenite dikes were largely identified from drill-core photographs, as with the extent of the magmatic-hydrothermal breccia complex in Lienetz. Future work could include a detailed core logging campaign to unravel the intricacies of the breccia complex and its relationships to the porphyritic dikes. Since porphyritic dikes and magmatic-hydrothermal breccia complexes are important features in large porphyry Cu deposits, it would be beneficial to do a detailed study of their compositions, combined with gold and copper assays and age dating. This might better constrain evolution of the early porphyry-stage, and help to evaluate the porphyry Au ± Cu mineralization potential at Lihir.

References

Abers, G.A., 2009, Slip on shallow-dipping normal faults: Geology, v. 37, p. 767–768.

Ageneau, M., 2012, Geology of the Kapit ore zone and comparative geochemistry with Minifie and Lienetz ore zones, Ladolam Gold Deposit, Lihir Island, Papua New Guinea: Unpublished PhD thesis, University of Tasmania, 269 p.

Anderson, E.M., 1951, The dynamics of faulting: Transactions of the Edinburgh Geological Society, v. 8, p. 387–402.

Anderson, W.B., and Eaton, P.C., 1990, Gold mineralisation at the Emperor Mine, Vatukoula, Fiji: Journal of Geochemical Exploration, v. 36, p. 267–296.

Atkinson, B.K., 1987, Introduction to fracture mechanics and its geophysical applications, *in* Atkinson, B.K., ed., Fracture mechanics of rock: New York, Academic Press, p. 1–26.

Bach, W., Roberts, S., and Binns, R., 2007, Data report: Chemical and isotopic (S, Sr) composition of anhydrite from ODP Leg 193, PACMANUS hydrothermal system, Manus Basin, Papua New Guinea, *in* Barriga, F.J.A.S., Binns, R.A., Miller, D.J., and Herzig, P. M., eds., Proceedings of the Ocean Drilling Program, Scientific Results, 193, p. 1–23.

Beach, A., 1975, The geometry of en échelon vein arrays: Tectonophysics, v. 28, p. 245–286.

Beane, R.E., 1974, Biotite stability in the porphyry copper environment: Economic Geology, v. 69, p. 241–256.

Beane, R.E., and Titley, S.R., 1981, Porphyry copper deposits: Economic Geology, v. 75, p. 214–269.

Begg, G., and Gray, D.R., 2002, Arc dynamics and tectonic history of Fiji based on stress and kinematic analysis of dikes and faults of the Tavua Volcano, Viti Levu Island, Fiji: Tectonics, v. 21, p. 1–14.

Begg, G.C., 1996, Genesis of the Emperor gold deposit, Fiji: Unpublished PhD thesis, Monash University, 447 p.

Belayneh, M., and Cosgrove, J.W., 2010, Hybrid veins from the southern margin of the Bristol Channel Basin, U.K.: Journal of Structural Geology, v. 32, p. 192–201.

Belousov, I., Large, R.R., Meffre, S., Danyushevsky, L.V., Steadman, J., and Beardsmore, T., 2016, Pyrite compositions from VHMS and orogenic Au deposits in the Yilgarn Craton, Western Australia: Implications for gold and copper exploration: Ore Geology Reviews, v. 79, p. 474–499.

Benz, H.M., Herman, M., Tarr, A.C., Hayes, G.P., Furlong, K.P., Villaseñor, A., Dart, R.L., and Rhea, S., 2011, Seismicity of the Earth 1900–2010 New Guinea and vicinity: U.S. Geological Survey open-file report 2010–1083-H, scale 1:8,000,000, United States Geological Survey.

Berger, E., Fong, W., and Chornock, R., 2013, An r-process Kilonova associated with the short-hard GRB 130603B: The Astrophysical Journal Letters, v. 774, p. 1–4.

Bird, P., 2003, An updated digital model of plate boundaries: Geochemistry, Geophysics, Geosystems, v. 4, p. 1–52.

Bissig, T., and Cooke, D.R., 2014, Introduction to the special issue devoted to alkalic porphyry Cu-Au and epithermal Au deposits: Economic Geology, v. 109, p. 819–825.

Blackwell, J.L., 2010, Characteristics and origins of breccias in a volcanic-hosted alkalic epithermal gold deposit, Ladolam, Lihir Island, Papua New Guinea: Unpublished PhD thesis, University of Tasmania, Australia, 203 p.

Blackwell, J.L., Cooke, D.R., McPhie, J., and Simpson, K.A., 2014, Lithofacies associations and evolution of the volcanic host succession to the Minifie ore zone, Ladolam gold deposit, Lihir Island, Papua New Guinea: Economic Geology, v. 109, p. 1137–1160.

Blake, D.H., and Miezitis, Y., 1967, Geology of the Bougainville and Buka Islands, Papua New Guinea, Bulletin 93, Australian Bureau of Mineral Resources, Geology and Geophysics, p. 1–56.

Blount, C.W., and Dickson, F.W., 1969, The solubility of anhydrite ($CaSO_4$) in NaCl-H_2O from 100 to 450°C and 1 to 1000 bars: Geochimica et Cosmochimica Acta, v. 33, p. 227–245.

Borgia, A., Delaney, P.T., and Denlinger, R.P., 2000, Spreading volcanoes: Annual Review of Earth and Planetary Sciences, v. 28, p. 539–570.

Brathwaite, R.L., Simpson, M.P., Faure, K., and Skinner, D.N.B., 2001, Telescoped porphyry Cu–Mo–Au mineralisation, advanced argillic alteration and quartz-sulphide-gold-anhydrite veins in the Thames District, New Zealand: Mineralium Deposita, v. 36, p. 623–640.

Brown, K.L., and Bixley, P.F., 2005, Geochemistry of the Lihir geothermal field, Papua New Guinea: World Geothermal Congress, Antalya, Turkey, 2005, p. 24–29.

Browne, P., 1978, Hydrothermal alteration in active geothermal fields: Annual Review of Earth and Planetary Sciences, v. 6, p. 229–250.

Bruns, T.R., Vedder, J.G., and Culotta, R.C., 1989, Structure and tectonics along the Kilinailau Trench, Bougainville ± Buka island region, Papua New Guinea, *in* Vedder, J.G., and Bruns, T.R., eds., Geology and offshore resources of Pacific Islands arcs: Solomon Islands and Bougainville, Papua New Guinea regions. Circum-Pacific Council for Energy and Mineral Resources Earth Science Series, 12: Houston, Texas, p. 93–123.

Bryner, L., 1961, Breccia and pebble columns associated with epigenetic ore deposits: Economic Geology, v. 56, p. 488–508.

Buchanan, L.J., 1981, Precious metal deposits associated with volcanic environments in the southwest: Arizona Geological Society Digest, v. 14, p. 237–262.

Burnham, C., 1979, Magmas and hydrothermal fluids, *in* Barnes, H.L., ed., Geochemistry of hydrothermal ore deposits, 2nd ed.: New York, John Wiley & Sons, p. 71–136.

Meyer, C., and Hemley, J.J., 1967, Wall-rock alteration, *in* Barnes, H. L., ed., Geochemistry of hydrothermal ore deposits, 1st ed.: New York, Holt, Rinehart & Winston, p. 166–235.

Burnham, C.W., and Ohmoto, H., 1980, Late-stage processes of felsic magmatism: Mining Geology Special Issue, v. 8, p. 1–11.

Byrne, K., and Tosdal, R.M., 2014, Genesis of the late Triassic southwest zone breccia-hosted alkalic porphyry Cu-Au Deposit, Galore Creek, British Columbia, Canada: Economic Geology, v. 109, p. 915–938.

Byrne, P.K., Holohan, E.P., Kervyn, M., de Vries, B.V., Troll, V.R., and Murray, J.B., 2013, A sagging-spreading continuum of large volcano structure: Geology, v. 41, p. 339–342.

Candela, P., and Piccoli, P., 2005, Magmatic processes in the development of porphyry-type ore systems: Economic Geology 100th Anniversary Volume, p. 25–37.

Cannell, J., Cooke, D.R., Walshe, J.L., and Stein, H., 2005, Geology, mineralization, alteration, and structural evolution of the El Teniente porphyry Cu–Mo deposit: Economic Geology, v. 100, p. 979–1003.

Carman, G.D., 1994, Genesis of the Ladolam gold deposit, Lihir Island, Papua New Guinea: Unpublished PhD thesis, Monash University, Australia, 381 p.

Carman, G.D., 2002, Factors contributing to the formation of the giant Ladolam gold deposit, Lihir Island, PNG: AusIMM, Auckland, New Zealand, September, 2002, p. 185–189.

Carman, G.D., 2003, Geology, mineralization, and hydrothermal evolution of the Ladolam gold deposit, Lihir Island, Papua New Guinea: Society of Economic Geologists, Special Publication, no. 10, p. 247–284.

Carroll, M.R., and Rutherford, M.J., 1987, The stability of igneous anhydrite: Experimental results and implications for sulfur behavior in the 1982 El-Chichon trachyandesite and other evolved magmas: Journal of Petrology, v. 28, p. 781–801.

Carroll, M.R., and Webster, J.D., 1994, Solubilities of sulfur, noble gases, nitrogen, chlorine, and fluorine in magmas: Reviews in Mineralogy and Geochemistry, v. 30, p. 231–279.

Cater, 2002, Deep hydrothermal alteration at the Ladolam epithermal gold deposit, Lihir Island, Papua New Guinea: Unpublished MSc thesis, University of Auckland, New Zealand, 94 p.

Chambefort, I., Dilles, J.H., and Kent, A.J.R., 2008, Anhydrite-bearing andesite and dacite as a source for sulfur in magmatic-hydrothermal mineral deposits: Geology, v. 36, p. 719–722.

Chiba, H., Uchiyama, N., and Teagle, D.A., 1998, Stable isotope study of anhydrite and sulfide minerals at the TAG hydrothermal mound, Mid-Atlantic Ridge, 26°N, *in* Herzig, P.M., Humphris, S.E., Miller, D.J., and Zierenberg, R.A., eds., Proceedings of the Ocean Drilling Program, Scientific Results, 158, p. 85–90.

Claypool, G.E., Holser, W.T., Kaplan, I.R., Sakai, H., and Zak, I., 1980, The age curves of sulfur and oxygen isotopes in marine sulfate and their mutual interpretation: Chemical Geology, v. 28, p. 199–260.

Cline, J.S., 2001, Timing of gold and arsenic sulfide mineral deposition at the Getchell Carlin-type gold deposit, north-central Nevada: Economic Geology, v. 96, p. 75–89.

Cline, J.S., Hofstra, A.H., Muntean, J.L., Tosdal, R.M., and Hickey, K.A., 2005, Carlin-type gold deposits in Nevada: Critical geologic characteristics and viable models: Economic Geology, v. 100, p. 451–484.

Coffin, M.F., and Eldholm, O., 1993, Scratching the surface: Estimating dimensions of large igneous provinces: Geology, v. 21, p. 515–518.

Collettini, C., 2011, The mechanical paradox of low-angle normal faults: Current understanding and open questions: Tectonophysics, v. 510, p. 253–268.

Collettini, C., Viti, C., Smith, S.A.F., and Holdsworth, R.E., 2009, Development of interconnected talc networks and weakening of continental low-angle normal faults: Geology, v. 37, p. 567–570.

Cook, N.J., and Chryssoulis, S.L., 1990, Concentrations of invisible gold in the common sulfides: Canadian Mineralogist, v. 28, p. 1–16.

Cook, N.J., Ciobanu, C.L., and Mao, J.W., 2009, Textural control on gold distribution in As-free pyrite from the Dongping, Huangtuliang and Hougou gold deposits, North China Craton (Hebei Province, China): Chemical Geology, v. 264, p. 101–121.

Cooke, D.R., and Bloom, M.S., 1990, Epithermal and subjacent porphyry mineralization, Acupan, Baguio District, Philippines: A fluid-inclusion and paragenetic study: Journal of Geochemical Exploration, v. 35, p. 297–340.

Cooke, D.R., Deyell, C.L., Waters, P.J., Gonzales, R.I., and Zaw, K., 2011, Evidence for magmatic-hydrothermal fluids and ore-forming processes in epithermal and porphyry deposits of the Baguio District, Philippines: Economic Geology, v. 106, p. 1399–1424.

Cooke, D.R., and McPhail, D.C., 2001, Epithermal Au-Ag-Te mineralization, Acupan, Baguio district, Philippines: Numerical simulations of mineral deposition: Economic Geology, v. 96, p. 109–131.

Cooke, D.R., and Simmons, S.F., 2000, Characteristics and genesis of epithermal gold deposits: Reviews in Economic Geology, v. 13, p. 221–244.

Cooper, P.A., and Taylor, B., 1985, Polarity reversal in the Solomon Islands Arc: Nature, v. 314, p. 428–430.

Corbett, G., Hunt, S., Cook, A., Tamaduk, P., and Leach, T., 2001, Geology of the Ladolam gold deposit, Lihir Island, from exposures in the Minifie open pit: PNG Geology, Exploration and Mining Conference June, 2001, p. 69–77.

Corbett, G., and Leach, T., 1998, Southwest Pacific Rim gold-copper systems: Structure, alteration, and mineralization, Short course manual, p. 318.

Cosgrove, J.W., 1995, The expression of hydraulic fracturing in rocks and sediments: Geological Society Special Publication, v. 92, p. 187–196.

Cox, S.F., 1987, Antitaxial crack-seal vein microstructures and their relationship to displacement paths: Journal of Structural Geology, v. 9, p. 779–787.

Cox, S.F., 1995, Faulting processes at high fluid pressures: An example of fault valve behavior from the Wattle Gully Fault, Victoria, Australia: Journal of Geophysical Research: Solid Earth, v. 100, p. 12841–12859.

Cox, S.F., and Etheridge, M.A., 1983, Crack-seal fiber growth mechanisms and their significance in the development of oriented layer silicate microstructures: Tectonophysics, v. 92, p. 147–170.

Craig, J.R., and Solberg, T.N., 1999, Compositional zoning in ore minerals at the Craig mine, Sudbury, Ontario, Canada: Canadian Mineralogist, v. 37, p. 1163–1176.

Crowe, D., and Vaughan, R., 1996, Characterization and use of isotopically homogeneous standards for in situ laser microprobe analysis of $^{34}S/^{32}S$ ratios: American Mineralogist, v. 81, p. 187–193.

Curtis, J.W., 1973, Plate tectonics and the Papua New Guinea–Solomon Islands region: Journal of the Geological Society of Australia, v. 20, p. 21–35.

Danyushevsky, L., Robinson, P., Gilbert, S., Norman, M., Large, R., McGoldrick, P., and Shelley, M., 2011, Routine quantitative multi-element analysis of sulphide minerals by laser ablation ICP-MS: Standard development and consideration of matrix effects: Geochemistry–Exploration Environment Analysis, v. 11, p. 51–60.

Davies, A.G.S., 2002, Geology and genesis of the Kelian gold deposit, East Kalimantan, Indonesia: Unpublished PhD thesis, University of Tasmania, 404 p.

Davies, A.G.S., Cooke, D.R., Gemmell, J.B., and Simpson, K.A., 2008, Diatreme breccias at the Kelian gold mine, Kalimantan, Indonesia: Precursors to epithermal gold mineralization: Economic Geology, v. 103, p. 689–716.

Davies, R.H., and Ballantyne, G.H., 1987, Geology of the Ladolam gold deposit Lihir Island, Papua New Guinea: Pacific Rim Congress, Gold Coast Queensland, Australia, 1987, p. 943–949.

Davis, D.M., and Engelder, T., 1985, The role of salt in fold-and-thrust belts: Tectonophysics, v. 119, p. 67–88.

Deditius, A.P., Reich, M., Kesler, S.E., Utsunomiya, S., Chryssoulis, S.L., Walshe, J., and Ewing, R.C., 2014, The coupled geochemistry of Au and As in pyrite from hydrothermal ore deposits: Geochimica et Cosmochimica Acta, v. 140, p. 644–670.

Deditius, A.P., Utsunomiya, S., Ewing, R.C., Chryssoulis, S.L., Venter, D., and Kesler, S.E., 2009, Decoupled geochemical behavior of As and Cu in hydrothermal systems: Geology, v. 37, p. 707–710.

Deditius, A.P., Utsunomiya, S., Reich, M., Kesler, S.E., Ewing, R.C., Hough, R., and Walshe, J., 2011, Trace metal nanoparticles in pyrite: Ore Geology Reviews, v. 42, p. 32–46.

Deditius, A.P., Utsunomiya, S., Renock, D., Ewing, R.C., Ramana, C.V., Becker, U., and Kesler, S.E., 2008, A proposed new type of arsenian pyrite: Composition, nanostructure and geological significance: Geochimica et Cosmochimica Acta, v. 72, p. 2919–2933.

DeMets, C., Gordon, R.G., Argus, D.F., and Stein, S., 1990, Current plate motions: Geophysical Journal International, v. 101, p. 425–478.

Dieterich, J.H., 1988, Growth and persistence of Hawaiian volcanic rift zones: Journal of Geophysical Research: Solid Earth, v. 93, p. 4258–4270.

Eldrige, C., Compston, W., Williams, I., Walshe, J., and Both, R., 1987, In situ microanalysis for $^{34}S/^{32}S$ ratios using the ion microprobe SHRIMP: International Journal of Mass Spectrometry and Ion Processes, v. 76, p. 65–83.

Falvey, D.A., and Pritchard, T., 1982, Preliminary paleomagnetic results from northern Papua New Guinea: Evidence for large microplate rotations: Circum-Pacific Energy and Mineral Resources Conference, 1982, p. 593–600.

Farmin, R., 1934, “Pebble dikes” and associated mineralization at Tintic, Utah: Economic Geology, v. 29, p. 356–370.

Farrell, C., Holland, H., and Petersen, U., 1978, The isotopic composition of strontium in barites and anhydrites from Kuroko deposits: Mining Geology, v. 28, p. 281–291.

Finlayson, D., and Cull, J., 1973, Structural profiles in the New Britain/New Ireland region: Journal of the Geological Society of Australia, v. 20, p. 37–47.

Fleet, M., MacLean, P., and Barbier, J., 1989, Oscillatory-zoned As-bearing pyrite from strata-bound and stratiform gold deposits: An indicator of ore fluid evolution: Economic Geology Monograph, v. 6, p. 356–362.

Fleet, M.E., Chryssoulis, S.L., Maclean, P.J., Davidson, R., and Weisener, C.G., 1993, Arsenian pyrite from gold deposits: Au and as distribution investigated by SIMS and EMP, and color staining and surface oxidation by XPS and LIMS: Canadian Mineralogist, v. 31, p. 1–17.

Fournier, R.O., 1999, Hydrothermal processes related to movement of fluid from plastic into brittle rock in the magmatic-epithermal environment: Economic Geology, v. 94, p. 1193–1211.

Fowler, T.J., 1996, Flexural-slip generated bedding-parallel veins from central Victoria, Australia: Journal of Structural Geology, v. 18, p. 1399–1415.

Fox, N., Cooke, D.R., Harris, A.C., Collett, D., and Eastwood, G., 2015, Porphyry Au-Cu mineralization controlled by reactivation of an arc-transverse volcanosedimentary subbasin: Geology, v. 43, p. 811–814.

Frikken, P.H., Cooke, D.R., Walshe, J.L., Archibald, D., Skarmeta, J., Serrano, L., and Vargas, R., 2005, Mineralogical and isotopic zonation in the Sur-Sur tourmaline breccia, Rio Blanco-Los Bronces Cu-Mo deposit, Chile: Implications for ore genesis: Economic Geology, v. 100, p. 935–961.

Gemmell, J.B., Sharpe, R., Jonasson, I.R., and Herzig, P.M., 2004, Sulfur isotope evidence for magmatic contributions to submarine and subaerial gold mineralization: Conical seamount and the Ladolam gold deposit, Papua New Guinea: Economic Geology, v. 99, p. 1711–1725.

Giggenbach, W.F., 1987, Redox processes governing the chemistry of fumarolic gas discharges from White Island, New Zealand: Applied Geochemistry, v. 2, p. 143–161.

Giggenbach, W.F., 1997, The origin and evolution of fluids in magmatic-hydrothermal systems, *in* Barnes, H.L., ed., Geochemistry of hydrothermal ore deposits, 3rd ed.: New York, John Wiley & Sons, p. 737–796.

Giggenbach, W.F., Hendenquist, J.W., Houghton, B.F., Otway, P.M., and Allis, R.G., 1989, Research drilling into the volcanic hydrothermal system on White Island, New Zealand: EOS, Transactions of the American Geophysical Union, v. 70, p. 98–108.

Gilbert, S.E., Danyushevsky, L.V., Rodemann, T., Shimizu, N., Gurenko, A., Meffre, S., Thomas, H., Large, R.R., and Death, D., 2014, Optimisation of laser parameters for the analysis of sulphur isotopes in sulphide minerals by laser ablation ICP-MS: Journal of Analytical Atomic Spectrometry, v. 29, p. 1042–1051.

Gordon, R.G., Cox, A., and Harter, C.E., 1978, Absolute motion of an individual plate estimated from its ridge and trench boundaries: Nature, v. 274, p. 752–755.

Green, D., 1972, Magmatic activity as the major process in the chemical evolution of the Earth's crust and mantle: Tectonophysics, v. 13, p. 47–71.

Green, G.R., Solomon, M., and Walshe, J.L., 1981, The formation of the volcanic-hosted massive sulfide ore deposit at Rosebery, Tasmania: Economic Geology, v. 76, p. 304–338.

Gregory, M.J., Lang, J.R., Gilbert, S., and Hoal, K.O., 2013, Geometallurgy of the Pebble porphyry Cu-Au-Mo deposit, Alaska: Implications for gold distribution and paragenesis: Economic Geology, v. 108, p. 463–482.

Gruen, G., Heinrich, C.A., and Schroeder, K., 2010, The Bingham Canyon porphyry Cu-Mo-Au deposit. II: Vein geometry and ore shell formation by pressure-driven rock extension: Economic Geology, v. 105, p. 69–90.

Gustafson, L.B., and Hunt, J.P., 1975, The porphyry copper deposit at El Salvador, Chile: Economic Geology, v. 70, p. 857–912.

Gysel, M., 2002, Anhydrite dissolution phenomena: Three case histories of anhydrite karst caused by water tunnel operation: Rock Mechanics and Rock Engineering, v. 35, p. 1–21.

Hall, R., 2002, Cenozoic geological and plate tectonic evolution of SE Asia and the SW Pacific: Computer-based reconstructions, model and animations: Journal of Asian Earth Sciences, v. 20, p. 353–431.

Halley, S., Dilles, J., and Tosdal, R., 2015, Footprints: hydrothermal alteration and geochemical dispersion around porphyry copper deposits: Society of Economic Geologists Newsletter, v. 100, p. 12–17.

Haneberg, W.C., Creighton, A.L., Medly, E.W., and Jonas, D.A., 2005, Use of LiDAR to assess slope hazards at the Lihir gold mine, Papua New Guinea: International Conference on Landslide Risk Management, Vancouver, Canada, 2005, p. 1–11.

Hanley, J.J., and MacKenzie, M.K., 2009, Incorporation of platinum-group elements and cobalt into subsidiary pyrite in alkalic Cu–Au porphyry deposits: Significant implications for precious metal distribution in felsic magmatic-hydrothermal systems: AGU Spring Meeting Abstracts, 2009.

Hannington, M., Herzig, P., Stoffers, P., Scholten, J., Botz, R., Garbe-Schonberg, D., Jonasson, I.R., Roest, W., and Party, S.S., 2001, First observations of high-temperature submarine hydrothermal vents and massive anhydrite deposits off the north coast of Iceland: Marine Geology, v. 177, p. 199–220.

Hanor, J.S., 2000, Barite–celestine geochemistry and environments of formation, *in* Alpers, C.N., Jambor, J.L., and Nordstrom, D.K., eds., Sulfate minerals: Crystallography, geochemistry and environmental significance, 40: Blacksburg, Virginia, p. 193–275.

Heald, P., Foley, N.K., and Hayba, D.O., 1987, Comparative anatomy of volcanic-hosted epithermal deposits: Acid-sulfate and adularia-sericite types: Economic Geology, v. 82, p. 1–26.

Hedenquist, J.W., and Henley, R.W., 1985, The importance of CO_2 on freezing point measurements of fluid inclusions: Evidence from active geothermal systems and implications for epithermal ore deposition: Economic Geology, v. 80, p. 1379–1406.

Hedenquist, J.W., and Lowenstern, J.B., 1994, The role of magmas in the formation of hydrothermal ore deposits: Nature, v. 370, p. 519–527.

Hedenquist, J.W., Simmons, S.F., Giggenbach, W.F., and Eldridge, C.S., 1993, White Island, New Zealand, volcanic-hydrothermal system represents the geochemical environment of high-sulfidation Cu and Au ore deposition: Geology, v. 21, p. 731–734.

Heming, R.F., 1979, Undersaturated lavas from Ambittle Island, Papua New-Guinea: Lithos, v. 12, p. 173–186.

Hemley, J., Montoya, J., Marinenko, J., and Luce, R., 1980, Equilibria in the system Al_2O_3-SiO_2-H_2O and some general implications for alteration/mineralization processes: Economic Geology, v. 75, p. 210–228.

Henley, R.W., and Ellis, A.J., 1983, Geothermal systems ancient and modern: A geochemical review: Earth Science Reviews, v. 19, p. 1–50.

Herzig, P., Hannington, M., Staffers, P., Becker, K.-P., Drischel, M., Franz, L., Gemmell, B., Hoppner, B., Horn, C., Horz, K., Franklin, J., Jellineck, T., Jonasson, I., Kia, P., Muhlhan, N., Nickelsen, S., Percival, J., Perfit, M., Petersen, S., Schmidt, M., Seifert, T., Thiessen, O., Turkay, M., Tunnicliffe, V., and Winn, K., 1998, Volcanism, hydrothermal processes and biological communities at shallow submarine volcanoes of the New Ireland Fore-Arc (Papua New Guinea), Cruise Report SONNE-133,(BMBF FK 03G0133A) Manila-Kavieng-Rabaul-Suva, Freiberg University of Mining and Technology, p. 1–146.

Herzig, P.M., and Hannington, M.D., 1995, Hydrothermal activity, vent fauna, and submarine gold mineralization at alkaline fore-arc seamounts near Lihir Island, Papua New Guinea: Pacific Rim Congress, Melbourne, Australia, 1995, p. 279–284.

Hill, C.A., 1987, Geology of Carlsbad cavern and other caves in the Guadalupe Mountains, New Mexico and Texas: New Mexico Bureau of Mines & Mineral Resources, Bulletin 117, p. 150.

Hohnen, P.D., 1978, Geology of New Ireland, Papua New Guinea, 194, Bureau of Mineral Resources, Geology and Geophysics, p. 1–39.

Holdsworth, R.E., 2004, Weak faults – Rotten cores: Science, v. 303, p. 181–182.

Hole, M.J., Rogers, G., Saunders, A.D., and Storey, M., 1991, Relation between alkalic volcanism and slab-window formation: Geology, v. 19, p. 657–660.

Holland, H.D., 1965, Some applications of thermochemical data to problems of ore deposits II: Mineral assemblages and the composition of ore forming fluids: Economic Geology, v. 60, p. 1101–1166.

Holland, H.D., and Malinin, S.D., 1979, The solubility and occurrence of non-ore minerals, *in* Barnes, H.L., ed., Geochemistry of hydrothermal ore deposits, 2nd ed.: New York, John Wiley & Sons, p. 461–508.

Holm, R.J., and Richards, S.W., 2013, A re-evaluation of arc-continent collision and along-arc variation in the Bismarck Sea region, Papua New Guinea: Australian Journal of Earth Sciences, v. 60, p. 605–619.

Holm, R.J., Spandler, C., and Richards, S.W., 2013, Melanesian arc far-field response to collision of the Ontong Java Plateau: Geochronology and petrogenesis of the Simuku Igneous Complex, New Britain, Papua New Guinea: Tectonophysics, v. 603, p. 189–212.

Hope, A., 2011, The hope factor: Mineral discoveries in Australia, Papua New Guinea and the Philippines, 507 p.

Humphris, S.E., Herzig, P., Miller, D., Alt, J., Becker, K., Brown, D., Brügmann, G., Chiba, H., Fouquet, Y., and Gemmell, J., 1995, The internal structure of an active sea-floor massive sulphide deposit: Nature, v. 377, p. 713–716.

Huston, D.L., Sie, S.H., Suter, G.F., Cooke, D.R., and Both, R.A., 1995, Trace-elements in sulfide minerals from Eastern Australian volcanic-hosted massive sulfide deposits: Part 1. Proton microprobe analyses of pyrite, chalcopyrite and sphalerite, and Part 2. Selenium levels in pyrite: Comparison with $\delta^{34}S$ values and implications for the source of sulfur in volcanogenic hydrothermal systems: Economic Geology, v. 90, p. 1167–1196.

International Seismological Centre, 2016, On-line bulletin, International Seismological Centre, April 2016: Thatcham, United Kingdom, International Seismological Centre.

Ireland, T., Clement, S., Compston, W., Foster, J., Holden, P., Jenkins, B., Lanc, P., Schram, N., and Williams, I., 2008, Development of SHRIMP: Australian Journal of Earth Sciences, v. 55, p. 937–954.

Irvine, T.N., and Baragar, W.R.A., 1971, A guide to the chemical classification of the common volcanic rocks: Canadian Journal of Earth Sciences, v. 8, p. 523–548.

Jébrak, M., 1997, Hydrothermal breccias in vein-type ore deposits: A review of mechanisms, morphology and size distribution: Ore Geology Reviews, v. 12, p. 111–134.

Jensen, E.P., 2003, Magmatic and hydrothermal evolution of the Cripple Creek gold deposit, Colorado, and comparisons with regional and global magmatic-hydrothermal systems associated with alkaline magmatism: Unpublished PhD thesis, University of Arizona, 846 p.

Jensen, E.P., and Barton, M.D., 2000, Gold deposits related to alkaline magmatism: Reviews in Economic Geology, v. 13, p. 279–314.

Johnson, R.W., Mackenzie, D.E., and Smith, I.E.M., 1978a, Delayed partial melting of subduction-modified mantle in Papua New Guinea: Tectonophysics, v. 46, p. 197–216.

Johnson, R.W., Mackenzie, D.E., and Smith, I.E.M., 1978b, Volcanic rock associations at convergent plate boundaries: Reappraisal of the concept using case histories from Papua New Guinea: Geological Society of America Bulletin, v. 89, p. 96–106.

Johnson, R.W., Wallace, D.A., and Ellis, D.J., 1976, Feldspathoid-bearing potassic rocks and associated types from volcanic islands off the coast of New Ireland, Papua New Guinea: A preliminary account of geology and petrology, *in* Johnson, R.W., ed., Volcanism in Australasia, Elsevier Amsterdam, p. 297–316.

Johnstone, R., Brown, K., and Bruce, C., 2007, Geothermal geochemistry Lihir gold mine, Papua New Guinea: New Zealand Geochemical and Mineralogical Society Newsletter, p. 3–4.

Kamber, B.S., and Webb, G.E., 2001, The geochemistry of late Archaean microbial carbonate: Implications for ocean chemistry and continental erosion history: Geochimica et Cosmochimica Acta, v. 65, p. 2509–2525.

Kamenov, G.D., Perfit, M.R., Mueller, P.A., and Jonasson, I.R., 2008, Controls on magmatism in an island arc environment: Study of lavas and sub-arc xenoliths from the Tabar-Lihir-Tanga-Feni island chain, Papua New Guinea: Contributions to Mineralogy and Petrology, v. 155, p. 635–656.

Katsura, T., and Nagashima, S., 1974, Solubility of sulfur in some magmas at 1 atmosphere: Geochimica et Cosmochimica Acta, v. 38, p. 517–531.

Kelly, W.C., and Rye, R.O., 1979, Geologic, fluid inclusion, and stable isotope studies of the tin-tungsten deposits of Panasqueira, Portugal: Economic Geology, v. 74, p. 1721–1822.

Kennedy, A.K., Groves, D.I., and Johnson, R.W., 1990a, Experimental and major element contraints on the evolution of lavas from Lihir Island, Papua New Guinea: Contributions to Mineralogy and Petrology, v. 104, p. 722–734.

Kennedy, A.K., Hart, S.R., and Frey, F.A., 1990b, Composition and isotopic constraints on the petrogenesis of alkaline arc lavas, Lihir Island, Papua New Guinea: Journal of Geophysical Research: Solid Earth, v. 95, p. 6929–6942.

Kidd, R.P., and Robinson, J.R., 2004, A review of the Kapit orebody, Lihir Island Group, Papua New Guinea, Pacific Rim Congress: Adelaide, Australia, p. 323–331.

Klein, E.M., and Langmuir, C.H., 1987, Global correlations of ocean ridge basalt chemistry with axial depth and crustal thickness: Journal of Geophysical Research: Solid Earth, v. 92, p. 8089–8115.

Klemm, D.D., 1965, Synthesen und Analysen in den Dreiecksdiagrammen FeAsS-CoAsS-NiAsS und FeS_2-CoS_2-NiS_2: Neues Jahrbuch für Mineralogie, v. 103, p. 205–255.

Knesel, K.M., Cohen, B.E., Vasconcelos, P.M., and Thiede, D.S., 2008, Rapid change in drift of the Australian plate records collision with Ontong Java plateau: Nature, v. 454, p. 754–757.

Koehn, D., and Passchier, C.W., 2000, Shear sense indicators in striped bedding-veins: Journal of Structural Geology, v. 22, p. 1141–1151.

Kouzmanov, K., Ramboz, C., Bailly, L., and Bogdanov, K., 2004, Genesis of high-sulfidation vinciennite-bearing Cu–As–Sn (< Au) assemblage from the Radka epithermal copper deposit, Bulgaria: Evidence from mineralogy and infrared microthermometry of enargite: The Canadian Mineralogist, v. 42, p. 1501–1521.

Kouzmanov, K., Pettke, T., and Heinrich, C.A., 2010, Direct analysis of ore-precipitating fluids: Combined IR microscopy and LA-ICP-MS study of fluid inclusions in opaque ore minerals: Economic Geology, v. 105, p. 351–373.

Kroenke, L.W., and Rodda, P., 1984, Cenozoic tectonic development of the Southwest Pacific, Technical bulletin 6, United Nations Economic and Social Commission for Asia and the Pacific, p. 1–106.

Kroenke, L.W., Wessel, P., and Sterling, A., 2004, Motion of the Ontong Java Plateau in the hot-spot frame of reference: 122 Ma–present, *in* Fitton, J.G., Mahoney, J.J., Wallace, P.J., and Saunders, A.D., eds., Origin and evolution of the Ontong Java Plateau, Macmillan Publishers Ltd., p. 9–20.

Krupp, R.E., and Seward, T.M., 1987, The Rotokawa geothermal system, New-Zealand: An active epithermal gold-depositing environment: Economic Geology, v. 82, p. 1109–1129.

Krupp, R.E., and Seward, T.M., 1990, Transport and deposition of metals in the Rotokawa geothermal system, New Zealand: Mineralium Deposita, v. 25, p. 7–81.

Kuhn, T., Herzig, P.M., Hannington, M.D., Garbe-Sehonberg, D., and Stoffers, P., 2003, Origin of fluids and anhydrite precipitation in the sediment-hosted Grimsey hydrothermal field north of Iceland: Chemical Geology, v. 202, p. 5–21.

Lagmay, A.M.F., de Vries, B.V., Kerle, N., and Pyle, D.M., 2000, Volcano instability induced by strike-slip faulting: Bulletin of Volcanology, v. 62, p. 331–346.

Lang, J.R., Lueck, B., Mortensen, J.K., Russell, J.K., Stanley, C.R., and Thompson, J.F.H., 1995, Triassic–Jurassic silica-undersaturated and silica-saturated alkalic intrusions in the Cordillera of British Columbia: Implications for arc magmatism: Geology, v. 23, p. 451–454.

Large, R.R., Danyushevsky, L., Hollit, C., Maslennikov, V., Meffre, S., Gilbert, S., Bull, S., Scott, R., Emsbo, P., Thomas, H., Singh, B., and Foster, J., 2009, Gold and trace element zonation in pyrite using a laser imaging technique: Implications for the timing of gold in orogenic and Carlin-style sediment-hosted deposits: Economic Geology, v. 104, p. 635–668.

Latti, D., Doyle, J., and Adair, B.J.I., 2001, A QEM * SEM study of a suite of pressure leach products from a gold circuit: Minerals Engineering, v. 14, p. 1671–1678.

Lawlis, E., in prep., Geology and geochemistry of the Kapit NE prospect, Lihir gold deposit, Papua New Guinea: Unpublished PhD thesis, University of Tasmania, Australia.

Lawlis, E., Cooke, D.R., and Harris, A.C., 2015, Volcanic-hydrothermal breccias at the Lihir alkalic gold deposits, Papua New Guinea: 13th Biennial SGA Meeting, Nancy, France, 24–27 August, 2015, p. 317–320.

Laznicka, P., 1988, Breccias and coarse fragmentites: Petrology, environments, associations, ores. Developments in Economic Geology Series: Amsterdam, Elsevier, 832 p.

Leslie, R.A.J., Danyushevsky, L.V., Crawford, A.J., and Verbeeten, A.C., 2009, Primitive shoshonites from Fiji: Geochemistry and source components: Geochemistry Geophysics Geosystems, v. 10, p. 1–24.

Licence, P., Terrill, J., and Fergusson, L., 1987, Epithermal gold mineralisation, Ambitle Island, Papua New Guinea: Pacific Rim Congress, 1987, p. 273–278.

Lindley, I.D., 1988, Early Cainozoic stratigraphy and structure of the Gazelle Peninsula, East New Britain: An example of extensional tectonics in the New Britain arc-trench complex: Australian Journal of Earth Sciences, v. 35, p. 231–244.

Lindley, I.D., 2015, Late Quaternary geology of Ambitle Volcano, Feni Island Group, Papua New Guinea: Australian Journal of Earth Sciences, v. 62, p. 529–545.

Lindley, I.D., 2016, Plate flexure and volcanism: Late Cenozoic tectonics of the Tabar–Lihir–Tanga–Feni alkalic province, New Ireland Basin, Papua New Guinea: Tectonophysics, p. 312–323.

Longerich, H.P., Jackson, S.E., and Günther, D., 1996, Inter-laboratory note. Laser ablation inductively coupled plasma mass spectrometric transient signal data acquisition and analyte concentration calculation: Journal of Analytical Atomic Spectrometry, v. 11(9), p. 899–904.

Longo, A.A., Dilles, J.H., Grunder, A.L., and Duncan, R., 2010, Evolution of calc-alkaline volcanism and associated hydrothermal gold deposits at Yanacocha, Peru: Economic Geology, v. 105, p. 1191–1240.

López, D.L., and Williams, S.N., 1993, Catastrophic volcanic collapse: Relation to hydrothermal processes: Science, v. 260, p. 1794–1796.

Lowell, J.D., and Guilbert, J.M., 1970, Lateral and vertical alteration-mineralization zoning in porphyry ore deposits: Economic Geology, v. 65, p. 373–408.

Macdonald, G.A., 1968, Composition and origin of Hawaiian lavas: Geological Society of America Memoirs, v. 116, p. 477–522.

Mann, P., and Taira, A., 2004, Global tectonic significance of the Solomon Islands and Ontong Java Plateau convergent zone: Tectonophysics, v. 389, p. 137–190.

Marschik, R., and Fontboté, L., 2001, The Candelaria-Punta del Cobre iron oxide Cu-Au (-Zn-Ag) deposits, Chile: Economic Geology, v. 96, p. 1799–1826.

Martinez, F., and Taylor, B., 1996, Back arc spreading, rifting and microplate rotation, between transform faults in the Manus basin: Marine Geophysical Researches, v. 18, p. 203–224.

Masterman, G., 2003, Geology of the Rosario Cu-Mo-Ag Mine, Collahuasi, Chile: Unpublished PhD thesis, University of Tasmania, Australia, 253 p.

Mathieu, L., and de Vries, B.V., 2011, The impact of strike-slip, transtensional and transpressional fault zones on volcanoes. Part 1: Scaled experiments: Journal of Structural Geology, v. 33, p. 907–917.

Mathieu, L., van Wyk de Vries, B., Pilato, M., and Troll, V.R., 2011, The interaction between volcanoes and strike-slip, transtensional and transpressional fault zones: Analogue models and natural examples: Journal of Structural Geology, v. 33, p. 898–906.

McInnes, B.I.A., and Cameron, E.M., 1994, Carbonated, alkaline hybridizing melts from a sub-arc environment: Mantle wedge samples from the Tabar–Lihir–Tanga–Feni arc, Papua New Guinea: Earth and Planetary Science Letters, v. 122, p. 125–141.

McInnes, B.I.A., Gregoire, M., Binns, R.A., Herzig, P.M., and Hannington, M.D., 2001, Hydrous metasomatism of oceanic sub-arc mantle, Lihir, Papua New Guinea: Petrology and geochemistry of fluid-metasomatised mantle wedge xenoliths: Earth and Planetary Science Letters, v. 188, p. 169–183.

Micko, J., 2010, The geology and genesis of the Central Zone alkalic copper-gold porphyry deposit, Galore Creek district, northwestern British Columbia, Canada: Unpublished PhD thesis, University of British Columbia, Canada, 359 p.

Mills, R., and Tivey, M., 1999, Seawater entrainment and fluid evolution within the TAG hydrothermal mound: evidence from analyses of anhydrite*, in* Cann, J.R., Elderfield, H., and Laughton, A.S., eds., Mid-ocean ridges: Dynamics of processes associated with creation of new ocean crust, p. 225–248.

Mills, R.A., Teagle, D.A., and Tivey, M.K., 1998, Fluid mixing and anhydrite precipitation within the TAG mound, *in* Herzig, P.M., Humphris, S.E., Miller, D.J., and Zierenberg, R.A., eds., Proceedings of the Ocean Drilling Program, Scientific Results, 158, p. 119–127.

Moyle, A.J., Doyle, B.J., Hoogvliet, H., and Ware, A.R., 1990, Ladolam gold deposit, Lihir Island, *in* Hughes, F.E., ed., Geology of the mineral deposits of Australia and Papua New Guinea, 14: Melbourne, Australia, The Australasian Institute of Mining and Metallurgy, p. 1793–1805.

Müller, D., Franz, L., Herzig, P.M., and Hunt, S., 2001, Potassic igneous rocks from the vicinity of epithermal gold mineralization, Lihir Island, Papua New Guinea: Lithos, v. 57, p. 163–186.

Müller, D., Franz, L., Petersen, S., Herzig, P.M., and Hannington, M.D., 2003, Comparison between magmatic activity and gold mineralization at Conical Seamount and Lihir Island, Papua New Guinea: Mineralogy and Petrology, v. 79, p. 259–283.

Müller, D., Herzig, P., Scholten, J., and Hunt, S., 2002a, Ladolam gold deposit, Lihir Island, Papua New Guinea: Gold mineralization hosted by alkaline rocks: Society of Economic Geologists, Special Publication, no. 9, p. 367–382.

Müller, D., Kaminski, K., Uhlig, S., Graupner, T., Herzig, P.M., and Hunt, S., 2002b, The transition from porphyry- to epithermal-style gold mineralization at Ladolam, Lihir Island, Papua New Guinea: A reconnaissance study: Mineralium Deposita, v. 37, p. 61–74.

Müller, W.H., Schmid, S.M., and Briegel, U., 1981, Deformation experiments on anhydrite rocks of different grain sizes: Rheology and microfabric: Tectonophysics, v. 78, p. 527–543.

Neal, C.R., Mahoney, J.J., Kroenke, L.W., Duncan, R.A., and Petterson, M.G., 1997, The Ontong Java Plateau, *in* Mahoney, J.J., and Coffin, M.F., eds., Large igneous provinces: Continental, oceanic and planetary flood volcanism, Geophysical Monograph 100, American Geophysical Union, p. 183–216.

Nenna, F., and Aydin, A., 2011, The formation and growth of pressure solution seams in clastic rocks: A field and analytical study: Journal of Structural Geology, v. 33, p. 633–643.

Newcrest Mining Ltd., 2015, Lihir fact sheets, October 2015 http://www.newcrest.com.au/, October 2016.

Newcrest Mining Ltd., 2016, Annual mineral resources and ore reserves statement market release, 31 December 2015 http://www.newcrest.com.au/, May 2016.

Numelin, T., Marone, C., and Kirby, E., 2007, Frictional properties of natural fault gouge from a low-angle normal fault, Panamint Valley, California: Tectonics, v. 26, p. 1–14.

O'Kane, T., 2008, 3-D structure and tectonic evolution of the Papua New Guinea and Solomon Islands region and its relationship to Cu–Au mineralization: Unpublished BSc Honours thesis, Australian National University, 74 p.

Ogawa, Y., Shikazono, N., Ishiyama, D., Sato, H., Mizuta, T., and Nakano, T., 2007, Mechanisms for anhydrite and gypsum formation in the Kuroko massive sulfide-sulfate deposits, north Japan: Mineralium Deposita, v. 42, p. 219–233.

Ohmoto, H., 1986, Stable isotope geochemistry of ore deposits: Reviews in Mineralogy and Geochemistry, v. 16, p. 491–559.

Ohmoto, H., and Rye, R.O., 1979, Isotopes of sulfur and carbon, *in* Barnes, H.L., ed., Geochemistry of hydrothermal ore deposits, 2nd ed.: New York, John Wiley & Sons, p. 509–567.

Ohmoto, H., and Skinner, B.J., 1983, The Kuroko and related volcanogenic massive sulfide deposits, 608 p.

Olson, J.E., and Pollard, D.D., 1991, The initiation and growth of en échelon veins: Journal of Structural Geology, v. 13, p. 595–608.

Ossandón, G., Gustafson, L.B., Lindsay, D.D., and Zentilli, M., 2001, Geology of the Chuquicamata mine: A progress report: Economic Geology, v. 96, p. 249–270.

Page, R., and Johnson, R., 1974, Strontium isotope ratios of Quaternary volcanic rocks from Papua New Guinea: Lithos, v. 7, p. 91–100.

Pascal, G., 1979, Seismotectonics of the Papua New Guinea–Solomon Islands region: Tectonophysics, v. 57, p. 7–34.

Pass, H.E., 2010, Breccia-hosted chemical and mineralogical zonation patterns of the northeast zone, Mt. Polley Cu-Ag-Au alkalic porphyry deposit, British Columbia, Canada: Unpublished PhD thesis, University of Tasmania, 219 p.

Pass, H.E., Cooke, D.R., Davidson, G., Maas, R., Dipple, G., Rees, C., Ferreira, L., Taylor, C., and Deyell, C.L., 2014, Isotope geochemistry of the northeast zone, Mount Polley alkalic Cu-Au-Ag porphyry deposit, British Columbia: A case for carbonate assimilation: Economic Geology, v. 109, p. 859–890.

Passchier, C.W., and Simpson, C., 1986, Porphyroclast systems as kinematic indicators: Journal of Structural Geology, v. 8, p. 831–843.

Paytan, A., Kastner, M., Campbell, D., and Thiemens, M.H., 1998, Sulfur isotopic composition of Cenozoic seawater sulfate: Science, v. 282, p. 1459–1462.

Peterman, Z.E., Hedge, C.E., and Tourtelo.Ha, 1970, Isotopic composition of strontium in sea water throughout Phanerozoic time: Geochimica et Cosmochimica Acta, v. 34, p. 105–120.

Petersen, U., 1972, Nuevas investigaciones de yacimientos peruanos: Bulletin of the Geological Society of Peru, v. 42, p. 36–52.

Peterson, E.C., and Mavrogenes, J.A., 2014, Linking high-grade gold mineralization to earthquake-induced fault-valve processes in the Porgera gold deposit, Papua New Guinea: Geology, v. 42, p. 383–386.

Petterson, M.G., Neal, C.R., Mahoney, J.J., Kroenke, L.W., Saunders, A.D., Babbs, T.L., Duncan, R.A., Tolia, D., and McGrail, B., 1997, Structure and deformation of north and central Malaita, Solomon Islands: Tectonic implications for the Ontong Java Plateau Solomon arc collision, and for the fate of oceanic plateaus: Tectonophysics, v. 283, p. 1–33.

Phillips, W.J., 1972, Hydraulic fracturing and mineralisation: Journal of the Geological Society, v. 128, p. 337–359.

Pichler, T., Giggenbach, W.F., and Buhl, D., 1999, Fe sulfide formation due to the seawater-gas-sediment interaction in a shallow-water hydrothermal system at Lihir Island, Papua New Guinea: Economic Geology, v. 94, p. 281–287.

Plank, T., and Langmuir, C.H., 1988, An evaluation of the global variations in the major element chemistry of arc basalts: Earth and Planetary Science Letters, v. 90, p. 349–370.

Pollard, P.J., Taylor, R.G., and Peters, L., 2005, Ages of intrusion, alteration, and mineralization at the Grasberg Cu-Au deposit, Papua, Indonesia: Economic Geology, v. 100, p. 1005–1020.

Rae, A.J., Cooke, D.R., and Brown, K.L., 2011, The trace metal chemistry of deep geothermal water, Palinpinon geothermal field, Negros Island, Philippines: Implications for precious metal deposition in epithermal gold deposits: Economic Geology, v. 106, p. 1425–1446.

Rae, A.J., Ramirez, E.L., Villafuerte, G., Kilgour, G., Milicich, S.D., and Fraser, H., 2010, Recent exploration drilling at Lihir geothermal field, PNG: Effects of catastrophic sector collapse on a magmatic–hydrothermal system: World Geothermal Congress, Bali, Indonesia, 2010, p. 25–29.

Ramsay, J.G., 1980, The crack-seal mechanism of rock deformation: Nature, v. 284, p. 135–139.

Ramsay, J.G., and Huber, M.I., 1983, The techniques of modern structural geology: Strain analysis: London, Academic Press Ltd.

Rees, C., Jenkins, W., and Monster, J., 1978, The sulphur isotopic composition of ocean water sulphate: Geochimica et Cosmochimica Acta, v. 42, p. 377–381.

Reich, M., Deditius, A., Chryssoulis, S., Li, J.W., Ma, C.Q., Parada, M.A., Barra, F., and Mittermayr, F., 2013, Pyrite as a record of hydrothermal fluid evolution in a porphyry copper system: A SIMS/EMPA trace element study: Geochimica et Cosmochimica Acta, v. 104, p. 42–62.

Reich, M., Kesler, S.E., Utsunomiya, S., Palenik, C.S., Chryssoulis, S.L., and Ewing, R.C., 2005, Solubility of gold in arsenian pyrite: Geochimica et Cosmochimica Acta, v. 69, p. 2781–2796.

Reid, M.E., Sisson, T.W., and Brien, D.L., 2001, Volcano collapse promoted by hydrothermal alteration and edifice shape, Mount Rainier, Washington: Geology, v. 29, p. 779–782.

Reyes, A.G., 1990, Petrology of Philippine geothermal systems and the application of alteration mineralogy to their assessment: Journal of Volcanology and Geothermal Research, v. 43, p. 279–309.

Richards, J.P., 1992, Magmatic-epithermal transitions in alkalic systems: Porgera gold deposit, Papua New Guinea: Geology, v. 20, p. 547–550.

Richards, J.P., 1995, Alkalic epithermal gold deposits: A review, *in* Thompson, J.F.H., ed., Mineralogical association of Canada short course, 23, p. 367–400.

Richards, J.P., and Kerrich, R., 1993, The Porgera gold mine, Papua New Guinea: Magmatic hydrothermal to epithermal evolution of an alkalic-type precious-metal deposit: Economic Geology, v. 88, p. 1017–1052.

Richards, J.P., Mcculloch, M.T., Chappell, B.W., and Kerrich, R., 1991, Sources of metals in the Porgera gold deposit, Papua New Guinea: Evidence from alteration, isotope, and noble-metal geochemistry: Geochimica Et Cosmochimica Acta, v. 55, p. 565–580.

Rickard, M.J., and Rixon, L.K., 1983, Stress configurations in conjugate quartz-vein arrays: Journal of Structural Geology, v. 5, p. 573–578.

Rivera, S., Alcota, H., Proffett, J., Díaz, J., Leiva, G., and Vergara, M., 2012, Update of the geologic setting and porphyry Cu-Mo deposits of the Chuquicamata district, northern Chile: Society of Economic Geologists Special Publication, no. 16, p. 19–54.

Robinson, B.W., and Kusakabe, M., 1975, Quantitative preparation of sulfur dioxide, for $^{34}S/^{32}S$ analyses, from sulfides by combustion with cuprous oxide: Analytical Chemistry, v. 47, p. 1179–1181.

Rogers, N.W., and Setterfield, T.N., 1994, Potassium and incompatible-element enrichment in shoshonitic lavas from the Tavua volcano, Fiji: Chemical Geology, v. 118, p. 43–62.

Rohrlach, B.D., and Loucks, R.R., 2005, Multi-million-year cyclic ramp-up of volatiles in a lower crustal magma reservoir trapped below the Tampakan copper-gold deposit by Mio-Pliocene crustal compression in the southern Philippines, *in* Porter, T.M., ed., Super porphyry copper and gold deposits: A global perspective, 2: Adelaide, PGC Publishing, p. 369–407.

Ronacher, E., Richards, J.P., Reed, M.H., Bray, C.J., Spooner, E.T.C., and Adams, P.D., 2004, Characteristics and evolution of the hydrothermal fluid in the North zone high-grade area, Porgera gold deposit, Papua New Guinea: Economic Geology, v. 99, p. 843–867.

Rye, R.O., 1993, The evolution of magmatic fluids in the epithermal environment: The stable isotope perspective: Economic Geology, v. 88, p. 733–753.

Rye, R.O., and Ohmoto, H., 1974, Sulfur and carbon isotopes and ore genesis: A Review: Economic Geology, v. 69, p. 826–842.

Rytuba, J.J., McKee, E.H., and Cox, D.P., 1993, Geochronology and geochemistry of the Ladolam gold deposit, Lihir Island, and gold deposits and volcanoes of Tabar and Tatau, Papua New Guinea: United States Geological Survey Bulletin, v. 2039, p. 119–126.

Sander, M.V., and Einaudi, M.T., 1990, Epithermal deposition of gold during transition from propylitic to potassic alteration at Round Mountain, Nevada: Economic Geology, v. 85, p. 285–311.

Schreiber, B.C., and Helman, M.L., 2005, Criteria for distinguishing primary evaporite features from deformation features in sulfate evaporites: Journal of Sedimentary Research, v. 75, p. 525–533.

Seedorff, E., Dilles, J.H., Proffett, J.M., Einaudi, M.T., Zurcher, L., Stavast, W.J.A., Johnson, D.A., and Barton, M.D., 2005, Porphyry deposits: characteristics and origin of hypogene features: Economic Geology v. 100, p. 251–298.

Sharp, W.D., and Clague, D.A., 2006, 50 Ma initiation of Hawaiian-Emperor bend records major change in Pacific plate motion: Science, v. 313, p. 1281–1284.

Shikazono, N., Holland, H.D., and Quirk, R.F., 1983, Anhydrite in Kuroko deposits: mode of occurrence and depositional mechanisms: Economic Geology Monograph Series, v. 5, p. 329–344.

Sibson, R.H., 1996, Structural permeability of fluid-driven fault-fracture meshes: Journal of Structural Geology, v. 18, p. 1031–1042.

Sibson, R.H., Robert, F., and Poulsen, K.H., 1988, High-angle reverse faults, fluid-pressure cycling, and mesothermal gold-quartz deposits: Geology, v. 16, p. 551–555.

Sielfeld, G., Cembrano, J., and Lara, L., 2017, Transtension driving volcano-edifice anatomy: Insights from Andean transverse-to-the-orogen tectonic domains: Quaternary International, v. 438a, p. 33–49.

Sillitoe, R.H., 1985, Ore-related breccias in volcanoplutonic arcs: Economic Geology, v. 80, p. 1467–1514.

Sillitoe, R.H., 1994, Erosion and collapse of volcanos: Causes of telescoping in intrusion-centered ore deposits: Geology, v. 22, p. 945–948.

Sillitoe, R.H., 2000, Gold-rich porphyry deposits: Descriptive and genetic models and their role in exploration and discovery: Reviews in Economic Geology, v. 13, p. 315–345.

Sillitoe, R.H., 2010, Porphyry copper systems: Economic Geology, v. 105, p. 3–41.

Sillitoe, R.H., Tolman, J., and Van Kerkvoort, G., 2013, Geology of the Caspiche porphyry gold-copper deposit, Maricunga Belt, northern Chile: Economic Geology, v. 108, p. 585–604.

Simmons, S.F., and Brown, K.L., 2006, Gold in magmatic hydrothermal solutions and the rapid formation of a giant ore deposit: Science, v. 314, p. 288–291.

Simmons, S.F., White, N.C., and John, D.A., 2005, Geological characteristics of epithermal precious and base metal deposits: Economic Geology 100th Anniversary Volume, v. 29, p. 485–522.

Simon, A.C., and Ripley, E.M., 2011, The role of magmatic sulfur in the formation of ore deposits: Reviews in Mineralogy and Geochemistry, v. 73, p. 513–578.

Sinclair, W.D., 2007, Porphyry deposits, Mineral deposits of Canada: A synthesis of major deposit-types, district metallogeny, the evolution of geological provinces, and exploration methods, Geological Association of Canada, Mineral Deposits Division, Special Publication, p. 223–243.

Sinton, J.M., Ford, L.L., Chappell, B., and McCulloch, M.T., 2003, Magma genesis and mantle heterogeneity in the Manus back arc basin, Papua New Guinea: Journal of Petrology, v. 44, p. 159–195.

Skewes, M., Arévalo, A., Floody, R., Zuñiga, P., and Stern, C.R., 2002, The giant El Teniente breccia deposit: Hypogene copper distribution and emplacement: Society of Economic Geologists, Special Publication, no. 9, p. 299–332.

Solomon, M., 1990, Subduction, arc reversal, and the origin of porphyry copper-gold deposits in island arcs: Geology, v. 18, p. 630–633.

Spycher, N., and Reed, M., 1986, Boiling of geothermal waters, precipitation of base and precious metals, speciations of arsenic and antimony, and the role of gas phase metal transport: Proceedings of the workshop on geochemical modelling, Fallen Leaf Lake, 1986, p. 58–65.

Spycher, N.F., and Reed, M.H., 1989, Evolution of a Broadlands-type epithermal ore fluid along alternative P-T paths: Implications for the transport and deposition of base, precious, and volatile metals: Economic Geology, v. 84, p. 328–359.

Stracke, A., and Hegner, E., 1998, Rifting-related volcanism in an oceanic post-collisional setting: The Tabar-Lihir-Tanga-Feni (TLTF) island chain, Papua New Guinea: Lithos, v. 45, p. 545–560.

Strashimirov, S., and Kovachev, V., 1992, Temperatures of ore-formation in copper deposits from the Srednogorie zone based on fluid inclusion studies of minerals: Review of Bulgarian Geological Society, v. 53, p. 1–12.

Sykora, S., Selley, D., Cooke, D.R., and Harris, A.C., submitted May 2016, The structure of anhydrite-bearing veins and breccia veins at the Lihir gold deposit, Papua New Guinea: Economic Geology.

Sykora, S., Cooke, D.R., Meffre, S., Stepanov, S., Gardner, K., Selley, D., Scott, R., and Harris, A.C., submitted December 2016, Evolution of pyrite trace element compositions from porphyry-style and epithermal conditions at the Lihir gold deposit: Implications for ore genesis and mineral processing: Economic Geology.

Symonds, R.B., Rose, W.I., Bluth, G.J., and Gerlach, T.M., 1994, Volcanic-gas studies: Methods, results, and applications: Reviews in Mineralogy and Geochemistry, v. 30, p. 1–66.

Taylor, B., 1979, Bismarck Sea: Evolution of a back-arc basin: Geology, v. 7, p. 171–174.

Taylor, B., Crook, K., and Sinton, J., 1994, Extensional transform zones and oblique spreading centers: Journal of Geophysical Research: Solid Earth, v. 99, p. 19707–19718.

Taylor, B., and Karner, G., 1983, On the evolution of marginal basins: Reviews of Geophysics, v. 21, p. 1727–1741.

Taylor, B.E., 2007, Epithermal gold deposits, Mineral deposits of Canada: A synthesis of major deposit-types, district metallogeny, the evolution of geological provinces, and exploration methods, Geological Association of Canada, Mineral Deposits Division, Special Publication, p. 113–139.

Thode, H., and Monster, J., 1965, Sulfur-isotope geochemistry of petroleum, evaporites, and ancient seas, *in* Galley, J.E., ed., Fluids in subsurface environments, p. 367–377.

Thode, H.G., Monster, J., and Dunford, H.B., 1961, Sulphur isotope geochemistry: Geochimica et Cosmochimica Acta, v. 25, p. 159–174.

Thompson, T.B., Trippel, A.D., and Dwelley, P.C., 1985, Mineralized veins and breccias of the Cripple Creek district, Colorado: Economic Geology, v. 80, p. 1669–1688.

Tregoning, P., 2002, Plate kinematics in the western Pacific derived from geodetic observations: Journal of Geophysical Research: Solid Earth, v. 107, p. 1–7.

Tregoning, P., Jackson, R.J., McQueen, H., Lambeck, K., Stevens, C., Little, R.P., Curley, R., and Rosa, R., 1999, Motion of the South Bismarck Plate, Papua New Guinea: Geophysical Research Letters, v. 26, p. 3517–3520.

Tregoning, P., Lambeck, K., Stolz, A., Morgan, P., McClusky, S.C., van der Beek, P., McQueen, H., Jackson, R.J., Little, R.P., Laing, A., and Murphy, B., 1998, Estimation of current plate motions in Papua New Guinea from Global Positioning System observations: Journal of Geophysical Research: Solid Earth, v. 103, p. 12181–12203.

Tregoning, P., McQueen, H., Lambeck, K., Jackson, R., Little, R., Saunders, S., and Rosa, R., 2000, Present-day crustal motion in Papua New Guinea: Earth Planets and Space, v. 52, p. 727–730.

Ullrich, T., and Clark, A., 1999, The Candelaria copper-gold deposit, Region III, Chile: Paragenesis, geochronology and fluid composition: Mineral deposits: Processes to processing, Rotterdam, Balkema, 1999, p. 201–204.

Urai, J.L., Williams, P.F., and Vanroermund, H.L.M., 1991, Kinematics of crystal-growth in syntectonic fibrous veins: Journal of Structural Geology, v. 13, p. 823–836.

Verbeek, E.R., 1995, Activators in fluorescent minerals, *in* Warren, T.S., ed., Ultraviolet light and fluorescent minerals: Understanding, collecting, and displaying fluorescent minerals, Gem Guides Book Co, p. 135–201.

Villaguerte, G., Gumo, S., and Rodriguez, R., 2007, Mitigating geothermal hazards at Lihir gold mine, Large Open Pit Mining Conference: Perth, WA, Australia, p. 153–157.

Vogwill, R.I.J., Williamson, S., and Kote, J., 2009, Hydrogeology of the coastal mining area, Lihir gold mine, Papua New Guinea: Australian Journal of Earth Sciences, v. 56, p. 41–52.

Voight, B., and Elsworth, D., 1997, Failure of volcano slopes: Geotechnique, v. 47, p. 1–31.

Vry, V.H., Wilkinson, J.J., Seguel, J., and Millan, J., 2010, Multistage intrusion, brecciation, and veining at El Teniente, Chile: Evolution of a nested porphyry system: Economic Geology, v. 105, p. 119–153.

Wallace, D.A., Johnson, R.W., Chappell, B.W., Arculus, R.J., Perfit, M.R., and Crick, I.M., 1983, Cainozoic volcanism of the Tabar, Lihir, Tanga and Feni Islands, Papua New Guinea: Geology whole-rock analyses, and rock-forming mineral compositions, Australian Government Bureau of Mineral Resources, Geology and Geophysics, p. 1–140.

Wallace, L.M., Stevens, C., Silver, E., McCaffrey, R., Loratung, W., Hasiata, S., Stanaway, R., Curley, R., Rosa, R., and Taugaloidi, J., 2004, GPS and seismological constraints on active tectonics and arc-continent collision in Papua New Guinea: Implications for mechanics of microplate rotations in a plate boundary zone: Journal of Geophysical Research: Solid Earth, v. 109, p. 1–16.

Walshe, J.L., and Cleverley, J.S., 2009, Gold deposits: Where, when and why: Elements, v. 5, p. 288–288.

Walshe, J.L., and Solomon, M., 1981, An investigation into the environment of formation of the volcanic-hosted Mt. Lyell copper deposits using geology, mineralogy, stable isotopes, and a six-component chlorite solid solution model: Economic Geology, v. 76, p. 246–284.

Warnaars, F.W., Holmgren, C., and Barassi, S., 1985, Porphyry copper and tourmaline breccias at Los-Bronces-Rio-Blanco, Chile: Economic Geology, v. 80, p. 1544–1565.

Webb, G.E., and Kamber, B.S., 2000, Rare earth elements in Holocene reefal microbialites: A new shallow seawater proxy: Geochimica et Cosmochimica Acta, v. 64, p. 1557–1565.

Weissel, J.K., Taylor, B., and Karner, G.D., 1982, The opening of the Woodlark Basin, subduction of the Woodlark spreading system, and the evolution of Northern Melanesia since Mid-Pliocene time: Tectonophysics, v. 87, p. 253–277.

Wessel, P., and Kroenke, L.W., 2000, Ontong Java Plateau and late Neogene changes in Pacific plate motion: Journal of Geophysical Research: Solid Earth, v. 105, p. 28255–28277.

White, N.C., and Hedenquist, J.W., 1990, Epithermal environments and styles of mineralization: Variations and their causes, and guidelines for exploration: Journal of Geochemical Exploration, v. 36, p. 445–474.

White, P., Ussher, G., and Hermoso, D., 2010, Evolution of the Ladolam geothermal system on Lihir Island, Papua New Guinea: World Geothermal Congress, Bali, Indonesia, 2010, p. 25–29.

White, S.P., Creighton, A.L., Bixley, P.E., and Kissling, W.M., 2004, Modeling the dewatering and depressurization of the Lihir open-pit gold mine, Papua New Guinea: Geothermics, v. 33, p. 443–456.

Whitney, J., 1984, Volatiles in magmatic systems: Reviews in Economic Geology, v. 1, p. 155–175.

Willbold, M., Elliott, T., and Moorbath, S., 2011, The tungsten isotopic composition of the Earth's mantle before the terminal bombardment: Nature, v. 477, p. 195–198.

Williamson, A., 1983, Thermal activity on Lihir Island, New Ireland Province, Geological Survey of Papua New Guinea, Geological Survey of Papua New Guinea, p. 1–21.

Williford, K.H., Van Kranendonk, M.J., Ushikubo, T., Kozdon, R., and Valley, J.W., 2011, Constraining atmospheric oxygen and seawater sulfate concentrations during Paleoproterozoic glaciation: In situ sulfur three-isotope microanalysis of pyrite from the Turee Creek Group, Western Australia: Geochimica et Cosmochimica Acta, v. 75, p. 5686–5705.

Wilson, A.J., Cooke, D.R., Harper, B.J., and Deyell, C.L., 2007, Sulfur isotopic zonation in the Cadia district, southeastern Australia: Exploration significance and implications for the genesis of alkalic porphyry gold-copper deposits: Mineralium Deposita, v. 42, p. 465–487.

Woodcock, N.H., and Mort, K., 2008, Classification of fault breccias and related fault rocks: Geological Magazine, v. 145, p. 435–440.

Woodhead, J.D., Eggins, S.M., and Johnson, R.W., 1998, Magma genesis in the New Britain island arc: Further insights into melting and mass transfer processes: Journal of Petrology, v. 39, p. 1641–1668.